

MULTISCALE SIMULATION OF ATMOSPHERIC PRESSURE PULSED
DISCHARGES USED IN POLYMER SURFACE FUNCTIONALIZATION

BY

ANANTH NUGGEHALLI BHOJ

B.Tech., Indian Institute of Technology, Madras, 2001
M.S., University of Illinois at Urbana-Champaign, 2004

DISSERTATION

Submitted in partial fulfillment of the requirements
for the degree of Doctor of Philosophy in Chemical & Biomolecular Engineering
in the Graduate College of the
University of Illinois at Urbana-Champaign, 2006

Urbana, Illinois

CERTIFICATE OF COMMITTEE APPROVAL

University of Illinois at Urbana-Champaign
Graduate College

December 7, 2006

We hereby recommend that the thesis by:

ANANTH N. BHOJ

Entitled:

**MULTISCALE SIMULATION OF ATMOSPHERIC PRESSURE PULSED
DISCHARGES USED IN POLYMER SURFACE FUNCTIONALIZATION**

Be accepted in partial fulfillment of the requirements for the degree of:

Doctor of Philosophy

Signatures:



Director of Research - Professor Mark J. Kushner

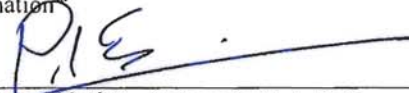


Head of Department - Professor Edmund G. Seebauer

Committee on Final Examination*



Chairperson - Professor Mark J. Kushner



Committee Member - Professor Paul J. A. Kenis



Committee Member - Professor Richard C. Alkire

Committee Member -



Committee Member - Professor Daniel Wayne Pack

Committee Member -

* Required for doctoral degree but not for master's degree

MULTISCALE SIMULATION OF ATMOSPHERIC PRESSURE PULSED DISCHARGES USED IN POLYMER SURFACE FUNCTIONALIZATION

Ananth Nuggehalli Bhoj, Ph.D.
Department of Chemical & Biomolecular Engineering
University of Illinois at Urbana-Champaign, 2006
Mark J. Kushner, Advisor

Atmospheric pressure pulsed plasma discharges are widely used for surface functionalization or treatment of commodity polymers to improve properties such as adhesion and wettability. Newer applications include textile fabric treatment to improve color fastness and biomedical surface functionalization. In this work, an unstructured mesh-based two-dimensional Plasma Equipment Model (PEM) was developed to investigate the physical and chemical processes in these discharges, which occur on temporal and spatial scales spanning many orders of magnitude and affect their interaction with polymer surfaces. Better insight into these processes will enable the tailoring and optimization of processing conditions.

Transient phenomena (time variation of plasma properties) during breakdown in atmospheric pressure discharges are addressed, since the spatial distribution of radicals generated in the discharge is determined by the dynamics of breakdown. The breakdown dynamics is governed by a multitude of physical and chemical processes such as reaction kinetics, photoionization, electron energy transport, charged species and neutral transport. The ability to address non-equilibrium electron energy transport in plasma discharges was developed by enhancing an existing electron Monte-Carlo simulation to address multiple regions of non-equilibrium, and was demonstrated for breakdown in high pressure discharges.

A high degree of uniformity in surface treatment is important for value-added materials. Increasing the proximity of reactive plasma produced species to the surface enables better uniformity, especially with polymers having complex surface shapes. The propagation of

atmospheric pressure discharges in microchannels, such as those used in lab-on-a-chip devices was investigated to determine the possibility of producing reactive gas-phase radicals within small spaces, close to the surfaces requiring treatment.

An integrated surface kinetics module was developed to address the cumulative surface treatment of polypropylene with microstructure, such as rough and porous surfaces, in repetitively pulsed O₂ and NH₃ containing discharges. Parameters such as gas composition, humidity, discharge polarity and applied power regulate the transport and reaction processes that ultimately affect the relative abundance and uniformity of various O and N surface functional groups. Electrons may penetrate gaps in the microstructure depending on discharge polarity and surface charging dynamics. The penetration of positive ions is limited due to ambipolar effects. Higher radical densities are produced near spaces in the microstructure in negative discharges. While reactive radicals are consumed here, slow-reacting radicals diffuse deeper into these spaces, treating surfaces not directly in the line-of-sight of the discharge over time. Photons generated in the discharge react with surface sites in the line-of-sight, increasing spatial non-uniformity in functionalization.

An integrated incompressible fluid dynamics model was developed to investigate the impact of gas flow on radical generation and surface treatment. Convective gas flow alters the relative abundance of reactive species in the discharge that affects the surface composition. Continuous surface processing was simulated, wherein radicals formed on the polymer move out of the discharge zone but continue to react downstream. Changes in gas composition affect the relative importance of local reaction kinetics and convective transport of reactive species in the discharge.

ACKNOWLEDGEMENTS

I am most grateful to my advisor Prof. Mark J. Kushner for introducing me to the world of low temperature plasmas and providing me numerous opportunities to deepen my knowledge and enhance my professional skills. I also thank him for his patience and his guidance, insights and cooperation that were instrumental in making this thesis a reality. I am also grateful to the members of my committee – Prof. Richard Alkire, Prof. Paul Kenis and Prof. Dan Pack for their many thoughtful comments and suggestions.

I am thankful to the past and present members of the Optical and Discharge Physics Group for their friendship and support – Rajesh Dorai, Arvind Sankaran, Pramod Subramonium, Alex Vasenkov, Richard Moss, Kapil Rajaraman, Vivek Vyas, Shane Stafford, Kelly Collier, Junqing Lu, Ramesh Arakoni, Ankur Agarwal, Natalia Babaeva and Yang Yang. I'd like to acknowledge the staff at the Dean's office and Chemical and Biomolecular Engineering at Iowa State for helping make a transition to the Ames campus. Many thanks also to Deb Vance at Iowa State for helping me through a lot of important paperwork in a relatively short period of time. I'd also like to thank Nena Richards in Chemical and Biomolecular Engineering at Urbana for helping with scheduling and paperwork related to my defense.

I'd like to acknowledge the support of many friends both on the Urbana-Champaign and the Ames campuses who made my stay enjoyable. My parents and brother and many relatives have been always very supportive of me throughout the many years of my education. I am deeply grateful to them for their unwavering love and encouragement. Finally, I'd like to acknowledge the energies of many *samskaras* and *deekshas* bestowed on me that've guided my life and helped me stay focused over the long duration of my graduate career.

TABLE OF CONTENTS

1. INTRODUCTION	1
1.1 Plasma Treatment of Polymer Surfaces	1
1.2 Modeling of Atmospheric Pressure Discharges.....	7
1.3 Figures.....	13
1.4 References.....	20
2. DESCRIPTION OF THE MODEL	26
2.1 Introduction.....	26
2.2 Geometry and Mesh Generation	26
2.3 Plasma Dynamics Module	27
2.4 Fluid Dynamics Module	39
2.5 Surface Kinetics Module.....	42
2.6 Reaction Mechanisms	45
2.7 Concluding Remarks.....	61
2.8 Figures.....	62
2.9 References.....	65
3. BREAKDOWN DYNAMICS IN ATMOSPHERIC PRESSURE DISCHARGES	68
3.1 Introduction.....	68
3.2 Geometry and Reaction Mechanism.....	69
3.3 Breakdown Dynamics in Negative Air Discharge.....	71
3.4 Breakdown Dynamics in Positive Air Discharge	73
3.5 Effect of Voltage on Breakdown Dynamics	76
3.6 Concluding Remarks.....	77
3.7 Figures.....	79
3.8 References.....	98
4. NON-EQUILIRBIUM ELECTRON TRANSPORT USING MONTE-CARLO METHODS ON AN ADAPTIVE MESH.....	100
4.1 Introduction.....	100
4.2 Description of the Model	102
4.3 Ar Discharges at 10s Torr.....	105
4.4 Breakdown in Corona Discharges at 100s Torr.....	109
4.5 Concluding Remarks.....	111
4.6 Figures.....	113
4.7 References.....	126

5. ATMOSPHERIC PRESSURE DISCHARGES IN SMALL SPACES	127
5.1 Introduction.....	127
5.2 Streamer Propagation through Microchannels.....	129
5.3 Effect of Microchannel Characteristics on Discharge Propagation	132
5.4 Concluding Remarks.....	138
5.5 Figures.....	140
5.6 References.....	169
6. TREATMENT OF ROUGH POLYMER SURFACES IN REPETITIVELY PULSED O ₂ DISCHARGES	171
6.1 Introduction.....	171
6.2 Reactor Configuration and Reaction Mechanism.....	174
6.3 Surface Treatment in Humid Air Discharges.....	176
6.4 Surface Treatment in He/O ₂ /H ₂ O Discharges.....	181
6.5 Concluding Remarks.....	185
6.6 Figures.....	187
6.7 References.....	205
7. TREATMENT OF ROUGH SURFACES AND POROUS POLYMER MICROSPHERES IN PULSED NH ₃ AND O ₂ DISCHARGES	206
7.1 Introduction.....	206
7.2 Treatment of Rough Polymer Surfaces.....	209
7.3 Treatment of Porous Surfaces.....	212
7.4 Concluding Remarks.....	217
7.5 Figures.....	218
7.6 References.....	236
8. CONTINUOUS PROCESSING OF POLYMERS IN REPETITIVELY PULSED DISCHARGES WITH GAS FLOW.....	237
8.1 Introduction.....	237
8.2 Repetitively Pulsed He/O ₂ /H ₂ O Discharge.....	238
8.3 Effect of Gas Composition and Surface Residence Time.....	242
8.4 Effect of Gas Flow Rate.....	246
8.5 Multiple Pulsed Discharges	248
8.6 Concluding Remarks.....	250
8.7 Figures.....	251
8.8 References.....	269
APPENDIX A: LIST OF REACTIONS FOR HUMID AIR.....	270
A.1 References.....	278

APPENDIX B: LIST OF REACTIONS FOR He/O ₂ /H ₂ O MIXTURES	280
B.1 References	289
APPENDIX C: LIST OF REACTIONS FOR He/NH ₃ MIXTURES	292
C.1 References	302
APPENDIX D: POLYPROPYLENE SURFACE REACTION CHEMISTRY	306
D.1 References	308

1. INTRODUCTION

1.1 Plasma Treatment of Polymer Surfaces

Polymers are used in a wide variety of applications and commonly categorized into fibers, plastics and elastomers depending on the modulus of elasticity.[1] Fibers include commonly used textiles such as polyester, nylon and acrylic. Commodity plastics such as polypropylene and polyethylene are used for packaging in the food processing industry. Styrene-butadiene is a common elastomer used in the manufacture of tires and gaskets. Polymers are also used extensively in automobile parts, specialized high-value components in electronic devices, as biomedical substrates, in medicines and artificial organs. Other types of polymers include coatings and adhesives such as phenol-formaldehyde, frequently used in the wood industry to bond plywood. Medical polymers are an important class of materials in their own right and are widely used in tissue engineering and medical devices that are implanted in thousands of people every year. Polystyrene is one of the commonly used substrates for tissue culture applications and polyurethane is used to make artificial hearts.

The selection and design of a polymer for a particular application depends on the desired bulk properties such as elasticity, strength, weight and corrosion resistance as well as surface physico-chemical properties such as adhesion and reactivity, besides primary economic considerations.[2,3] From a design point of view, many polymers usually meet application-specific bulk property requirements, but very few actually possess essential surface properties such as hydrophilicity, roughness, and adhesivity that may be critical to the application.[4,5] For instance, most hydrocarbon polymers are hydrophobic and have low surface energies, whereas surface wettability is an important criterion for adhesion in many commercial applications.[6]

Biomedical polymers need to satisfy more stringent criteria for their applications. Knee implants that should be able to withstand the mechanical stresses of everyday use and vascular grafts need to have reliable anti-coagulant properties.[7, 8] While the mechanical considerations are governed by both surface and bulk properties, the biological interactions of the implants are dominated by the *in-vivo* surface interactions of the polymer.[9] The requirements for surfaces for biocompatibility can be quite different from those for adhesive bonding and so the surface treatment will vary depending on the application and the polymer structure. Most polymers are often treated or functionalized with the rationale of modifying their surface behavior while retaining the bulk properties. A number of different methods [10] are used for surface functionalization. They include flame treatments [11], wet processing [12], ultraviolet irradiation [13], ozone activation [14], ion beams [15] besides self assembled monolayer techniques [16] and technological plasmas [17, 18]. The technique chosen depends on the practical suitability for the polymer, the application it is being used for, safety, economics of scaling-up, and environmental effects.

Technological plasmas or low temperature non-equilibrium plasmas refer to partially ionized gases with electrons at highly elevated temperatures (few to 10s of eV) that are larger than the ion and neutral gas temperatures, which remain close to room temperature. A variety of plasma sources have been developed for the processing of gases and surfaces.[19] Plasmas are integral to a number of technologies from remediation of toxic gases to plasma display panels.[20, 21] Plasmas sustained at low pressures (usually < 1 Torr) are extensively used to etch and deposit materials in the semiconductor industry for microelectronics fabrication.[22]

There is great interest in the use of plasmas to produce desired surface properties on polymer surfaces by surface functionalization.[23] Surface functionalization refers to the

alteration of the chemical composition of the top few surface layers. The words ‘treatment’, ‘functionalization’ and ‘modification’ are used interchangeably. Surface functionalization using plasmas involves the reactive species including ions, electrons, radicals and photons generated in the plasma. These species are transported to the surface and where they react to alter surface composition and bring about marked changes in surface properties. The process is dry which eliminates the need for subsequent cleaning and waste disposal when using liquids. Materials like expanded polytetrafluoroethylene (e-PTFE) have been functionalized in radio frequency glow discharges, similar to the low pressure plasma reactors used in the microelectronics industry.[24]

In the industry, a class of technological plasmas that operate around atmospheric pressure has been widely used for surface functionalization of polymers for many years. The primary advantage of using atmospheric pressure plasma treatment is the absence of expensive vacuum equipment required for low pressure operation. Typical examples of such devices are the dielectric barrier discharge (DBD), shown in Fig. 1, also called the ‘corona discharge’.[25, 26] The device is about 1 m wide and uses roller drums rotating at controlled speeds to move polymer sheets across the device to enable continuous treatment in a web arrangement. In industry, these systems tend to be used for functionalization of low-value added, commodity materials, such as polypropylene used in packaging. Functionalization improves the surface energy and consequently the wettability and adhesion properties of these polymer surfaces.

A schematic for the web treatment of polymer films is in Fig. 2. The apparatus consists of a powered electrode embedded within dielectric structure that is exposed to the processing gas at its tip. There is a gas gap of a few mm between the powered electrode and the polymer which is placed on the grounded surface. The discharge is generated by the application of few to 10s of

kVs voltage pulses at a few to 10s of kHz to breakdown the gas gap. Discharges generated at atmospheric pressure may be either diffuse or filamentary; a condition which depends on the gas composition and other factors such as the frequency of pulsing.[27-29] Typically, the gas is simply room air or O₂ containing mixtures, but other gases and mixtures including Ar, He, N₂, and NH₃ plasmas have also been used for polymer surface functionalization.[30-36] A range of polymers such as polypropylene [37], polyethylene [38], polyetheretherketone [39 used in packaging, polyamide fibers [40], polymethylmethacrylate [41], polystyrene [42], polyethylene terephthalate [43], polytetrafluoroethylene [44] and polyvinyl chloride [45] have been functionalized using plasmas.

Commodity polymers like polypropylene and polyethylene are routinely treated in atmospheric pressure plasmas for a few cents per m² to incorporate oxygen atoms on the surface. For example, untreated pure polypropylene (PP) is not amenable to printing and adhesion because of its low surface energy. Plasma treatment in air was found to add different polar O containing groups [46] such as alcohol (C–OH), carbonyl (C=O), peroxy (C–OO) and carboxylic acid (C=O(OH)) to the PP surface (Fig. 3), that increased its hydrophilic character. The improved hydrophilic character of another polymer, poly(D,L-lactide) after plasma treatment using the sessile drop method is evident in Fig. 4. Similarly, the peel strength of polyethylene was increased by a factor of 2 after plasma treatment as shown in Fig. 5. Ammonia plasma treatment results in N containing functional groups such as amine (C–NH₂), imine (C=NH) on the hydrocarbon surface that support the immobilization of specific macromolecules through covalent bonding. For instance, chitosan when covalently immobilized on ammonia-plasma treated PP surfaces exhibits strong antimicrobial activity and is used for food packaging.[47]

More recently, there has been greater interest in using plasma treatments to modify the surface properties of natural and synthetic textiles since it is environmentally benign compared to wet processing techniques. Textile fibers have been plasma-treated and found to improve properties such as color fastness and hydrophobicity.[48] Functionalizing the surface with F atoms using fluorine containing plasmas is known to increase hydrophobicity by decreasing the surface energy. Some of the issues that have been investigated include the ability of the plasma to penetrate into the complex surface features and retain the ability to uniformly functionalize the entire surface. Penetration of plasmas into surface features was found to be closely linked to the mean free path of reactive species and the operating pressure.[49] Vohrer *et al*, studied the optimization of process parameters including power input and treatment duration to obtain water-repellant properties on cotton-polyester fabrics.[50] Tsai *et al* have investigated the use of atmospheric pressure glow discharges for textile treatment and the resulting changes in fabric strength and surface energy.[51] Carneiro *et al*, have suggested that the use of corona pretreatment prior to dyeing can reduce production costs by more than 60% in addition to reducing the use of environmentally harmful chemicals.[52]

Castner and Ratner have reviewed the considerable challenges faced in the engineering of biomedical surfaces due to the complex biological interactions with living cells.[53] Investigations with different plasmas and biomedical polymers suggest that plasma treatment can be used to effectively implant functional groups that play a key role in immobilization of cells and enzymes. Immobilization is usually achieved by using macromolecules to serve as spacers and connect a biological cell or enzyme at one end and to the surface at the other. Spacer-ends may have charge characteristics that allow them to interlock with specific functional groups present on the surface, such as amino groups.

Plasmas are being used *in vitro*, for cell micropatterning (Fig. 6) on polymer substrates by creating chemical surface microstructures that consist of selectively activated regions of functional groups in order to promote cell adhesion.[54] Tissue engineering routinely involves the functionalization of topologically rough scaffold-like surfaces that are used to promote cell adhesion and proliferation.[55, 56] *In vivo*, the use of plasma treated implants and grafts have been used successfully for many years. For instance, ammonia plasma treated PTFE surfaces used in vascular grafts support 5 times more endothelial cell growth compared to untreated PTFE.[57] Many biomaterials and even commercially available biocompatible artificial skin are usually processed in low pressure discharges that are expensive to operate and maintain. As a result, the cost of biomaterial surface processing can be high with artificial skin costing up to \$1000 per m². [58] It may be possible to adapt the atmospheric pressure treatment processes used in commodity polymer processing to biomedical surface processing to reduce production costs that can potentially have huge economic and social benefits.

The ability to sustain atmospheric pressure discharges at small dimensions (< few mm) (Fig. 6) opens the possibility of using them to treat materials having complex 3-dimensional polymer surfaces, such as those of miniature lab-on-a-chip diagnostic arrays or the surfaces of polymer beads. The availability of reactive species increases and the dependence on diffusion is reduced when the plasma is generated close to the surfaces being functionalized. Besch *et al*, reported on the functionalization and subsequent diagnostic measurements of specially designed microfluidic channel surfaces.[59] The surfaces of polymer beads and powders were found to be effectively treated using plasma discharges.[60] Polymeric microspheres were used to implant functional groups on their surfaces for subsequent covalent bonding to enzymes or for drug delivery applications.

In general, poor control over the distribution of radicals and functional groups formed on the polymer surface during treatment is one of the drawbacks of using plasma discharges. Improvements in design of plasma sources would enable tailoring the fluxes of reactive radicals, for instance, to create gradient surfaces (Fig. 7). For instance, microplasmas have been recently investigated as a means to modify the surfaces of small-scale biomedical devices such as tubing.[61, 62] Almost always, the active species generated in the discharge proceed to react along a number of simultaneous pathways to form a distribution of functional groups on the polymer surface.[63-65] The quality of the resulting treatment is often quite acceptable for commodity polymer surfaces where a favorable macroscopic change in surface properties is obtained and microscopic uniformity of surface treatment is not a great concern. However, the extent and uniformity of surface functionalization using atmospheric pressure discharges will be critical in the case of biomaterial surface processing to ensure reproducibility, reliability and effectiveness of the treatment.[66, 67] Advanced *in situ* monitoring diagnostics are being developed to enable a better understanding of surface reaction mechanisms by tracking the reactions of plasma generated species on the polymer surface.[68, 69] New understanding from such diagnostics would help identify process variables that are key to tailoring the relative distribution of the various functional groups formed on the surface.

1.2 Modeling of Atmospheric Pressure Discharges

Plasma Equipment Models (PEMs) have contributed significantly to the knowledge base of low pressure plasma processing technologies in the microelectronics industry. Though atmospheric pressure plasma equipment are commercially used to process millions of square meters of polymer surfaces each year, there are few equipment models describing the plasma-surface interactions that lead to functionalization. As a result, the use and optimization of

atmospheric pressure plasmas for polymer surface functionalization has been largely guided by empirical use rather than the knowledge of the fundamental processes governing such treatment. The development of PEMs for atmospheric pressure discharges can aid in understanding their formation mechanisms, the effect of process variables such as gas flow and chemical composition and their interactions with different types of surfaces. A broader knowledge base can then be leveraged for using these devices to treat high-value materials with economic benefits.

Industrial atmospheric pressure plasma devices often have multiple microdischarges, each a few hundred μm in diameter and lasting for a few to 10s ns. The total fraction of gas ionized is typically quite small, about 10^{-5} . The peak plasma density in the microdischarge channel varies between $10^{13} - 10^{15} \text{ cm}^{-3}$, and the peak electron temperature does not usually exceed 10 eV. Charged species striking the polymer charge the surface and this rapidly counteracts the voltage drop across the gap, extinguishing the plasma. The reactive radical species generated in the discharge have longer lifetimes and continue to react over 10s of μs . Repetitive pulsing of the discharge exposes the polymer surface to a series of discharges and enables surface treatment over a period of ms or longer. Since the pulse itself is extinguished very quickly, the relative composition of radicals produced by the pulse during the interpulse period critically determines the extent of functionalization.

Various approaches have been used to model atmospheric pressure discharges, depending on the physical processes and the range of time scales and spatial scales being modeled. Kogelschatz and coworkers performed early numerical modeling studies of breakdown mechanisms and microdischarge formation in the context of dielectric barrier discharges.[70] Since then, many 1-dimensional and 2-dimensional simulations have been developed by various

investigators, some focusing on the discharge formation mechanisms at atmospheric pressure, while others looking at plasma chemistry, in many different gases as reported in literature.[71-78] Wang and Kunhardt [71] developed a model to describe the space-time evolution of streamer fronts to elucidate the properties of positive and negative streamers.

Vitello *et al.*, [72] used results from two-dimensional and three-dimensional simulations of streamer dynamics in nitrogen to demonstrate the various phases in streamer evolution. Babaeva and Naidis [73] developed two-dimensional simulations of positive and negative streamers in air in the presence of weak electric fields. They found that the form of the streamer channel and the rate of increase in streamer velocity with streamer length are determined by both the magnitude and polarity of the applied electric field. Kulikovsky [74] used two-dimensional simulations to examine in detail the role of photoionization in the propagation of positive discharges in air and proposed that the fundamental space scale of streamers are defined by the space charge layer width and the length of absorption of the photoionizing radiation.

Plasma chemistry models in repetitively pulsed DBDs have been developed in the context of toxic gas remediation and ozone generation.[78-81] Gentile and Kushner [78] identified the main reaction channels leading to remediation as well as three phases in the remediation function of DBDs consisting of the current pulse, the postpulse remediative period and the interpulse period to suggest scaling laws for energy deposition and optimization of these discharges. Similar discharges are used for polymer surface functionalization, where surface reactions occur due to impinging gas phase radicals from the plasma, so the surface kinetics and gas phase chemistry are inherently coupled. Additionally, convective transport of reactive species to the surface will be affected by the presence of gas flow through the device, so the radical chemistry and surface functionalization are coupled to gas flow as well. A comprehensive model would

account for all of these simultaneous physical and chemical processes in a self-consistent manner. Most models described in literature, such as those cited above, focus on either the discharge physics or the gas phase reaction kinetics only.

While detailed mechanisms for the plasma surface functionalization of most polymers are yet to be developed, common themes have emerged from experimental studies with a variety of plasma and ultraviolet radiation sources and polymeric materials found in literature. Using these sources, Dorai and Kushner [63], investigated the surface treatment of polypropylene in humid air discharges using a zero-dimensional plasma kinetics model coupled to a surface site-balance model and developed a surface reaction mechanism for the treatment of polypropylene.

For instance, it is known that radicals, ions and photons from the plasma are all involved and simultaneously react with the polymer surface.[63, 64, 82-88] Reactive radicals, energetic ions and excited species as well as photons from the plasma initiate surface reaction pathways by abstracting atoms from the surface and creating active surface radicals. The surface radicals then crosslink among themselves in the absence of reactive gas phase radicals [83], or undergo chain scission or react further with gas phase radicals to create new functional groups [84] on the surface.

The relative contribution of various plasma species in creating surface radicals varies with pressure. In discharges generated at low pressure, the energetic ion bombardment [86] is an important contribution. The high collisionality and the transient nature of atmospheric pressure pulsed discharges make radicals rather than ions largely responsible for surface functionalization. Photons are also generated in plasmas and can have significantly important contributions to the surface reaction kinetics during functionalization. It is known that, for instance, vacuum ultraviolet radiation (VUV) alone can significantly affect polymer surfaces. For instance,

Hollander *et al* [87] used VUV radiation on polyethylene-terephthalate surfaces in an oxygen atmosphere to generate new surface functional groups.

Multiscale modeling of atmospheric pressure plasma devices involves tracking the different physical processes such as discharge breakdown, fluid dynamics, radical chemistry and surface kinetics occurring over vastly different scales in space and time. By coupling the model with knowledge bases for surface reaction mechanisms, parameter spaces in process variables such as power, gas composition and flow rate can be investigated to determine the optimal processing conditions for surface functionalization.

In this work, such a multiscale modeling hierarchy has been developed to investigate processes occurring over multiple temporal and spatial scales during the atmospheric pressure plasma treatment. A two-dimensional (2-D) plasma hydrodynamics modeling platform has been developed that address the spatial dynamics during the breakdown process. To investigate the treatment of polymer surfaces or arbitrary shapes treated over timescales spanning many pulses over many ms, a surface kinetics model was integrated to the plasma hydrodynamics model. The effect of convective transport on surface functionalization was investigated by coupling an incompressible fluid dynamics model to the platform. The details of these models are presented in Chapter 2.

In Chapter 3, the two-dimensional hydrodynamics model is used to present results for the breakdown process in atmospheric pressure corona discharges in humid air with both negative and positive applied voltage. It was found that the breakdown process occurs over a few ns and is faster in the negative discharge. In either case, an ionization front with a spatial extent of 100-200 μm is formed ahead of the breakdown avalanche due to space charge accumulation and makes its way across the gas gap. Gradients in plasma characteristics at the ionization front

occur in both discharges but are more marked in the positive discharge due to its structure and plasma density.

The dynamics at the ionization front is examined in more detail by implementing a Monte-Carlo simulation for electrons in the region of the front in Chapter 4. Changes in electron transport across the ionization front due to the steep gradients affect the breakdown dynamics by changing the rates of electron-impact process and electron energies. These changes can be effectively captured using the Monte-Carlo technique and was demonstrated for discharges in Ar at 10s Torr and in air at atmospheric pressure and the non-equilibrium character of the ionization front is described.

The ability of the discharge to penetrate into structures placed in the breakdown path, such as dielectric disks containing microchannels like those encountered in lab-on-a-chip kind of devices are examined in Chapter 5. The widths of these channels are a few to 10s of μm while the disk thickness could range from 0.1 to 1 mm. Parametric investigations on the channel width and disk thickness indicate that the breakdown process stops due to surface charging at lower channel widths and the inability of the ionization front to make it through the channel across larger slab thicknesses, but makes it through the channel in other instances. Successful plasma penetration indicates that reactive radicals can be locally generated with the channels and can be used to functionalize the channel walls for biomolecule attachment. The presence of multiple channels in the disk leads to interesting breakdown dynamics as the discharge succeeds in penetrating some but not all of them depending on the impedance of each channel.

In Chapter 6, the integrated plasma hydrodynamics – surface kinetics model was used to investigate the process of radical generation and treatment of rough surfaces such as those of textiles or scaffolds used for cell adhesion or tissue culturing. Different gas chemistries

including air, He/O₂/H₂O and He/NH₃/H₂O were considered. The roughness of the surface was resolved to a sub- μm level and the spatial and temporal variations in radical flux due to repetitive pulsing were used. With a surface reaction mechanism developed in an earlier work for a polypropylene surface, the uniformity of surface treatment to implant oxygen and nitrogen-containing groups over 100s of ms was found to depend strongly on the gas composition and voltage polarity. The shadowing effect of microscopic structures on the surface results in non-uniformity of treatment on a micro-scale while macroscopic non-uniformities result from the gradients in reactive species fluxes.

The porous surfaces of micron-sized polymeric beads can be functionalized with N-containing groups for applications related to enzyme immobilization and drug delivery. The plasma penetration and subsequent functionalization of porous polymeric beads 10s μm in diameter with pore openings of a few μm in He/NH₃/H₂O and He/O₂/H₂O discharges was investigated in Chapter 7. The penetration of the plasma into the pores depends on the position of the pore in the discharge, the orientation of the pore opening relative to the discharge and the size of the opening. It was found that with larger pore openings oriented towards the discharge, plasma penetration was higher than pores oriented away or those that were smaller. Radicals do penetrate into the porous structure but the more reactive ones are consumed close to the pore opening and do not reach deep into the porous network. This ultimately affects treatment uniformity with the outer bead surfaces being treated more than the internal surfaces.

The effect of gas flow and continuous processing on the degree of surface treatment was investigated using the integrated plasma hydrodynamics – fluid dynamics – surface kinetics model and results are presented in Chapter 8. In the presence of gas flow of a few to 10s of liters per minute, radical transport to the surface is altered. This leads to a change in the relative

proportions of surface functional groups on the polymer. With continuous processing, the polymer surface moves at a few meters per second and so surface radicals encounter a different distribution of fluxes during their residence time downstream of the discharge leading to a marked change in the degree of treatment.

Concluding remarks are presented in Chapter 9.

1.3 Figures



Fig. 1 Typical atmospheric pressure plasma treatment devices used to functionalize the surfaces of polymers (a) above, courtesy Tantec Inc. (b) below, courtesy Sigma Inc.

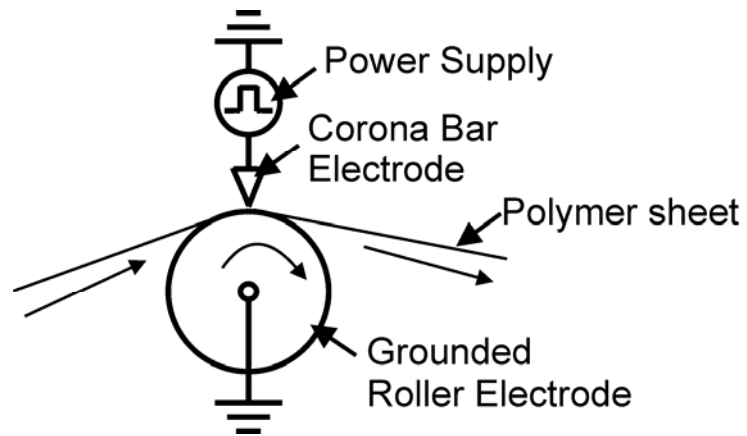


Fig. 2 Schematic of the web treatment arrangement used for the continuous plasma treatment of polymer sheets

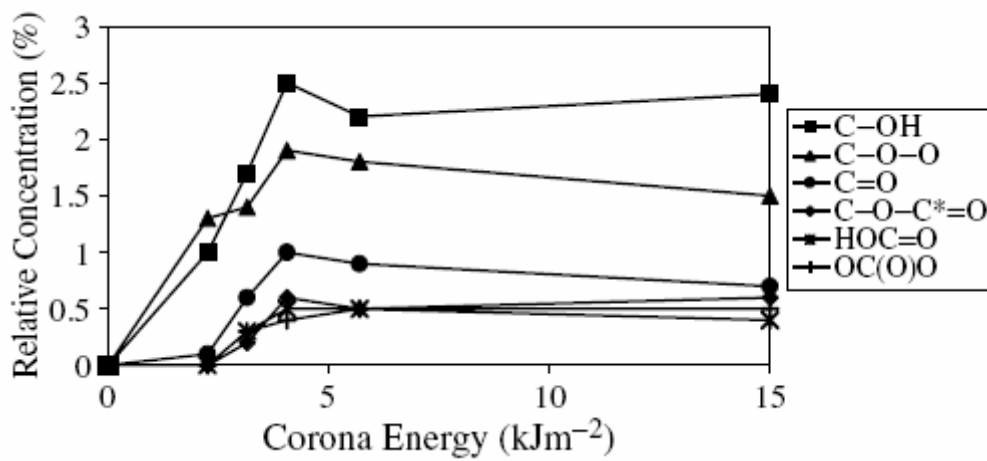


Fig. 3 Functional groups formed on the surface of polypropylene after treatment in an air corona discharge at different energies.[46]

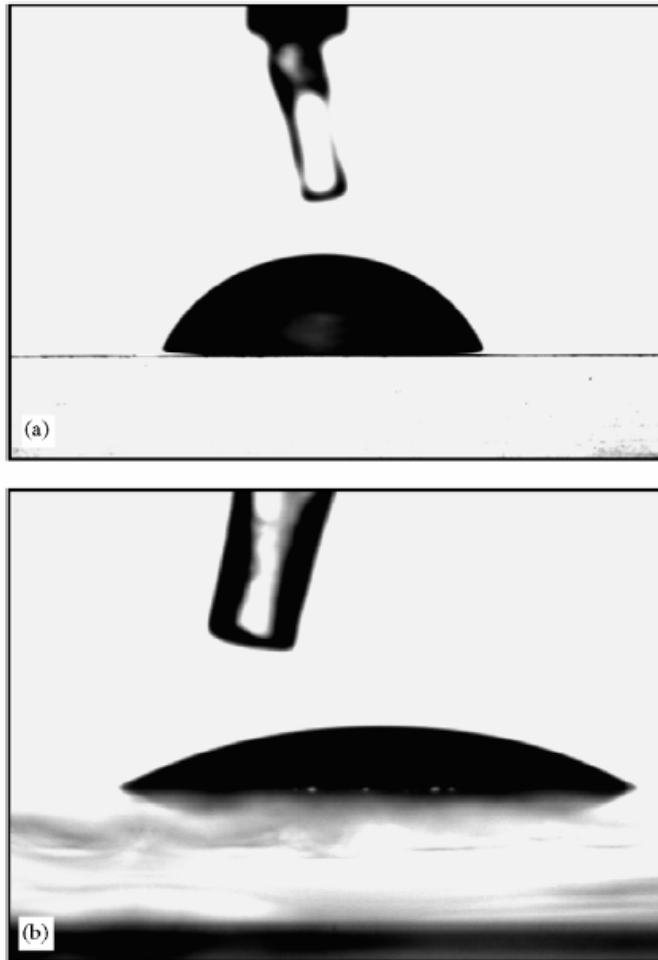


Fig. 4 Contact angle measurements using sessile drop method on porous poly (D,L- lactide) (a) before plasma treatment and (b) after plasma treatment. [89] Spreading of the droplet indicates greater surface wettability.

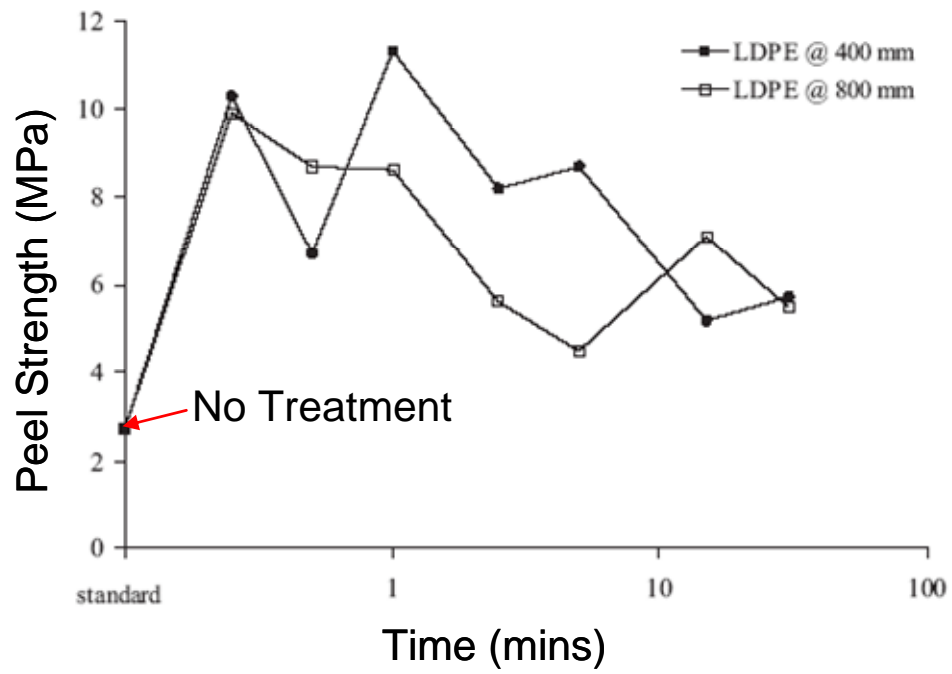


Fig. 5 Improvement in the peel strength of polyethylene after plasma treatment.[17]

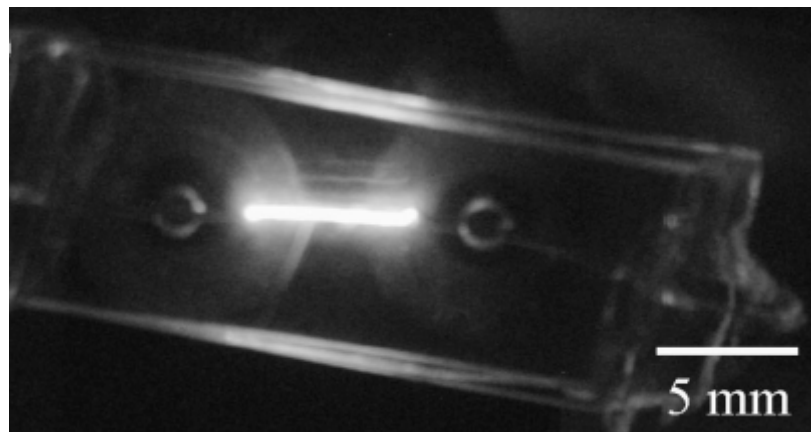
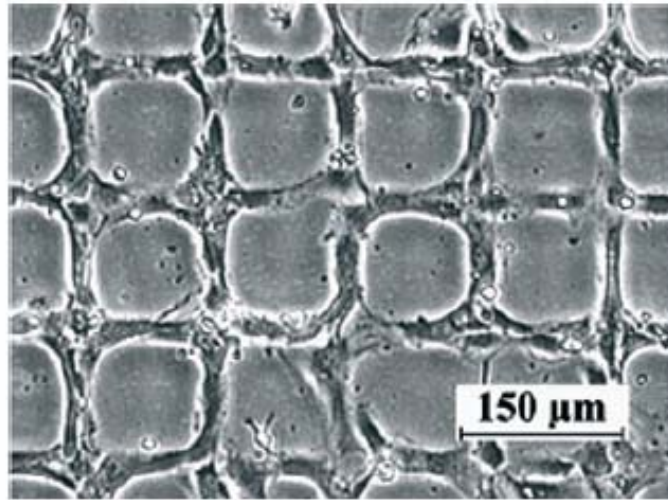


Fig. 6 (a) Chemical cell micropatterning on polystyrene surfaces using ammonia and hydrogen plasmas.[90] (b) Atmospheric pressure He/H₂O discharge in a polystyrene channel between two platinum electrodes.[90]

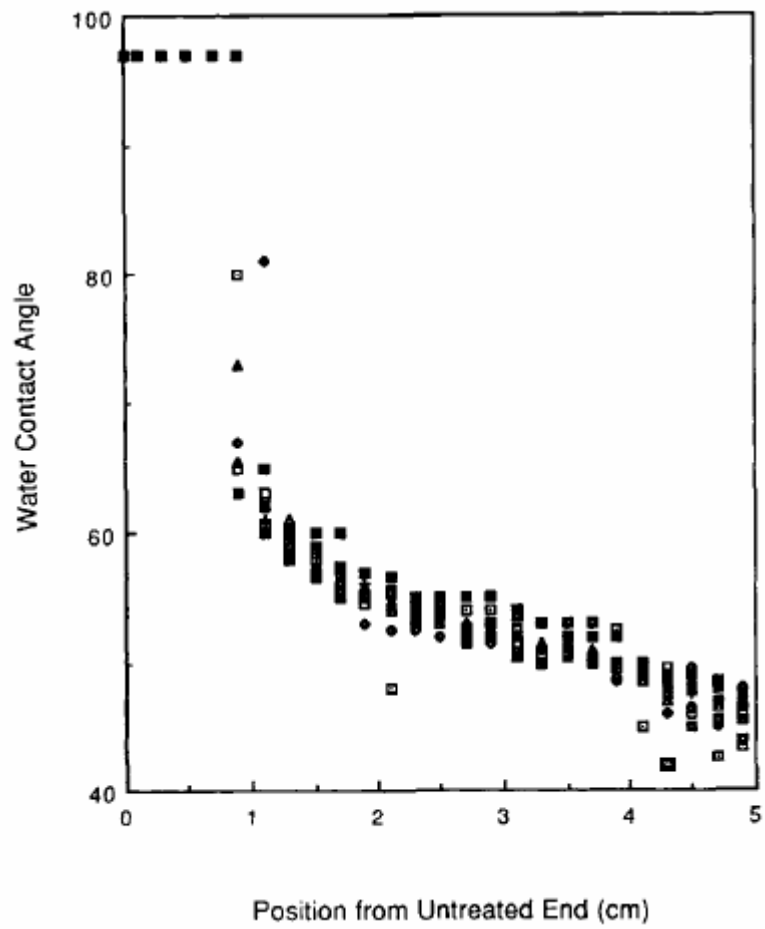


Fig. 7 Spatial gradients in the water contact angle for corona treated polyethylene.[91]

1.4 References

1. M. P. Stevens, *Polymer Chemistry – An Introduction*, Oxford University Press Inc., New York, 1990.
2. N. Angelova and D. Hunkeler, *Trends in Biotechnology*, **17**, 409 (1999).
3. L. Y. Ljungberg, *Materials and Design*, **24**, 383–390 (2003).
4. C.-M. Chan, *Polymer Surface Modification and Characterization*, 1 ed. (Hanser/Gardner Publications, Inc., New York, 1994).
5. L. Dai, H. A. W. StJohn, J. Bi, P. Zientek, R. C. Chatelier and H. J. Griesser, *Surface Interface Anal.*, **29**, 46–55 (2000)
6. G. Fourche, *Polymer Engineering and Science*, **35**, 957 (1995)
7. D.A. Puleo and A. Nanci, *Biomaterials*, **20**, 2311 (1999).
8. B. D. Ratner, *Journal of Biomaterial Science Polymer Edition*, **11**, 1107 (2000).
9. D. L. Elbert and J. A. Hubbell, *Annual Review in Material Science*, **26**, 365 (1996).
10. Y. Uyama, K. Kato, and Y. Ikada, *Advances in Polymer Science*, **13**, 1 (1998).
11. I. Sutherland, D. M. Brewis, R. J. Health and E. Sheng, *Surface and Interface Analysis*, **17**, 507 (1991).
12. K.-W. Lee and A. Viehbeck, *IBM Journal of Research and Development*, **38**, 457 (1994).
13. K. Pochner, S. Beil, H. Horn and M. Blomer, *Surface and Coatings Technology*, **97**, 372 (1997).
14. L. F. Macmanus, M. J. Walzak and N. S. McIntyre, *Journal of Polymer Science: Part A: Polymer Chemistry*, **37**, 2489 (1999).
15. A. N. Netravali, J. M. Caceres, M. O. Thompson and T. J. Renk, *Journal of Adhesion Science and Technology*, **13**, 1331 (1999).

16. O. Prucker and J. Ruhe Langmuir, **14**, 6893 (1998).
17. M. J. Shenton, M. C. Lovell-Hoare and G. C. Stevens, Journal of Physics D: Applied Physics, **34**, 2754 (2001).
18. C. Oehr, Nuclear Instruments and Methods in Physics Research B, **208**, 40 (2003).
19. A. Bogaerts, E. Neyts , R. Gijbels , J. van der Mullen, Spectrochimica Acta Part B, **57**, 609 (2002).
20. I. Orlandini and U. Riedel, Journal of Physics D: Applied Physics, **33**, 467 (2000).
21. J. P. Boeuf, Journal of Physics D: Applied Physics, **36**, R53–R79 (2003).
22. D. B. Graves, IEEE Transactions on Plasma Science, **22**, 31 (1994).
23. J. M. Grace and L. J. Gerenser, Journal of Dispersion Science and Technology, **24**, 305 (2003).
24. Ch. Baquey, F. Palumbo, M. C. Porte-Durrieu, G. Legeay, A. Tressaud and R. d’Agostino, Nuclear Instruments and Methods in Physics Research B, **151**, 255 (1999).
25. U. Kogelschatz, Plasma Chemistry and Plasma Processing, **23**, 1 (2003).
26. H.-E. Wagner, R. Brandenburg, K.V. Kozlov, A. Sonnenfeld, P. Michel and J.F. Behnk, Vacuum, **71**, 417, (2003).
27. F. Massines and G. Gouda, Journal of Physics D: Applied Physics, **31**, 3411 (1998).
28. U. Kogelschatz, IEEE Transactions on Plasma Science, **30**, 1400 (2002).
29. J. Rahel and D. M. Sherman, Journal of Physics D: Applied Physics, **38**, 547 (2005).
30. G. Borcia, C. A. Anderson, N. M. D. Brown, Applied Surface Science **221**, 203 (2004).
31. J. B. Lynch, P. D. Spence, D. E. Baker and T. A. Postlethwaite, Journal of Applied Polymer Science, **71**, 319 (1999).

32. Yu. S. Akishev, M. E. Grushin, A. E. Monich, A. P. Napartovich, and N. I. Trushkin, *High Energy Chemistry*, **37**, 286 (2003).
33. S. De, R. Sharma, N. Ali, and M. K. Mazumder, *IEEE IAS*, **39**, 932 (2004).
34. S. Guimond, I. Radu, G. Czeremuszkina, D. J. Carlsson, and M. R. Wertheimer, *Plasmas and Polymers*, **7**, 71 (2002)
35. G. Borcia, C. A. Anderson and N. M. D. Brown, *Plasma Sources Science and Technology*, **14**, 259 (2005).
36. M. Sira, D. Trunec, P. Stahel, V. Bursikova, Z. Navratil and J. Bursik., *Journal of Physics D: Applied Physics*, **38**, 621 (2005)
37. N. Sellin and J. S-C. Campos, *Materials Research*, **6**, 163 (2003).
38. G. Borcia, N. M. D. Brown, D. Dixon and R. McIlhagger, *Surface and Coatings Technology*, **179**, 70 (2004).
39. J. Comyn, L. Mascia, G. Xiao and B.M. Parker, *Int. J. Adhesion and Adhesives*, **16**, 301 (1996) .
40. G. Borcia, N. Dumitrascu and G. Popa, *Surface & Coatings Technology*, **197**, 316 (2005).
41. U. Schulz, P. Munzert and N. Kaiser, *Surface and Coatings Technology*, **142-144**, 507 (2001).
42. K. Schroder, G. Babucke and A. Ohl, *Surface and Interface Analysis*, **36**, 702 (2004).
43. L-A. O'Hare, J. A. Smith, S. R. Leadley, B. Parbhoo, A. J. Goodwin and J. F. Watts, *Surface and Interface Analysis*, **33**, 617 (2002).
44. S. Ishikawa, K. Yukimura, K. Matsunaga and T. Maruyama, *Surface and Coatings Technology*, **130**, 52, (2000).

45. N. Dumitrascu, G. Borcia and G. Popa, *Journal of Applied Polymer Science*, **81**, 2419 (2001).
46. L-A. O'Hare, S. Leadley and B. Parbhoo, *Surface and Interface Analysis*, **33**, 335 (2002).
47. J. Vartiainen, M. Rättö, U. Tapper, S. Paulussen and E. Hurme, *Polymer Bulletin*, **54**, 343 (2005).
48. N. De Geyter, R. Morent and C. Leys, *Plasma Sources Science and Technology*, **15**, 78, (2006).
49. H.U. Poll, U. Schladitz and S. Schreiter, *Surface and Coatings Technology*, **142-144**, 489 (2001).
50. U. Vohrer, M. Muller and C. Oehr, *Surface and Coatings Technology*, **98**, 1128 (1998).
51. P. P. Tsai, J. R. Roth and W. W. Chen, *Textile Research Journal*, **75**, 819 (2005).
52. N. Carneiro, A. P. Souto, E. Silva, A. Marimba, B. Tena, H. Ferreira and V. Magalhaes, *Coloration Technology*, **117**, 298 (2001).
53. D. G. Castner and B. D. Ratner, *Surface Science*, **500**, 28 (2002).
54. H. Chim, J. L. Ong, J.-T. Schantz, D. W. Hutmacher, C. M. Agrawal, *Journal of Biomedical Materials Research A*, **65A**, 327 (2002).
55. K. Schroder, A. Meyer-Plath, D. Keller and Andreas Ohl, *Plasmas and Polymers*, **7**, 103 (2002).
56. M. Morra and C. Cassinelli, *Plasmas and Polymers*, **7**, 89 (2002).
57. F. R. Pu, R. L. Williams, T. K. Markkula and J. A. Hunt, *Biomaterials*, **23**, 2411 (2002).
58. I. Jones, L. Currie and R. Martin, *British Journal of Plastic Surgery*, **55**, 185 (2002).
59. W. Besch, O. Lippold, H. Reinecke, K. Schroder and A. Ohl, *Surface and Coatings Technology*, **174-175**, 112 (2003).

60. F. Arefi-Khonsari, M. Tatoulian, F. Bretagnol, O. Bouloussa and F. Rondelez, *Surface and Coatings Technology*, **200**, 14 (2005).
61. J. L. Lauer, J. L. Shohet, R. M. Albrecht, S. Esnault, J. S. Malter, U. H. vonAndrian and S. B. Shohet, *IEEE Transactions on Plasma Science*, **33**, 791 (2005).
62. J. L. Lauer, J. L. Shohet, R. M. Albrecht, C. Pratoomtong, R. Murugesan, S. Esnault, J. S. Malter, U. H. von Andrian, R. D. Bathke, and S. B. Shohet, *Journal of Applied Physics*, **96**, 4539 (2004).
63. R. Dorai and M. J. Kushner, *Journal of Physics D: Applied Physics*, **36**, 666 (2003).
64. R. M. France and R. D. Short, *Langmuir* **14**, 4827 (1998)
65. S. Cao and Y. Zeng, *Journal of Applied Polymer Science*, **47**, 2093 (1993).
66. F. Massines, R. Messaoudi, and C. Mayoux, *Plasmas and Polymers*, **3**, 43 (1998).
67. P. K. Chu, J. Y. Chen, L. P. Wang and N. Huang, *Materials Science and Engineering Reports*, **36**, 143 (2002).
68. C. I. Butoi, N. M. Mackie, P. R. McCurdy, J. R. D. Peers and E. R. Fisher, *Plasmas and Polymers*, **4**, 77 (1999).
69. A. Meyer-Plath, *VIP Vacuum's Best*, 40 (2005).
70. B. Eliasson, W. Egli and U. Kogelschatz, *Pure and Applied Chemistry*, **66**, 1275 (1994).
71. M. C. Wang and E. E. Kunhardt, *Physical Review A*, **42**, 2366 (1990).
72. P. A. Vitello, B. M. Penetrante and J. N. Bardsley, *Physical Review E*, **49**, 5574 (1994).
73. N. Y. Babaeva and G. V. Naidis, *IEEE Transactions on Plasma Science*, **25**, 375 (1997).
74. A. A. Kulikovskiy, *Journal of Physics D: Applied Physics*, **33**, 1514 (2000).
75. Y. B. Golubovskii, V. A. Maiorov, J. Behnke and J. F. Behnke, *Journal of Physics D: Applied Physics*, **36**, 39 (2003).

76. F. Massines, P. Segur, N. Gherardi, C. Khamphan and A. Ricard, *Surface and Coatings Technology*, **174–175**, 8 (2003).
77. D. Braun, V. Gibalovt and G. Pietsch, *Plasma Sources Science and Technology*, **7**, 166 (1992).
78. A. C. Gentile and M. J. Kushner, *Journal of Applied Physics*, **78**, 2074 (1995).
79. R. Dorai and M. J. Kushner, *Journal of Physics D: Applied Physics*, **34**, 574 (2001).
80. B. Eliasson, *IEEE Transactions on Plasma Science*, **19**, 309 (1991).
81. J. Chen and J. H. Davidson, *Plasma Chemistry and Plasma Processing*, **22**, 495 (2002).
82. S. Cao and Y. Zeng, *Journal of Applied Polymer Science*, **47**, 2093 (1993).
83. D. T. Clark and A. Dilks, *Journal of Polymer Science: Polymer Chemistry Edition*, **15**, 2321 (1977).
84. D. T. Clark and D. R. Hutton, *Journal of Polymer Science: Part A: Polymer Chemistry*, **25**, 2643 (1987).
85. F. Poncin-Epaillard, *Macromolecular Chemical Physics*, **198**, 2439 (1997).
86. J. Hong, F. Truica-Marasescu, L. Martinu and M. R. Wertheimer, *Plasmas and Polymers*, **7**, 245 (2002).
87. A. Hollander, J. E. Klemberc-sapieha and M. R. Wertheimer, *Journal of Polymer Science: Part A: Polymer Chemistry*, **34**, 1511 (1996).
88. C. Sarra-Bournet, S. Turgeon, D. Mantovani and G. Laroche, *Journal of Physics D: Applied Physics*, **39**, 3461 (2006).
89. L. Safinia, et al, *Biomaterials*, **26**, 7537 (2005).
90. J. K. Evju et al, *Applied Physics Letters*, **84**, 1668 (2004).
91. J. H. Lee, et al, *Journal of Polymer Science, Part A, Polymer Chemistry*, **32**, 1569 (1994).

2. DESCRIPTION OF THE MODEL

2.1 Introduction

In this chapter, the two-dimensional plasma equipment model (PEM) called nonPDPSIM is described. A representative flowchart of the various modules that constitute this multiphysics platform is shown in Fig. 2.1. Processes occurring over a wide range of temporal and spatial scales are addressed by these modules. The PEM has been used, for instance, to model electrical breakdown [1] on sub- μ s timescales in gas gaps of a few cm to flowing discharges for oxygen-iodine lasers [3] in tubes 10s of cm in length over many 10s of ms to microdischarges operating in sub-mm geometries [2]. Some of these modules, along with the fundamental algorithms used, are detailed in the following sections.

2.2 Geometry and Mesh Generation

A detailed description of the geometry module is found in the thesis by B. Lay [4]. An unstructured mesh generator, (Skymesh2 was used in this study but is no longer commercially available), is used to create a two-dimensional (2D) schematic representation of the discharge apparatus and map over this, an unstructured mesh composed of triangles. The geometry can be Cartesian or cylindrically symmetric. Once the unstructured mesh is created, it is kept static for the complete duration of a simulation. The mesh generation has some simple refinement capabilities whereby certain regions in the geometry may be more refined than others. This enables finer resolution of features where necessary and saves computational time by having coarser resolution in other regions.

The vertices of each of the triangles that constitute the unstructured mesh are called ‘nodes’. Any two nodes forming the sides of a triangle constitute a ‘neighbor’ to each of the nodes. An element consists of the three nodes that form a triangle. The mesh file contains the coordinates of each node, the material defined for each node, a boundary condition, if any, the number of neighbors it has, and the connectivity list of elements that make up the mesh. Using this information, the geometry module of the PEM determines internal mappings for each of the nodes. Around each node, a ‘cell’ is defined as shown in Fig. 2.2. The cell volume for a particular node, V_i , is the summation of the volumes shared between the node and each of its neighbors, δV_{ij} . In this manner, geometrical factors such as cell volumes and cell face areas (δA_{ij}) are computed on the entire mesh accounting for the depth in the case of Cartesian meshes and the radial positions to compute volumes on a cylindrically symmetric mesh.

Each node is tagged as the material of the face or edge or vertex it represents on the mesh and therefore contains the properties of that material. The properties of a material include its conductivity, permittivity, resistivity, work function, whether it is a metal, its ability to retain surface charge or to have secondary electron emission or electric field emission, initial temperature, whether it is a nozzle or pump port and so on. When a node lies on the edge between a metal and non-metal, it is designated to have the properties of the metal. Similarly a node lying on the edge between the plasma and a non-plasma material will take on the properties of the non-plasma material. In this manner, every node on the mesh is assigned material properties.

2.3 Plasma Dynamics Module

The plasma dynamics module addresses the solution of electrostatic and electromagnetic fields, the multi-fluid charged species transport, electron energy transport and gas phase reaction kinetics. The fundamental equations for the electric potential computed throughout the computational domain, transport of charged species and neutrals computed in the plasma domain and surface charge computed only on dielectric materials are

$$-\nabla \cdot \varepsilon \nabla \Phi - \sum_j n_j q_j + \rho_s = F_1 = 0 \quad (2.1)$$

$$\frac{\partial N_i}{\partial t} - \left(-\bar{\nabla} \cdot \vec{\phi}_i + S_i \right) = F_2 = 0 \quad (2.2)$$

$$\frac{\partial \rho_s}{\partial t} - \left(\sum_i -\nabla \cdot (q_i \vec{\phi}_i (1 + \gamma_i)) - \nabla \cdot (\sigma (-\nabla \Phi)) \right) = F_3 = 0 \quad (2.3)$$

where ε , Φ , ρ , N , D , μ , ϕ , γ , σ , S , and q refer to the permittivity, electric potential, charge density, species number density, diffusion coefficient, mobility, species flux, secondary emission coefficient, conductivity of solid materials, source terms, and elementary charge respectively. The subscript denotes the identity of the species. Poisson's equation (Equation 2.1) describing the electric potential, transport equations (Equation 2.2) describing conservation for the charged species, and surface charge balance (Equation 2.3), are solved as a simultaneous set of equations.

To numerically discretize these equations, finite volume techniques were used. This requires that the operators take into account the geometrical factors around each node. For instance, the gradient operator on a variable X between nodes i and j with coordinates \vec{x}_i and \vec{x}_j is calculated as the difference,

$$\nabla X_{ij} = \frac{X_j - X_i}{\Delta x_{ij}}, \quad \Delta x_{ij} = \bar{x}_j - \bar{x}_i. \quad (2.4)$$

The divergence operator on X at any node i is defined as,

$$\nabla \cdot X_i = \frac{\sum_j \nabla X_{ij} \delta A_{ij}}{V_i} \quad (2.5)$$

The tagging of individual nodes with material properties, as described earlier, helps in the discretization of the governing equations. For instance, during the discretization of the Poisson equation, the permittivity has to often be determined at cell faces that lie between unlike materials.

Fluxes for charged species are formulated using the optimum exponential discretization scheme of Scharfetter-Gummel [5], which is robust and provides stable solutions even in the presence of steep spatial gradients. In this method, the flux between node i and neighbor j is given by

$$\bar{\phi}_{i,j} = \alpha \bar{D} \left(\frac{n_j - n_i \exp(\alpha_{ij} \Delta x_{ij})}{1 - \exp(\alpha_{ij} \Delta x_{ij})} \right) \quad (2.6)$$

where α is given by

$$\alpha_{ij} = \frac{\left(\frac{q}{|q|} \right) \bar{\mu} \left(\frac{\Phi_j - \Phi_i}{\Delta x_{ij}} \right)}{\bar{D}} \quad (2.7)$$

$$\Delta x_{ij} = \bar{x}_j - \bar{x}_i, \quad \bar{D} = \left(\frac{D_i + D_j}{2} \right), \quad \bar{\mu} = \left(\frac{\mu_i + \mu_j}{2} \right)$$

and $\bar{\mu}$ and \bar{D} are the average mobility and diffusion coefficient in the interval.

The source function includes gain and loss terms due to gas phase and surface chemistry.

The system of equations (2.1)-(2.3) need to be solved for the variables X_l , consisting of electric potential (ϕ_i) at every node i and charged species densities (n_i) at every plasma node and surface charge (ρ_i) at every dielectric node bordering the plasma. The solution process involves linearization of this system of equations around the current solution and perturbing each of the individual variables at every node to numerically evaluate a Jacobian element. For instance, the Jacobian element for equation k due to perturbation in variable X_l at node m is given by,

$$J_{km,l} = \left[\frac{\partial F_k}{\partial X_l} \right]_m, \quad B_{km} = F_{k,m} \quad (2.8)$$

This results in the formation of a system of equations $J \cdot \delta X = F$ where the matrix J is the Jacobian matrix, the vector δX contains the corresponding solution variables $\delta X_{l,m}$ and the vector B contains elements $F_{k,m}$ which are the corresponding evaluated functions F_k evaluated at node m as shown below.

$$\begin{bmatrix} \frac{\partial F_{i,1}}{\partial \phi_i} & \frac{\partial F_{i,1}}{\partial n_i} & \frac{\partial F_{i,1}}{\partial \rho_i} & \frac{\partial F_{i,1}}{\partial \phi_{i+N}} & \frac{\partial F_{i,2}}{\partial \phi_i} & \frac{\partial F_{i,2}}{\partial n_i} & \frac{\partial F_{i,2}}{\partial \rho_i} & \frac{\partial F_{i,2}}{\partial \phi_{i+N}} & \frac{\partial F_{i,3}}{\partial \phi_i} & \frac{\partial F_{i,3}}{\partial n_i} & \frac{\partial F_{i,3}}{\partial \rho_i} & \frac{\partial F_{i,3}}{\partial \phi_{i+N}} & \frac{\partial F_{i+N,1}}{\partial \phi_i} & \frac{\partial F_{i+N,1}}{\partial n_i} & \frac{\partial F_{i+N,1}}{\partial \rho_{i+N}} & \frac{\partial F_{i+N,2}}{\partial \phi_i} & \frac{\partial F_{i+N,2}}{\partial n_i} & \frac{\partial F_{i+N,2}}{\partial \rho_{i+N}} & \frac{\partial F_{i+N,3}}{\partial \phi_i} & \frac{\partial F_{i+N,3}}{\partial n_i} & \frac{\partial F_{i+N,3}}{\partial \rho_{i+N}} \\ \frac{\partial F_{i,1}}{\partial \phi_i} & \frac{\partial F_{i,1}}{\partial n_i} & \frac{\partial F_{i,1}}{\partial \rho_i} & \frac{\partial F_{i,1}}{\partial \phi_{i+N}} & \frac{\partial F_{i,2}}{\partial \phi_i} & \frac{\partial F_{i,2}}{\partial n_i} & \frac{\partial F_{i,2}}{\partial \rho_i} & \frac{\partial F_{i,2}}{\partial \phi_{i+N}} & \frac{\partial F_{i,3}}{\partial \phi_i} & \frac{\partial F_{i,3}}{\partial n_i} & \frac{\partial F_{i,3}}{\partial \rho_i} & \frac{\partial F_{i,3}}{\partial \phi_{i+N}} & \frac{\partial F_{i+N,1}}{\partial \phi_i} & \frac{\partial F_{i+N,1}}{\partial n_i} & \frac{\partial F_{i+N,1}}{\partial \rho_{i+N}} & \frac{\partial F_{i+N,2}}{\partial \phi_i} & \frac{\partial F_{i+N,2}}{\partial n_i} & \frac{\partial F_{i+N,2}}{\partial \rho_{i+N}} & \frac{\partial F_{i+N,3}}{\partial \phi_i} & \frac{\partial F_{i+N,3}}{\partial n_i} & \frac{\partial F_{i+N,3}}{\partial \rho_{i+N}} \end{bmatrix} \begin{bmatrix} \Delta \phi_{i,g} \\ \Delta n_{i,g} \\ \Delta \rho_{i,g} \\ \vdots \\ \Delta \phi_{i+N,g} \\ \Delta n_{i+N,g} \\ \Delta \rho_{i+N,g} \end{bmatrix} = \begin{bmatrix} -F_{i,1} \\ -F_{i,2} \\ -F_{i,3} \\ \vdots \\ -F_{i+N,1} \\ -F_{i+N,2} \\ -F_{i+N,3} \end{bmatrix}$$

An implicit Newton's method is employed to update each variable X_l

$$X_l = X_l(t) + \delta X_l \quad (2.9)$$

and convergence is declared when the error criterion ε_{max} is satisfied for all variables l .

$$\frac{\delta X_l}{X_l} < \varepsilon_{max} \quad (2.10)$$

Numerical packages such as *dslucs*, *dslugm* obtained from the SLAP Sparse Matrix Library [6] or *sparskit* [7] obtained from the University of Minnesota are used. These solvers use bi-conjugate gradient matrix solution methods with incomplete LU factorization for preconditioning. The solution process requires an initial estimated solution for each variable,

$$\delta X_{l,guess} = (X_l(t_1) - X_l(t_2)) \cdot \frac{\Delta t_1}{\Delta t_2} \quad (2.11)$$

where Δt_1 and Δt_2 are the preceding time steps.

If an explicit formulation of the coupled system of equations (2.1)-(2.3) had been used, the time steps would be limited by the dielectric relaxation time, which is the ratio

$$\Delta t < \frac{\varepsilon_0}{\sigma} \quad (2.12)$$

of the permittivity of free space (ε_0) to the plasma conductivity (σ). However, the implicit formulation used here allows for larger time steps. At any point the time step taken is governed by the number of Newton iterations that was needed to solve the previous few time steps. The work required is high when the number of Newton iterations for a particular time step is large, while a lower number of Newton iterations indicate lesser work. The code uses this to signal a change in time step and accordingly changes the

next time step. This allows for variable and internally automated adjusting of the time step.

The equation (2.1) is used to obtain the electric potential, which is governed by the net charge at a location. The net charge is the difference between the total positive ion density and the sum of the electron and negative ion densities. Since this involves a difference of large numbers, precision is required to accurately solve for the electric potential. The solution of equations (2.1)-(2.3) may be especially laborious in situations where the net charge is small compared to the plasma density. To circumvent this limitation, the ambipolar approximation model was developed.

The assumptions made in the ambipolar approximation include a zero net charge in the plasma, which requires that the electron density and fluxes at all locations match the summed ion densities and fluxes. In place equations (2.1) and (2.2), the set of

$$\begin{aligned} \sum_i q_i (-\vec{\nabla} \cdot \vec{\phi}_i + S_i) &= F_2 = 0 \\ \sum_j n_j q_j &= F_1 = 0 \end{aligned} \quad (2.13)$$

equations (2.13) is solved in a similar Newton iteration scheme as described above.

In addition, neutral transport for each neutral species i is included with updates in an time-spliced manner after the updates to charged species' densities, using successive over-relaxation (SOR) techniques and including the contribution of advective flow fields if any and sources due to volumetric and surface kinetics. In the time-splicing approach, the neutral densities are kept constant during the integration of the charged particle transport equations and vice-versa. The equation (2.14) is discretized using finite-volume techniques described above and is implicitly integrated.

$$\frac{dN_i}{dt} = \bar{v}N_i - D_i N_T \nabla \left(\frac{N_i}{N_T} \right) + S_{Vi} + S_{Si}$$

$$N_i(t + \Delta t) = \left(N_i(t) + \left[\frac{dN_i}{dt} \right]_{t+\Delta t} \cdot \Delta t \right) \alpha + (1 - \alpha) \cdot N_i(t) \quad (2.14)$$

Successive over-relaxation uses a weighted solution from the previous time step and the present solution via a parameter α (usually between 1.0 – 2.0, specified as 1.7 here) and helps ensure rapid convergence of the solution.

A simple circuit model using resistors, capacitors and/or inductors in series provides the interface to the external circuit. This is implemented by designating select materials in contact with the plasma as circuit legs. The conduction current from the plasma in each leg, I_{leg} , is determined from the fluxes of charged species on the material nodes k bounding the plasma. The voltage on any leg is adjusted using the conduction current and any displacement currents.

$$I_{leg} = \sum_k I_k, \quad I_k = \sum_l \phi_{l,k} \cdot A_k, \quad A_k = \sum_j p(j) \cdot \delta A_{ij}$$

$$V_{leg} = \varepsilon \frac{d\vec{E}}{dt} + I_{leg} \cdot R_{leg} + L_{leg} \frac{dI_{leg}}{dt} + \int \frac{I_{leg} dt}{C_{leg}} \quad (2.15)$$

Boundary conditions for potential are calculated using the applied bias to the metal surfaces. For species' densities, a flux-in/flux-out boundary condition is implemented wherein of the total species flux striking a surface ('striking species'), a fraction can be specified to disappear and produce a similar or different 'returning species'. There may be more than one returning species for a particular striking species and this may be different for different material surfaces in contact with the plasma. For

instance, an excited species can be designated to disappear on striking the surface and reappear as the ground state species by imparting its energy to the surface,

$$\phi_i = \phi_i^0 (1 - \alpha_i) + \sum_k \phi_k^0 \beta_{k,i} \quad (2.16)$$

where ϕ_i^0 is the flux of species i into the surface, α_i is the fraction of that flux that disappears at the surface, and $\beta_{k,i}$ is the fraction that gets converted to species k that is returned from the surface back to the plasma. When the striking species are ions, the returning species are usually the corresponding neutral species. Another example would be secondary electron emission from surfaces due to ion bombardment. In this case, secondary emission coefficients for the respective ion species on the surface material are used to specify the fraction of species influx emitted as secondary electrons. When the surface kinetics module is also being used, these returning fractions and sticking coefficients are recalculated to be in-sync with the actual reactions rates of these species at the specified surfaces as explained in section 2.5. In this manner, for every species i listed in the gas phase reaction mechanism, one (or more) ‘returning species’ k , α_i and $\beta_{k,i}$ must always be specified.

To obtain the electron temperature, the electron energy equation is solved for average electron energy ε ,

$$\frac{d}{dt}(n_e \varepsilon) = \vec{j} \cdot \vec{E} - n_e \sum_i N_i \kappa_i - \nabla \cdot \left(\frac{5}{2} \varepsilon \vec{\phi}_e - \lambda \nabla T_e \right) \quad (2.17)$$

$$\vec{j} = q \vec{\phi}_e$$

where T_e is the electron temperature defined as $(2\varepsilon/3)$, n_e is the electron density, κ_i is the rate coefficient for power loss for collisions of electrons with species i having density N_i ,

κ is the thermal conductivity, and $\vec{\phi}_e$ is the electron flux. This equation is implicitly integrated in time using the successive over-relaxation technique with an SOR parameter β of 1.8.

$$T_{e,i}^{n+1} = \frac{T_{e,i}^n + \frac{\Delta t \cdot \vec{j} \cdot \vec{E}}{1.5n_{e,i}} - \sum_k k_k N_k \Delta \varepsilon \frac{2}{3} \Delta t - \Delta t \left(\sum_j \frac{5}{3} T_{e,j} \frac{\phi_{e,ij}}{n_{e,i}} \delta A_{ij} - \sum_j \delta A_{ij} \frac{\lambda_j T_{e,j}}{1.5n_{e,i}} \right)}{1 - \sum_j \frac{5}{3} \frac{\phi_{e,ij} \Delta t}{n_{e,i}} \delta A_{ij} + \sum_j \delta A_{ij} \frac{\lambda_j \Delta t}{1.5n_{e,i}}}$$

$$T_{e,i}^{n+1} = T_{e,i}^n (1 - \beta) + \beta T_{e,i}^{n+1} \quad (2.18)$$

Where $n+1$ indicates the new time and n indicates the time before taking the time step Δt and i refers to the node, j the neighbors and k refers to all inelastic collisions, λ_e refers to the electron thermal conductivity and ϕ_e refers to the electron Scharfetter Gummel flux between i and j .

The electron energy transport coefficients (μ_e , D_e) and rate coefficients (k_k) used above are obtained as a function of T_e by solving Boltzmann's equation for the electron energy distribution (EED) using a two-term spherical harmonic expansion [8]. The EED is computed for a range of E/N values from which the rate coefficients and electron temperature are obtained. These are then used to compute reaction sources for electron impact reactions and are updated as the electron energy distribution changes with gas composition.

Gas phase chemistry contributes to source terms in charged species and neutral transport equations. Source terms due to electron impact reactions and heavy particle collisions are included. Source terms are computed at each node in the mesh depending on the local electron and gas temperatures. Rate coefficients for electron impact reactions

are computed in the electron energy transport module and expressions for heavy particle reactions using gas temperatures are normally of the Arrhenius form.

Seeding of electrons far away from the avalanche is possible due to photons from excited species in the ionized regions. A radiation transport module calculates sources due to photoionization,

$$S_{k,j}(\vec{r}) = N_k(\vec{r}) \int N_j(\vec{r}') \sigma_{k,j} G_j(\vec{r}', \vec{r}) d^3 \vec{r}'$$

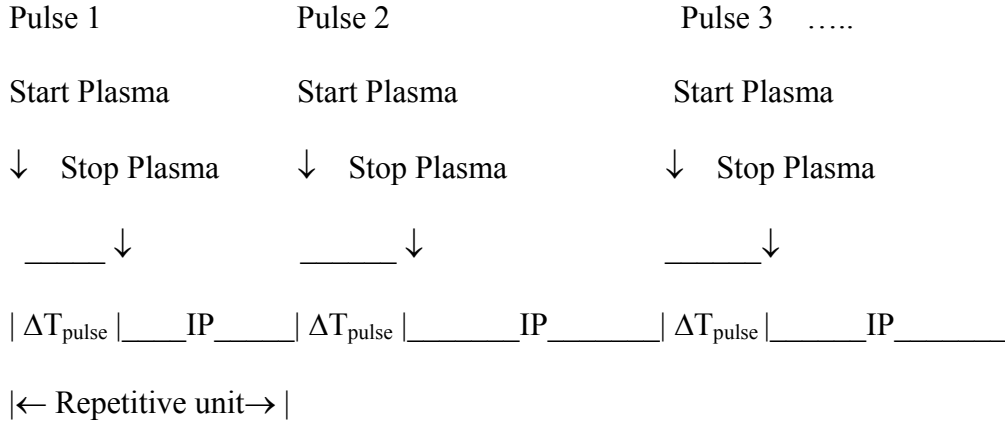
$$G_j(\vec{r}', \vec{r}) = \frac{\exp(-|\vec{r}' - \vec{r}| / \lambda_j)}{4\pi |\vec{r}' - \vec{r}|^2} \quad (2.19)$$

where $S_{k,j}(\vec{r})$ is the photoionization source for species k at location \vec{r} due to photons emitted from species j at location \vec{r}' , N refers to species densities, $\sigma_{k,j}$ is the photoionization cross section for species k , and the Green function $G_j(\vec{r}', \vec{r})$ is used to account for view angles that might block radiation. Source terms would comprise photoionization in the gas and photoemission from electrode surfaces. Photoemission from surfaces due to internal photons emitted by excited species in the discharge volume is also included.

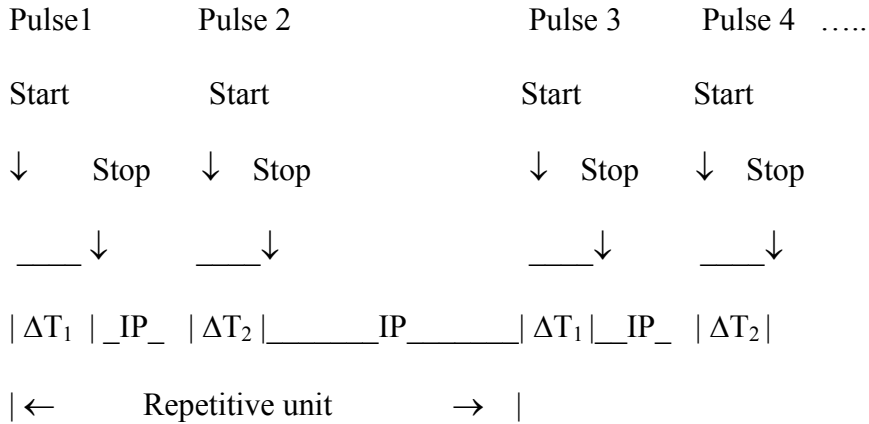
To enable the two-dimensional modeling of repetitively pulsed discharges, frequently encountered in atmospheric pressure plasma processing, the ability to simulate multiple pulses was added called the pulsed plasma module. Since the actual discharge duration can be quite small (a few to tens of ns) compared to the pulsing frequency (up to 100 μ s), the computational time to track more than a few pulses can quickly become unmanageable. To enable faster computation, a pulse-width ΔT_{pulse} is specified, which may be different for different pulses. When the duration of integration during a particular pulse exceeds its ΔT_{pulse} , the decay of all charged species i , is accelerated by adding its

density n_i to the density of the corresponding primary ‘returning species’ n_k and then setting $n_i=0$, at every plasma node. In the interpulse period (IP) between two pulses, neutral gas phase and surface kinetics and any evolving flow fields continue to be tracked as before.

A sequence of similar repetitively pulses schematically looks like this,



It is possible to specify repetitive pulse-trains, where the unit of repetition may itself contain a series of pulses,



The time steps in the interpulse period, usually on the order of 100s of ns to a few μs are only limited by the stability of the integration in the fluid dynamics module and the update of individual neutral species densities. The pulse repetition frequency determines $T_{\text{next_pulse}}$, the time at which the next pulse begins. When the time of

integration exceeds T_{next_pulse} , the equations for the plasma dynamics (2.1)-(2.3) and (2.17) are solved again until the time exceeds $T_{next_pulse} + \Delta T_{pulse}$ and the process is repeated.

Trajectories of beam electrons, such as energetic secondary electrons arising due to ion bombardment of surfaces, can be tracked with the Secondary Emission Electron Monte Carlo Simulation (SEeMCS).[3] The SEeMCS is performed on a separate Cartesian Mesh (CM) appropriately defined near the regions where beam electron transport is important and overlapping the unstructured mesh. Pseudoparticles are released from electron emitting nodes on the CM periodically with weighting proportional to the source of electrons at that particular node as a result of ion bombardment or photons or external electron beam source. The trajectories of pseudoparticles are computed using electric fields interpolated from the unstructured mesh. Those electrons with energies below a certain threshold (about 3 eV) are removed from the simulation and are clubbed into a source of bulk electrons that are used in the continuity equation for electrons.

The results of the SEeMCS are electron impact source functions and sources of secondary electrons resulting from these beam electrons. SEeMCS is called at regular intervals and sources of electron impact and secondary emission are held constant between calls to the SEeMCS. The frequency of calls to the SEeMCS depends on the conditions in the plasma, for instance, if steady state is reached, this allows for less frequent calls. The source functions are obtained by computing $f(\epsilon)$, the electron energy distributions (EEDs) of the beam electrons and their progeny in the SEeMCS as a function of position on the CM, and convolving these EEDs with reaction cross sections.

2.4 Fluid Dynamics Module

In order to account for advective flow, a modified form of the Navier-Stokes equations is solved³ which adds sources of momentum and energy due to the presence of electric fields and charged species. The fundamental equations solved in the fluid module are the compressible form of the Navier-Stokes equations,

$$\frac{\partial \rho}{\partial t} = -\vec{\nabla} \cdot (\rho \vec{v}) = G_1 \quad (2.20)$$

$$\frac{\partial \rho \vec{v}}{\partial t} = -\vec{\nabla} \cdot (\rho \vec{v} \vec{v}) + \left(-\vec{\nabla} p + \vec{\nabla} \cdot \left(\mu \left(\vec{\nabla} \vec{v} + (\vec{\nabla} \vec{v})^T - \frac{2}{3} (\vec{\nabla} \vec{v}) \cdot I \right) \right) - \rho \vec{g} + \vec{S}_{M,plasma} \right) = G_{2,3} \quad (2.21)$$

$$\frac{\partial \rho C_p T}{\partial t} = \left(C_p T \frac{\partial}{\partial t} (\rho) - \vec{\nabla} \cdot (\rho C_p T \vec{v}) - \vec{\nabla} \cdot (k \vec{\nabla} T) + S_{E,plasma} \right) = G_4 \quad (2.22)$$

$$\rho = \frac{P_0 M_w}{R_g T} \quad (2.23)$$

where P_0 is operating pressure, C_p is the heat capacity (constant pressure), M_w is the molecular weight of the gas, ρ is the gas density, T is the gas temperature, \vec{v} is the gas velocity, and R_g is the ideal gas constant. The additional terms in the momentum and energy equations account for source terms to the neutral fluid arising from the presence of the plasma and are given by the expressions,

$$\vec{S}_{M,plasma} = \sum_k \sum_i \sigma_{i,k} \frac{2M_i M_k}{(M_i + M_k)^2} N_i N_k M_k v_{th} (\vec{v} - \vec{v}_i) \quad (2.24)$$

$$S_{E,plasma} = \sum_i q_i \vec{\phi}_i \cdot \vec{E} + \sum_r H_r \quad (2.25)$$

where $\vec{S}_{M,plasma}$ is the momentum source term accounting for ion-neutral collisions that result in momentum transfer to neutrals arising from motion of ions in the electric field and $S_{E,plasma}$ is the source term for the energy equation accounting for ion joule heating

and heats of reaction, i denotes species that are ions, k denotes neutral species, M_i denotes molecular mass of species i (ions or neutrals), v_{th} is the thermal speed, \vec{v}_i is the velocity of ion species i , v is the single fluid velocity for the neutral gas, $\sigma_{i,k}$ is the cross-section for ion-neutral collisions between ion species i and neutral species k , H_r is the net heat of reaction r , and other symbols have their usual meaning.

The continuity equation (2.20), Navier-Stokes' equations for momentum (2.21) and the energy equation (2.22) are solved by direct integration in time, taking time steps of Δt to determine the variables δY_l – the increments to the gas velocity and density at each plasma node, and temperature throughout the computational domain.

$$Y_l = Y_l(t) + \delta Y_l \text{ where}$$

$$\delta Y_l = \frac{dY_l}{dt} \cdot \Delta t = G_l(t + \Delta t) \cdot \Delta t = \left(G_l(t) + \sum_m \frac{\partial G_l}{\partial Y_m} \delta Y_m \right) \cdot \Delta t \quad (2.26)$$

This is done by rearranging the above equation grouping the terms containing δY_l on the left hand side, so that the system of equations can then be rearranged in such a way that a matrix formulation,

$J' Y = C$ results where each element of the Jacobian matrix J' is

$$J'_{xy} = \frac{\partial G_x}{\partial Y_y} \text{ for non-diagonal elements where } x \neq y \text{ and}$$

$$J'_{xx} = \frac{1}{\Delta t} - \frac{\partial G_x}{\partial Y_x} \text{ for diagonal elements.} \quad (2.27)$$

which is written out in the expanded matrix-vector form below.

$$\begin{bmatrix}
\frac{1}{\Delta} \frac{\partial G_{i,1}}{\partial \rho_i} & \frac{\partial G_{i,1}}{\partial u_i} & \frac{\partial G_{i,1}}{\partial v_i} & \frac{\partial G_{i,1}}{\partial T_i} & \dots & \frac{\partial G_{i,1}}{\partial \rho_{i+n}} & \frac{\partial G_{i,1}}{\partial u_{i+n}} & \frac{\partial G_{i,1}}{\partial v_{i+n}} & \frac{\partial G_{i,1}}{\partial T_{i+n}} \\
\frac{\partial G_{i,2}}{\partial \rho_i} & \frac{1}{\Delta} \frac{\partial G_{i,2}}{\partial u_i} & \frac{\partial G_{i,2}}{\partial v_i} & \frac{\partial G_{i,2}}{\partial T_i} & \dots & \frac{\partial G_{i,2}}{\partial \rho_{i+n}} & \frac{\partial G_{i,2}}{\partial u_{i+n}} & \frac{\partial G_{i,2}}{\partial v_{i+n}} & \frac{\partial G_{i,2}}{\partial T_{i+n}} \\
\frac{\partial G_{i,3}}{\partial \rho_i} & \frac{\partial G_{i,3}}{\partial u_i} & \frac{1}{\Delta} \frac{\partial G_{i,3}}{\partial v_i} & \frac{\partial G_{i,3}}{\partial T_i} & \dots & \frac{\partial G_{i,3}}{\partial \rho_{i+n}} & \frac{\partial G_{i,3}}{\partial u_{i+n}} & \frac{\partial G_{i,3}}{\partial v_{i+n}} & \frac{\partial G_{i,3}}{\partial T_{i+n}} \\
\frac{\partial G_{i,4}}{\partial \rho_i} & \frac{\partial G_{i,4}}{\partial u_i} & \frac{\partial G_{i,4}}{\partial v_i} & \frac{1}{\Delta} \frac{\partial G_{i,4}}{\partial T_i} & \dots & \frac{\partial G_{i,4}}{\partial \rho_{i+n}} & \frac{\partial G_{i,4}}{\partial u_{i+n}} & \frac{\partial G_{i,4}}{\partial v_{i+n}} & \frac{\partial G_{i,4}}{\partial T_{i+n}} \\
\vdots & \vdots & \vdots & \vdots & \ddots & \vdots & \vdots & \vdots & \vdots \\
\vdots & \vdots & \vdots & \vdots & \ddots & \vdots & \vdots & \vdots & \vdots \\
\frac{\partial G_{i+n,1}}{\partial \rho_i} & \frac{\partial G_{i+n,1}}{\partial u_i} & \frac{\partial G_{i+n,1}}{\partial v_i} & \frac{\partial G_{i+n,1}}{\partial T_i} & \dots & \frac{1}{\Delta} \frac{\partial G_{i+n,1}}{\partial \rho_{i+n}} & \frac{\partial G_{i+n,1}}{\partial u_{i+n}} & \frac{\partial G_{i+n,1}}{\partial v_{i+n}} & \frac{\partial G_{i+n,1}}{\partial T_{i+n}} \\
\frac{\partial G_{i+n,2}}{\partial \rho_i} & \frac{\partial G_{i+n,2}}{\partial u_i} & \frac{\partial G_{i+n,2}}{\partial v_i} & \frac{\partial G_{i+n,2}}{\partial T_i} & \dots & \frac{\partial G_{i+n,2}}{\partial \rho_{i+n}} & \frac{1}{\Delta} \frac{\partial G_{i+n,2}}{\partial u_{i+n}} & \frac{\partial G_{i+n,2}}{\partial v_{i+n}} & \frac{\partial G_{i+n,2}}{\partial T_{i+n}} \\
\frac{\partial G_{i+n,3}}{\partial \rho_i} & \frac{\partial G_{i+n,3}}{\partial u_i} & \frac{\partial G_{i+n,3}}{\partial v_i} & \frac{\partial G_{i+n,3}}{\partial T_i} & \dots & \frac{\partial G_{i+n,3}}{\partial \rho_{i+n}} & \frac{\partial G_{i+n,3}}{\partial u_{i+n}} & \frac{1}{\Delta} \frac{\partial G_{i+n,3}}{\partial v_{i+n}} & \frac{\partial G_{i+n,3}}{\partial T_{i+n}} \\
\frac{\partial G_{i+n,4}}{\partial \rho_i} & \frac{\partial G_{i+n,4}}{\partial u_i} & \frac{\partial G_{i+n,4}}{\partial v_i} & \frac{\partial G_{i+n,4}}{\partial T_i} & \dots & \frac{\partial G_{i+n,4}}{\partial \rho_{i+n}} & \frac{\partial G_{i+n,4}}{\partial u_{i+n}} & \frac{\partial G_{i+n,4}}{\partial v_{i+n}} & \frac{1}{\Delta} \frac{\partial G_{i+n,4}}{\partial T_{i+n}}
\end{bmatrix}
\begin{bmatrix}
\Delta \rho_i \\
\Delta u_i \\
\Delta v_i \\
\Delta T_i \\
\vdots \\
\vdots \\
\Delta \rho_{i+n} \\
\Delta u_{i+n} \\
\Delta v_{i+n} \\
\Delta T_{i+n}
\end{bmatrix}
=
\begin{bmatrix}
-G_{i,1} \\
-G_{i,2} \\
-G_{i,3} \\
-G_{i,4} \\
\vdots \\
\vdots \\
-G_{i+n,1} \\
-G_{i+n,2} \\
-G_{i+n,3} \\
-G_{i+n,4}
\end{bmatrix}$$

The ideal gas law (2.23) is used to relate density to pressure. Optionally, temperature can also be solved in materials if significant gas heating is present that would cause materials to heat up.

When Mach number of the flow is significantly below the sonic threshold, and in the absence of large temperature or density gradients such as the case of repetitively pulsed atmospheric pressure discharges with ultra-short voltage pulses, a solution of the incompressible form of equations (2.20)-(2.23) may be more desirable. In order to take advantage of the solution technique implemented for compressible flow fields, a commonly used variation of incompressible flow solution techniques called the artificial compressibility method was implemented to solve equations (2.20)-(2.23). Briefly, the

artificial compressibility method involves the solution of the continuity equation with a temporal gradient of pressure in-place of the temporal variation of density,

$$\frac{\partial p}{\partial t} + \beta^2 (\vec{\nabla} \cdot (\vec{v})) = 0, \quad p = \beta^2 \rho \quad (2.28)$$

where, β is a compressibility parameter with a value between 0.5 and 2.0. The corrections to the pressure obtained are fed back in through the pressure terms in the momentum equations (2.21) to obtain the flow fields while holding the density constant. The energy equation is decoupled from the momentum and continuity equations in this method. Updates to density are obtained as a function of the local temperature from the incompressible ideal gas law equation (2.23). For consistency with the calculation of individual neutral species densities in the plasma dynamics model, the fluid density is renormalized.

2.5 Surface Kinetics Module

Plasma-surface interactions are integral to surface processing technologies, but the complex nature of these interactions mean that very few models have attempted to capture them in a self-consistent manner. The surface kinetics module described in this section is a modified version of a model developed earlier [9] for studying surface interactions in low pressure plasma processing reactors. A flowchart depicting the SKM is shown in Fig. 2.3 and a brief description follows.

The user specifies materials for the surface kinetics module and also provides a surface reaction mechanism which is discussed later. When the geometry module creates the initial mappings, each non-plasma node that borders the plasma is flagged as a site where surface chemistry may be tracked. Algorithms were implemented to trace these surface nodes on complex surface shapes that may be created on the unstructured mesh.

These boundary tracing algorithms enable the tracking of surfaces of materials not only bordering the plasma domain but also for materials wholly within the plasma itself, such as surfaces of suspended particles.

The details of the algorithm are briefly elucidated. Once a surface site is flagged, all its neighbors are scanned for two, or in rare cases with microscopic surface features, three surface nodes. In this manner a list of surface chemistry nodes is compiled. This list is reordered to have nodes in a contiguous fashion by starting from a terminal end and looping through it in either a clockwise or anticlockwise direction to build a connectivity list. The method is invaluable for the investigation of the treatment of non-planar polymer surfaces, as it helps track position *along* the surface exposed to the plasma in an orderly manner and visualize spatial variations in treatment.

The SKM consists of a modified surface site-balance algorithm implemented along the boundary nodes of specified materials that border the plasma domain. Initial conditions to the SKM consist of surface coverage of species found on the virgin surface. The SKM accepts fluxes of gas phase species such as ions, electrons and neutral species as well as photons and applies a user-specified surface reaction mechanism to calculate the rate of surface reactions. The reaction mechanism consists primarily of gas phase species reacting on the surface sites, but it also allows for photochemistry and surface-surface sites reacting with each other. The general form of surface reactions is,



where the subscript g denotes a gas phase species and the subscript s denotes a surface resident species or a surface site, and k_i is the reaction probability of the i^{th} surface

reaction, similar to the Eley-Rideal scheme. The evolution of the surface coverage of species B on a material whose surface is reacting is given by,

$$\left(\frac{\partial \theta_B}{\partial t}\right)_i = -\left(\frac{1}{T}\right)R_i \quad (2.30)$$

where T is the total surface site density ($\sim 10^{14}$ - 10^{15} cm⁻²) and

$$R_i = k_i \Phi_A \theta_B \quad (2.31)$$

is the rate of the i^{th} surface reaction due to the flux of species A (Φ_A) on the surface and θ_B is the fractional coverage of B on the surface. Photon-initiated surface reactions are similar in form to equation (2.29) with A denoting the flux of photons. For surface-surface reactions (similar to the Langmuir Hinshelwood scheme) such as abstraction by a surface resident group from its surrounding surface sites, reactions are of the form,



where P and Q are surface resident groups and U and V are usually products that are also surface resident groups. The reaction probability is scaled by the total density of surface sites to be compatible with gas-surface reactions such as those in equation (2.29). In general the reaction probability for surface-surface reactions is higher than for gas-surface reactions because of the greater residence time available to reacting species already on the surface, but the overall reaction rates may be higher in gas-surface reactions due to higher gas-phase species fluxes.

Differential equations for the set of reactions such as equation (2.29, 2.32) that make up the reaction mechanism are then integrated as a function of time. Outputs from the SKM include the fractional coverage of different surface resident species and returning fractions for gas phase reactants and products as a result of these surface

reactions. The SKM is integrated with the plasma model via the surface sticking coefficient α_A for the incident gas phase species A,

$$\alpha_A = \sum_i \frac{R_i}{\Phi_A} \quad (2.33)$$

where the summation is over all surface reactions i that species A undergoes on the surface and returning fraction β_{CG} which is the fraction of the incident gas species G that returns as species C,

$$\beta_{CG} = \alpha_G \Phi_A \quad (2.34)$$

for each reaction containing C as a product.

Radical fluxes in repetitive pulsed atmospheric pressure discharges exhibit large variation on timescales of a few microseconds and the surface treatment of polymers occurs over milliseconds. The surface kinetics model was modified to record the fluxes of all plasma generated species on the polymer surface during the course of an entire pulse and the following interpulse period, after a certain number of pulses, when approximately periodic steady state conditions have been reached in the plasma. The recorded fluxes are then repeatedly used to simulate surface treatment over tens to hundreds of milliseconds.

2.6 Reaction Mechanisms

Atmospheric pressure discharges investigated in this work are repetitively pulsed at high voltages (up to few kV) to breakdown of the gas, resulting in the creation of electrons, ions and radicals. Reactions occurring in the gas phase include electronic impact vibration, excitation, dissociation, attachment and ionization, heavy particle reactions including charge and excitation transfer and Penning ionization, photoemission, photoabsorption and photoionization. Plasma-produced species react with the polymer

surfaces resulting in the formation of new surface resident species and gaseous products. Photons emitted by the relaxation of excited species in the discharge especially in the ultraviolet wavelengths, are energetic enough to break bonds on the polymer surface. Radicals have longer lifetimes than charged species and react with each other and with the polymer surface, even after the plasma is extinguished in between pulses.

Surface functionalization of the polymer results from the simultaneous action of all plasma species, over multiple discharges spanning a few 10s of ms. In this work, we investigated the functionalization of polypropylene (PP) surfaces in atmospheric pressure discharges generated in various gas mixtures. Humid air and He/O₂/H₂O discharges were examined for the functionalization of PP with O-containing groups which are of primary interest in many industrial applications related to printability and adhesion. Discharges in He/NH₃/H₂O mixtures were considered for the functionalization of PP with N-containing groups that have necessary for applications such as enzyme immobilization. Some of the features of the gas phase reaction mechanisms for discharges generated in these mixtures as well as surface reaction mechanisms for the interactions of various discharge species with the PP surface are briefly described in this section. The detailed reaction mechanisms as well as references are listed in Appendices A through D.

2.6.1 Gas Phase Kinetics in Air

The reaction mechanism used for humid air gas-phase chemistry is found in Appendix A and has been described in detail by Dorai and Kushner.[10] Gas species included in the humid air chemistry are N₂, N₂^{*}, N₂^{**}, N₂⁺, N⁺, N₄⁺, N, N(²D), O₂, O₂(a¹Δ), O₂(b¹Σ), O₂⁺, O₂⁻, O, O(¹D), O(¹S), O⁺, O, O₃, H₂O, H₂O⁺, H₂, H, OH and HO₂. N₂^{*} and N₂^{**} denote the states N₂(A³Σ) and N₂(b¹Π, b¹Σ). The latter is treated as a

lumped state including transitions higher than $N_2(A^3\Sigma)$, while O_2^* denotes the $O_2(^1\Delta)$ state respectively. Photoionization was included with N_2^{**} being the emitting species with a lifetime of 5 ns, resulting in the photoionization of O_2 with a cross section of 10^{-19} cm^{-2} .

Electron impact reactions with N_2 , O_2 and H_2O including the vibrational excitation, electronic excitation, attachment and ionization are included. The major ions generated by electron impact include N_2^+ and O_2^+ , while N_2^{**} and O_2^* are the major excited species.

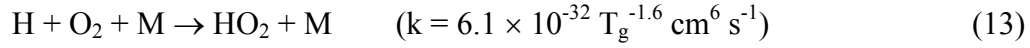
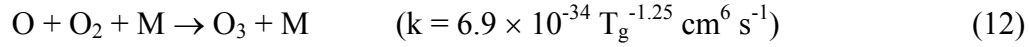


where M represents any third species and $\Delta\varepsilon$ is the threshold energy.

One of the major pathways for the generation of radicals such as O, H and OH is by electron impact reactions of O_2 and H_2O .

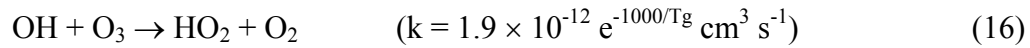
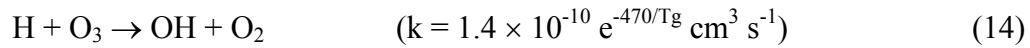


At atmospheric pressure, three body reactions play an important role. O is very reactive and undergoes three body reactions with O₂ to form O₃. H reacts at slower rates with O₂ in the presence of a third body to form HO₂.

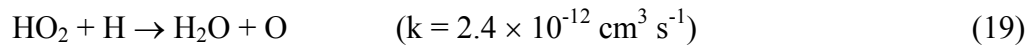


where k is the rate coefficient at room temperature unless noted otherwise.

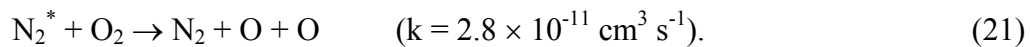
There are no major consumption pathways for radicals such as O₃, which is relatively unreactive and tends to accumulate. O₃ does react at slow rates with H to form OH, with O to form O₂ and with OH to form HO₂.



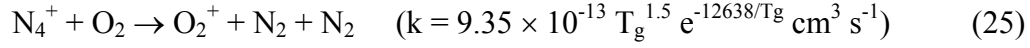
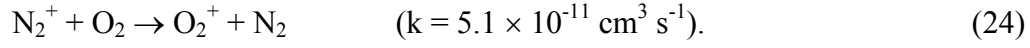
HO₂ reacts slowly with radicals such as O, H and OH forming other radicals or stable products. OH and O react mutually at slow rates to form H.



Excited species such as N₂^{*} and O₂^{*} are either quenched to the ground state in collisions or react to dissociate other molecules.



Much of the N_2^+ reacts with N_2 to form N_4^+ or undergoes charge exchange collisions to with O_2 resulting in O_2^+ . N_4^+ also reacts to form more O_2^+ .



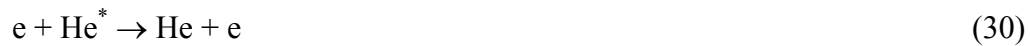
Ion-ion neutralization reactions forming neutral species are included in the mechanism. For instance,



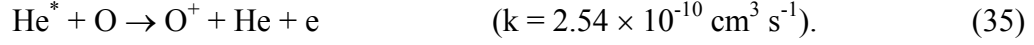
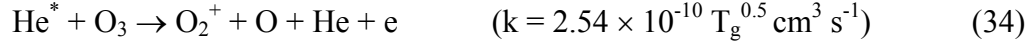
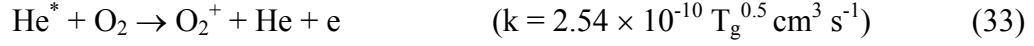
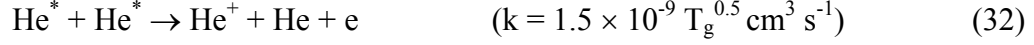
2.6.2 Gas Phase Kinetics in He/O₂/H₂O Plasmas

The gas phase reaction mechanism used for He/O₂/H₂O discharges is found in Appendix B and a detailed description is found in Stafford and Kushner.[11] The species considered in the gas phase mechanism include: He, He(²S) (denoted as He^{*}), He⁺, O₂, O₂(v), O₂^{*}, O₂(b¹Σ), O₂⁺, O₂⁻, O, O(¹D), O(¹S), O⁺, O⁻, O₃, O₃⁻, H₂O, H₂O⁺, H, OH.

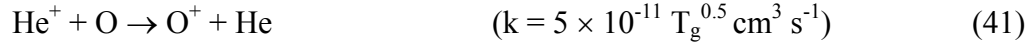
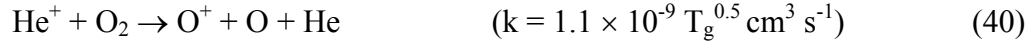
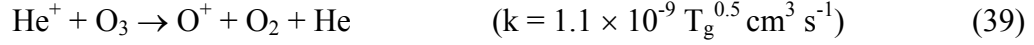
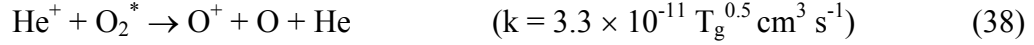
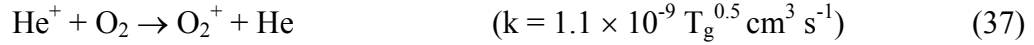
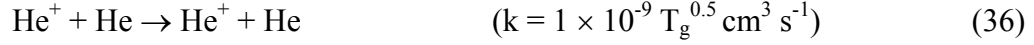
Electron impact and heavy particle reactions for O₂ and H₂O such as those discussed in Sec. 5.2.2 are also included in this mechanism. In addition, electron impact processes such as electronic excitation, ionization and recombination,



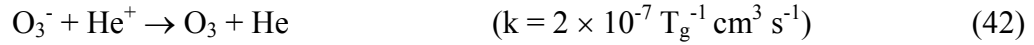
and heavy particle reactions for various He species are included. Penning ionization resulting from the reactions of He^{*} with O, O₂ and O₃ are included.



He^+ has a higher ionization potential (24.5 eV) than other species in the discharge and undergoes charge exchange reactions with O, O₂ and O₃ to form O⁺ and O₂⁺.



Ion-ion neutralization reactions of He ions forming neutral species are also included in the mechanism. For instance,



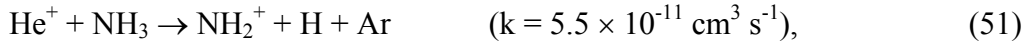
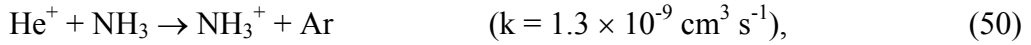
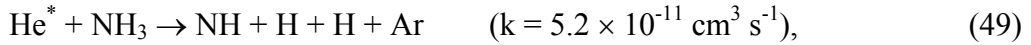
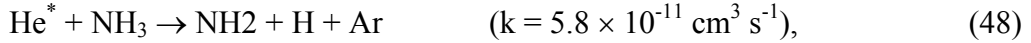
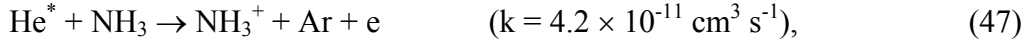
2.7.3 Gas Phase Kinetics in He/NH₃/H₂O Plasmas

The gas phase reaction mechanism used for the He/NH₃/H₂O discharges is detailed in Appendix C and includes the following species: e, NH₃, NH₃⁺, NH₃(v), NH₄⁺, NH₂, NH₂⁺, NH₂⁻, NH, NH⁺, N, N⁺, H, H⁺, H⁻, H₂, H₂⁺, H₃⁺, N₂, N₂H₂, N₂H₃, N₂H₄, H and OH.

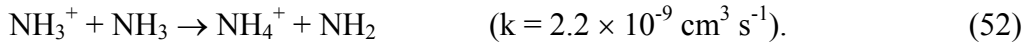
Electron-impact reactions of NH₃ resulting in vibrational excitation, electronic excitation and ionization are included. Electronic excitation pathways result in subsequent dissociation of the excited state forming fragments such as NH₂ and NH.



Electron impact reactions for He and H₂O are similar to those discussed in the Secs. 5.2.1 and 5.2.2 above. He* and He⁺, with energies of 19.8 and 24.5 eV respectively have enough energy to charge-exchange or Penning ionize, and so dissociate NH₃,

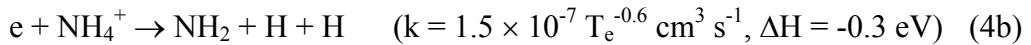


Charge exchange reactions of He⁺ with NH, NH₂ and NH₃ results in the formation of the respective NH_x⁺ ions. Further charge exchange reactions between these NH_x⁺ ions and other species leads to formation of NH₄⁺ which has the smallest ionization potential among all the ions in the mechanism,



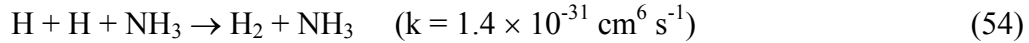
As such, the density of NH₄⁺ is large if NH_x species are not significantly depleted.

Dissociative recombination of NH_x⁺ produces NH_{x-1} and H as the dominant channels.

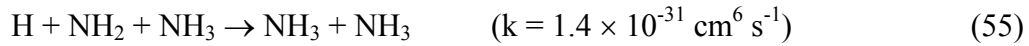


where the T_e is in eV.

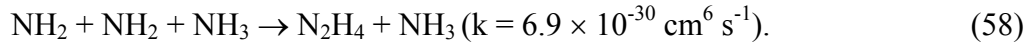
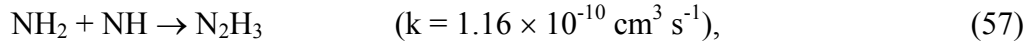
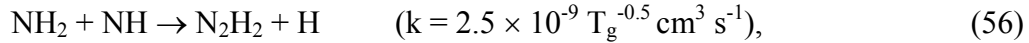
In the interpulse period, neutral radical chemistry dominates the reaction mechanism. At this time the bulk of the dissociated NH_3 is in the form of H and NH_2 . Rapid three-body reactions result in the recombination of reactive radicals into more stable products in a few ms.



The consumption of H radicals by three-body reactions with NH_2 to form NH_3 can be important as the rate coefficient for this reaction is large, particularly with NH_3 as the third body ($k = 6.0 \times 10^{-30} \text{ cm}^6 \text{ s}^{-1}$).



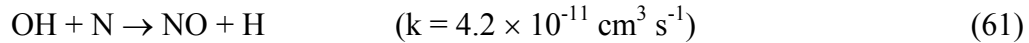
Formation of N_2H_x ($x=2, 3, 4$) by 2 and 3-body reactions results in the depletion of NH_2 . The primary pathways for producing N_2H_x ($x=2, 3, 4$) are,

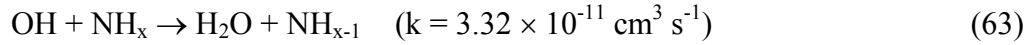


NNH is a relatively short-lived species as its rate of decomposition to N_2 and H is much faster than its production from N_2H_2 ,

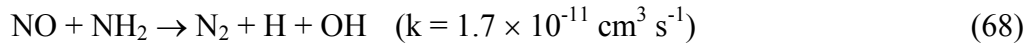
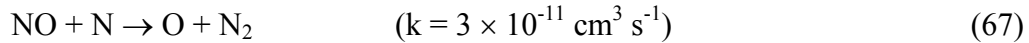
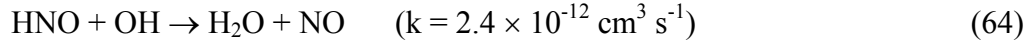


NH_x species can also react with O containing species generated due to electron impact dissociation of H_2O , such as OH creating other species such as NO and HNO.





The products of these reactions can further react with other species, such as,



About 40 individual species in all, including more than 15 charged species were tracked with this mechanism.

2.7.4 Surface Reaction Mechanism on Polypropylene

The chemical structure of polypropylene is a series of hydrogen (H) and methyl (-CH₃) groups alternately bonded to carbon centers forming a hydrocarbon backbone (denoted as RH). The functionalization of PP surfaces in gas discharges, usually to introduce O atoms into the backbone, is extensively reported in literature, since it is frequently used in industry to increase wettability, adhesion and printability. Therefore, good general understanding exists for the various surface reaction pathways on PP surfaces.

The surface reaction mechanism developed by Dorai and Kushner [10] is used in these investigations. They considered the functionalization of PP surface by radicals generated in a humid air corona discharge. The main gas phase species in this mechanism that react with the PP surface include O, OH, O₃ and O₂. In principle, a reaction mechanism consisting of a set of reactants must be unaffected by the precursors used to generate those reactants. The surface reaction mechanism in [10] is therefore

extended to the treatment of PP in He/O₂/H₂O discharges, where the similar gas phase radicals are formed, and react with the PP surface.

The hierarchical set of reactions in the mechanism in [10] for functionalization of PP consists of initiation, propagation and termination pathways, similar to free radical gas phase chemistry. The initiation reactions typically consist of reactions of a gas phase species with a surface site, which is similar to the Eley-Rideal mechanism for reaction of gaseous species on surfaces. Reactions between gas species and the surface are assigned a probability, either based on reported experimental observations in the literature or by analogy with similar reactions in the gas phase.

The probability of a reaction may vary with the type of C atom. Tertiary C atoms are far more reactive than secondary, which in turn are more reactive than primary C atoms. These variations are accounted for in the mechanism developed in [10], where surface reaction pathways are initiated with the abstraction of H atoms from the hydrocarbon backbone by reactive O and OH generated in the discharge, creating surface radical sites called alkyl (R•) radicals with probabilities of 0.001 and 0.1 for tertiary carbon atoms with a factor of 5-10 decrease for secondary carbon centers and a further reduction by a similar factor for reactions that occur at primary carbon centers due to bond-polarity effects.



R• radicals react with O and O₃ present in the discharge to form alkoxy (R-O•) groups, which is a rapid pathway with assigned probabilities of 0.1 and 1.0.





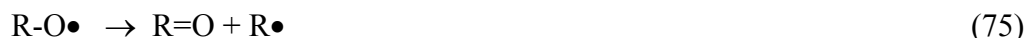
By contrast, a slower pathway is the reaction of $\text{R}\bullet$ radicals with O_2 to form peroxy ($\text{R-OO}\bullet$) groups with probabilities of $10^{-4} - 10^{-3}$.



Reactions among surface sites can also occur (with the rate coefficients specified in units of cm^2s^{-1}) which are subsequently scaled by the total density of surface sites in our model. These reactions can be thought to occur in a manner similar to Langmuir-Hinshelwood mechanisms, where species from the gas phase first react on a surface site and then with other surface resident groups. For instance, rapid abstraction of H atoms from surrounding sites by $\text{R-O}\bullet$ groups results in alcohol (R-OH) groups with a rate of $10^{-16} - 10^{-15} \text{ cm}^2\text{s}^{-1}$.



Alternatively the C-C bond at the $\text{R-O}\bullet$ site cleaves, leading to chain scission and the formation of carbonyl (R=O) groups and the creation of a new $\text{R}\bullet$ radical site at rates of 10^3 s^{-1} .



Surface radicals created by the further abstraction of H atoms from carbonyl groups ($\bullet\text{R=O}$) followed by the addition of OH results in an acid group (HO-R=O).



Continued chain scission leads to CO_2 formation, a byproduct of surface treatment.



The termination steps include the recombination of alkyl radicals on the backbone by H and OH radicals with a probability of 0.2.



In He/NH₃/H₂O discharges, the reactive species in the gas phase are expected to be OH, H and various N containing species such as N, NH and NH₂. Other species such as N₂H₄ and N₂H₂ are known to be relatively stable at the temperatures encountered in atmospheric pressure pulsed discharges and are therefore not considered in the mechanism. OH and H are created by electron impact dissociation of H₂O while the various N containing groups result from the degradation of NH₃ by electron impact and heavy particle reactions. The discharge dynamics ultimately determines the relative abundance of various species.

The heterogeneous reaction probabilities leading to the N-functionalization are not as exhaustively explored as for O-functionalization in the literature, though many probable pathways have been proposed from experimental observations. Nevertheless, N-functionalization can be thought to occur on a similar set of hierarchical reactions as detailed for O-containing groups above. A discussion on experimental techniques that are being used to determine the surface reaction mechanisms responsible for amine functionalization of polymer surfaces is found in [12].

N-containing groups can be formed on the polymer surface either by the direct insertion of N containing species into the backbone or C-H bonds or by addition to a free radical R• site. The direct insertion of N or NH into backbone is relatively improbable given the high reaction endothermicity, but the direct insertion of excited N atoms and

NH radicals into C-H bonds has been reported in analogous gas phase reactions in the literature.



The insertion of NH has a low rate of $< 10^{-15} \text{ cm}^3\text{s}^{-1}$ in the gas phase [13] corresponding to a probability of 10^{-5} in our model.

Excited N atoms (N^*) may react with alkanes in the gas phase at rates of $10^{-12} \text{ cm}^3\text{s}^{-1}$ in the gas phase [14] and are thought to undergo direct insertion into C-H bonds,



but the density of N^* atoms is typically low ($< 10^9 \text{ cm}^{-3}$ in simulations of humid air discharges [10]), so this pathway is expected to be insignificant.

The addition of N-containing groups to the backbone proceeds can be considered to occur via the multi-step initiation-propagation-termination hierarchy described for functionalization with O-containing groups earlier. Initiation reactions occur with the abstraction of H atom from the PP surface. The abstraction reaction of OH plays an important role in PP functionalization in humid air discharges with an abstraction probability of 0.1 and is repeated here.



The gas phase reactions of H and OH with C_4H_{10} [15] were used as references to determine the relative reactivity of H atoms compared to OH for abstraction reactions. This allows the calculation of the ratio of the rate of an H abstraction reaction from the hydrocarbon backbone by H atoms relative to OH atoms to be between 10^{-3} - 10^{-5} depending on the primary, secondary or tertiary carbon center. Since the density of H atoms in NH_3 -containing discharges can be high due to the efficient fragmentation of

NH₃, the contribution of H atoms to abstraction pathway is significant. The abstraction step proceeds with the H atoms is designated to have a probability of 10⁻⁵ for tertiary carbon atoms decreasing one order of magnitude for secondary and primary carbon atoms in turn..



The possibility of NH and NH₂ abstracting H from the hydrocarbon backbone was considered, but not included in the mechanism. This was because the analogous gas kinetic rate of abstraction of H atoms by NH and NH₂ with C_nH_{2n+2} for various *n*, is very low relative to the reactivity of OH (by a factor of approximately 10⁻⁶).

Further H abstraction from sites adjacent to R• sites can lead to the formation of unsaturation sites (R=R) on the surface. Addition reactions across this double bond would reform R• sites.



Amine groups (R-NH₂) can be formed on the surface by the addition of NH₂ and to R• radicals. The analogous gas phase reaction rate of NH₂ radicals with alkyl radicals is about 4 x 10⁻¹¹ cm³s⁻¹ [16], so a probability of 0.4 is used for the corresponding heterogeneous reaction. The addition NH was assigned a probability of 0.4 by analogy to NH₂.

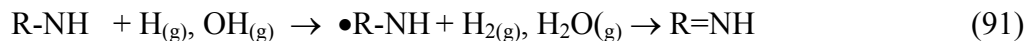


H abstraction from R-NH₂ groups by H and OH can form R-NH groups, which can again react with gas phase H atoms to re-form R-NH₂. The probabilities for these

abstraction and addition reactions are taken to be similar to those of abstraction from C-H bonds and addition to R• radicals.



H abstraction at the carbon centers of primary and secondary R-NH sites could lead to the formation of imines (R=NH).



The contribution of ions to the surface reactions in atmospheric pressure discharges is less clear. The high collisionality of atmospheric pressure discharges results in ions having near thermal energy close to the surface. Ion surface reactions are differentiated since we are interested in ability of different species to penetrate through gaps in surface features. It is feasible for ions arriving at the surface to contribute to surface chemical reactions in a manner similar to the reactive radicals. For instance, O^+ and O_2^+ can react on the surface in a manner similar to O and O_2 respectively.



Non-reactive ions arriving at the polymer surface may still break chemical bonds due to secondary electron emission from the surface. There is no specific data available in the literature for the secondary electron emission coefficient (γ) on dielectric surfaces due to ion bombardment at atmospheric pressure. However, various investigators have concluded that secondary electrons emitted from the dielectric surfaces due to ion bombardment, even at atmospheric pressures, contribute significantly to the discharge, with one study estimating with [17] estimating a γ of 0.01. In the context of surface

chemical reactions, ion bombardment accompanied by secondary electron emission most likely leads to the formation of surface radicals (R•). A sensitivity analysis was performed by varying γ from 10^{-5} – 1.0 and it was determined that for the transient discharges investigated in this work, the contribution of ion-initiated reactions to surface functionalization was not significant due to the short pulse durations.

Photons emitted from the plasma are thought to play an important role in surface kinetics.[18-20] UV photons emitted from the abundant density of excited species in the plasma have energies of 4-5 eV which can cleave C-C bonds on the surface forming R• radical sites. Skurat, *et al* [21] studied photon-initiated reactions on polymer surfaces and determined that photochemistry on the polymer surface proceeds via three major pathways. They found that the dominant pathway is the elimination of molecular H₂ from the hydrocarbon surface forming alkenes that subsequently react to form adjacent alkyl radical sites (-•RR•-), which have a higher probability of undergoing scission to form R• sites rather than recombining [17].



The other two pathways result in the formation of R• radicals by breaking either the C-H bond releasing atomic hydrogen or the C-C bond scission in the polypropylene backbone.

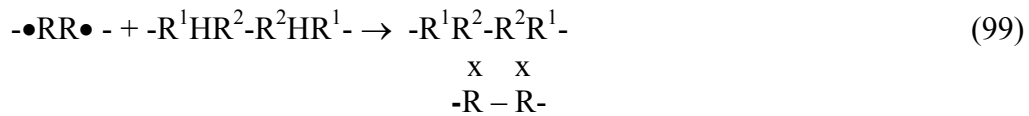


They estimated the relative rates that the chain scission pathway was about 4-5 times faster than the former.



In these investigations, the total quantum yield of photons leading to the formation of alkyl (R•) sites was taken to be 0.2 [22] and the constituent pathways (85)-(89) were scaled accordingly.

Surface radicals (R•) on different backbones can react with each other on polymer surfaces to crosslink [23-25] especially in inert gas atmospheres, reported often in literature as the CASING mechanism.[26-27] Surface radicals (R•) would probably react with gas phase radicals than crosslink with each other in the presence of reactive gas radicals as discussed in [19].



where x indicates the formation of cross-linkages. However, it is possible that surface radicals created by plasma species are not all consumed in further reactions with plasma species due to the dynamics of the discharge, so crosslinking among reactions amongst R• radicals was included as well with an estimated reaction rate of $10^{-15} \text{ cm}^2\text{s}^{-1}$.

2.7 Concluding Remarks

The multi-scale modeling platform described in this chapter enables the investigation of many different processes in atmospheric pressure discharges that occur simultaneously. A wide range of temporal scales can be addressed ranging from the electrical breakdown that initiates the discharge ($< 1 \mu\text{s}$) to gas flow fields and surface functionalization that reach steady state over 10s – 100s ms. Spatial scales including the equipment scale description of the plasma hydrodynamics (few cm) to plasma - surface

interactions that occur on non-planar surfaces with sub- μm features are simulated on a single unstructured mesh. The modeling philosophy is general enough to allow the use of different reactor configurations, gas phase and surface reaction mechanisms.

2.8 Figures

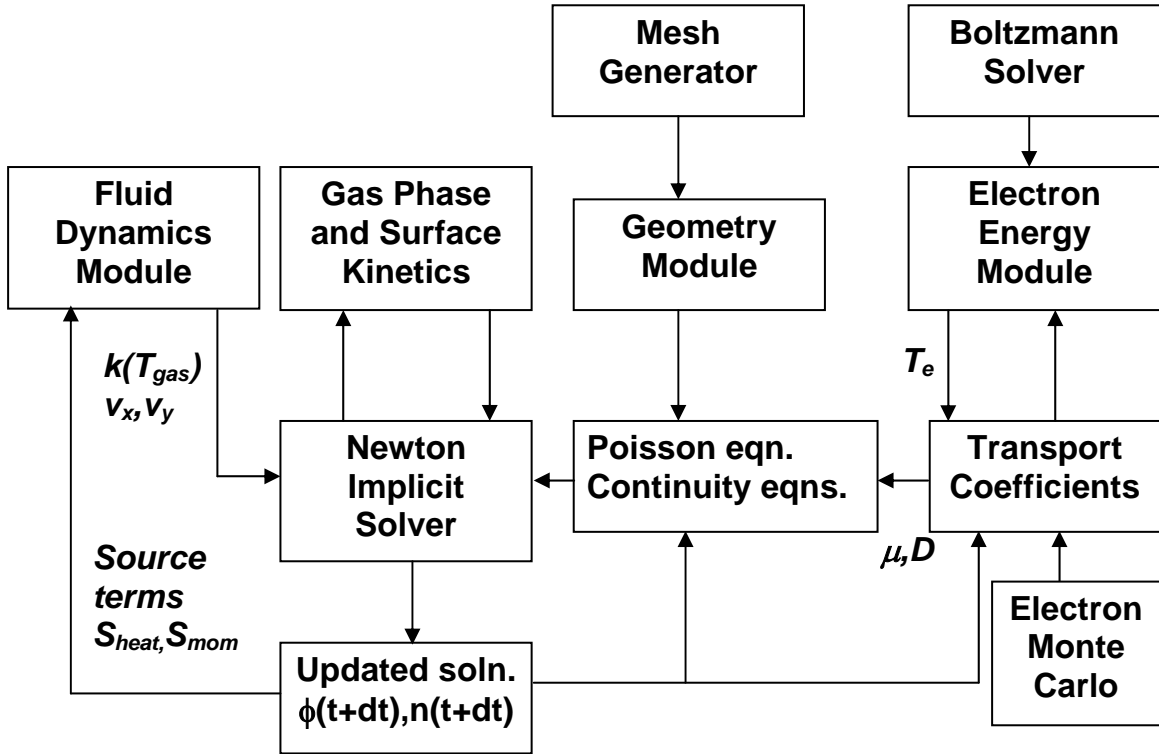
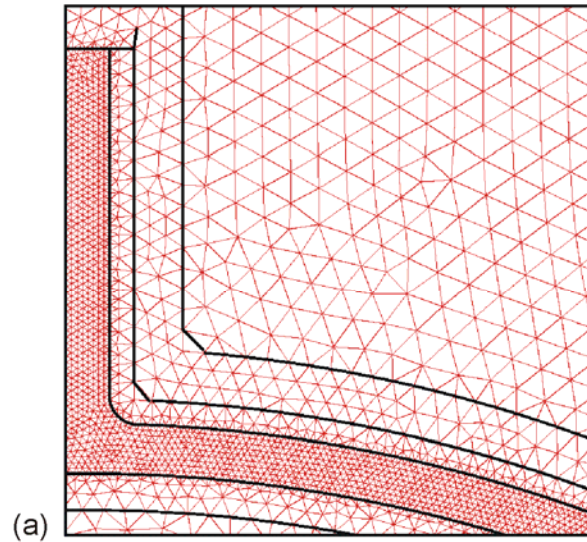
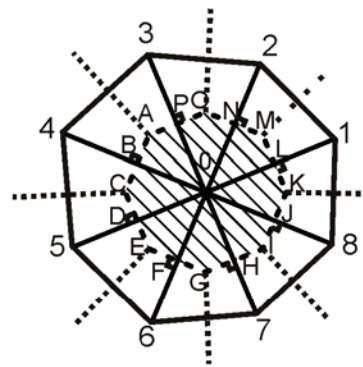


Fig. 1 Schematic of the modules in the plasma equipment model.



(a)



Finite volume cell



Actual mesh



Finite volume mesh

(b)

Fig. 2 (a) An unstructured mesh mapped onto a geometry for illustration. The mesh consists of triangles only and it is possible to refine different regions on the mesh as required. (b) Illustration of the finite volume cell and cell face areas. For node 0, the cell neighbors are labeled 1 - 8. Perpendicular bisectors to the segments connecting a node to its neighbors are drawn. The perpendicular bisectors and their intersection points form the boundary of the finite volume cell ABC...NOPA. The cell face areas between a node and its neighbor is the segment joining the points determined by the perpendicular bisectors. For instance, AC forms the cell face between 0 and 4. The actual cell face area and volume are determined by the depth for a Cartesian mesh or the radial locations of the nodes in a cylindrically symmetric mesh.

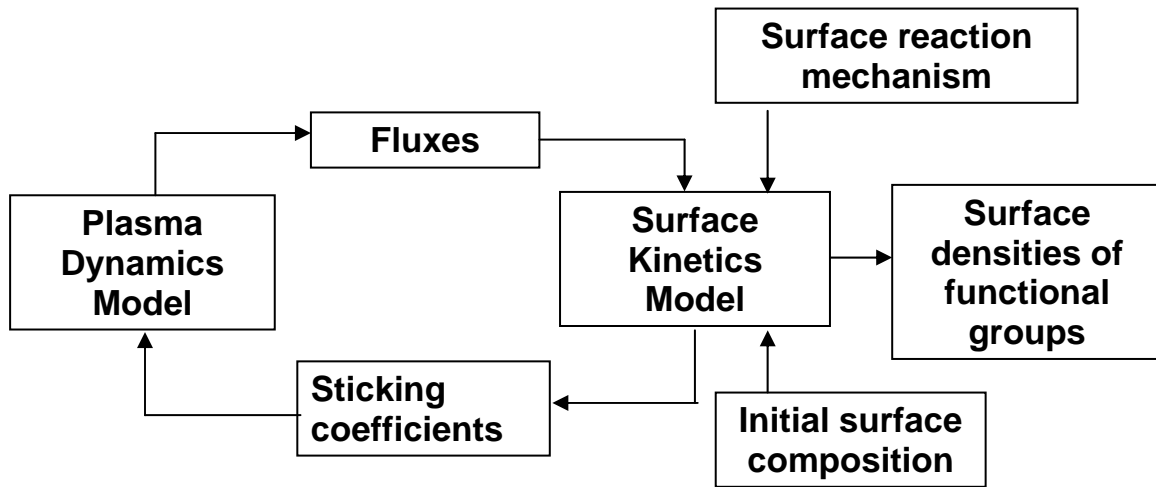


Fig. 3 Schematic of the integrated plasma dynamics – surface kinetics model.

2.9 References

1. B.M. Lay, Richard S Moss, S. Rauf and M. J. Kushner, Plasma Sources Science Technology, **12**, 8 (2003).
2. M. J. Kushner, Journal of Physics D, **38**, 1633 (2005).
3. R. Arakoni, D. Shane Stafford, N. Y. Babaeva and M. J. Kushner, Journal of Applied Physics, **98**, 073304 (2005).
4. B. Lay, *MS Thesis*, University of Illinois, 2000.
5. D. L. Scharfetter and H. K. Gummel, IEEE Trans. Electron Dev., **ED-16**, 64 (1969).
6. SLAP Sparse Matrix Library, <http://www.netlib.org>
7. Y.Saad, Department of Computer Science and Engg., University of Minnesota
<http://www-users.cs.umn.edu/~saad/software/SPARSKIT/sparskit.html>
8. S. D. Rockwood, Physical Review A, **8**, 2348 (1973).
9. D. Zhang and M. J. Kushner, Journal of Vacuum Science and Technology A, **19**, 524 (2001).
10. R. Dorai and M. J. Kushner, Journal of Physics D, **36**, 666 (2003).
11. D. S. Stafford and M. J. Kushner, Journal of Applied Physics **96**, 2451 (2004).
12. A. A. Meyer-Plath, Ph.D Dissertation, Ernst-Moritz-Arndt-Universität, Greifswald (2002).
13. Z. B. Alfassi, ed., *N-centered Radicals*, John Wiley and Sons, West Sussex, England (1998).
14. J. T. Herron, Journal of Physical and Chemical Reference Data, **28**, 1453 (1999).

15. *NIST Standard Reference Database 17-2Q98* (National Institute of Standards and Technology, Gaithersburg, MD, 1998).
16. R. Lesclaux and M. Desmissy, *International Journal of Chemical Kinetics*, **14**, 1 (1982).
17. F. Tochikubo, T. Chiba and T. Watanabe, *Japanese Journal of Applied Physics*, **38**, 5244 (1999).
18. M. R. Wertheimer, A. C. Fozza and A. Hollander, *Nuclear Instruments and Methods in Physics Research B*, **151**, 65 (1999).
19. R. Wilken, A. Hollander and J. Behnisch, *Surface and Coatings Technology*, **116-119**, 991 (1999).
20. F. Truica-Marasescu, P. Jedrzejowski, M. R. Wertheimer, *Plasma Processes and Polymers*, **1**, 153 (2004).
21. V. E. Skurat and Y. I. Dorofeev, *Die Angewandte Makromolekulare Chemie*, **216**, 205 (1994).
22. E. V. Kuvaldina, V. V. Rybkin, V. A. Titov, T. G. Shikova and D. A. Shutov, *High Energy Chemistry*, **38**, 411 (2004).
23. F. P-Epaillard, *Macromolecular Chemistry and Physics*, **198**, 2439 (1997).
24. F. P-Epaillard, J. C. Brosse and T. Falher, *Macromolecules*, **30**, 4415 (1997).
25. J. Hong, F. Truica-Marasescu, L. Martinu, and M. R. Wertheimer, *Plasmas and Polymers*, **7**, 245 (2002).
26. R. H. Hansen and H. Schonhorn, *Journal of Polymer Science, Polymer Letters Edition B*, **4**, 203 (1966).

27. M. Strobel, C. S. Lyons and K. L. Mittal, eds., *Plasma Surface Modification of Polymers*, VSP Press, Zeist (1994).

3. BREAKDOWN DYNAMICS IN ATMOSPHERIC PRESSURE DISCHARGES

3.1 Introduction

Atmospheric pressure corona treaters are often employed in industry to functionalize the surfaces of materials such as polymers. During functionalization, species such as electrons, ions, photons and radicals generated in the plasma react with the surface which significantly changes in the chemical composition of the top few surface atomic layers. Reactive species can be generated in abundance by using repetitively pulsed discharges. One such configuration is the corona discharge. The gas phase radicals generated as a result of electrical breakdown and streamer propagation continue to react with each other and with the surface. The spatial distribution of the plasma generated species resulting from breakdown influence the relative abundance of reactive species fluxes at the surface that ultimately determine the degree and uniformity of surface functionalization. The dynamics of the breakdown process therefore need to be considered while investigating surface functionalization processes.

In this chapter, results from computational investigations of the dynamics of breakdown in humid air atmospheric pressure corona discharges are discussed. Breakdown in air was studied for different voltages of positive and negative polarity. In all cases where breakdown occurred, a thin space charge region 100-200 μm in extent, referred to as the ionization front, with high electric fields (with $E/N > 500 \text{ Td}$), leads the breakdown process. The extent of the discharge is smaller with the positive discharge than a negative discharge of the same voltage magnitude, but the plasma density is higher. As a consequence, spatial gradients of charged species and radicals are higher in the positive discharge.

The density of radicals and ions generated in the discharge increases with the magnitude of voltage of either polarity due to higher energy deposition. For the same magnitude of voltage, the plasma density in the positive discharge is higher. Parameterization of breakdown time with the voltage indicates that the ionization front in a positive discharge has a lower propagation velocity than the corresponding negative discharge. Additionally, the propagation velocity of the ionization front in the positive discharge depends on the ability of the photoionization mechanism to seed sufficient electrons at the ionization front.

3.2 Geometry and Reaction Mechanism

A schematic of a typical corona discharge device commonly used in industrial polymer surface treatment processes is shown in Fig. 1(a). The basic arrangement consists of two metal electrodes, one of which is the powered bar electrode and the other a grounded roller electrode, separated by a small gas gap. At times, the grounded electrode may have an additional dielectric barrier to eliminate any possibility of arcing. During surface treatment, the polymer sheet to be treated is placed on the roller electrode and maybe processed in a continuous, web fashion by translating the sheet. The discharge used in these investigations is shown in Fig. 1(b). A close-up view of the discharge zone is shown in Fig. 1(c).

The powered metal electrode is housed in dielectric material and is exposed to the processing gas at its tip. For these investigations, the lower surface is a grounded metal electrode and the gas gap is 2 mm. The dynamics of discharge formation in positive and negative atmospheric pressure discharges in this configuration was investigated using the two-dimensional (2D) unstructured mesh based plasma hydrodynamics model described in

detail in Chapter 2. The magnitude of the applied dc voltage (V_0) was varied between 10-20 kV.

An unstructured mesh is overlaid on the geometry. The mesh is refined locally in regions close to the powered electrode and near the grounded surface and is coarser further away from the main discharge zone. The total number of nodes on the mesh is 7550, with 5097 plasma nodes. Refinements near the powered electrode result in node spacing of 10-15 μm while the coarse regions have spacing of 100 μm or more. The base case conditions correspond to humid air at atmospheric pressure with a composition of $\text{N}_2/\text{O}_2/\text{H}_2\text{O}=79/20/1$ reflecting a relative humidity of 30%. Gas species included in the chemistry are N_2 , N_2^* , N_2^{**} , N_2^+ , N^+ , N_4^+ , N , N^* , O_2 , O_2^* , O_2^+ , O_2^- , O , O^* , $\text{O}(^1\text{S})$, O^+ , O , O_3 , H_2O , H_2O^+ , H_2 , H , OH and HO_2 . N_2^* and N_2^{**} denote the states $\text{N}_2(\text{A}^3\Sigma)$ and lumped states higher than $\text{N}_2(\text{A}^3\Sigma)$ respectively, while O_2^* denotes the $\text{O}_2(^1\Delta)$ state. N^* and O^* denote the $\text{N}(^2\text{D})$ and $\text{O}(^1\text{D})$ states.

The reaction mechanism used for these simulations is found in Appendix A and has been described in detail by Dorai *et al.*[1] Briefly, this mechanism consists of reactions due to electron impact and heavy particle reactions among various species formed in humid air discharges. Electron impact reactions include the electronic and vibrational excitation, ionization and dissociation reactions for N_2 and O_2 . The major ions formed in the discharge include O_2^+ , N_2^+ , N_4^+ and O_2^- while excited species include N_2^{**} , O_2^* and O^* . Charge exchange reactions and Penning reactions among heavy species as well as ion-ion neutralization reactions are also included. Radicals such as O and OH are generated by electron impact reactions which react further to form species such as HO_2 . Since the device is operated at atmospheric pressure, three body reactions of O and O_2 to form O_3 are

significant. A photoionization reaction was added to this mechanism by designating N_2^{**} as the radiating species with a lifetime of 5 ns, which results in the ionization of O_2 with a cross section of 10^{-19} cm^2 .

3.3 Breakdown Dynamics in Negative Air Discharge

A commonly encountered scaling parameter in low temperature partially ionized gases is the normalized electric field denoted as E/N (electric field / number density). E/N is typically specified in the units of Townsend ($1 \text{ Td} = 10^{-17} \text{ V-cm}^2$). The variation of electric potential and E/N on application of a dc $V_0 = -15 \text{ kV}$ pulse of negligible rise time is shown in Fig. 2 at different times during breakdown. The temporal evolution of electron temperature (T_e) and electron impact ionization sources are shown in Fig. 3 while the electron density and net space charge are shown in Fig. 4 for the same instants of time. At 0.2 ns after the voltage is applied, electric field enhancement near the powered cathode raises the magnitude of E/N to 800 Td producing T_e of 6-7 eV and ionization sources of $10^{23} \text{ cm}^{-3}\text{s}^{-1}$. As a result electron density close to cathode quickly rises to 10^{13} cm^{-3} .

These electrons tend to drift away from the high electric field region near the powered cathode while positive ions move towards it resulting in the formation of a negative space charge region of high electric field gradients referred to as the ionization front. At the ionization front, the magnitude of the negative space charge is $0.1\text{-}0.2 \mu\text{C cm}^{-3}$. At 0.5 ns, E/N in the front peaks at 400 Td while T_e is around 5 eV. Ionization sources peak at $10^{23} \text{ cm}^{-3}\text{s}^{-1}$ as the front makes its way to the anode. The dominant ionization reactions at the front are the formation of N_2^+ and O_2^+ due to energetic electrons. Significant densities of O_2^- are formed as result of electron attachment. The radial and axial extents of the ionization front are 325 and 200 μm respectively. There are significant gradients in electron density on either

side of the ionization front. The electron density is about 10^{13} cm^{-3} in the ionized channel behind the front and 10^{11} cm^{-3} near its leading edge, but drops steeply to 10^8 cm^{-3} at $150 \mu\text{m}$ axially ahead of the front. The discharge is about $800 \mu\text{m}$ wide midway through the gap, if the electron density contour level of 10^{11} cm^{-3} is considered as the edge. The electrons at the ionization front drift against the electric field away from the cathode and tend to increase the extent of the discharge.

The channel behind the front is a conductive region of negligible space charge where T_e drops to 2-3 eV by 1 ns while sustaining an electron density of 10^{13} cm^{-3} . The magnitude of E/N in the channel decreases below 200 Td. The dominant positive ion at the ionization front is N_2^+ with a peak density of $3 \times 10^{12} \text{ cm}^{-3}$ at 1 ns as shown in Fig. 5. As the front moves, the peak in N_2^+ tracks the front. Most of the N_2^+ in the channel behind the front is converted to N_4^+ by reactions with N_2 . Other significant ions include O_2^+ , and O^- and are shown in Figs. 5 and 6. The major ion in the channel is O_2^+ with a density on the order of 10^{13} cm^{-3} , which results from charge exchange reactions of O_2 with N_2^+ and N_4^+ besides electron impact. Densities of ions such as H_2O^+ and O^- are in the range of 10^{11} - 10^{12} cm^{-3} with peak locations closer to the cathode where T_e is high in the cathode fall like region. The main pathways for the formation of H_2O^+ are electron impact with H_2O and charge exchange with N_2^+ . N_2^{**} and O_2^* are the major excited states species in the discharge with densities of 10^{13} cm^{-3} and 10^{14} cm^{-3} (Fig. 7) respectively. Large radical densities are also present in the channel as shown in Fig. 8. The density of O atoms primarily produced by electron impact dissociation of O_2 and by reactions of N_2^{**} with O_2 is about 10^{13} - 10^{14} cm^{-3} . The main pathway for the production of OH with densities of 10^{11} - 10^{12} cm^{-3} is the electron impact

dissociation of H₂O. The maxima in O and OH densities are near the cathode where the T_e also peaks.

The channel behind the ionization front is conductive and drops little voltage so much of the applied voltage at the cathode is compressed at the ionization front, where the magnitude of E/N increases to 450–550 Td at 1 ns. The enhancement of the electric field due to the space charge maintains T_e near 6 eV and ionization sources of 10²³ cm⁻³s⁻¹ at the front as it moves towards the grounded anode. As the front reaches the anode at 1.2 ns, voltage compression increases E/N to nearly 1000 Td gap closure occurs. After closure, the resistance of the channel is fairly uniform and so potential redistributes itself across the gap. This produces a cathode-directed avalanche. The magnitude of E/N increases to 200-250 Td as the electric field recovers in the channel. T_e and electron impact ionization sources increase in the channel. Electron density in the discharge peaks close to the anode at 10¹⁴ cm⁻³ at the end of breakdown.

3.4 Breakdown Dynamics in Positive Air Discharge

The positive discharge is initiated with a dc voltage pulse V₀ = 15 kV of negligible rise time. The time sequence of electric potential and E/N, T_e and electron impact ionization sources are shown in Figs. 9 and 10 respectively. Unlike the negative corona, the direction of electron drift is opposite to that of streamer propagation and seed electrons ahead of the ionization front must be provided by photoionization. Due to electric field enhancement near the powered anode, the magnitude of E/N in the vicinity of the anode at 1 ns is 1000 Td. The large electric field heats electrons to 6 eV and electron impact sources of 10²³ cm⁻³s⁻¹ are produced. This creates an electron density of 10¹³cm⁻³ in the vicinity of the anode (Fig. 11). Unlike the negative discharge, electrons drift towards the powered electrode and ions move

away towards the grounded electrode. A thin ionization front develops near the anode, as shown in Fig. 11, with positive space charge density of $1 \mu\text{C cm}^{-3}$. The electric field in the ionization front is higher in the positive discharge due to the larger space charge as a result of electrons drifting away from the front.

By 3.6 ns, the electron density near the anode increases to 10^{14} cm^{-3} and the plasma density in the channel is about 10^{13} cm^{-3} . Gradients across the ionization front are steeper in the positive discharge. The electron density is 10^{13} cm^{-3} in the conductive channel behind the ionization front but just 10^9 cm^{-3} ahead of it. The ionization front is midway through the gap at this point and its vertical and horizontal extents are $200 \mu\text{m}$ and $150 \mu\text{m}$ respectively. The discharge is also comparatively narrower with a width of $300 \mu\text{m}$ midway through the gap. This is because electrons in the positive discharge drift inwards into the front in the direction of the anode due to the electric field curtailing the expansion of the discharge. The magnitude of E/N remains high at close to 825 Td. The dominant positive ion at the ionization front is N_4^+ with a density of $2 \times 10^{13} \text{ cm}^{-3}$ as shown in Fig. 12. T_e in the channel decreases to less than 1 eV while E/N is below 100 Td. The major ion in the channel is O_2^+ with a density of $5 \times 10^{13} \text{ cm}^{-3}$ as shown in Fig. 13. Most of the N_2^+ is converted by reactions with N_2 into N_4^+ , which is the second most abundant ion.

By 4.8 ns, the applied voltage compressed at the ionization front creates E/N of about 1000 Td. The high electric fields enhanced by space charge result in T_e of 8 eV and ionization sources of $10^{23} \text{ cm}^{-3}\text{s}^{-1}$ at the ionization front. The density of N_4^+ increases to 10^{14} cm^{-3} as more N_2^+ is produced and converted into N_4^+ . Densities of ions such as H_2O^+ and O^- (Fig. 13) are in the range of 10^{11} - 10^{12} cm^{-3} but their peaks locations are closer to the ionization front because the elevated T_e at the front that increases the rate at which they are

produced. The densities of excited species such as N_2^{**} and O_2^* are 10^{13} cm^{-3} and 10^{14} cm^{-3} (Fig. 14) respectively in the ionized channel. Large radical densities are present in the channel too as shown in Fig. 15. The density of O atoms is about 10^{13} - 10^{14} cm^{-3} while that of OH is 10^{11} - 10^{12} cm^{-3} , with the peak locations being near the front.

The magnitude of E/N increases to nearly 2000 Td when the ionization front reaches the cathode. This is comparatively larger than in the negative corona due to higher plasma density and lower discharge radius, giving rise to larger space charge at the ionization front. At 5 ns, breakdown occurs with electron density peaking at 10^{14} cm^{-3} close to the anode. The ionization front collapses and the potential contours withdraw. The electric field in the channel recovers and E/N increases to 300 Td. As a result, T_e and electron impact sources in the channel increase after breakdown.

We found that photoionization plays an important role in the propagation of the ionization front in the positive discharge. This was verified when, by excluding photoionization altogether, the discharge stalled mid-way through the gap. The ionization front is unable to progress in the absence of seed electrons generated by photoionization. When included, breakdown is possible due to photoionization sources near the ionization front being significant. Seeded electrons drift into the high space charge region of the front where they are heated and produce ionization sources. The propagation velocity of the ionization front depends on the mean free path of photon absorption (λ), decreasing with smaller values of λ as shown in Fig. 16. For $\lambda = 10 \text{ }\mu\text{m}$, the discharge stalls without the occurrence of breakdown. By contrast, though photoionization in the negative discharge aids the breakdown process it is not vital for breakdown to occur. When photoionization was not included in the negative corona, breakdown times were larger by only 5-15%.

3.5 Effect of Voltage on Breakdown Dynamics

Parameterizations were performed for breakdown in negative and positive discharges by varying the magnitude of voltage in the range of 10-20 kV. For the conditions investigated here, no breakdown occurs at $V_0 < 10$ kV with either polarity. This is because the E/N at this voltage is insufficient to sustain a viable ionization front through breakdown. At higher voltages, breakdown does occur and the mechanisms are similar to the discussions for the 15 kV cases in the previous sections. In all cases, an ionization front with high E/N is sustained that breaks down the gas.

The dependence of the density of plasma species immediately after breakdown with the applied voltage in negative discharges is shown in Figs. 17 and 18 and for positive discharges in Figs. 19 and 20 respectively. The electron density midway through the gap at the end of breakdown is about $7.5 \times 10^{13} \text{ cm}^{-3}$ at $V_0 = 15$ kV and $2.0 \times 10^{14} \text{ cm}^{-3}$ at $V_0 = 20$ kV. In general, the density of species created in the discharge increases with the voltage of either polarity as expected since more energy deposition occurs. The plasma density for the same magnitude of voltage is higher in the positive discharges. The density of O atoms at the end of breakdown for $V_0 = 15$ kV and $V_0 = -15$ kV is 10^{15} cm^{-3} and 10^{14} cm^{-3} respectively. Since the electric field at the front is enhanced due to greater charge separation in the positive discharge, higher T_e and rates of production of radicals by electron impact are sustained at the ionization front creating a higher plasma density.

The variation in breakdown times in negative and positive discharges with voltage is shown in Fig. 21. The breakdown time in the negative discharge is lower than the positive discharge for the same magnitude of voltage. For instance, breakdown occurs at 1.2 ns and 5 ns for $V_0 = -15$ kV and $V_0 = 15$ kV respectively. The corresponding propagation velocities

for the breakdown avalanche are 1.6×10^8 cm/s and 4×10^7 cm/s. Propagation speeds in positive discharges compare favorably to experimentally measured values in similar configurations, but larger gas gaps, in the literature.[2] The speed of breakdown ultimately depends on the availability of seed electrons at the ionization front. In the negative discharge, electrons at the ionization front accelerate against the electric field picking up energy and creating more electrons by impact ionization ahead of the front. Electrons created due to photoionization near the front aid this process. On the other hand, in the positive discharge, electrons at the front accelerate inwards due to the electric field. The speed of the front then depends significantly on the availability of electrons seeded from photoionization.

3.6 Concluding Remarks

Two dimensional modeling of breakdown dynamics provides insights into the discharge formation mechanisms at atmospheric pressure in negative and positive air discharges sustained in the corona configuration. In general, breakdown proceeds with the formation of an ionization front of high electric field near the powered electrode resulting in high electron temperature and ionization sources of electrons and proceeds towards the ground. As a result of breakdown, a conductive channel 100s μm in width is created in the gap. The plasma density in the channel is 10^{13} - 10^{14} cm^{-3} , with peak densities closer to the powered electrode and the ground at the end of breakdown. Large radical densities are present in the channel, for instance, O atom density peaks at 10^{15} cm^{-3} .

The spatial distribution and density of reactive species resulting from breakdown is a function of the magnitude and the polarity of the applied voltage. For the same voltage magnitude, the positive discharge has a higher plasma density and a lower discharge radius.

With increasing voltage, the plasma density increases in both the positive and negative discharges. Propagation speeds for the avalanche on the order of 10^7 - 10^8 cm/s are obtained, which compare well with data in the literature. Breakdown times are inversely related to the applied voltage and are lower in the negative discharge. The propagation of the positive discharge depends to a large extent on the ability of photoionization to seed electrons at the ionization front.

3.7 Figures

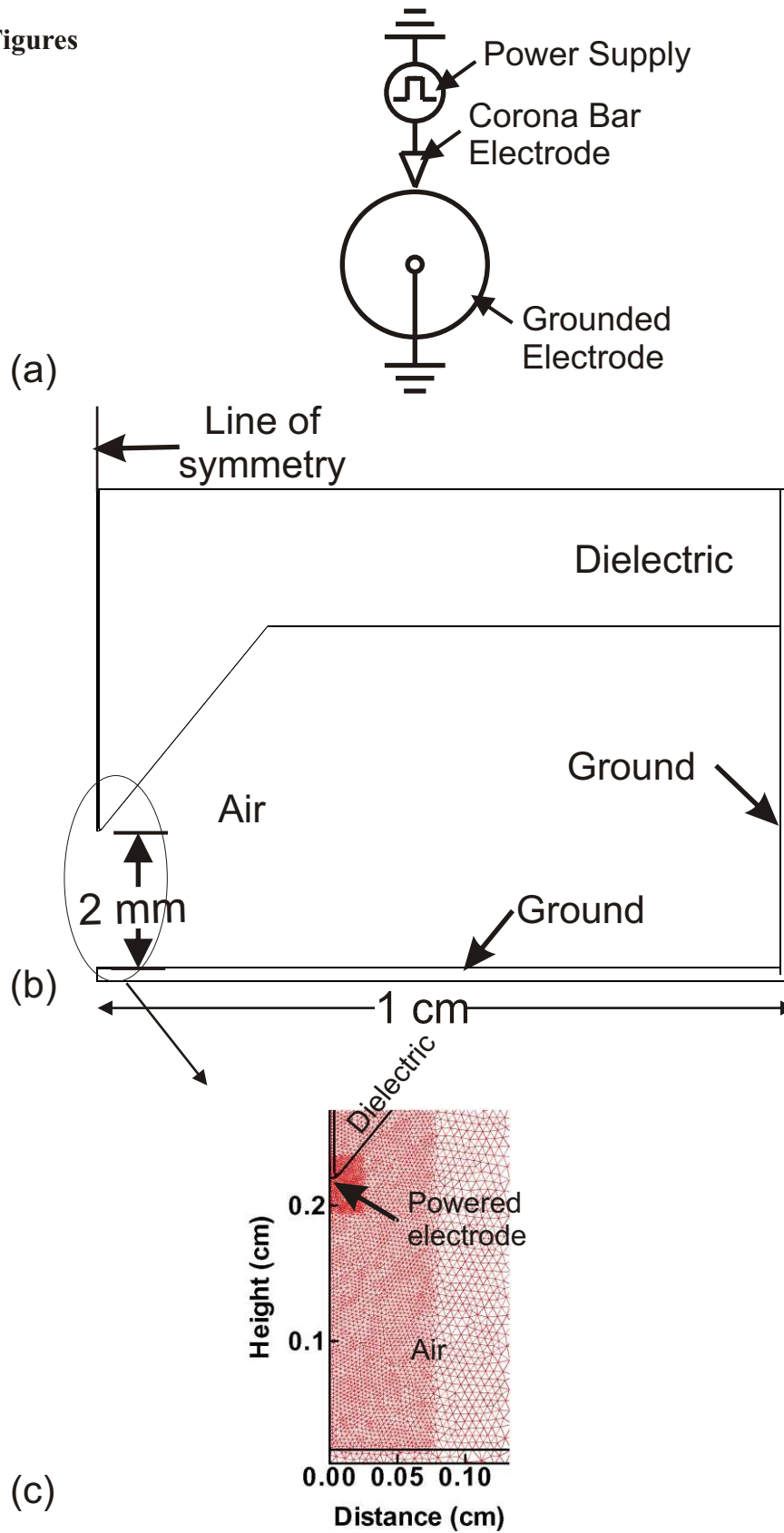


Fig. 1 (a) Schematic of a typical industrial corona device. (b) Cartesian symmetric representation of the discharge and (c) close-up view of the meshed discharge zone.

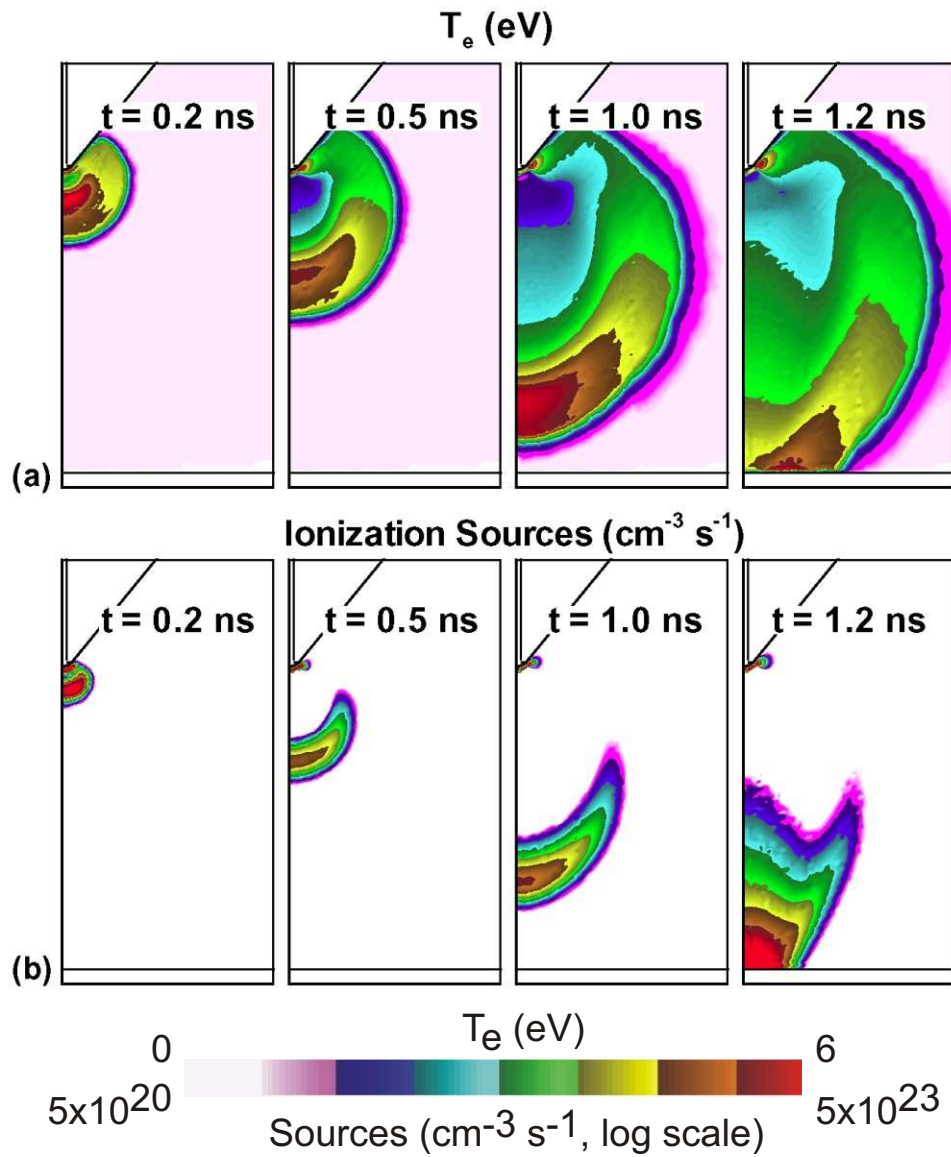


Fig. 3 The temporal variation of plasma characteristics (a) T_e and (b) electron impact ionization sources during breakdown in a negative discharge in air. Conditions are the same as in Fig. 2.

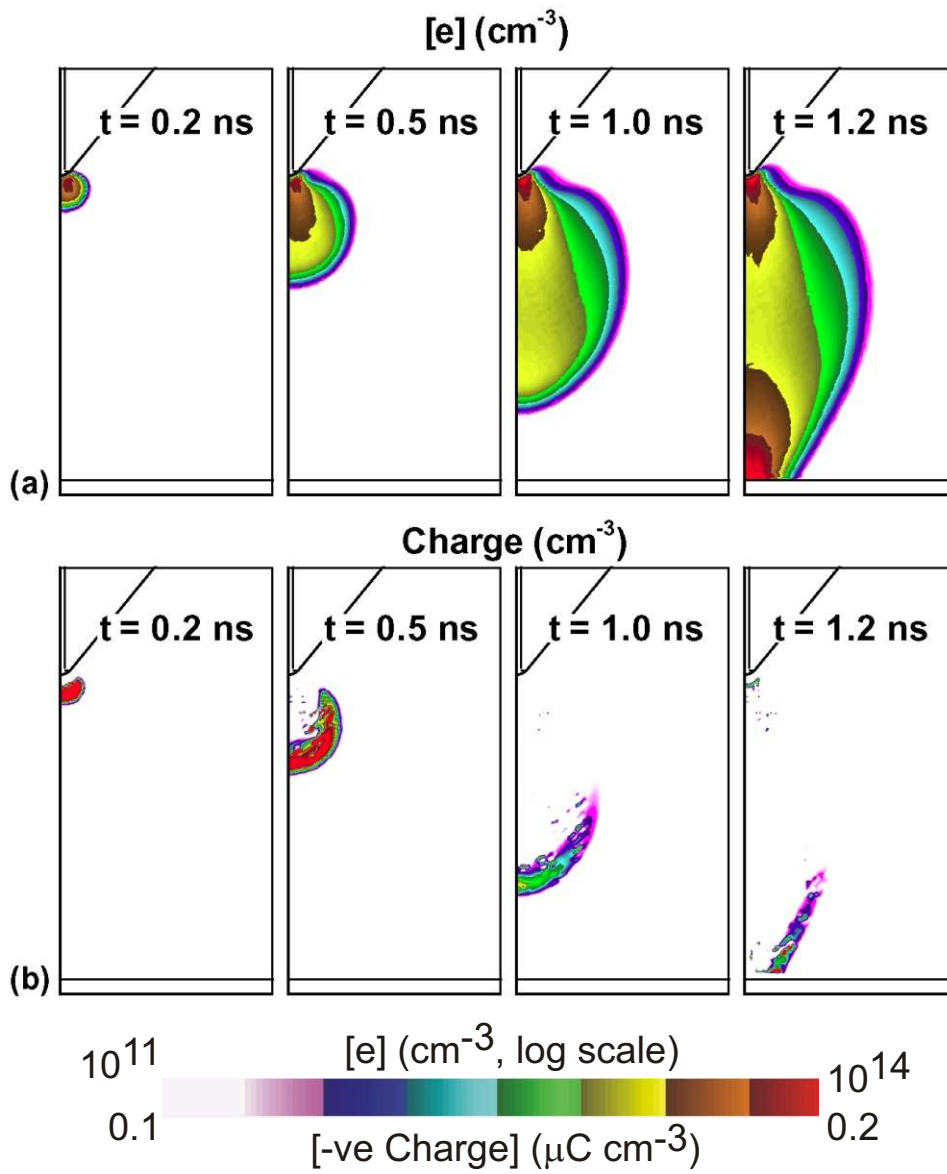


Fig. 4 The temporal variation of plasma characteristics (a) electron density and (b) space charge during breakdown in a negative discharge in air. Conditions are the same as in Fig. 2.

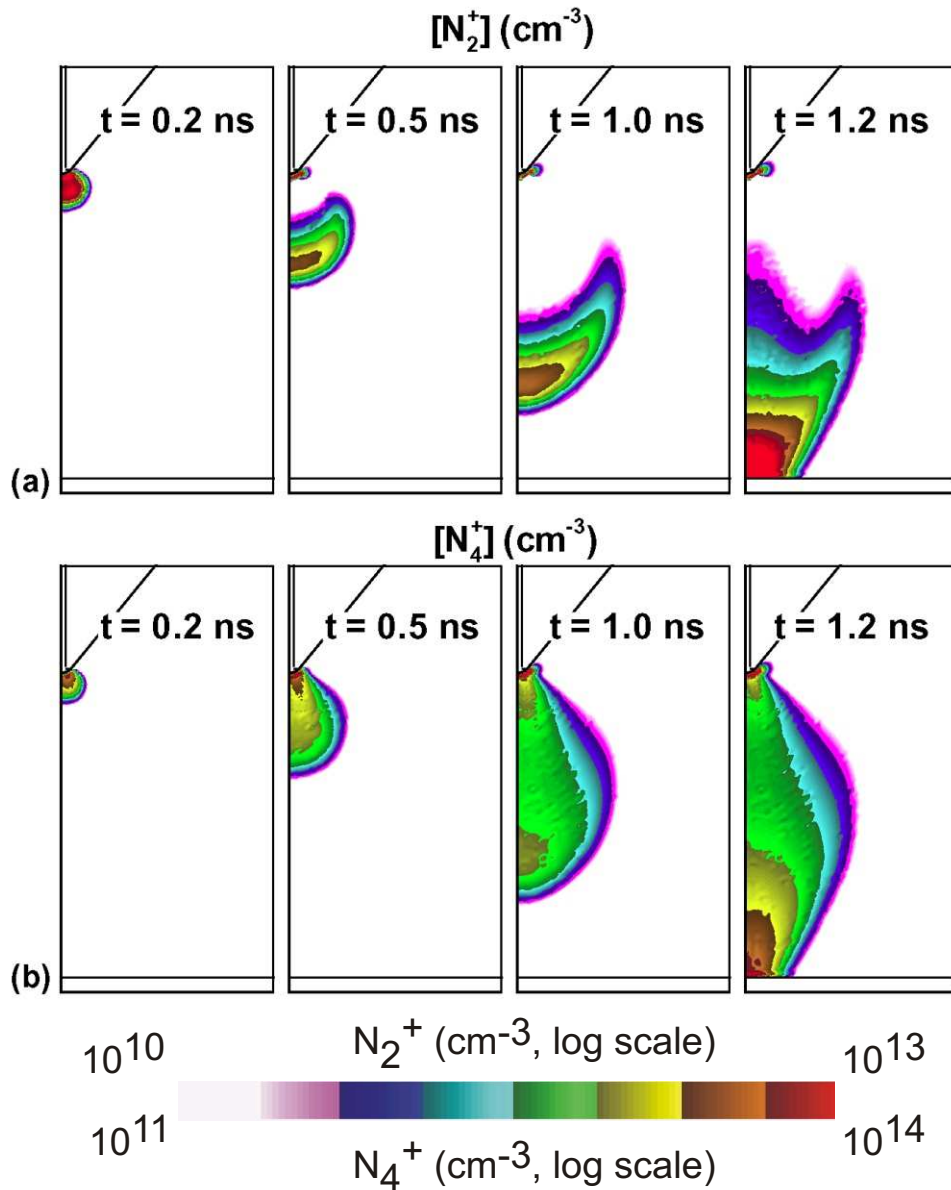


Fig. 5 The temporal variation of densities of (a) N_2^+ and (b) N_4^+ ions during breakdown in a negative discharge in air. Conditions are the same as in Fig. 2.

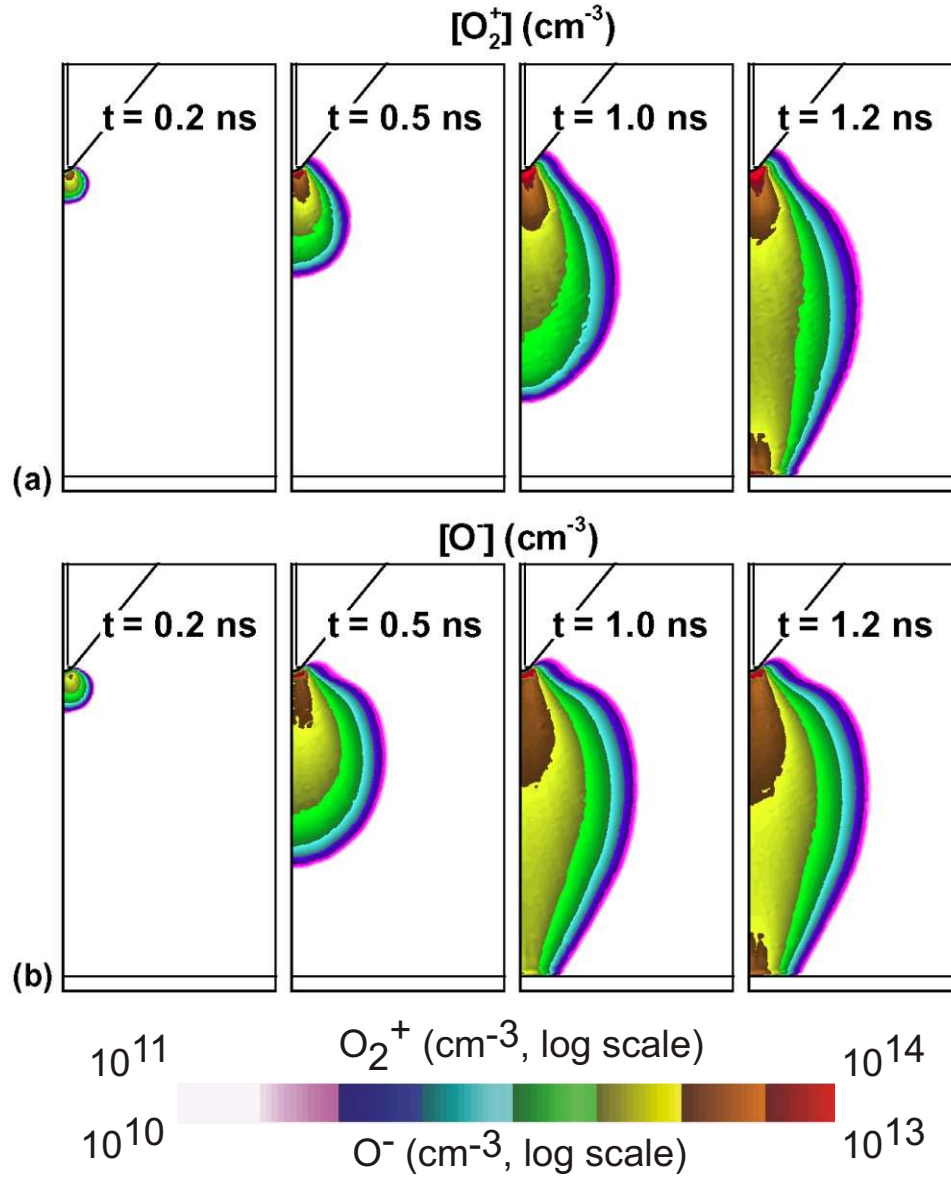


Fig. 6 The temporal variation in the densities of (a) O_2^+ and (b) O^- ions during breakdown in a negative discharge in air. Conditions are the same as in Fig. 2.

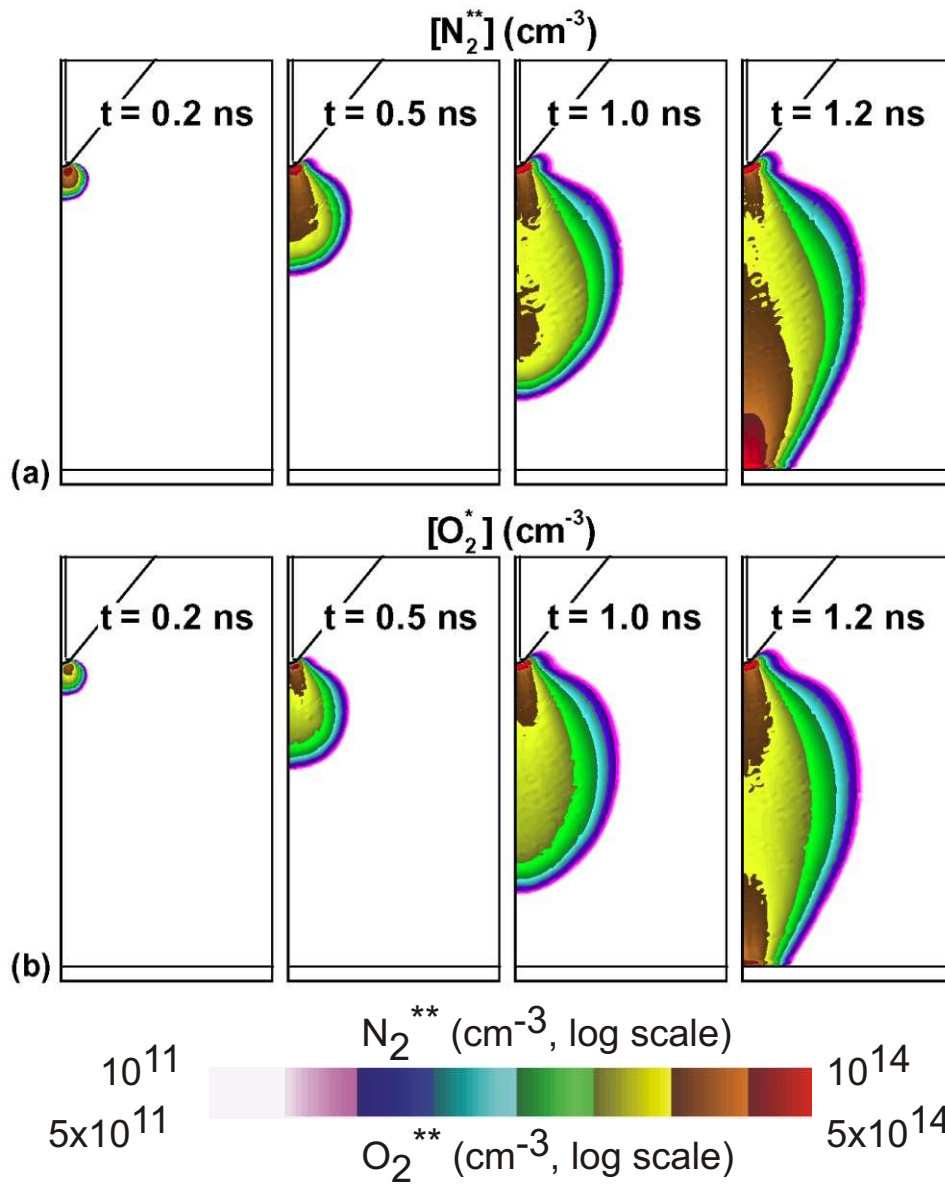


Fig. 7 The temporal variation of the densities of excited species (a) N_2^{**} and (b) O_2^* during breakdown in a negative discharge in air. Conditions are the same as in Fig. 2.

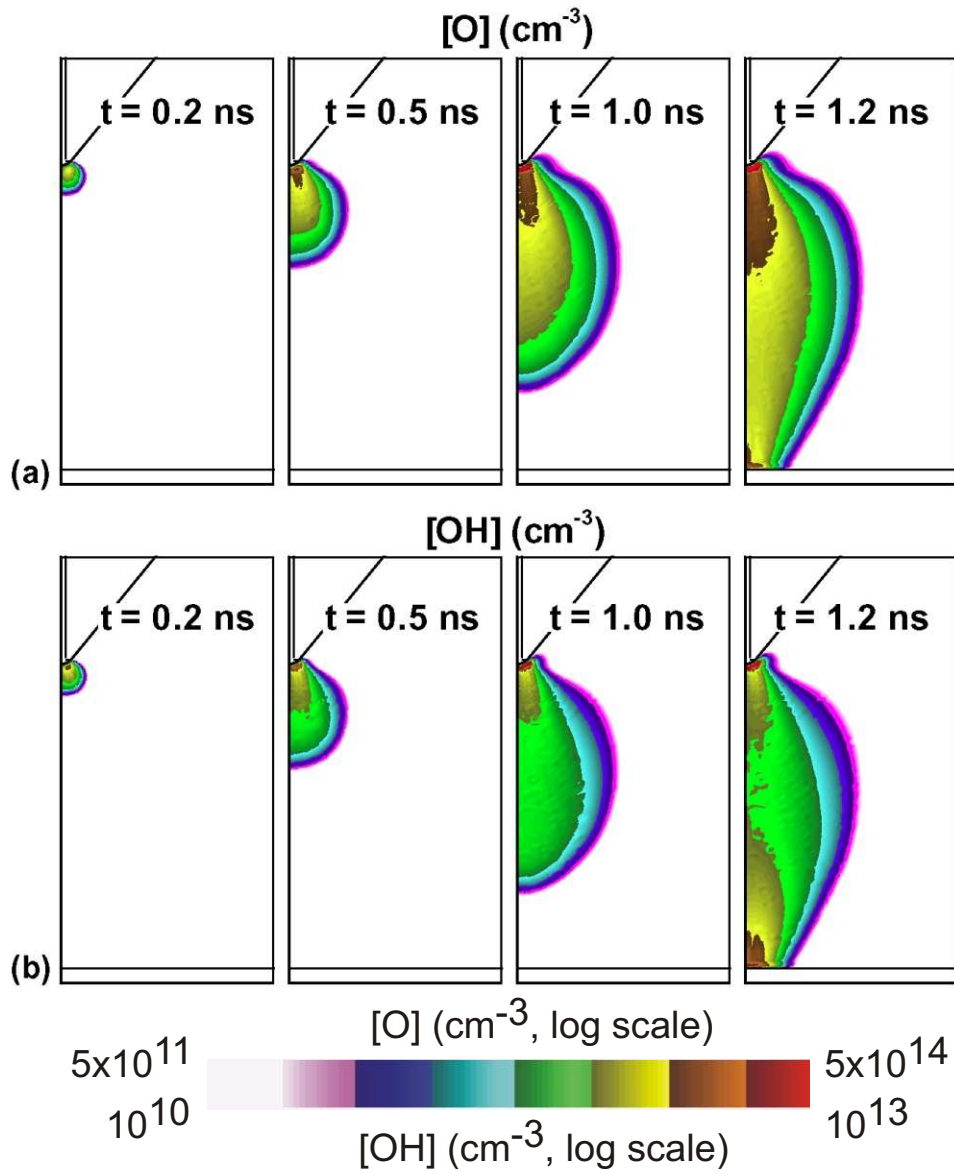


Fig. 8 The temporal variation of densities of radicals (a) O and (b) OH during breakdown in a negative discharge in air. Conditions are the same as in Fig. 2.

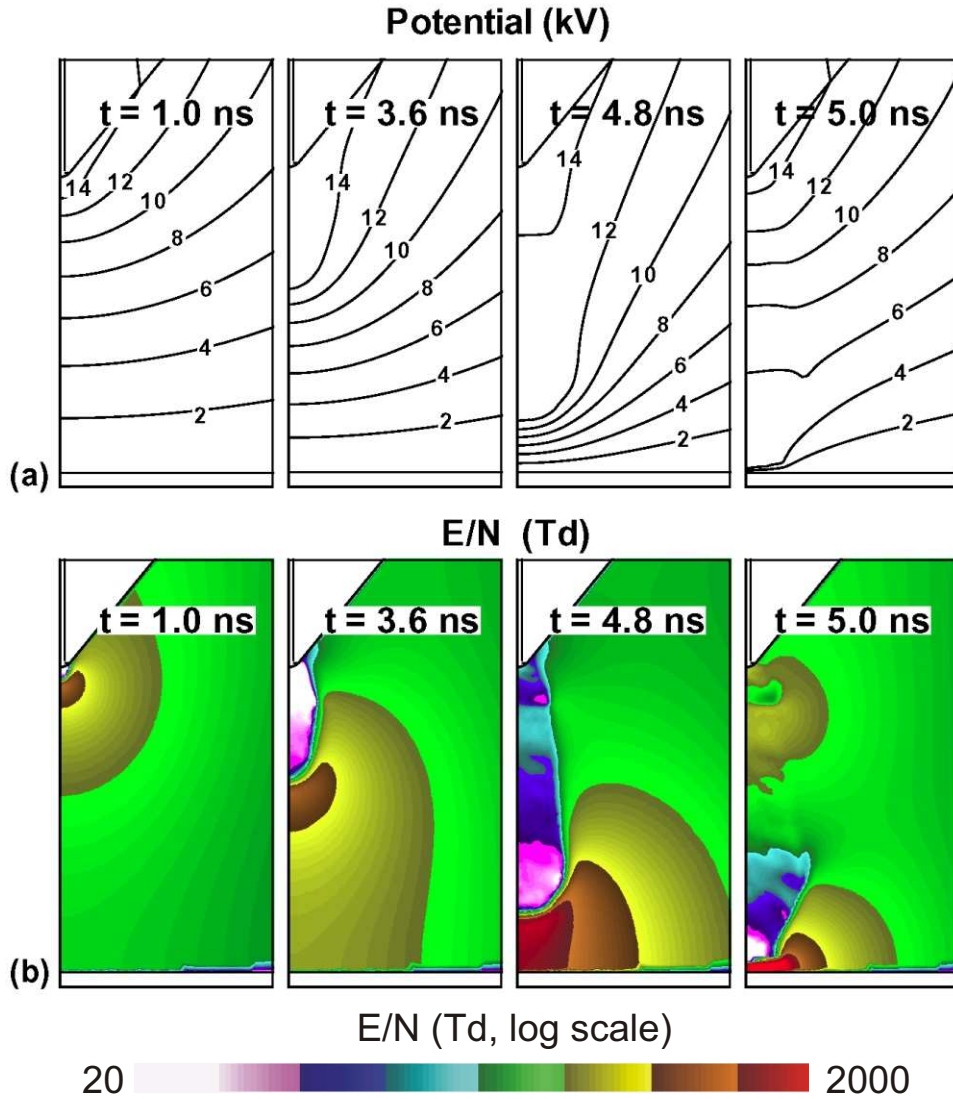


Fig. 9 The temporal variation of plasma characteristics (a) electric potential and (b) E/N during breakdown in a positive discharge in air. The conditions are an applied bias $V_0 = +15$ kV at the upper electrode and the gas is humid air ($N_2/O_2/H_2O = 79/20/1$) at atmospheric pressure.

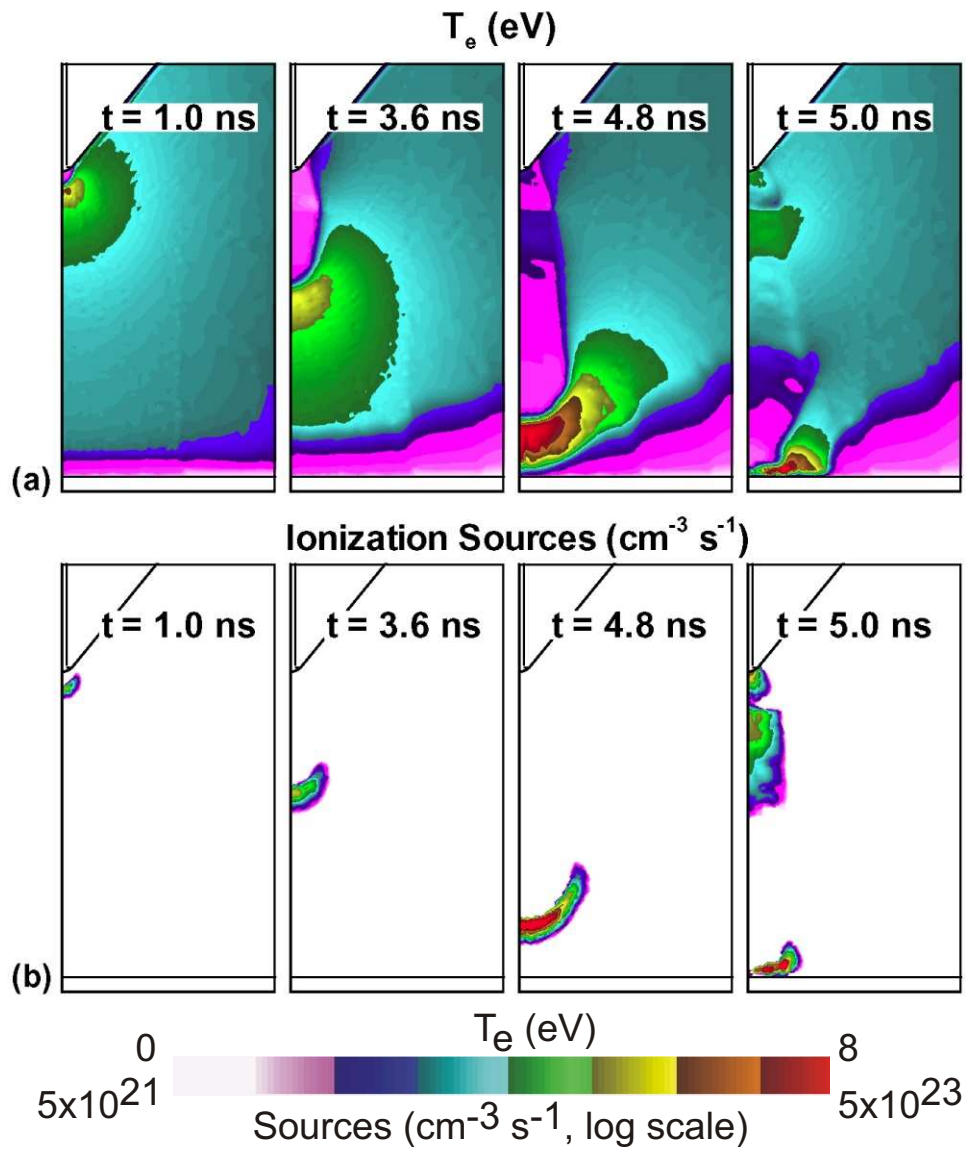


Fig. 10 The temporal variation of plasma characteristics (a) T_e and (b) electron impact ionization sources during breakdown in a positive discharge in air. Conditions are the same as in Fig. 9.

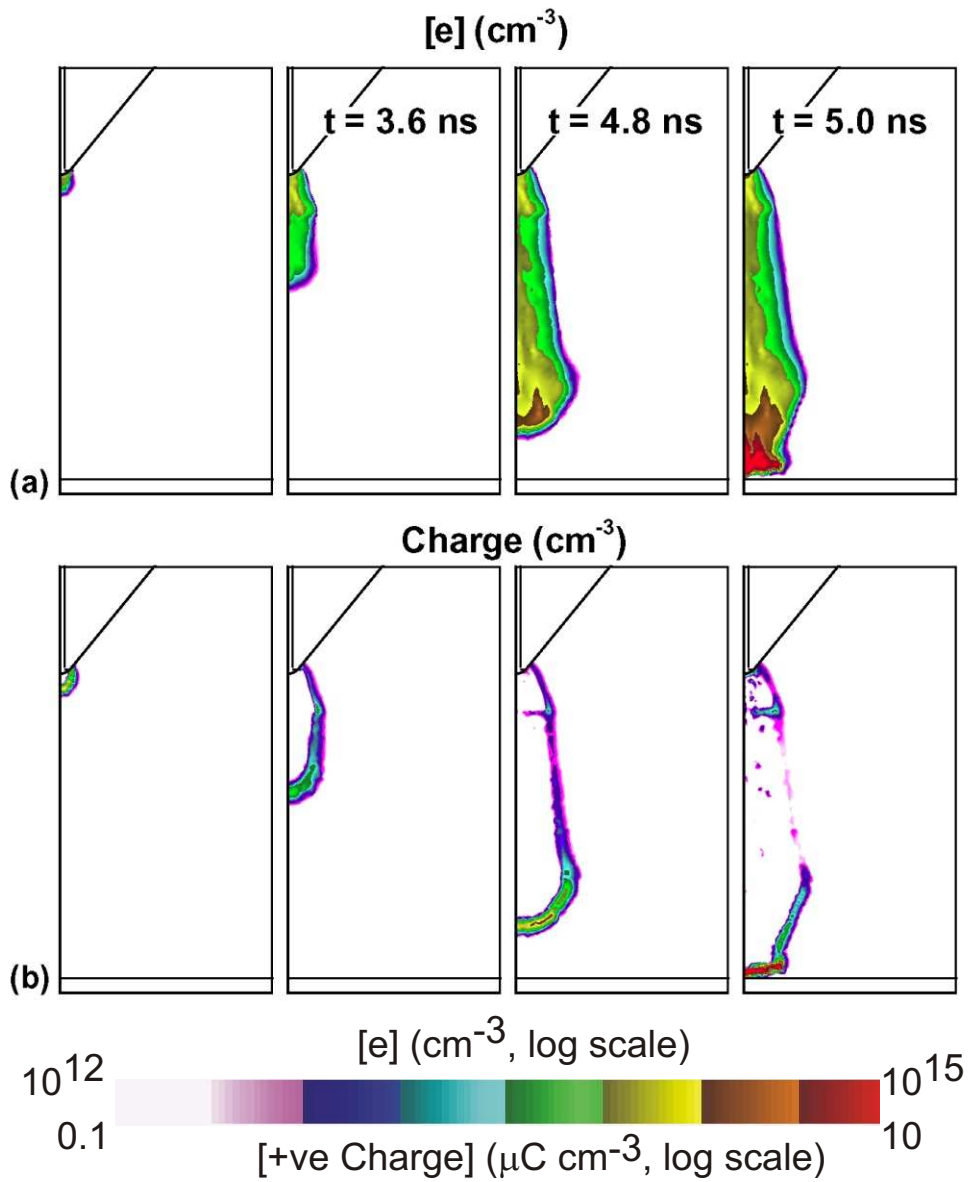


Fig. 11 The temporal variation of plasma characteristics (a) electron density and (b) space charge during breakdown in a positive discharge in air. Conditions are the same as in Fig. 9.

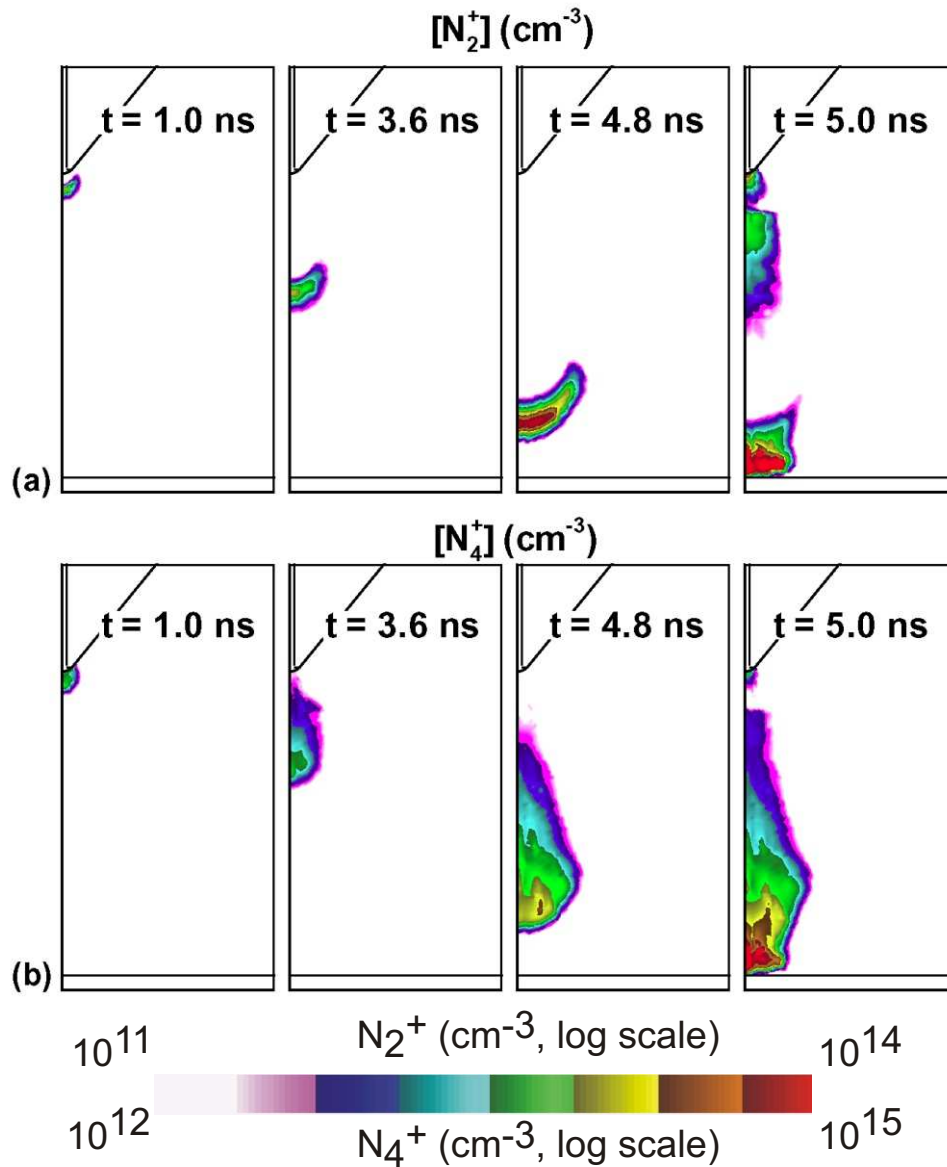


Fig. 12 The temporal variation of densities of (a) N_2^+ and (b) N_4^+ ions during breakdown in a positive discharge in air. Conditions are the same as in Fig. 9.

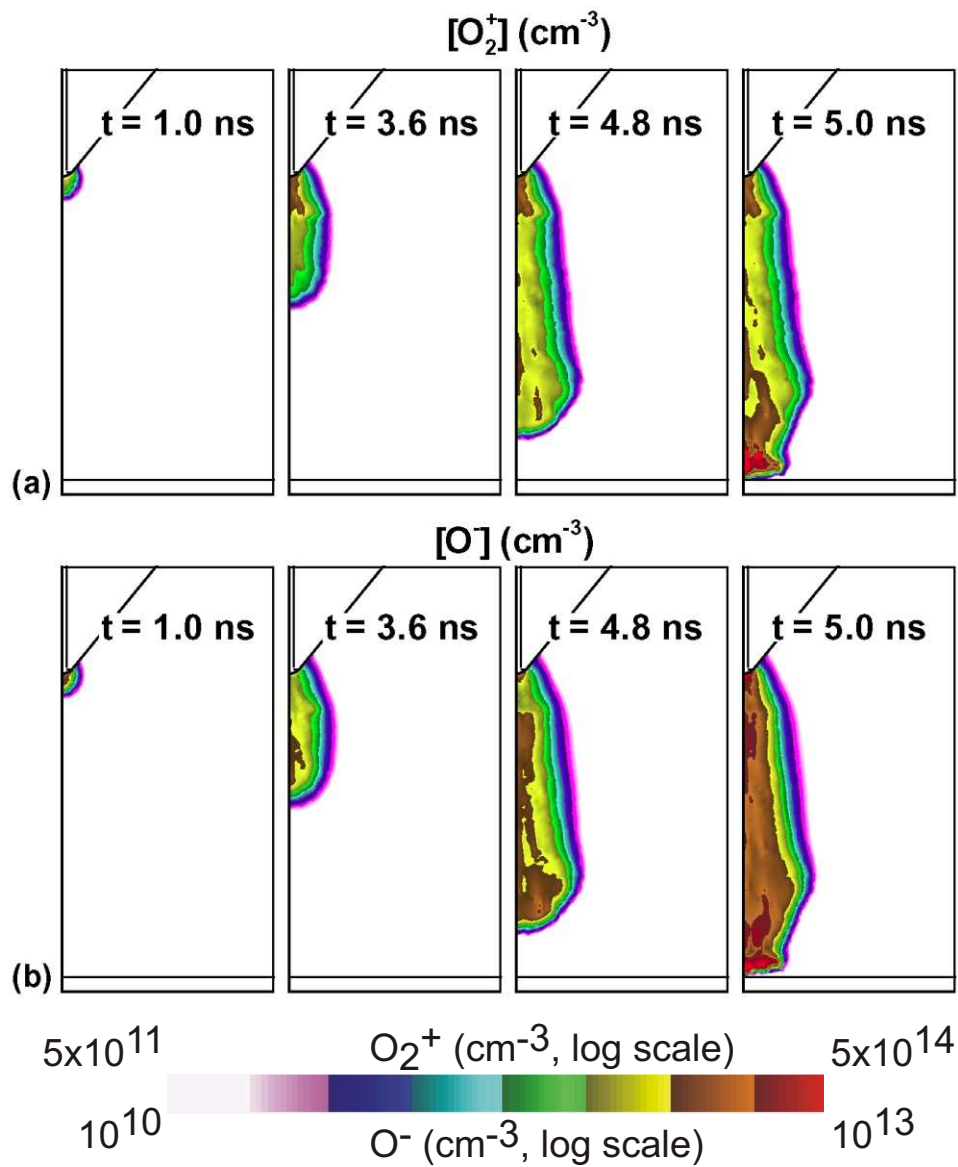


Fig. 13 The temporal variation in the densities of (a) O_2^+ and (b) O^- ions during breakdown in a positive discharge in air. Conditions are the same as in Fig. 9.

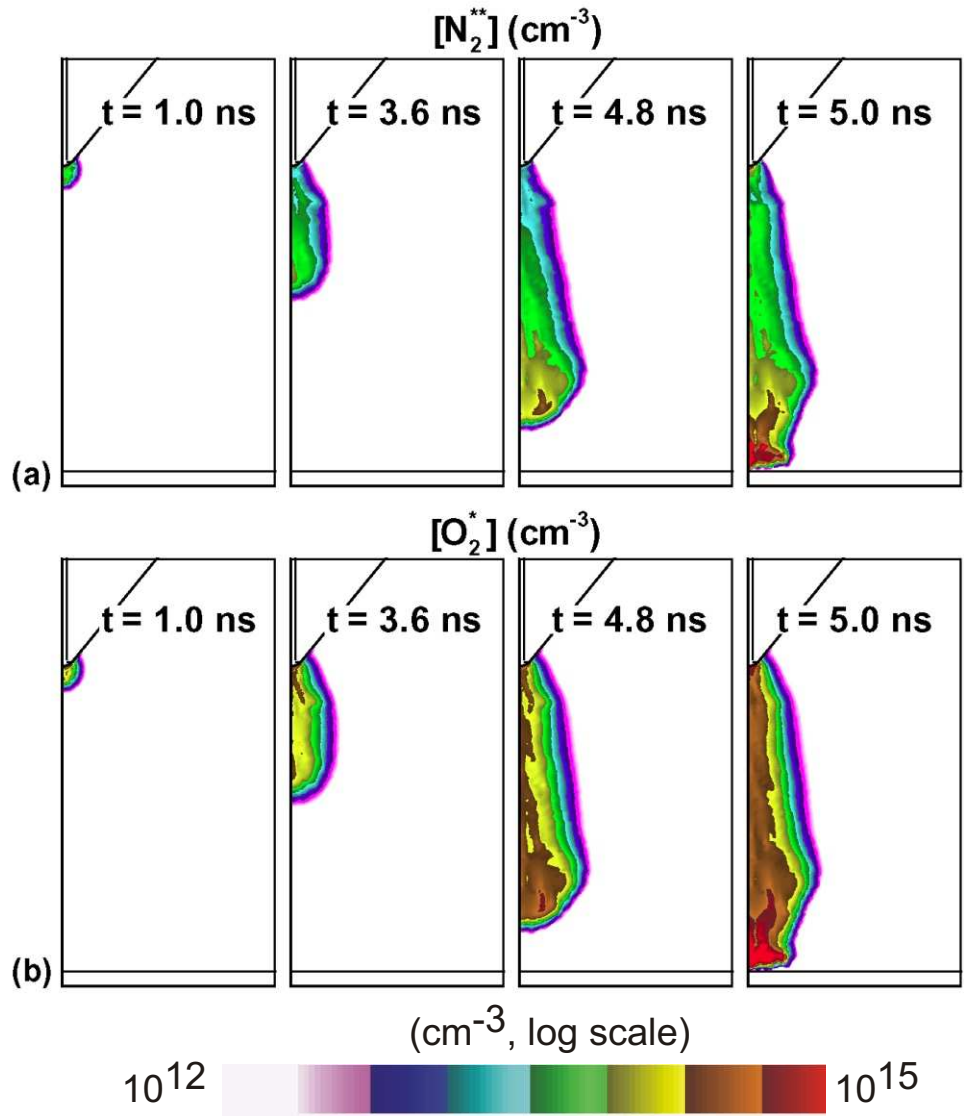


Fig. 14 The temporal variation of the densities of excited species (a) N_2^{**} and (b) O_2^* during breakdown in a positive discharge in air. Conditions are the same as in Fig. 9.

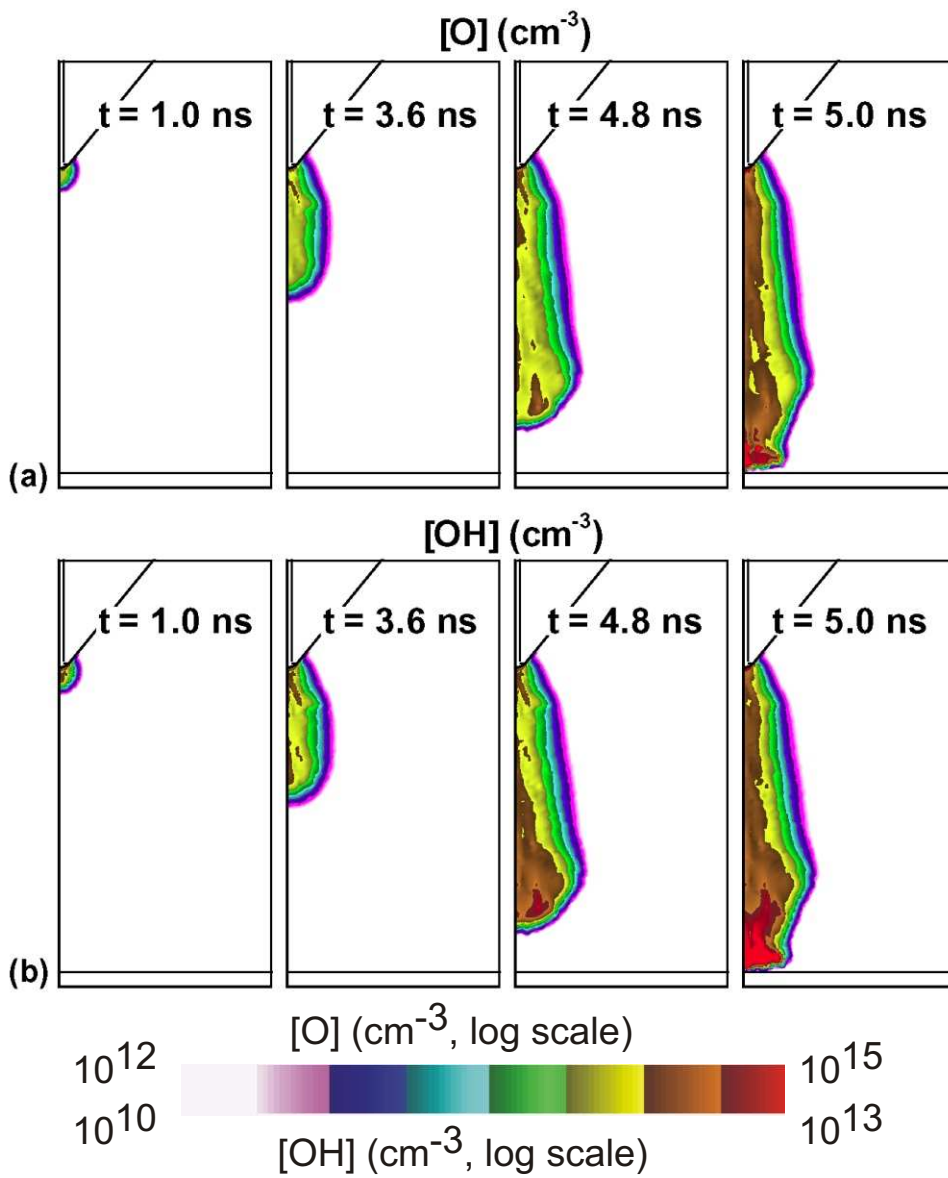


Fig. 15 The temporal variation of densities of radicals (a) O and (b) OH during breakdown in a positive discharge in air. Conditions are the same as in Fig. 9.

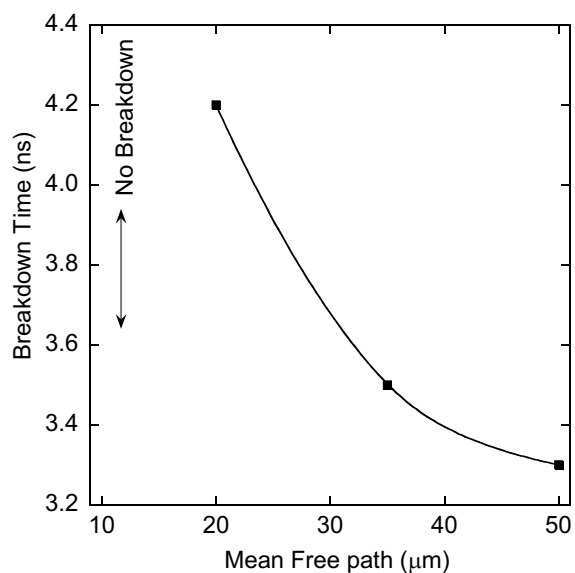


Fig. 16 Variation of breakdown time with the mean free path of absorption of photoionizing radiation (λ) in a positive discharge in air for an applied voltage of 15 kV. For $\lambda < 10 \mu\text{m}$, the discharge stalls and breakdown does not occur, so the positive discharge is critically dependent on photoionization for propagation.

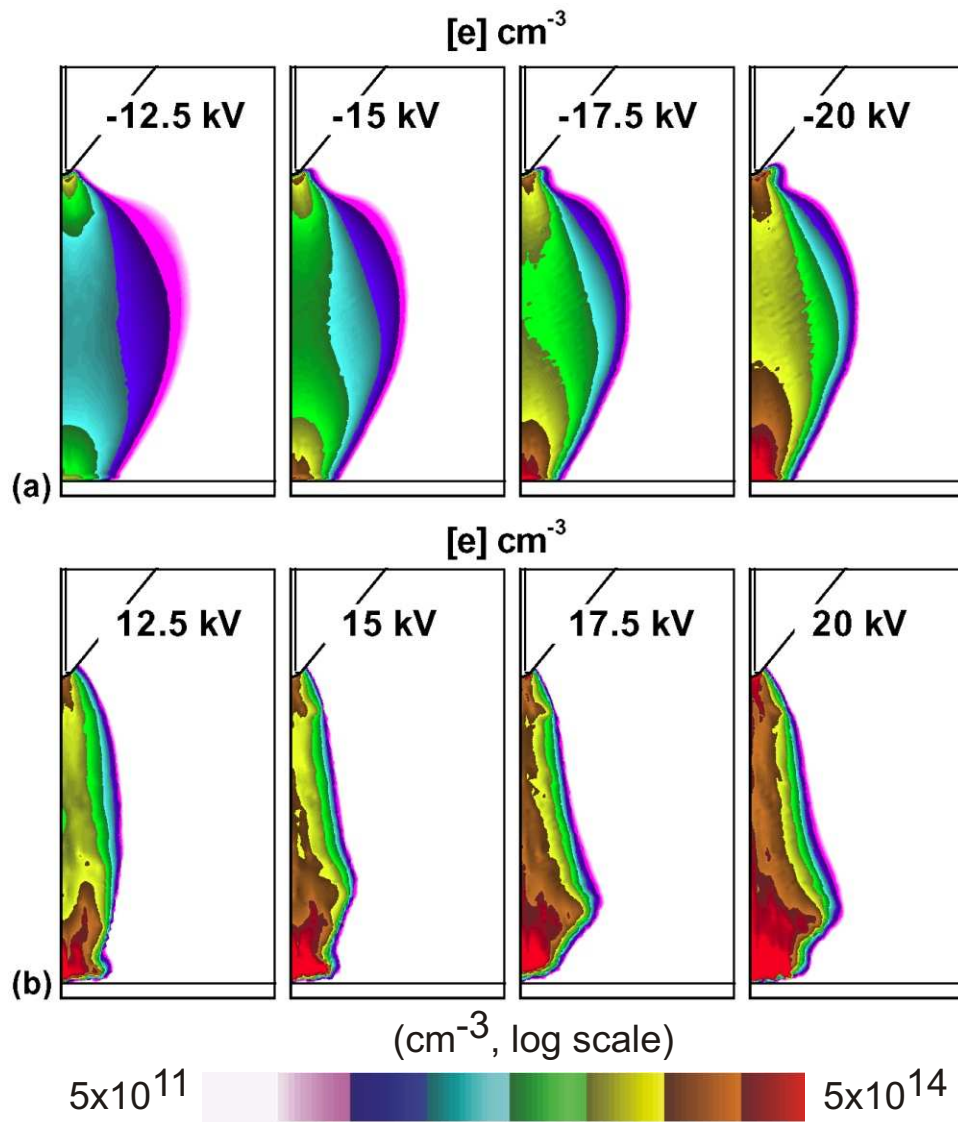


Fig. 17 Comparison of the electron density after breakdown for (a) negative and (b) positive discharges with applied voltage in air ($N_2/O_2/H_2O=79/20/1$) at atmospheric pressure.

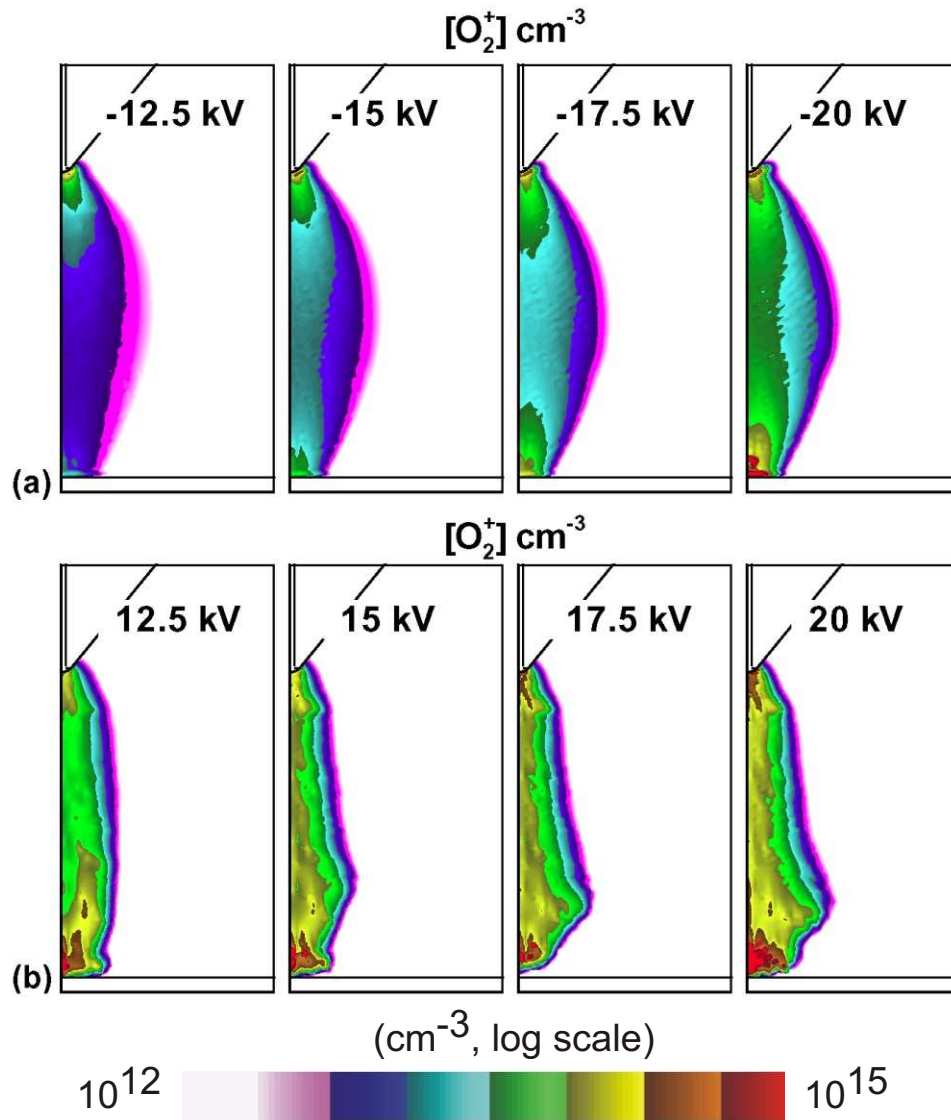


Fig. 18 Comparison of the density contours for O_2^+ after breakdown for (a) negative and (b) positive discharges with the applied voltage in air ($\text{N}_2/\text{O}_2/\text{H}_2\text{O}=79/20/1$) at atmospheric pressure.

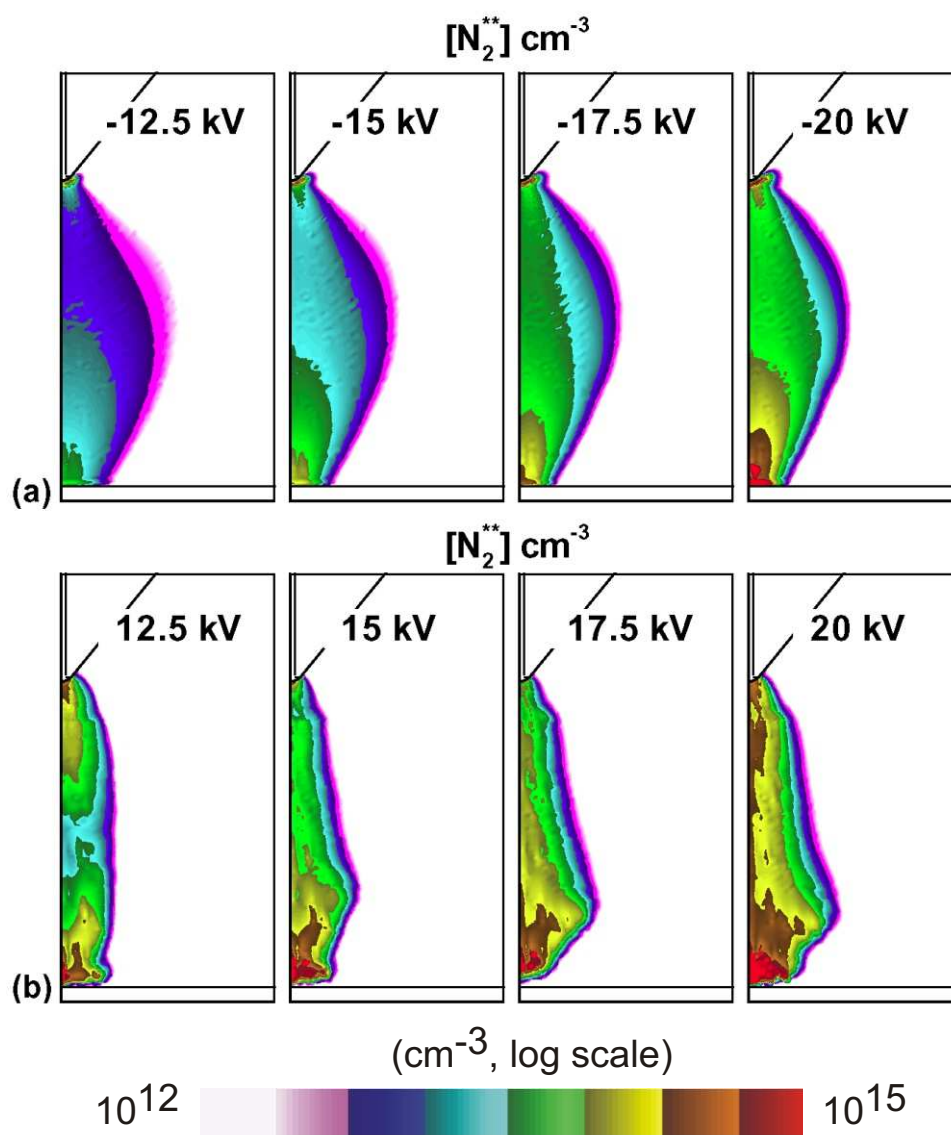


Fig. 19 Comparison of the N_2^{**} densities after breakdown for (a) negative and (b) positive discharges with applied voltage in air ($N_2/O_2/H_2O=79/20/1$) at atmospheric pressure.

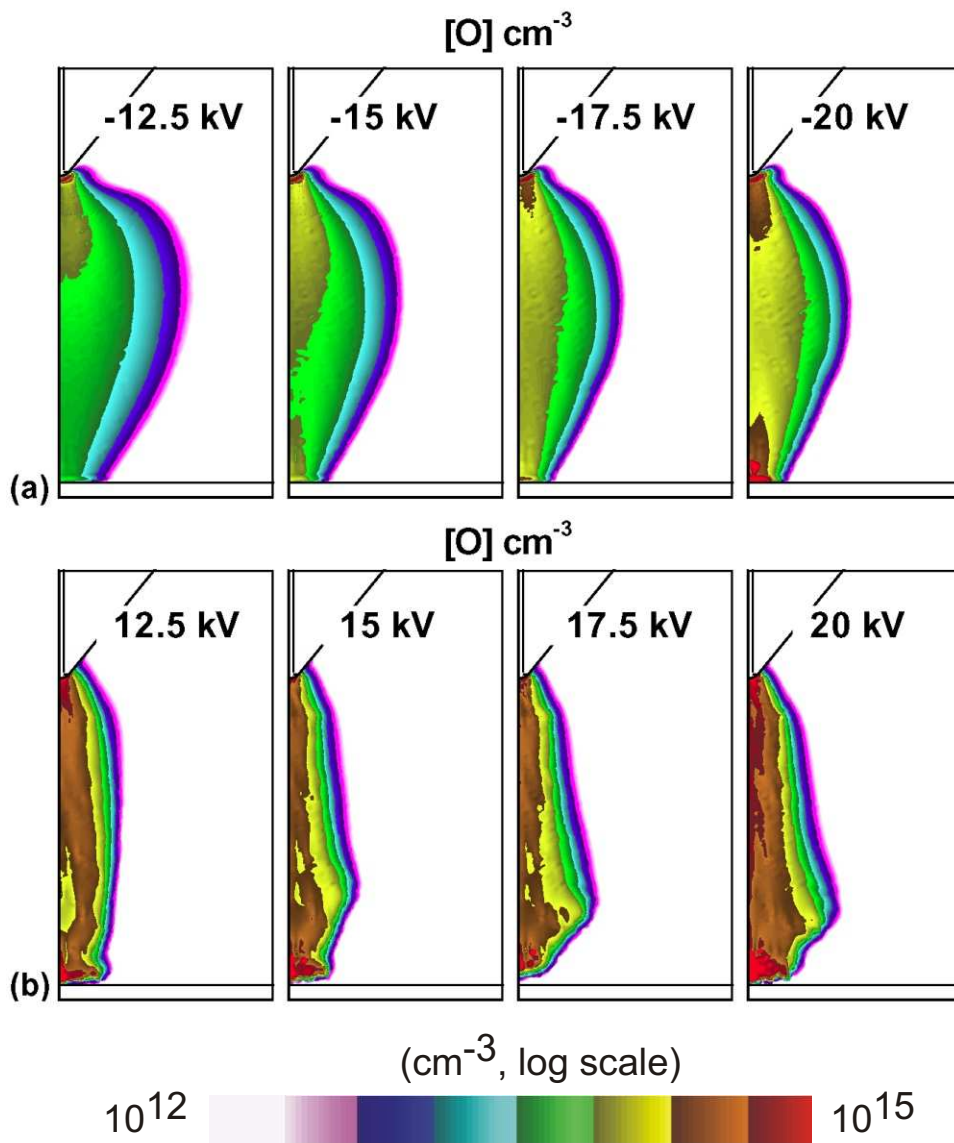


Fig. 20 Comparison of $[O]$ densities after breakdown for (a) negative and (b) positive discharges with applied voltage in air ($N_2/O_2/H_2O=79/20/1$) at atmospheric pressure.

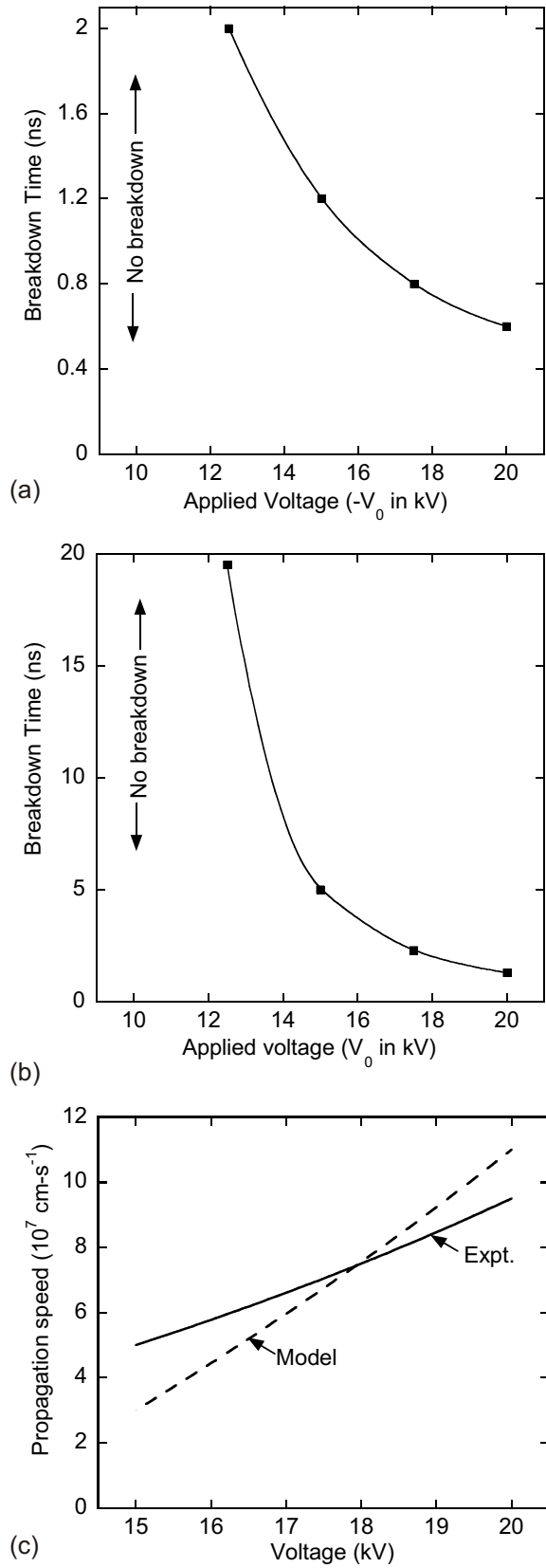


Fig. 21 Variation of breakdown time with the magnitude of applied voltage in (a) negative discharges and (b) positive discharges in air. (c) Comparison of propagation speed in positive discharges to experimentally measured values [2].

3.8 References

1. R. Dorai and M. J. Kushner, *Journal of Physics D*, **36**, 666 (2003).
2. P. Tardiveau and E. Marode, *Journal of Physics D*, **36**, 1204 (2003).

4. NON-EQUILIBRIUM ELECTRON TRANSPORT USING MONTE-CARLO METHODS ON AN ADAPTIVE MESH

4.1 Introduction

Low-temperature plasma modeling has played an important role in the understanding and development of many low pressure plasma-based tools used in the microelectronics industry.[1-3] More recently, models for plasma sources sustained at higher pressures are also being developed.[4-6] The fundamental basis for any low temperature plasma model is the electron energy distribution function (EEDF). This is because all the plasma characteristics are determined by the electron transport and rate coefficients, which in turn depend on the EEDF.

In principle, the complete spatio-temporal EEDF information is required to compute plasma properties exactly. However, in practice, this is a computationally intensive task, so simpler techniques have been developed in the literature to obtain the EEDF to a reasonable degree of accuracy. These approaches include the direct numerical integration [6] or solving the 2 term spherical harmonic expansion of the Boltzmann equation,[7] In general, the electron transport properties computed using any of these methods use assumptions to simplify computation (for instance spatially averaging, one-dimensional and so on) or statistics-based methods such as electron Monte Carlo simulations (eMCS) [8] and Particle-in-Cell (PiC) techniques [9]. eMCS methods make the least number of assumptions, and are regarded to be accurate enough to be used as benchmarks for the performance of other computational methods.[10]

Once the EEDF information is known, the electron temperature and sources of electron impact reactions can be calculated. Two approaches are commonly used to

obtain the electron temperature (a) the local-field approximation or (b) solving the average electron energy equation. In the local field approximation (commonly used in high-pressure discharge modeling), the local reduced electric field (E/N or electric field/number density) is used to calculate electron temperature (T_e), transport and reaction coefficients using tabulated data precompiled by solving the Boltzmann equation over a range of E/N . Solving the average energy equation, which is a more general hydrodynamic approximation derived by taking moments of the Boltzmann equation, allows for accounting of the electron energy fluxes (driven by spatial gradients and electron thermal conductivity) in the calculation of T_e .

Under certain conditions, such as the presence of large space charge electric fields in low pressure plasmas, non-equilibrium electron transport occurs.[10] In such conditions, the EEDF is not in equilibrium with the electric field. Typically, non-equilibrium electron transport is important in electrical discharges when the rates of momentum and energy relaxation (ν_e), or the mean free path of electrons (λ_e) exceed the rate of change of the magnitude of the electric field (E). Non-equilibrium (or non-local) techniques are commonly applied to model the discharge under these conditions.

$$\frac{1}{\lambda_e} \geq \frac{|\nabla E|}{E}, \quad \nu_e \geq \frac{dE}{dt} \quad (1)$$

Non-equilibrium electron transport may also arise in high pressure discharges in the presence of large space charge electric fields that exceed the applied field. For instance, the ionization front during breakdown in high-pressure discharges has steep spatial gradients in electric field which may be locations where non-equilibrium electron transport may occur. Since hydrodynamic descriptions cannot capture non-equilibrium

transport, kinetic methods need to be used in such cases to directly obtain the EEDF and calculate properties such as T_e and reaction rates. Fully kinetic simulations, especially in multidimensional models, are computationally burdensome. A new method has been developed which uses an electron kinetics simulation embedded within the larger two-dimensional plasma hydrodynamics model, described in Chapter 2, to kinetically calculate the EEDF at select locations identified in the discharge. This approach balances the need for accuracy and the large computational burden associated with kinetic simulations. Sensors that locate regions of possible non-equilibrium electron transport, where eMCS calculations are performed, dynamically during the simulation are used and the details are described in Section 8.2.

The application of this technique to model discharges operating at different pressures ranging from Ar discharges at 10s Torr to corona discharges in air at atmospheric pressure is demonstrated in Section 8.3. In Ar discharges at 10s Torr, we found significant non-equilibrium transport in the ionization front when the eMCS module was used, especially at lower pressures. This technique was also used to investigate breakdown in corona discharges at atmospheric pressure and is discussed in Section 8.4. With eMCS we found higher T_e and lower ionization rates at the ionization front leading to a narrower discharge channel, more in tune with experimental observations.

4.2 Description of the Model

A flowchart depicting the use of the adaptive eMCS module within the larger 2d plasma hydrodynamics model is shown in Fig. 1, and a brief description is given here. The user specifies the frequency δT at which the discharge characteristics on the

unstructured mesh (UM) are scanned by the eMCS module. At each eMCS call, the algorithms inside the eMCS module use a sensor-based approach to dynamically identify regions where non-equilibrium electron transport might possible occur. A combination of one or more plasma characteristics is designated as a “sensor” and is calculated dynamically on the UM, at every eMCS call. When sensor values at any location exceed pre-specified numerical non-equilibrium criteria, the location is flagged for inclusion in the eMCS.

For instance, a sensor could be made up of the combination of electron temperature (T_e) and ionization sources (S_e) with numerical threshold criteria of 4 eV and $10^{21} \text{ cm}^{-3}\text{s}^{-1}$. In this example, as the discharge evolves, the sensor scans the plasma conditions on the UM every δT seconds to flag locations where $T_e > 4 \text{ eV}$ and $S_e > 10^{21} \text{ cm}^{-3}\text{s}^{-1}$ are satisfied. Another example of a sensor could use the electron density or the electric field instead. In general, the user is free to customize the sensor using any appropriate combination of plasma characteristics and numerical threshold criteria, which can vary with the type of discharge being investigated. The judgment of an experienced user will aid in setting up sensor-threshold combinations that rely on an insight into the physics of the discharge to reliably track the non-equilibrium regions.

Since spatial locations where non-equilibrium is flagged can be discontinuous or arbitrarily shaped, a continuous rectangular region, called the eMCS box, is constructed. Some of the flagged locations may not be included because of user-specified limits on the minimum (l_{min}) and maximum (l_{max}) length of the sides of the eMCS box. These limits are specified to keep computational time reasonably low and usually vary depending on the underlying UM resolution (r). As a rule of thumb, setting $l_{min}/r = 5 - 10$ and $l_{max}/r = 80$

– 100 enables moderately fast computations while allowing eMCS algorithms to resize the eMCS box at every eMCS call as dictated by the plasma conditions. If an eMCS box of constant size is desired, the user needs to specify inputs l_{min} and l_{max} that satisfy $l_{max}=l_{min}+r$.

A separate Cartesian Mesh (CM) is overlaid on the UM on the identified eMCS box region as shown in Fig. 2. The resolution of the CM is set to be slightly lower than that of the underlying UM (r). At every eMCS call, interpolation is set up to transfer physical quantities such as electric potential and species densities, electron temperature and electron impact source functions back and forth between the CM and the UM, as depicted in Fig. 2. Trajectories of electrons entering the eMCS box are advanced on the CM, using interpolated values of electric fields and species densities onto the locations on the CM.

The net electron flux entering the eMCS box along its boundaries are calculated by including the thermal flux, computed using the thermal velocity (v_{th}),

$$\phi_{thermal,i} = \frac{1}{4} n_i v_{th,i}$$

and the convective flux due to the electric field, entering into the region.

$$\phi_{drift,i} = \sum_j \frac{\alpha D}{\mu} \left(\frac{n_j - n_i \exp(-\alpha \delta_{ij})}{1 - \exp(-\alpha \delta_{ij})} \right)$$

where n_k ($k=i, j$) is the electron density at node i or neighbor j and δ_{ij} is the distance between node i and neighbor j , D and μ are the local electron diffusion coefficient and mobility. The net electron velocity is

$$v_{net,i} = (\phi_{thermal,i} + \phi_{drift,i}) / n_i$$

The source of electrons entering the eMCS box ($S_{e,i}$ in #/s) from each bordering UM node i is calculated by multiplying the net electron velocity entering the eMCS box with the sum of the cell face areas (δA_{ij}) between node i and neighbors j that lie wholly within the box (Fig. 3(c)).

$$S_{b,i} = n_i v_{net,i} \times \sum_i \delta A_{ij}$$

Pseudo-particles are released from locations along the boundary of the eMCS box, where the net electron velocity is directed into the region. They are weighted in proportion to the net source of electrons entering the eMCS box,

$$W_{e,i} = S_{b,i} / N_p$$

where N_p is the number of particles. A few 100s of particles were used in our simulations. The initial velocity of each emitted pseudoparticle on the CM is the vector sum of the thermal velocity (v_{th}) at a randomly selected angle and the directed convective velocity (v_{drift}) at that location.

The trajectories of emitted pseudoparticles are integrated in time using electric fields interpolated from the UM. Electrons with energies that fall below a small value (usually 0.03 eV) are removed from the simulation. The results of the eMCS are electron impact source functions and electron temperatures. The source functions are obtained by computing the EEDF ($f(\epsilon)$) of the electrons entering the eMCS box and their progeny as a function of position on the CM, and convolving these EEDFs with reaction cross sections,

$$S_k(\vec{r}) = \int f(\epsilon, \vec{r}') \sigma_k(\epsilon) N_k(\vec{r}) d\epsilon$$

$$T_e(\vec{r}) = \frac{2}{3} \left(\int f(\varepsilon, \vec{r}') \varepsilon d\varepsilon \right) \quad (2.10)$$

where S_k refers to the rate of the k^{th} electron impact reaction having a reaction cross-section σ and species density N at the position \vec{r} on the CM. The electron temperatures so obtained on the CM locations are interpolated to the corresponding UM locations and replace T_e values computed using the average electron energy equation. Similarly, rates for electron impact reactions calculated at CM locations are interpolated on to the corresponding UM locations to replace reaction rates calculated using the hydrodynamics model. Both the sources of electron impact reactions and T_e interpolated on to the UM are held constant between calls to the eMCS while the hydrodynamics model computations proceed as before.

The frequency of calls to the eMCS module δT is user-specified. Each eMCS call can take from 0.5 - 5 mins, depending on the plasma conditions and a reasonably sized eMCS box, and can be computationally intensive if the eMCS is called very frequently. On the other hand, the eMCS calls should be sufficiently frequent as to track the evolution of the non-equilibrium region. An appropriate judgment can be made with an insight into the timescales of the plasma dynamics at the conditions of interest, by running a simulation without using the eMCS module. For instance, in atmospheric pressure corona discharges, where breakdown occurs in gas gaps of a few mm within 5 – 10 ns, the eMCS module is called every 50 – 100 ps to track the rapidly evolving ionization front.

4.3 Ar Discharges at 10s Torr

Non-equilibrium transport during breakdown in Ar discharges at 10s Torr was numerically investigated in a cylindrically symmetric representation of a high-intensity discharge lamp geometry as shown in Fig. 3, similar to that used in earlier breakdown studies.[11] The discharge region is a quartz tube of radius 0.5 cm having an inter-electrode gap of 1.6 cm. A 2000 V pulse with a rise time of 10s ns is applied to the upper electrode to breakdown the gas after many 100s of ns. Breakdown starts due to geometric electric field enhancement that produces large ionization sources near the powered anode. Due to the difference in electron and ion mobility, a positive space charge region is quickly created as electrons drift faster in the high electric field region. The space charge further enhances the electric field and the region, increasing ionization rates further. This region of high electric fields of magnitude 500s Td or more with spatial gradients of 1000s Td/mm, with large ionization rates is termed the ionization front and it propagates to the grounded cathode as shown in Fig. 4.

eMCS is employed at two locations on the mesh. The first is a fixed eMCS mesh at the cathode to track secondary electrons emitted due ion bombardment from the surface and is discussed in earlier investigations [11]. The second mesh is the adaptive eMCS mesh used to track the ionization front. In all cases discussed here, the fixed eMCS mesh is used. In the nomenclature used here ‘with eMCS’ refers to the use of the adaptive eMCS mesh to track the ionization front and ‘without eMCS’ or ‘no eMCS’ refers to the absence of the adaptive eMCS mesh only.

The eMCS is invoked every 2 – 5 ns to capture the plasma dynamics at the ionization front. The electron density and ionization sources are designated as the sensor in the eMCS, to dynamically locate the ionization front. At every eMCS call, the

normalized electron density and ionization sources are calculated using the respective maxima on the UM at that call. Numerical thresholds for the normalized electron density and ionization sources of 10^{-4} and 10^{-2} respectively are specified as input. Locations on the UM where the normalized sensor variables have exceeded these thresholds are flagged as potential ionization front locations during every eMCS call. Geometrical algorithms are used to accurately map a CM mesh on the identified region as shown in Fig. 4 and reliably track the evolution of the ionization front.

The base case refers to breakdown in Ar at 30 Torr using the hydrodynamics model over the complete UM. The corresponding eMCS case uses the same conditions, but the T_e and ionization rates calculated in the eMCS module and interpolated on to the UM and replace the hydrodynamics model values. A comparison of T_e , ionization sources (S_e) and electron density (n_e) for these two cases when the fronts are at similar locations midway through the gap is shown in Fig. 5. The peak T_e at the front using the eMCS model is higher than the corresponding hydrodynamic value by 0.8 - 1 eV. There are significant variations in the spatial contours of S_e with and without eMCS at the ionization front. Without eMCS, there is a well defined concentration in S_e at locations corresponding to high T_e at the ionization front. With eMCS, S_e at the front is in general lower by a factor of 2 – 3 and is more diffuse and spread out. Behind the front, S_e in the ionized channel is about a factor of 3 lower with eMCS. As a result, the n_e in the ionized channel with eMCS is lower.

The effect of pressure on non-equilibrium electron transport was determined by investigating breakdown with and without the eMCS module under different gas-fill pressures from 30 Torr to 90 Torr. Values of T_e along the centerline of symmetry, when

the ionization front is approximately midway between the electrodes, are compared in Fig. 6 at these pressures. The extents of the corresponding eMCS meshes at these times are also shown. In general, as pressure increases, the T_e at the front decreases due to lower E/N . However, the enhanced T_e regions are narrower as pressure is increased indicating the continued presence of significant gradients. The peak T_e with eMCS is still about 1 eV lower at 50 Torr and 90 Torr respectively.

The values of S_e along the centerline of symmetry are shown for similar conditions in Fig. 7. Steep gradients exist in S_e at the front and in the ionized channel. S_e calculated with eMCS is lower at 50 Torr by a factor of 2 at the ionization front compared to the hydrodynamics model. As the pressure is increased to 90 Torr, the differences at the front become negligible. This is because the ionization rates approach the equilibrium values calculated by the hydrodynamics model, as collisionality increases with pressure.

The values of n_e along the centerline of symmetry for similar conditions are shown in Fig. 8. At 30 Torr, electron density in the ionized channel is lower by up to a factor of 1.5 - 2 with the eMCS due to lower ionization sources. As pressure increases to 50 Torr, the variations in n_e in the ionized channel with and without eMCS decrease and become negligible at 90 Torr.

4.4 Corona Discharges at 100s Torr

The corona discharge setup similar to one used for polymer surface treatment is schematically shown in Fig. 9(a). The Cartesian symmetric representation of such a system is shown in detail in Figs. 9(b)-(c) and consists of a powered upper electrode embedded in dielectric with the tip exposed to the gas and separated from the grounded

electrode by a gas gap of 2 mm. Breakdown occurs in these discharges on application of 10s kV voltage pulses, with the formation of an ionization front that propagates through the gas gap, as described in detail in Chapter 3. Despite the collisional nature of discharge at atmospheric pressure, the presence of large electric field gradients at the front may cause non-equilibrium electron transport. In this investigation, the adaptive eMCS model was applied to capture possible non-equilibrium. To track the ionization front, a sensor comprising of the electron density and electric field gradient were specified. The numerical non-equilibrium thresholds were specified as 10^{11} cm^{-3} and 10^4 Td-cm^{-1} respectively. The sensor therefore flags locations where $n_e > 10^{11} \text{ cm}^{-3}$ and $\nabla E > 10^4 \text{ Td-cm}^{-1}$ are satisfied.

Breakdown was investigated with a 15 kV pulse of positive polarity and negligible rise time applied to the upper electrode. In all these cases, there is no eMCS mesh or a single adaptive eMCS mesh that tracks the ionization front. During the initial phase of breakdown the presence of large electric fields close to the powered electrode creates large ionization sources. Electrons produced in this region drift under the influence of the electric field faster than ions due to their high mobility, creating a thin region of space charge regions near the electrode. The space charge separation extends to a region of about 200 μm further enhancing the E/N to about 500-600 Td and S_e to $10^{23} \text{ cm}^{-3}\text{s}^{-1}$, creating an ionization front.

As a result, steep gradients in the electric field (10000 Td/mm) arise at the edge of the ionization front. The presence of large S_e propagates the front towards the grounded electrode. Spatial contours of the magnitude of the electric field and its gradient and the tracking eMCS box are shown in Fig. 10 for conditions when the ionization front is

midway through the gap. The sensor reliably tracks the regions of high ∇E at the ionization front, as it propagates through the gap.

The spatial contours of T_e when the front is midway through the gap are shown in Fig. 11(a). With eMCS, T_e near the leading edge of the ionization front is higher by 1 eV. Values of T_e along the centerline of symmetry are shown at two different times in Fig. 11(b). The enhanced T_e is the region of the ionization front. As the discharge propagates, the difference in the T_e calculated with eMCS over the hydrodynamics model decreases from 1.5 eV to < 0.5 eV. This is because the gradients in the discharge decrease with time as indicated by the widening of the ionization front.

Contours of S_e are shown in Fig. 12(a) for similar conditions. There are significant variations in spatial structure, with a more diffuse S_e pattern with the eMCS. Values of S_e along the centerline of symmetry are shown at two different times in Fig. 12(b). Close to the anode, there is little variation in S_e between the eMCS and hydrodynamics model values. As the discharge propagates, the peak values of S_e are lower by more than an order of magnitude with the eMCS, but this is compensated by their greater spatial spread. Contours of n_e after gap closure are shown for these cases in Fig. 13(a). The ionized channel with eMCS is narrower than the hydrodynamics-only calculations. Values of n_e along the centerline of symmetry are shown in Fig. 13(b). As the discharge propagates, n_e decreases with eMCS because of lower ionization sources.

4.5 Concluding Remarks

Under certain conditions non-equilibrium electron transport may also be occur in high pressure discharges at select spatial locations, such as the ionization front in the presence of large electric field gradients. In this paper, a new adaptive computational

technique using a kinetic eMCS module with a larger hydrodynamics platform was developed to simulate the plasma dynamics at the ionization front of moderate to high pressure discharges. Moderate non-equilibrium in electron transport was found in atmospheric pressure corona discharges. During breakdown in a positive corona at atmospheric pressure in air generated in a small gap, the peak electron temperature at the front was higher by 1 eV, whereas the ionization sources were lower by up to a factor of 2. The discharge channel was also narrower and more in tune with experimental observations. During breakdown in Ar-filled, cold high intensity discharge lamps at 30 Torr the peak electron temperature at the ionization front using the kinetic module was higher by 1.5 eV compared to the hydrodynamic model values. Ionization sources were lower indicating significant non-equilibrium in the ionization front. As pressure was increased from 30 Torr to 90 Torr, these differences reduced because of greater collisionality.

4.6 Figures

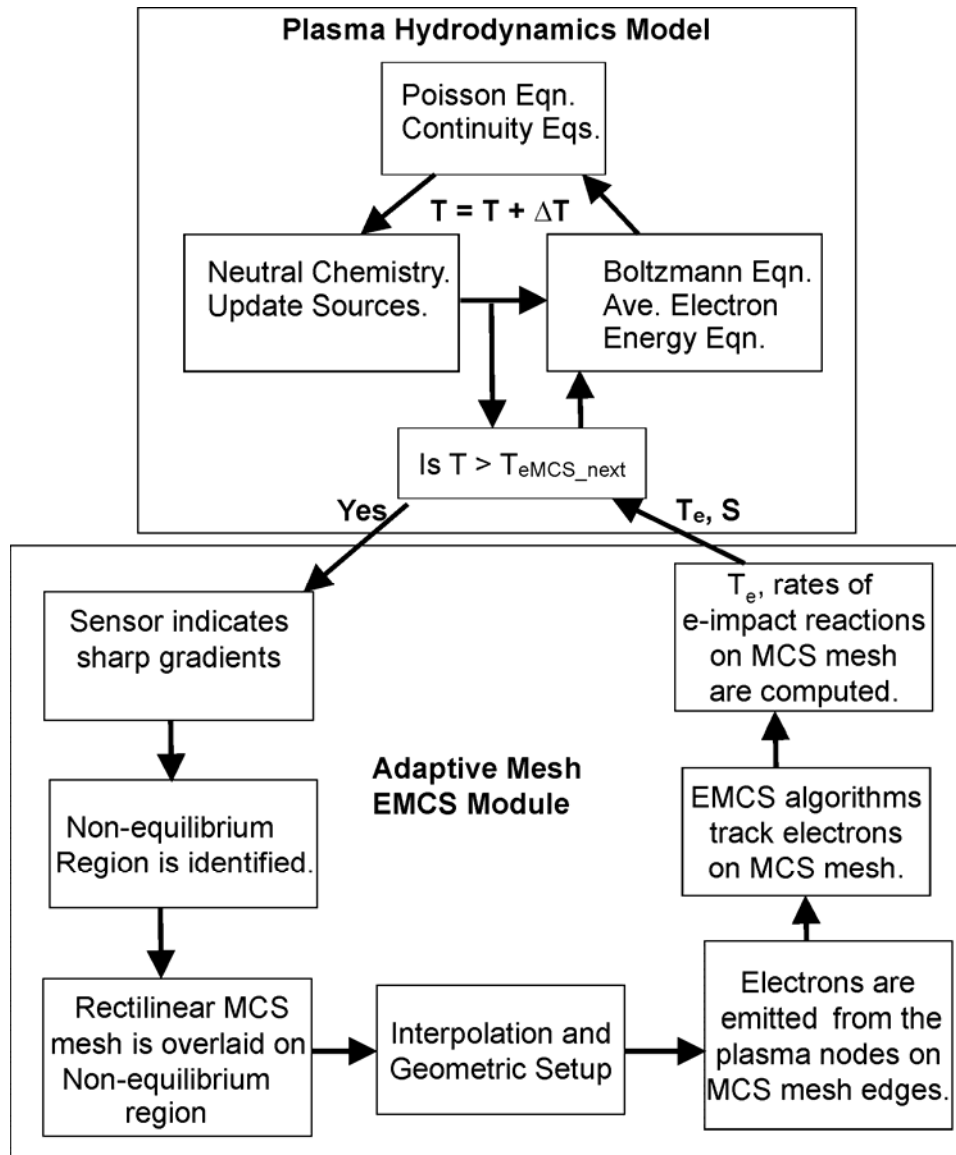


Fig. 1 Flowchart depicting the algorithm outline used in the adaptive eMCS module.

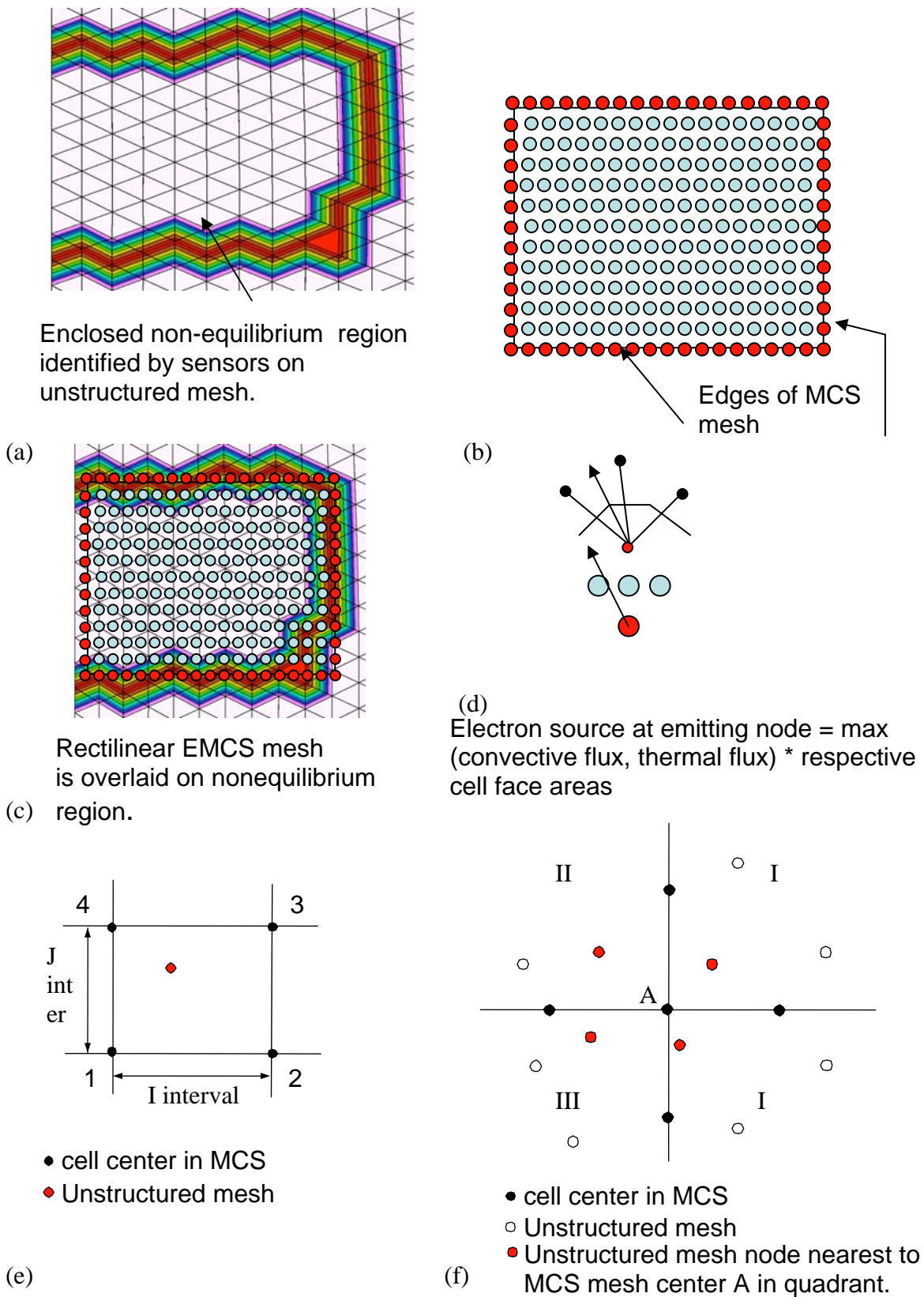
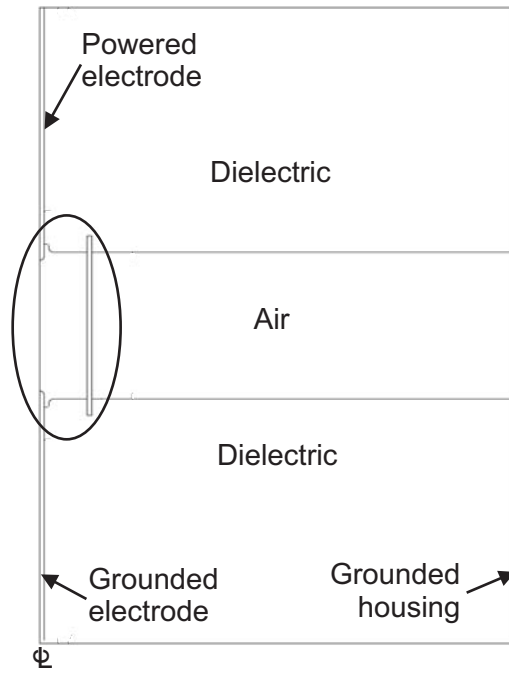
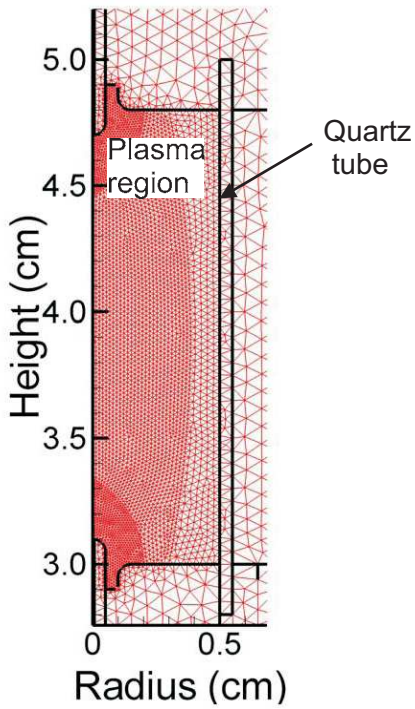


Fig. 2 (a)-(c) The eMCS region is identified by sensors on the unstructured mesh (UM) and a Cartesian Mesh (CM) is overlaid. (d) Particles are launched from nodes where net electron flux is into the eMCS box. (e)-(f) Interpolation setup between the CM and UM.



(a)



(b)

Fig. 3 Schematic of the lamp geometry (a) Breakdown occurs between the powered anode and grounded cathode placed in a quartz tube. (b) The interelectrode gap is 1.6 cm and is resolved using refined unstructured meshes.

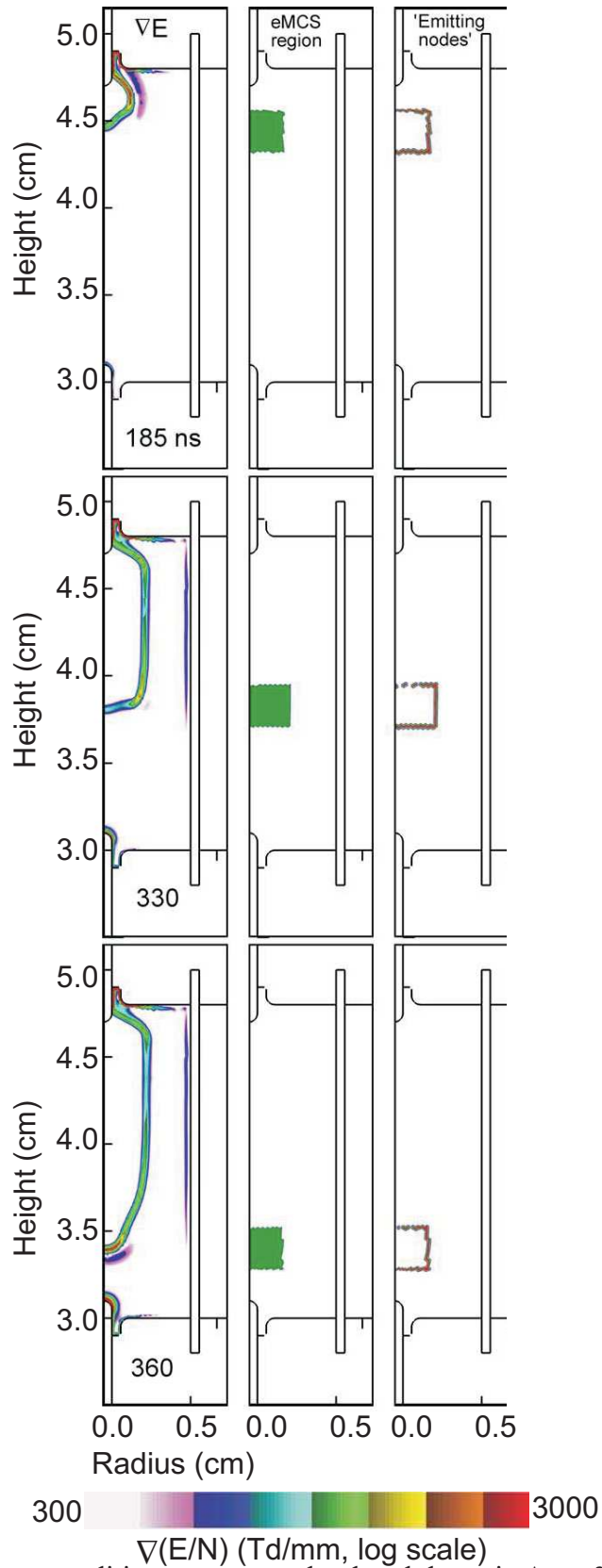


Fig. 4 The base case conditions correspond to breakdown in Ar at 30 Torr with 2000 V pulse. The ionization front during breakdown is a region of high electric field gradients where possible non-equilibrium electron transport may occur. The eMCS algorithms track the ionization front as it evolves. Pseudoparticles in the kinetic simulation are released from the boundary of the eMCS region.

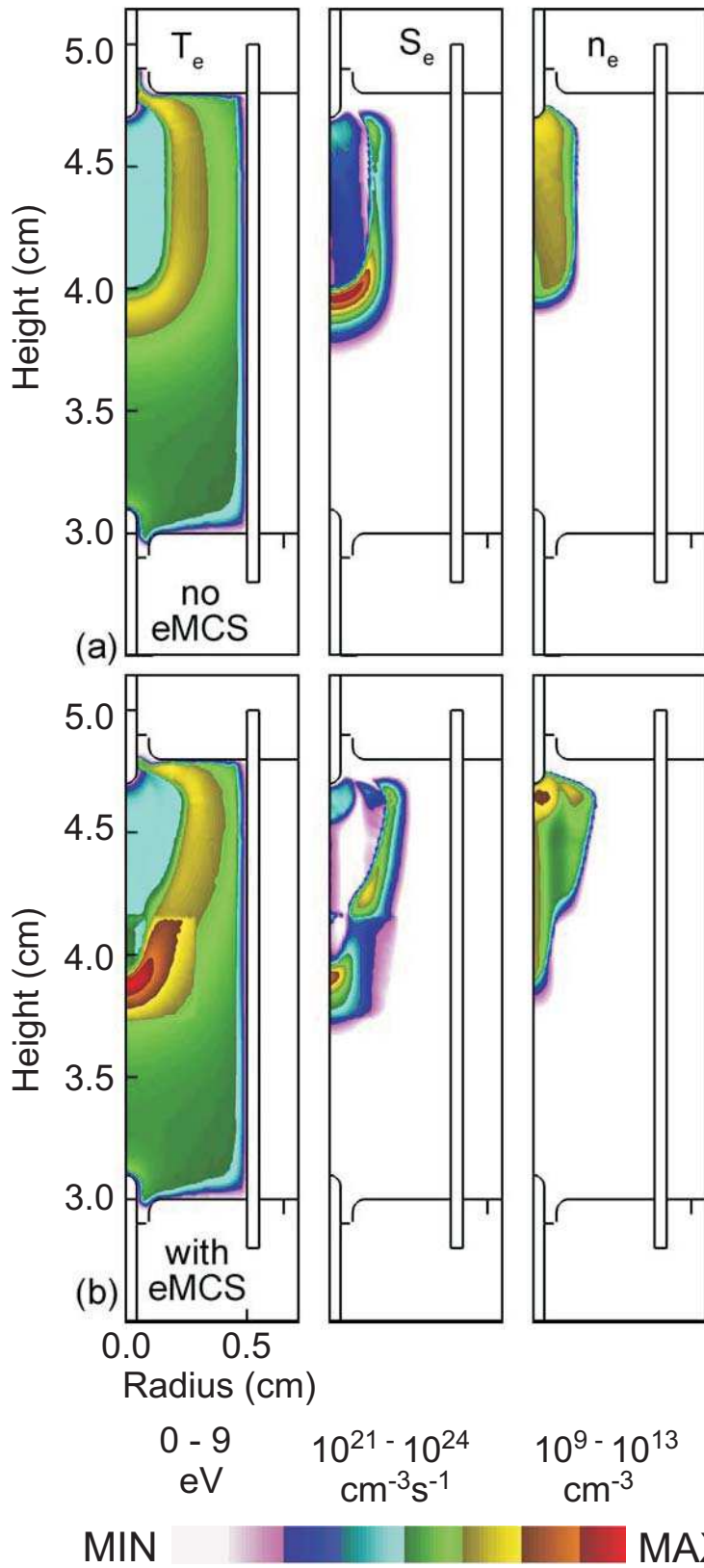


Fig. 5 Comparison of spatial plasma characteristics T_e , S_e and n_e calculated (a) without eMCS and (b) with eMCS midway during breakdown with a 2000 V pulse in Ar at 30 Torr.

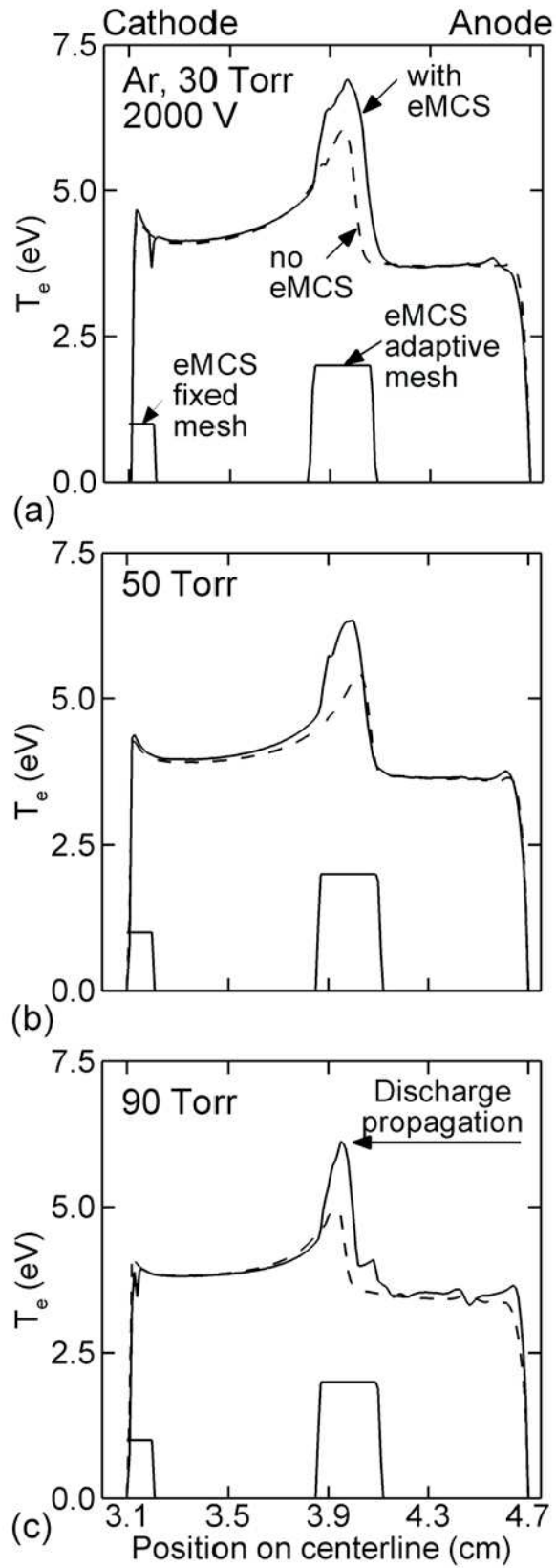


Fig. 6 Comparison of electron temperature calculated without and with the eMCS module during breakdown in Ar using 2000 V pulse at different Ar pressures (a) 30 Torr (b) 50 Torr and (c) 90 Torr.

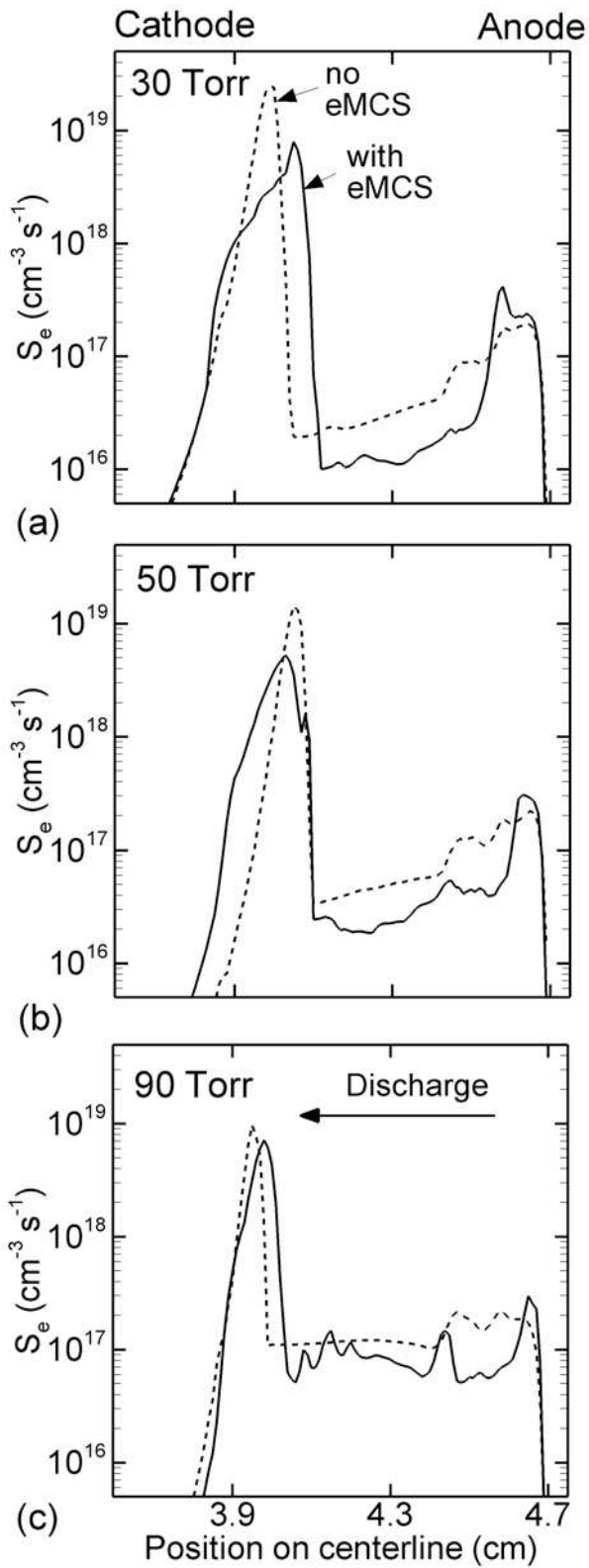


Fig. 7 Comparison of ionization sources calculated without and with the eMCS module during breakdown in Ar using 2000 V pulse at different Ar pressures (a) 30 Torr, (b) 50 Torr and (c) 90 Torr.

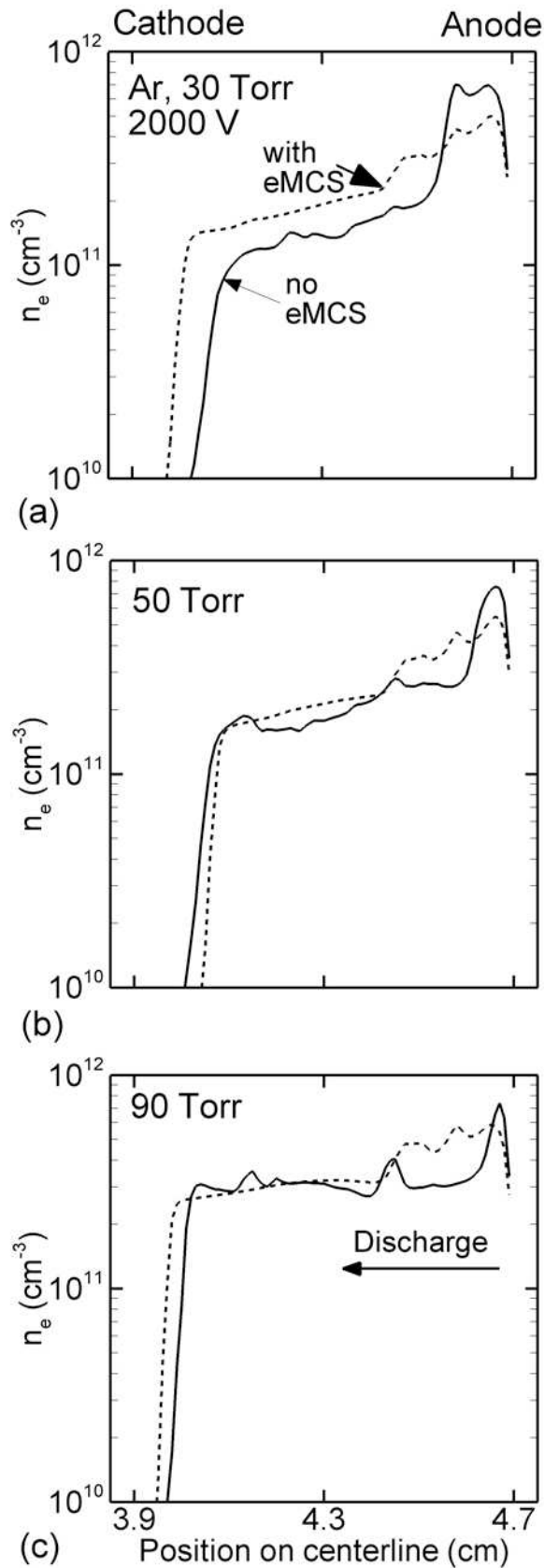


Fig. 8 Comparison of electron density calculated without and with the eMCS module during breakdown in Ar using 2000 V pulse at different Ar pressures (a) 30 Torr, (b) 50 Torr and (c) 90 Torr.

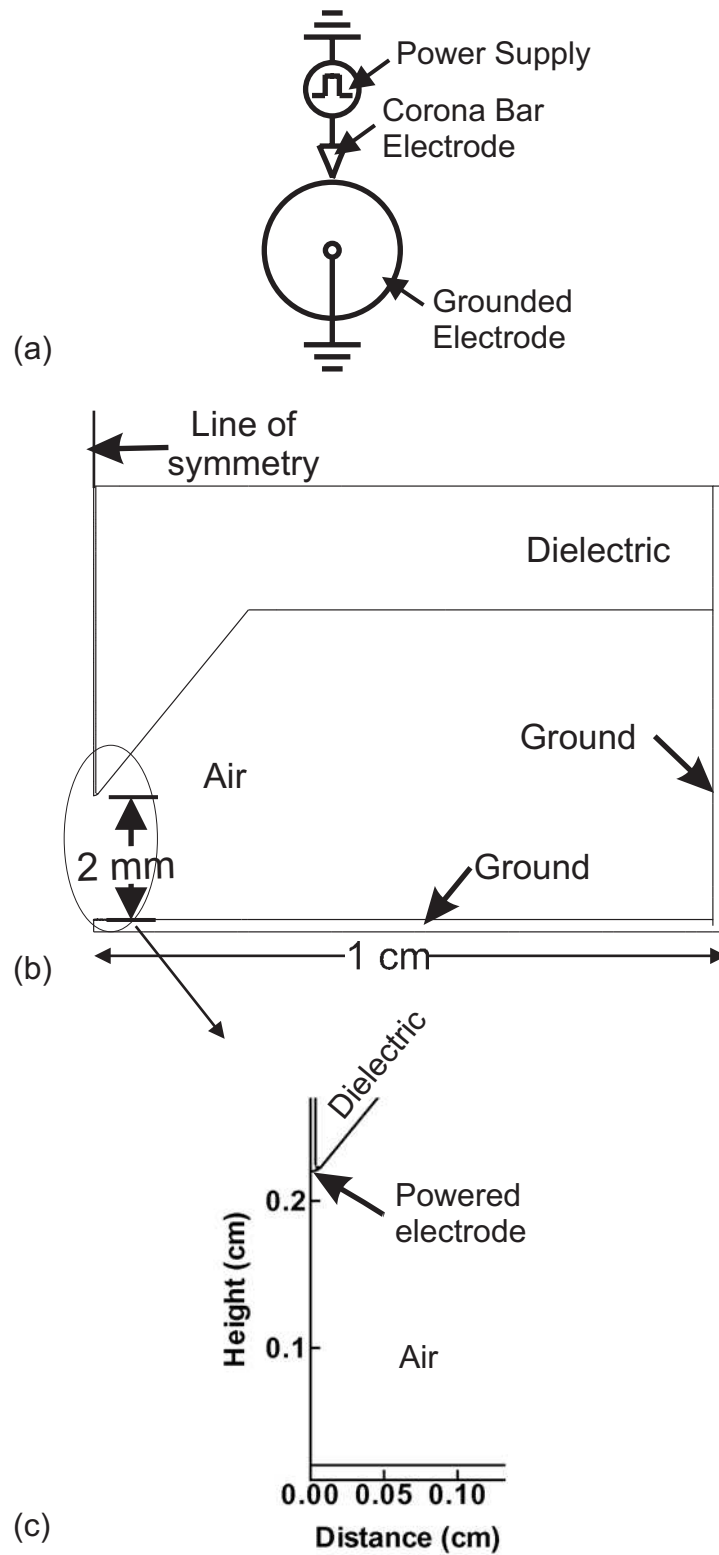


Fig. 9 (a) Schematic of a typical industrial corona device. (b) Cartesian symmetric representation of the discharge and (c) close-up view of the discharge zone.

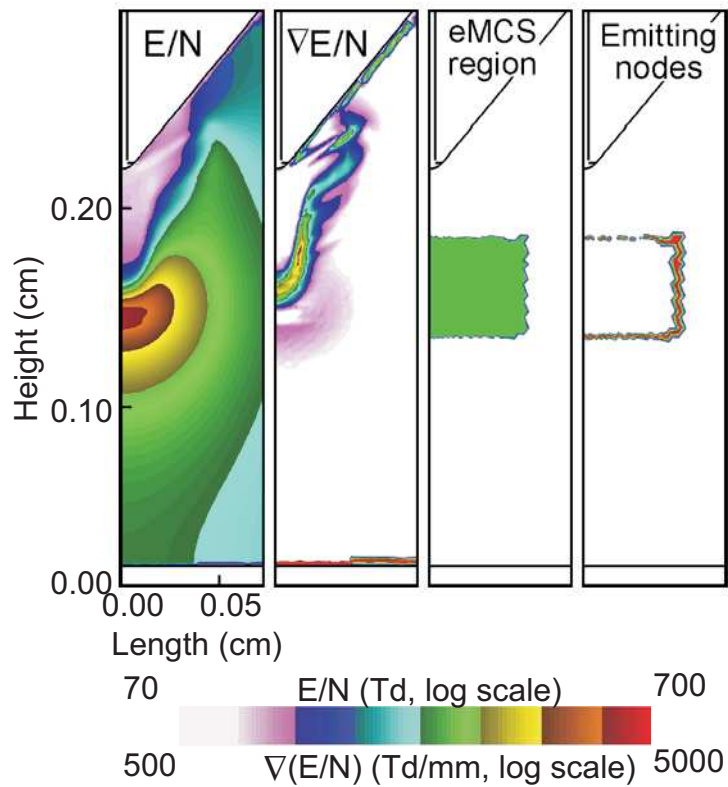


Fig. 10 Breakdown in positive corona discharge in air at atmospheric pressure with a 15 kV pulse. The ionization fronts is a region of high electric field magnitude and spatial gradients where possible non-equilibrium electron transport may occur. The eMCS algorithms track the ionization front as it evolves. Pseudoparticles in the kinetic simulation are released from the boundary of the eMCS region.

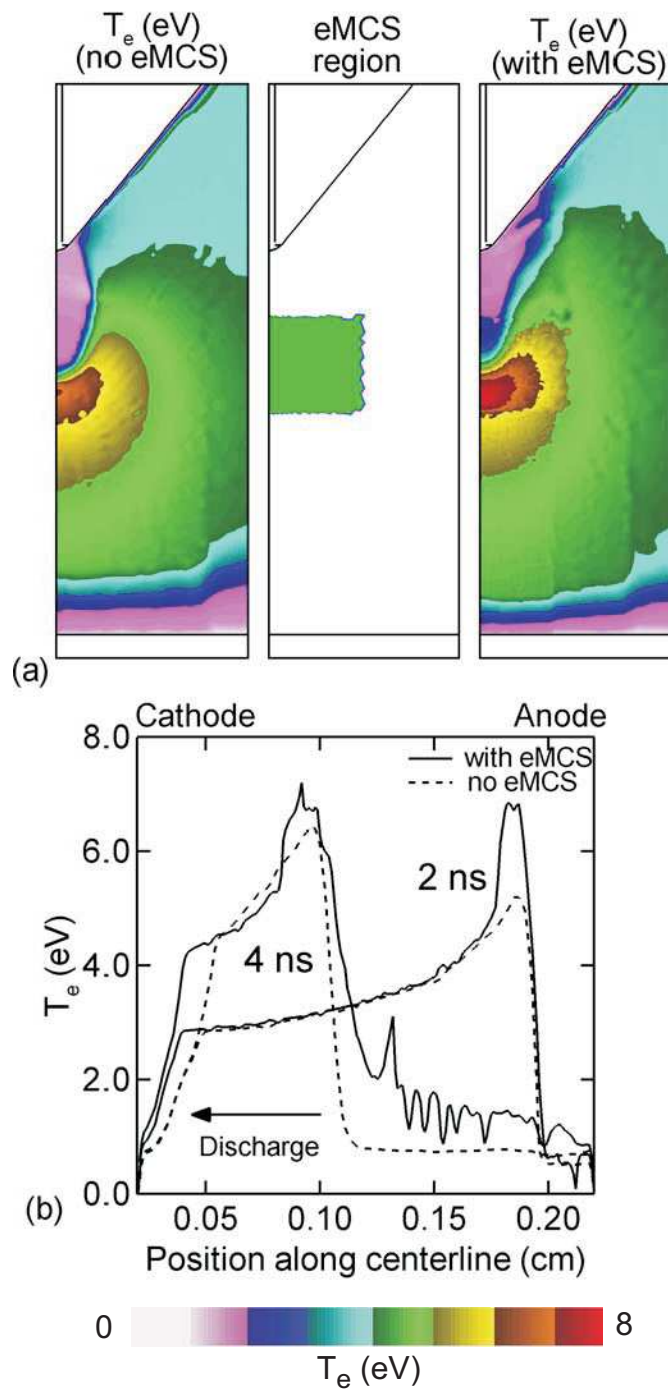


Fig. 11 Electron temperature calculated without and with the eMCS module during breakdown in air at 15 kV. A comparison of (a) spatial contours and (b) centerline values at different times during breakdown are shown. Electron temperature at the ionization front is about 1 eV higher when calculated with the eMCS module.

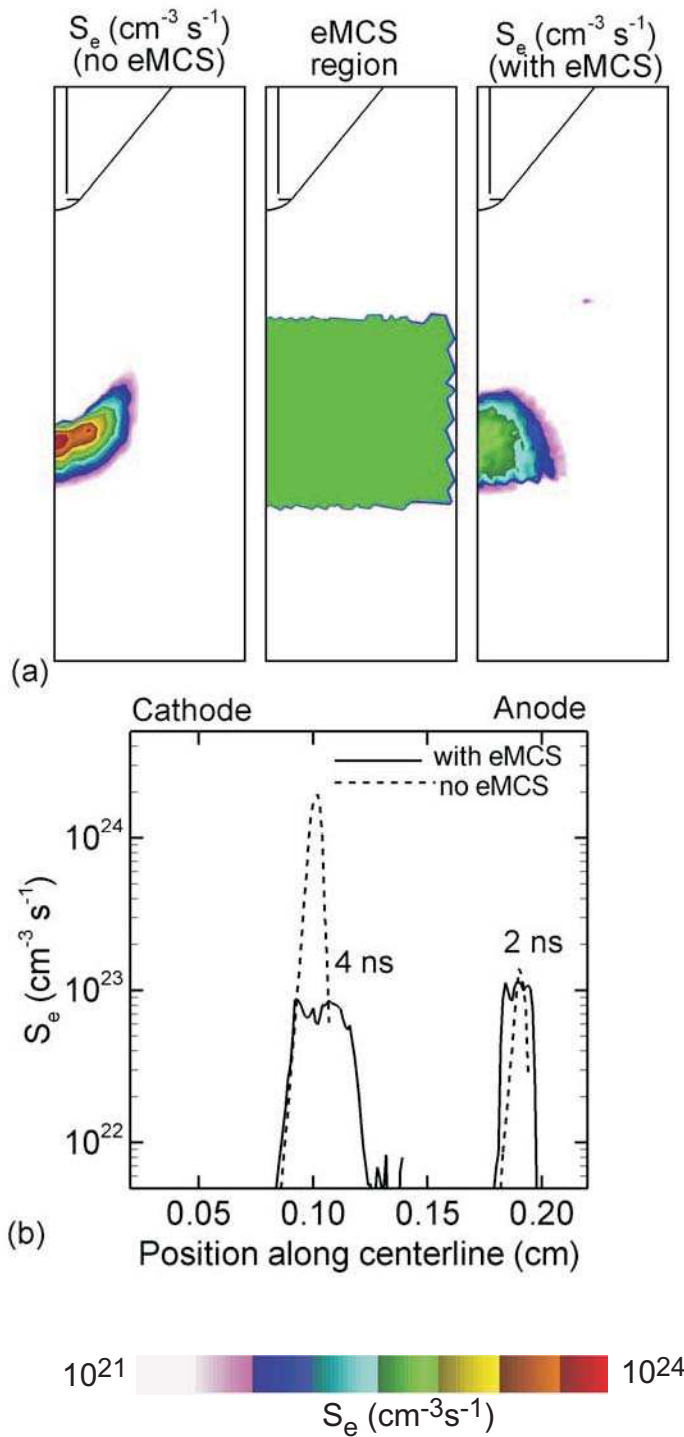


Fig. 12 Ionization sources calculated without and with the eMCS module during breakdown in air at 15 kV. A comparison of (a) spatial contours and (b) centerline values at different times during breakdown are shown. Ionization sources at the front are lower by upto a factor of 25 when calculated with the eMCS module.

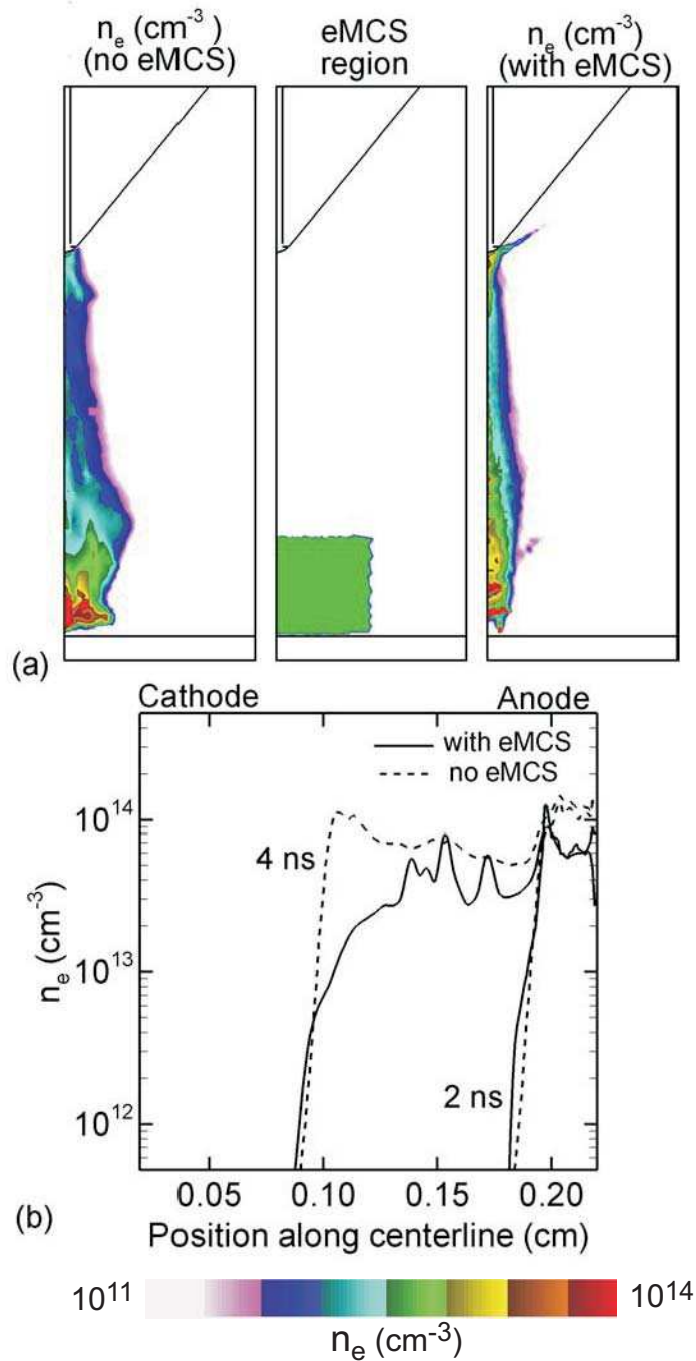


Fig. 13 Electron density calculated without and with the eMCS module during breakdown in air at 15 kV. A comparison of (a) spatial contours and (b) centerline values at different times during breakdown are shown. Electron density in the ionized channel is lower by upto a factor of 10 when calculated with the eMCS module and the channel is narrower.

4.7 References

1. D. B. Graves, IEEE Transactions on Plasma Science, **22**, 31 (1994).
2. D. J. Economou, Thin Film Solids, **365**, 348 (2000).
3. W. Z. Collison, T. Q. Ni and M. S. Barnes, Journal of Vacuum Science and Technology A, **16**, 100 (1998).
4. F. Massines, P. Ségur, N. Gherardi, C. Khamphan and A. Ricard, Surface and Coatings Technology, **174-175**, 8 (2003).
5. R. B. Gadri, IEEE Transactions on Plasma Science, **27**, 36 (1999).
6. T. J. Sommerer, W. N. G. Hitchon and J. E. Lawler, Physical Review Letters, **63**, 2361 (1989).
7. A. V. Phelps and L. C. Pitchford, Physical Review A, **31**, 2932 (1985).
8. D. Vendor and R. W. Boswell, IEEE Transactions on Plasma Science, **18**, 725 (1990).
9. M. Surendra, D. B. Graves and I. J. Morey, Applied Physics Letters, **56**, 1022 (1990).
10. U. Kortshagen, G. J. Parker and J. E. Lawler, Physical Review E, **54**, 6746 (1996).
11. A. N. Bhoj and M. J. Kushner, Journal of Physics D, **37**, 2510 (2004).

5. ATMOSPHERIC PRESSURE DISCHARGES IN SMALL SPACES

5.1 Introduction

The surfaces of many polymers used in specialized and high-value applications need to be chemically modified to impart desired properties such as wettability, adhesivity, permeability and reactivity. For instance, the surfaces of vascular prostheses [1], pharmaceutical powders [2], filtration membranes [3], 3-d scaffolds [4], artificial cornea and skin [5-6], polymer fibers [7-8] and other products with complex surface shapes need to be optimally processed to ensure reliable functionality. Low pressure plasmas operating at 100s mTorr, such as those used in the microelectronics industry, are commonly used for such treatments because of their efficacy and the minimal damage to the bulk material.

During plasma treatment, the surface to be treated may be placed downstream, away from the discharge where the reactive gas phase species are produced. During such 'remote' treatments, convective flow and diffusion transport processes bring these species to the surface where they undergo reactions.[9] The surface to be treated may also be placed within the discharge zone itself to react with locally produced radicals. This may be of advantage when it is required to treat the inner surfaces of complex shaped materials when radicals react before reaching the inner surfaces. In general, such treatment is straightforward when the presence of the surface in the discharge zone does not significantly feedback to disturb discharge characteristics, such as in the treatment of large rolls of polymer films or fibers in corona discharges.[7] Thicker materials when treated within the discharge zone can, however, alter plasma characteristics, which may impede the objective of locally producing the reactive species.

For example, polydimethylsiloxane (PDMS) is frequently used to make microfluidic devices such as micro-reactors [10] and diagnostics like lab-on-a-chip devices.[11] In more sophisticated applications, microfluidic channels may be patterned using masks to obtain spatial control over the degree of surface functionalization within the channel to develop of diagnostic assays.[12] These devices are a few 100s of μm thick and can have arrays of channels, each 10s μm in width, and the walls of these channels need to be treated to make them hydrophilic, for instance to support electro-osmotic flow, [13] or to implant specific chemical functional groups.[14] It is difficult to sustain plasmas at low pressure near or within these small spatial structures to locally generate reactive species, because of the pd scaling (pressure \times characteristic length dimension of device), which states that the product $pd = 1\text{-}10$ Torr-cm to sustain a discharge.

To satisfy the pd scaling, plasmas at these small dimensions must be generated at higher (closer to atmospheric) pressure. In such plasmas, the Debye length (λ_D) (the length scale over which the plasma may be non-neutral) may be similar to the characteristic length dimension d . In general, it is difficult to sustain a plasma if $\lambda_D > d$. The surface-to-volume ratio can be high enough that surface processes significantly influence the plasma properties. There is increased interest in the development of atmospheric pressure plasma based treatments of materials with complex surface shapes. For instance, atmospheric pressure dc microplasmas have recently been used in assembled microfluidic devices for the controlled chemical modification of the channel walls made of polystyrene [15] without the use of masks. Recently, Kurrat *et al*,[16] have demonstrated the production of atmospheric pressure plasmas within microchannels.

The uniform functionalization of high-value materials in a cost-effective manner will critically depend on the ability to produce atmospheric pressure plasmas near or within the small spaces enclosed by the surfaces of these materials. In this chapter, the dynamics of production of atmospheric pressure plasmas near and inside μm -sized channels of a plastic disk placed inside a corona-dielectric barrier discharge configuration are computationally investigated using the 2-d plasma hydrodynamics model described in Chapter 2. The extent of plasma propagation through these spaces is strongly influenced by their spatial dimensions and surface shapes.

Results from parametric studies of plasma dynamics near the disk surfaces including the effect of varying the channel width, the number of channels and their spacing, the surface contours of the channels, the thickness and location of the disk and the gas gap are presented. Under some conditions, such as the presence of a wide channel, the plasma propagates through the micro-channels generating significant gas phase radical densities inside them. In other conditions, such as in the presence of a thick disk, the discharge is unable to propagate through the channel.

5.2 Streamer Propagation through Microchannels

The Cartesian symmetric representation of the geometry used in these investigations is shown in Fig. 1. The discharge space consists of a powered electrode which lies along the centerline of symmetry enclosed in dielectric material and grounded metal surface on the remaining sides. The tip of the powered electrode is exposed to the processing gas as shown in Fig. 1(b). The gas gap between the powered electrode and the lower grounded surface is either 2 or 4 mm. The thickness of the plastic (dielectric) disk is varied from 100 – 1000 μm . The disk contains one or more channels or through-holes.

The position of the disk is either midway in the gas gap or on the grounded electrode.

In the base case, a 100 μm thick disk having a single 30 μm channel, located symmetrically across the centerline, is placed midway in the 2 mm gas gap. An unstructured mesh is overlaid on this geometry is shown in Fig. 1(c) and is refined in the channel and surrounding regions and near the powered electrode tip to adequately resolve the plasma. The total number of nodes is 6827 with 4041 nodes in the plasma. We look at the propagation of a negative streamer sustained in humid air of composition $\text{N}_2/\text{O}_2/\text{H}_2\text{O}=79/20/1$ with a -15 kV voltage of negligible rise time applied to the powered electrode.

The discharge is initiated at time $t = 0$ with a brief burst of electric field emission at the rough surfaces of the powered electrode creating a cloud of electrons around the cathode. Electrons move away from the cathode faster than the ions, creating a space charge region which develops into an ionization front. The ionization front moves towards the grounded anode and has a peak E/N of 600 Td as it crosses the gap as shown in Fig. 2. In the ionized gas above the disk, E/N falls below 60 Td, as the front passes across the disk at 1 ns. The temporal evolution of electron temperature, T_e , in the discharge is shown in Fig. 3. The maximum T_e at the ionization front is 6-7 eV at 0.25 ns. The dynamics of electron impact ionization sources, S_e , are shown in Fig. 4. S_e peaks at the ionization front as it propagates through the gas gap.

When the front strikes the upper disk surface, it begins to collapse. This is because the dielectric disk surface acts as a capacitor and starts to charge up. Electrons at the ionization front are quickly lost to the surface. There is rapid reduction in E/N and T_e as a result around 0.75 ns, resulting in a net loss of electrons decreasing S_e . The density

of electrons and the total positive ion density increases in the ionized gas behind the front as shown in Figs 5 and 6. The plasma density near the powered cathode is 10^{14} cm^{-3} . The plasma spreading horizontally above the upper dielectric surface produces a density of 10^{12} cm^{-3} . The density of O atoms is shown in Fig. 7 and it tracks the evolution in the plasma density.

The dynamics of E/N and T_e near the channel are shown in Fig. 8 and 9 respectively. E/N does not increase significantly as the avalanche enters at the top of the channel, since charge lost to the surface decreases field enhancement. The peak T_e in the channel is about 2-3 eV. Ionization sources near the channel are shown in Fig. 10. Ionization sources are about $10^{21} \text{ cm}^{-3}\text{s}^{-1}$ as the avalanche approaches the upper disk surface. Once the plasma enters the channel, ionization sources increase to $10^{23} \text{ cm}^{-3}\text{s}^{-1}$. But as the plasma moves further into the channel, sources diminish rapidly above the disk because the rest of the ionization front collapses at this time. In the channel, sources momentarily decrease to $10^{22} \text{ cm}^{-3}\text{s}^{-1}$ at 0.8 ns.

Plasma density increases to 10^{13} cm^{-3} in the channel as the front moves through at 0.7 ns, as shown in Fig. 11 and 12. The electrons being lighter move faster than the ions creating a negative space charge in the channel. Electrons are also lost to the walls, negatively charging them. The evolution of negative and positive surface charge on the channel walls are shown in Fig. 13. The walls of the channel are negatively charged to 10s of $\mu\text{C cm}^{-3}$ as the plasma moves down through the channel. The electrons present in the channel drift towards the channel exit. The plasma density is sufficiently high to seed electrons for the launch of a second streamer from the bottom of the channel aided by electric field enhancement with E/N of 400-500 Td at 0.85 ns. Ionization sources increase

to $10^{24} \text{ cm}^{-3}\text{s}^{-1}$ below the channel and a new ionization front re-emerges.

Electron density increases below the disk as the new streamer propagates below the disk and closes the gap at 1.4 ns. At this time, T_e momentarily reduces in the absence of ionization fronts. Soon, a third ionization front develops, this time for a cathode-directed return strike beginning at 1.7 ns and propagates back through the channel. During the return strike, E/N below the disk decreases to 300 Td, but is restored to higher magnitudes above the disk. Ionization sources peak at locations on this front as well. Unlike the first ionization front the returning front separates into two regions during the return strike as it encounters the disk. One region stays below the disk where large ionization sources are generated increasing electron density to 10^{14} cm^{-3} . Another portion detaches itself and moves back through the channel towards the cathode at 1.95 ns.

The detached front comprises a region of high T_e (7–8 eV) and produces large transient sources of $10^{25} \text{ cm}^{-3}\text{s}^{-1}$ in the channel, as it passes through. The plasma density in the channel rises to 10^{15} cm^{-3} . After the return strike has passed, T_e in the channel is about 4 eV. A sheath-like region with an E/N of about 800-1000 Td forms near the channel walls by 1.85 ns as the electron density next to the wall reduces exponentially. By contrast, significant density of positive ions is present next to the wall. The higher positive ion fluxes neutralize the accumulated negative charge and begin to positively charge the channel wall surfaces by 1.95 ns. The density of O atoms is shown in Fig. 14 near the channel. The return strike increases the O atom density to 10^{15} cm^{-3} .

5.3 Effect of Microchannel Characteristics on Discharge Propagation

The effect of channel width on the propagation of the negative streamer was examined. T_e , S_e and electron density are shown in Fig. 15 for channel widths of 10 μm ,

30 μm and 50 μm keeping a constant disk thickness of 100 μm after gap closure has occurred in the 50 μm case. In all cases where the channel is placed symmetrically about the axis, one-half the width is indicated on the figures. T_e and S_e are similar in all cases, however, the propagation time is higher for the 10 μm channel width. The electron density below the disk is also lower in this case. Charge accumulation on the microchannel surfaces and the density of electrons and O atoms are shown in Fig. 16. Electron density in the channel is about 100 times larger with the 50 μm channel because of lower diffusion losses to the walls and leads to higher O atom density. Charge on the 10 μm wide channel walls is similar to the 30 μm case for different reasons. In the 10 μm channel, the initial rate of surface charging is higher resulting in low electron densities entering the channel and consequently lower wall charging. With the 30 μm channel, higher positive ion fluxes neutralize and reduce the negative charge accumulation on the walls.

When the thickness of the disk is increased to 500 μm , dramatic changes occur in the ability of the discharge to propagate through the channel. T_e , S_e and electron density are shown in Fig. 17 after gap closure in the 50 μm case for channel widths of 10 μm , 30 μm and 50 μm located symmetrically along the axis with a constant disk thickness of 500 μm . No plasma penetration occurs in the 10 μm case and the discharge is fully confined to the gap above the disk surface. But with larger channel widths, discharge propagation through the channels continues to occur, with the plasma density below the disk reduced by a factor of 2-3 compared to the base case conditions.

Surface charge, electron and O atom density near the channel are shown in Fig. 18. The plasma density above the disk, on the other hand, increases because the effective

E/N in the gap above the disk surface increases resulting in larger ionization sources and plasma density. The plasma density inside the 10 μm channel is negligible and surface charge is restricted to the upper portions of the channel wall surface. At higher channel widths, the electron and O atom density in the channel increase.

The plasma conditions after gap closure for a disk placed in the middle of the gap with a thickness of 1000 μm and channel widths of 30 μm and 50 μm are shown in Fig. 19. The reduced gap between the upper disk surface and the powered electrode increases E/N, producing higher ionization sources than with the 500 μm thick disk. The discharge propagates through the channel in both these cases. Ionization sources of $10^{23} \text{ cm}^{-3}\text{s}^{-1}$ and plasma density of $10^{12}\text{-}10^{13} \text{ cm}^{-3}$ are produced below the disk. The electron density above the disk is shown in Fig. 20 and is about $7 \times 10^{13} \text{ cm}^{-3}$, 2 times higher than with the 500 μm disk. The maximum surface charge on the inner channel wall is $6 \mu\text{C cm}^{-3}$ and $3 \mu\text{C cm}^{-3}$ in the 30 and 50 μm channels respectively. More charge is removed from the plasma in the smaller channel, leading to a lower plasma density.

The effect of the gas gap was investigated by increasing it from 2 to 4 mm. The 1000 μm disk with the 50 μm channel was placed midway in the discharge. T_e , S_e , and electron density for this case is shown in Fig. 21(a). In contrast to the 2 mm gap (Fig. 19(c)), the discharge here barely penetrates the channel. Doubling the gas gap in effect reduces E/N by a factor of 2 at the same applied voltage, which results in lower T_e , ionization sources and electron density. The few electrons that do enter the channel charge the inside wall upto $20 \mu\text{C cm}^{-3}$, mostly near the upper portion of the wall (Fig. 22(a)).

When the channel is widened to 100 μm (Fig. 21(b)) the plasma propagates into

the channel, though the plasma density of 10^{10} - 10^{11} cm^{-3} below the disk is still relatively low. Much of the plasma is confined above the disk surface with a density of 10^{12} cm^{-3} . In this case, surface charging occurs all along channel wall due to electrons lost from the plasma. The density of electrons and O atoms in the channel is 10^{12} cm^{-3} 10^{13} cm^{-3} respectively (Fig. 22(b)).

The effect of disk position was examined by repositioning the disk with the 100 μm channel on the grounded electrode. The gap width is still 4 mm and the plasma properties for this case after gap closure are shown in Fig. 21(c). As a result of repositioning the dielectric disk, the effective E/N between the powered electrode and the upper disk surface is reduced. This decreases T_e and ionization sources in the gap above the disk surface leading to a lower electron density of 10^{12} cm^{-3} . The discharge spreads along the upper surface of disk in this case and propagates into the 100 μm channel charging the wall (Fig. 22(c)). Within the channel, the density of electrons is 10^{11} cm^{-3} , while the density of O atoms is 10^{12} cm^{-3} .

The propagation of the negative streamer in the presence of multiple channels was investigated by having 3 channels in a 100 μm thick disk placed midway in a 2 mm gas gap and the plasma properties after gap closure are shown in Fig. 23. The widths of the channels starting with the one of the axis are 10 μm , 15 μm and 25 μm in the first case shown in Fig. 23(a) and 10 μm , 30 μm and 30 μm respectively in the second case and they are spaced 80 – 100 μm apart as shown in Fig. 23(b). The plasma penetrates only slowly through the channels in the disk, as significant charge is removed from the streamer to charge the inner walls of the structure that have large surface-to-volume ratios. As the plasma emerges through the channel exits, new smaller streamers are

initiated by electric field enhancement at the end of the channel. These new streamers merge further downstream. The discharge propagates through all channels in both the cases but though the plasma characteristics above the disk are similar, they differ markedly below the disk. The ionization sources and electron density below the disk are higher in the second case being concentrated in the region near the middle (30 μm) channel.

The plasma characteristics near the disk are shown in detail for both the cases in Fig. 24. In the first case, the electron density is comparatively higher inside the largest (25 μm) channel than in the others. In the presence of channels of differing widths, the discharge preferentially propagates through the wider channel, though it is farthest from the axis. The electron density and O atom density inside the channel are 10^{11} - 10^{12} cm^{-3} . In the second case, the ionization sources peak in the middle (30 μm) channel (10^{24} $\text{cm}^{-3}\text{s}^{-1}$) and the plasma density is comparatively higher (10^{13} cm^{-3}). The presence of a wider (30 μm) channel closer to the axis leads to the concentration of ionization sources here, though a similar channel lies further away from the axis. Larger channels have lower surface-to-volume ratios, removing lesser charge from the discharge due to charging. This lowers the impedance of the channel and the discharge prefers this path.

The width of the channel on the axis was increased to 20 μm and the width of other channels was set to 10 μm while the inter-channel spacing was increased to 100 μm . Plasma characteristics after gap closure are shown for this case in Fig. 25. The larger channel on the axis offers lower impedance to the plasma and the discharge preferentially propagates through this channel. The reverse strike also occurs through this channel by the time the streamer propagates downward through the second channel.

The outer lying channels are high impedance paths and there is no plasma inside those channels.

Next, the inter-channel spacing was reduced to between 30-70 μm , allowing the streamer to choose from many possible paths. The plasma propagates through more than one channel in this case as shown in Fig. 26. The streamer splits above the disk and successfully transits through the channels closer to the axis before rejoining below the disk. Note that the plasma is unable to penetrate through the outer channels where the bulk plasma density is lower. This is due to the smaller current density available at the outer radius to charge the dielectric. As the plasma attempts to penetrate through the outer channels it is essentially extinguished. The plasma then seeks the lower impedance path towards the anode which is around the disk in spite of the path length being longer.

It may be necessary, at times, to produce plasmas inside spaces that may not have planar shapes. To investigate the effect of channel structure on the plasma propagation, the vertical nature of the channels was modified to be non-planar and tortuous. The plasma properties for discharge propagation through these curved channels are shown in Fig. 27. In the first case (Fig. 27(a)), the disk thickness is 100 μm in the second (Fig. 27(b)) 200 μm with a more tortuous channel path. The widths of the channels are 20 μm and 30 μm respectively and they are spaced 80 μm apart in both cases. The discharge propagates through the disk in the first case creating ionization sources of $10^{23} \text{ cm}^{-3}\text{s}^{-1}$ and plasma density of 10^{13} cm^{-3} below the disk, but it does not in the second case.

Plasma properties near the disk are shown in Fig. 28 for both these cases. In the first case, the plasma density is higher in the 30 μm channel, due to lower rate of surface charging, which enables it to seed a streamer at the channel exit. In the second case, the

discharge is unable to propagate through either channel. Whereas surface charging stops the plasma propagation in the narrower 20 μm path, electrons are unable to reach the exit of the wider channel because of opposing electric fields along the curvature of the channel near the exit.

The effect of varying microchannel characteristics on radical densities was examined. The peak density of O atoms along the centreline axis after the discharge is established is shown as a function of the microchannel radius and disk thickness in Fig. 29(a) and (b) respectively. The peak density of O atoms is lower at a smaller radius of 5 μm due to higher surface charging. At a larger radius of 25 μm , the field enhancement in the channel is reduced. Therefore, intermediate channel radius of 15 μm results in higher O atom densities. With 100 μm disk thickness, the density of O atoms peaks in the centre of the discharge. As the thickness is increased to 500 μm , the discharge propagates through the channel and O atom densities are lower and peak below the disk. When the disk thickness is increased further to 1000 μm , the discharge finds it difficult to propagate in the channel. In this case, peak O atom densities are found above the disk.

5.4 Concluding Remarks

The propagation of negative streamers in a humid air corona configuration in the presence of a plastic disk containing one or more microchannels was investigated. A variety of configurations were examined by varying the disk thickness, channel width, number of channels and their curvature. It was found that the plasma propagates easily through wider channels and through disks with lower thickness. The streamer will, in general, seek the lowest impedance path which is determined by the surface-to-volume ratio of the channel. This may result in plasmas not penetrating into smaller gaps that

have high impedances. The curvature of the channel significantly affects plasma propagation within the channel. In general, it may not be possible to have discharge propagation through porous spaces in materials where such arbitrary paths may be present. It may be possible to optimize the density of radicals generated within the microchannels by varying its dimensions.

The success using of atmospheric pressure plasmas and coronas in particular, to functionalize the surfaces of high value materials will depend on how uniformly the surface can be processed. One important aspect of this process is how the plasma behaves in and around small spaces. The interaction of these transient plasmas and streamers in particular, with small spaces is acutely affected by the dynamics of charging of the surfaces. Removal of charge from the streamer to charge these surfaces can significantly affect the dynamics of the streamer.

5.5 Figures

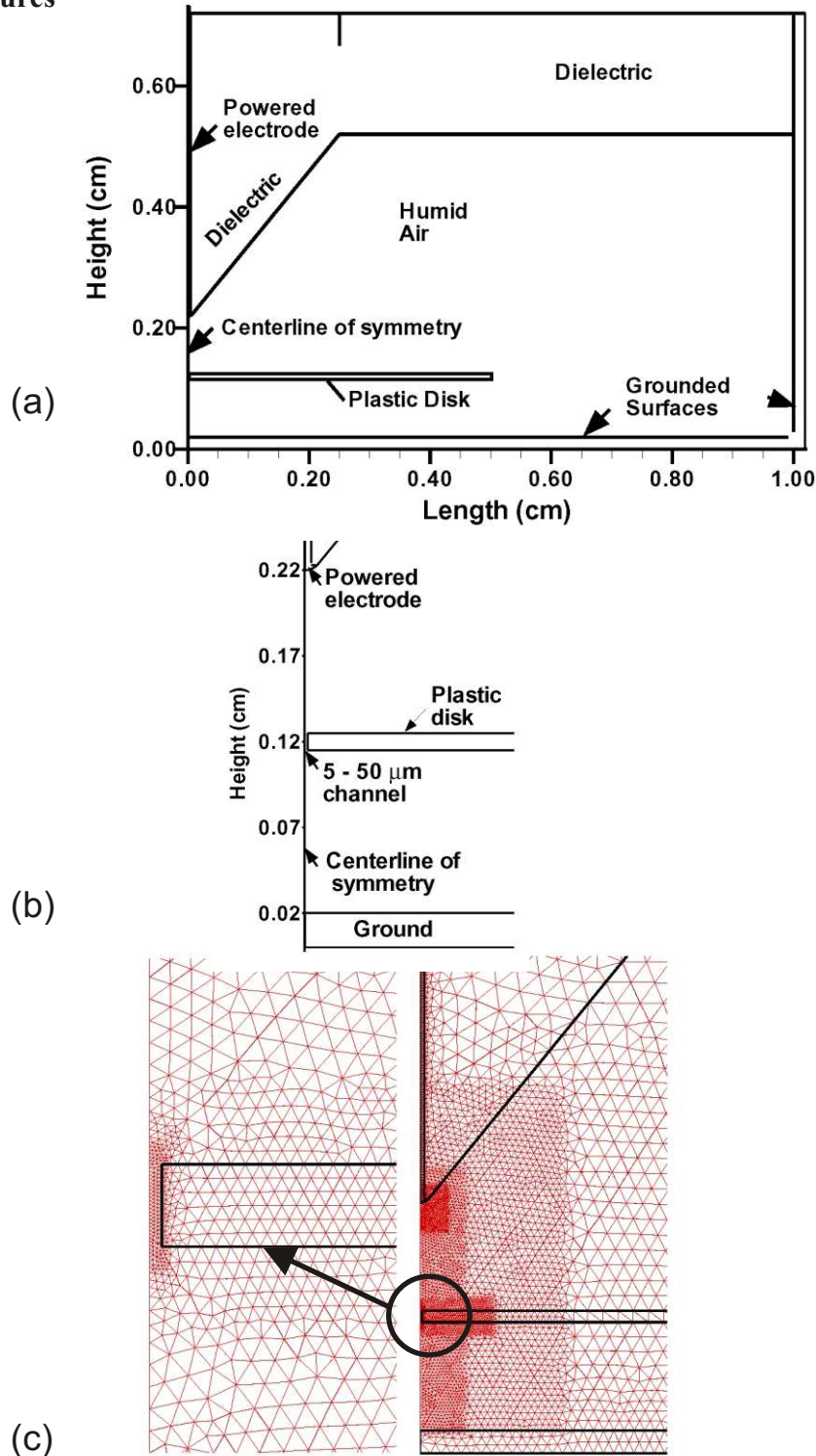


Fig. 1 A Cartesian symmetric representation of the discharge. (a) A plastic disk of 100s μm thickness having one of more μm -sized through-holes or channels is placed in the gap of a negative corona configuration. (b) Channel widths are varied from 10 - 100 μm . (c) An unstructured mesh is used with refinement zones to resolve plasma in the channels.

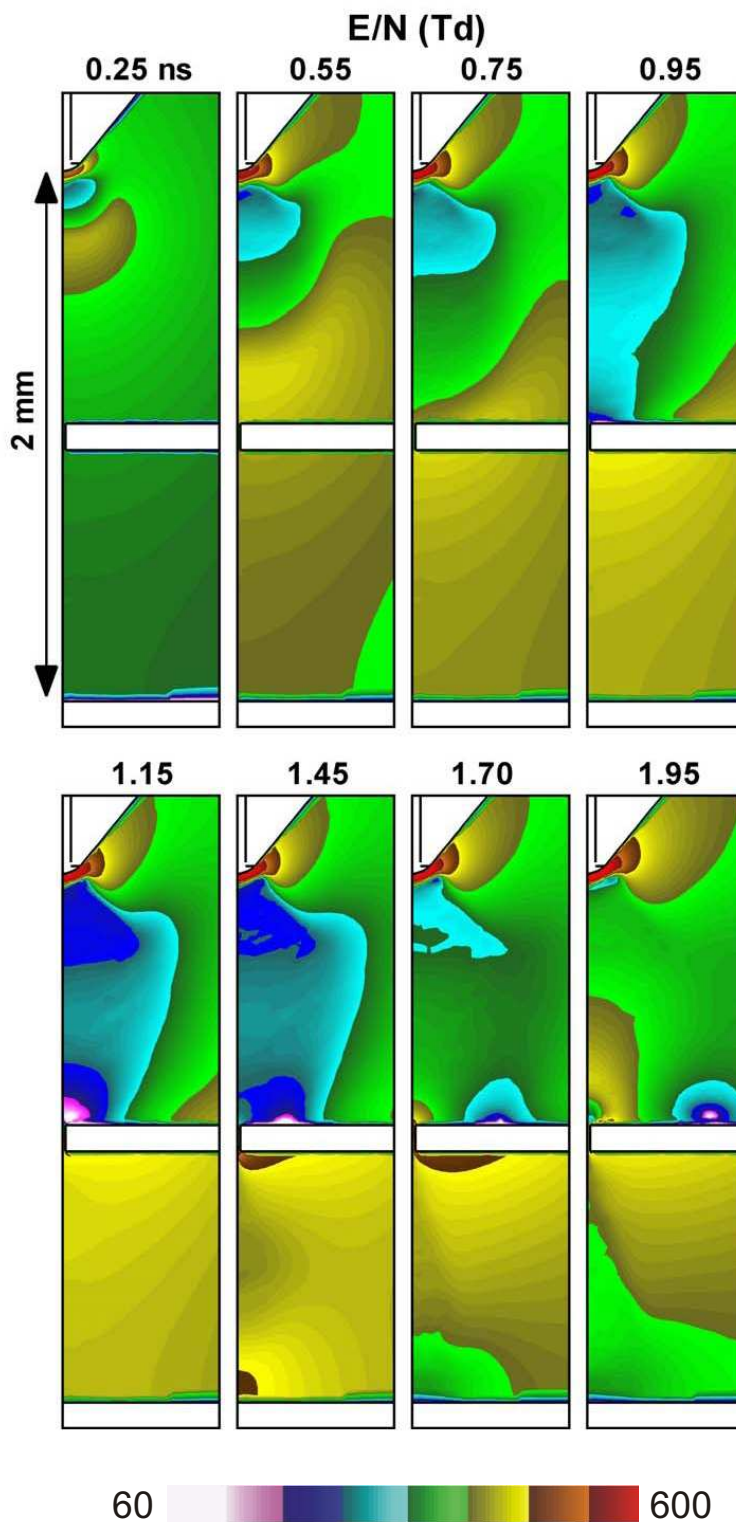


Fig. 2 Temporal dynamics of E/N (log scale) during breakdown in the base case configuration which is a -15 kV negative corona in humid air at atmospheric pressure. A dielectric plastic disk 100 μm thick having a 30 μm wide channel is placed symmetrically midway in the 2 mm gas gap. The ionization front located near the peak in E/N moves past the disk and separates, with a region of high E/N remaining on the underside of the disk.

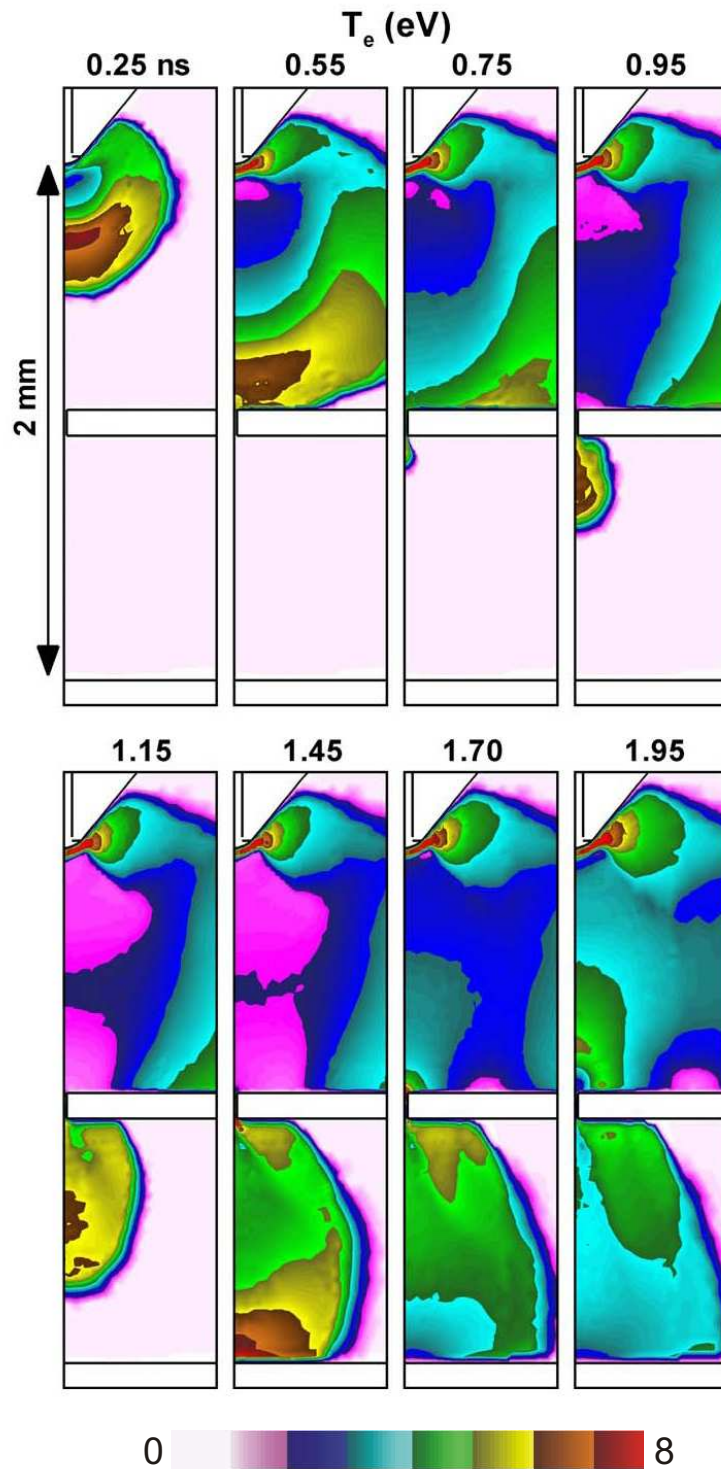


Fig. 3 Temporal dynamics of electron temperature during breakdown in the base case configuration. The peak in T_e at the front collapses as it strikes the upper surface of the disk, but returns as the front squeezes downwards through the microchannel.

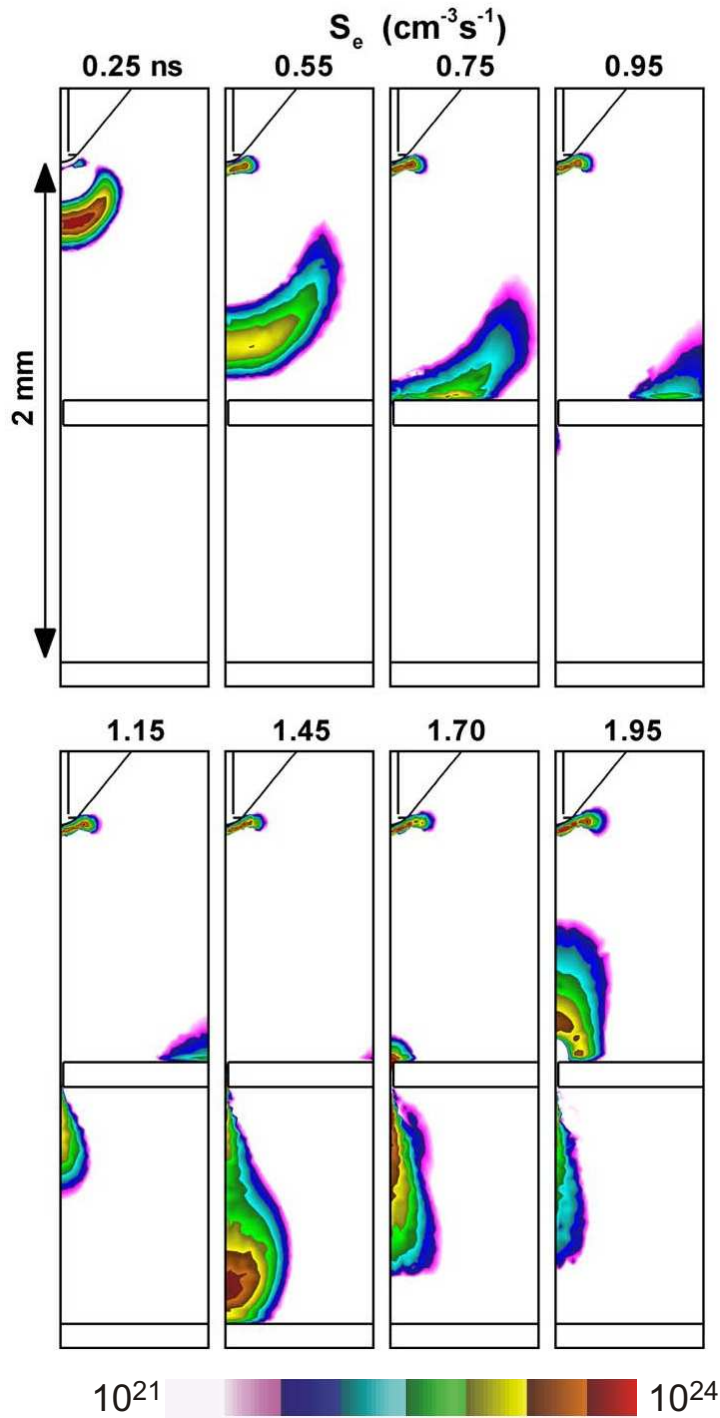


Fig. 4 Temporal dynamics of electron impact ionization sources (log scale) during breakdown in the base case configuration. Sources peak at the front and spread as the front strikes the upper surface of the disk. The front squeezes downwards through the microchannel and strikes the bottom grounded surface after which a cathode-directed reverse strike occurs.

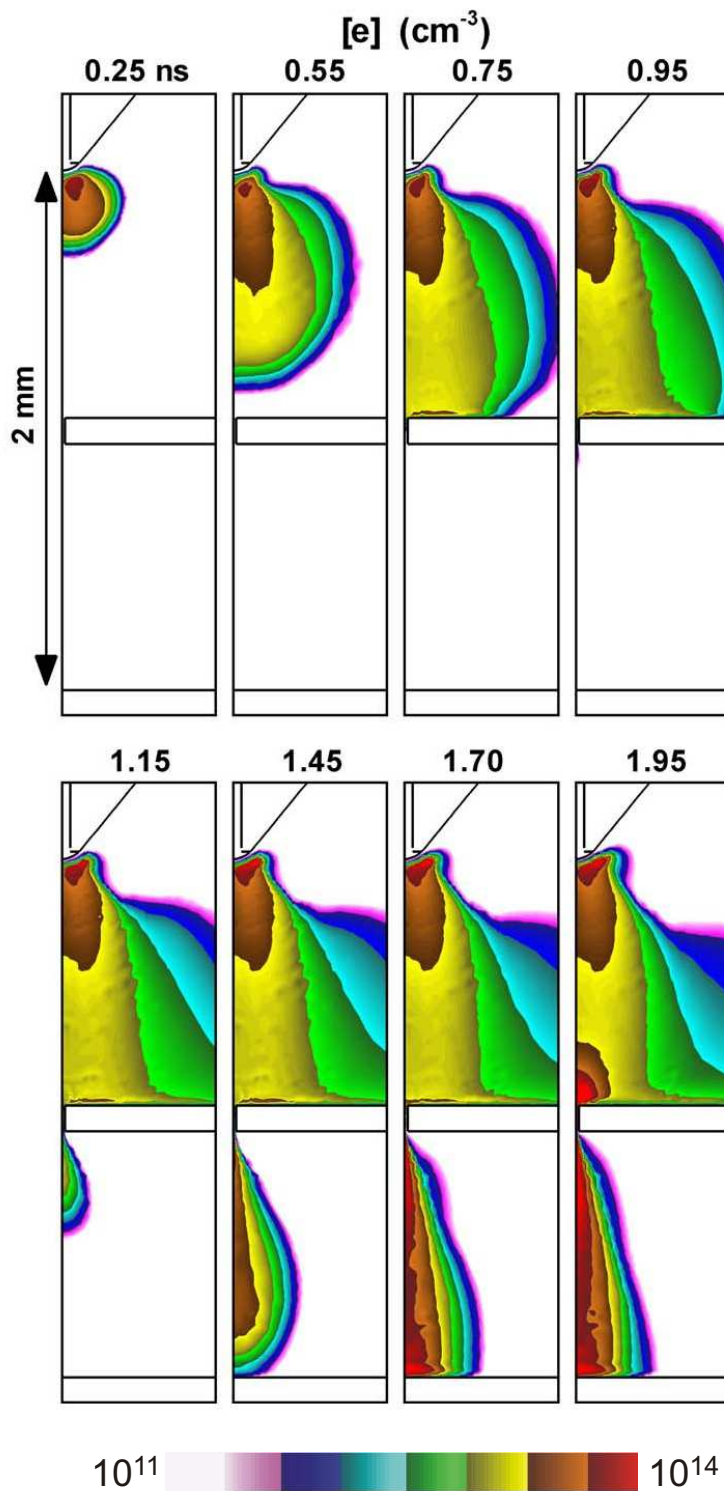


Fig. 5 Temporal dynamics of electron density (log scale) during breakdown in the base case configuration. The plasma spreads as it strikes the upper surface of the disk, and follows the front as it squeezes downwards through the microchannel. The plasma density below the disk is higher.

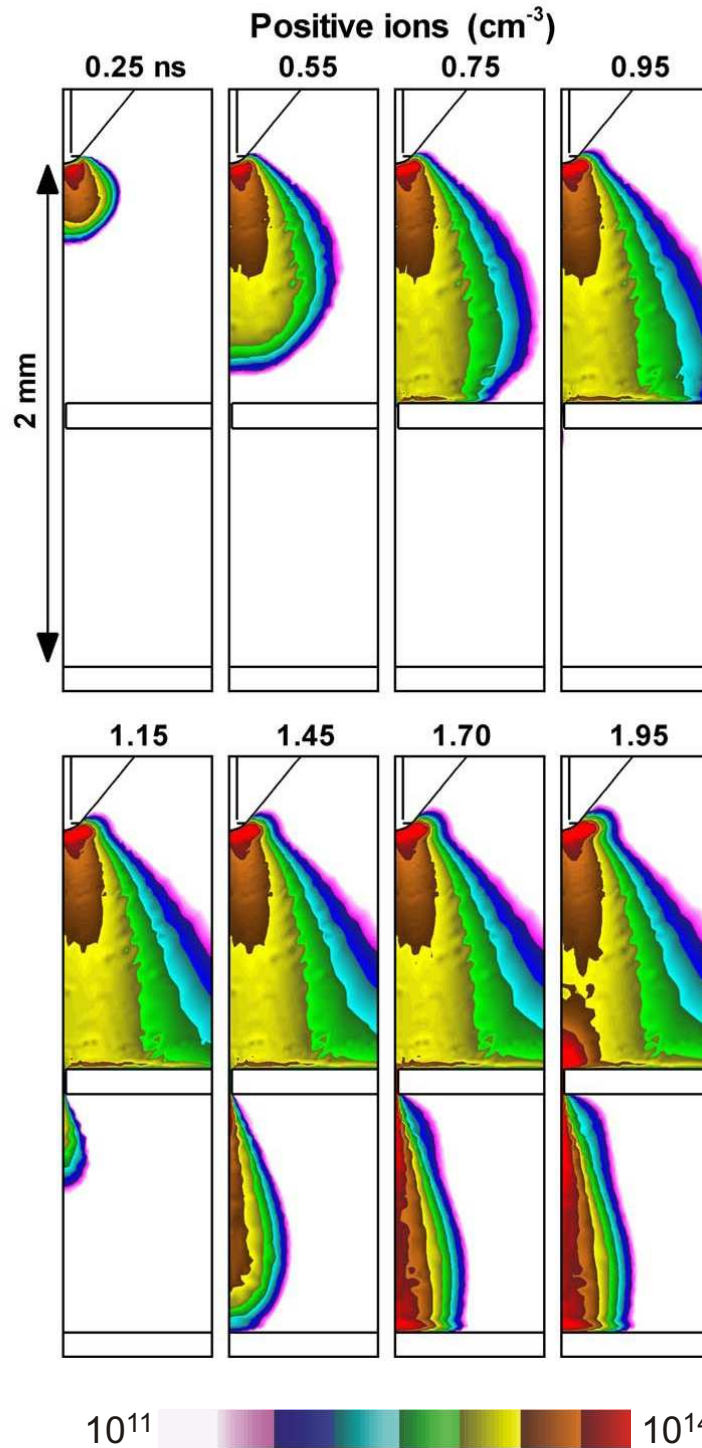


Fig. 6 Temporal dynamics of the total positive ion density (log scale) during breakdown in the base case. The plasma spreads as it strikes the upper surface of the disk, and follows the front as it squeezes downwards through the microchannel.

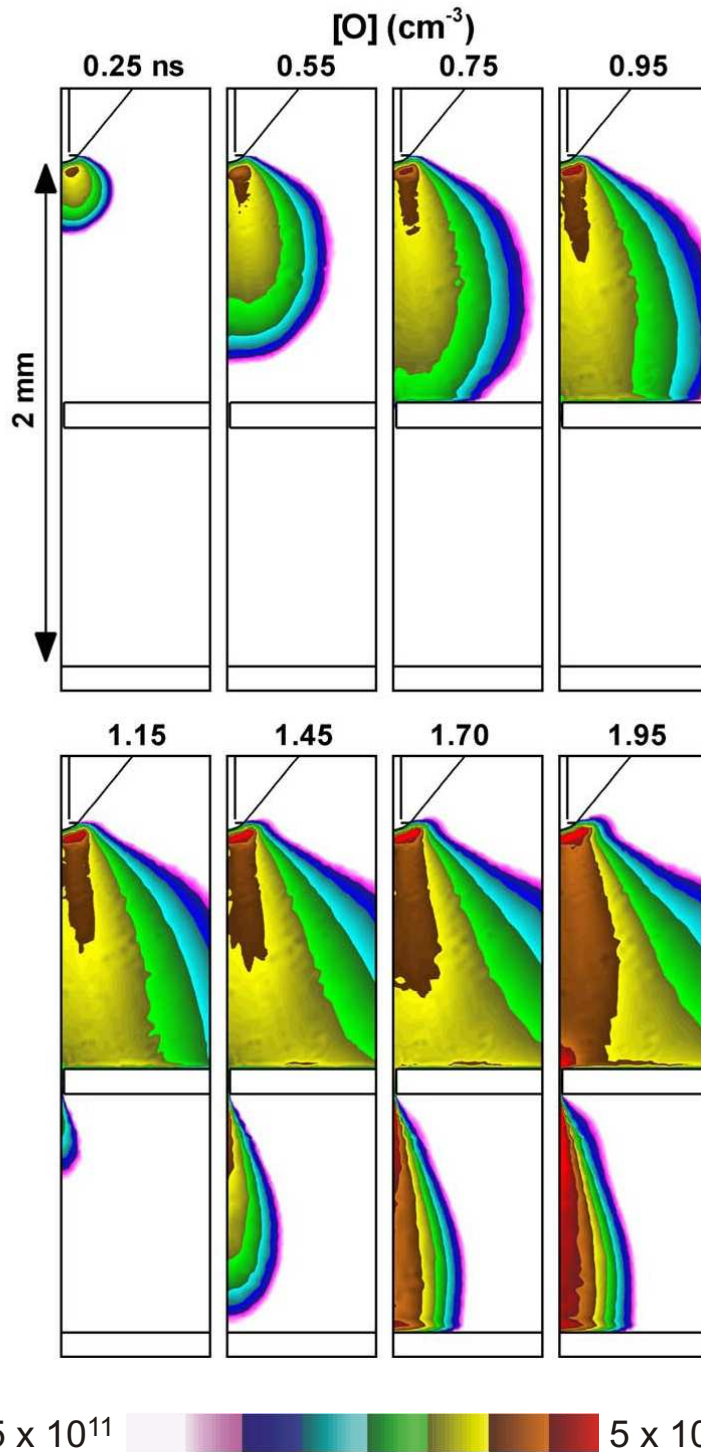


Fig. 7 Temporal dynamics of O atom density (log scale) during breakdown in the base case configuration. Density of O atoms is 10^{14} cm^{-3} above the disk where the discharge spreads. During thereverse strike, the density below the disk also increases to 10^{14} cm^{-3} .

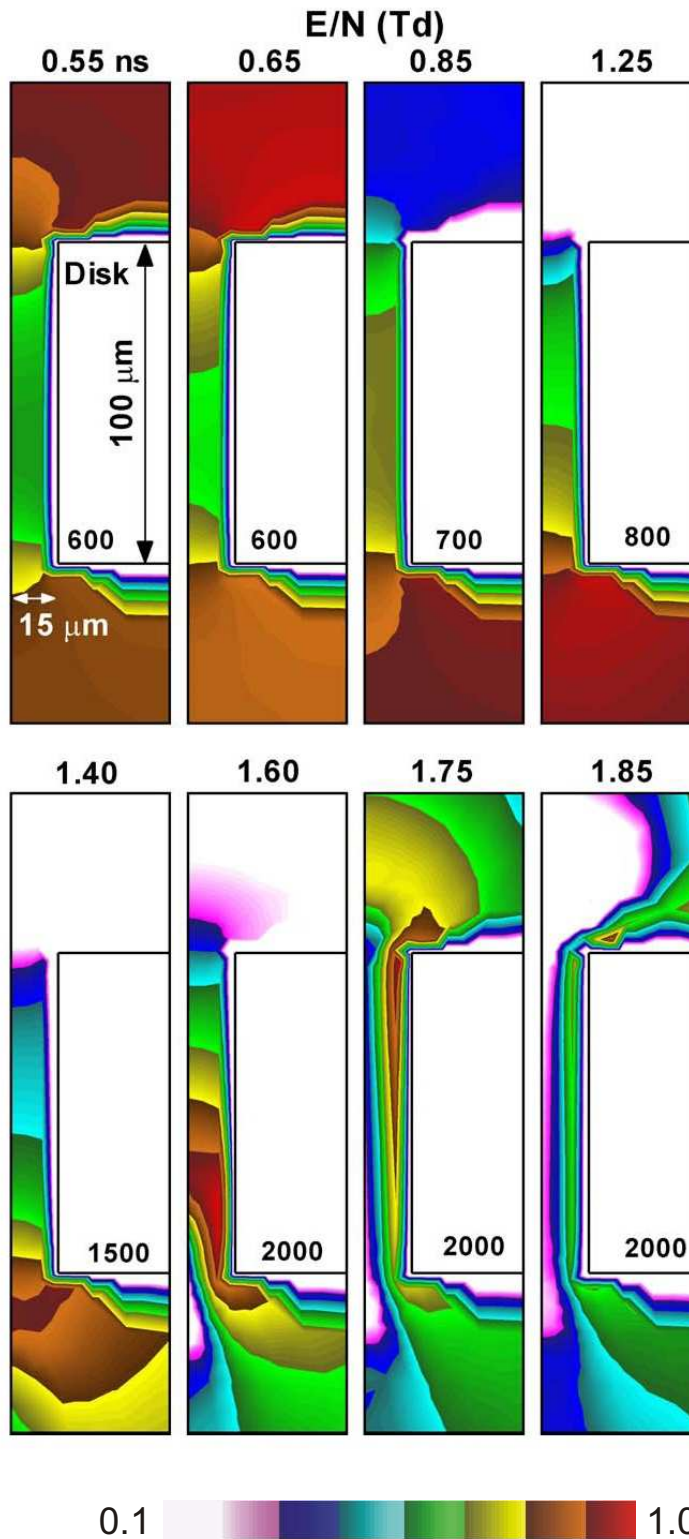


Fig. 8 Temporal dynamics of E/N (log scale) during breakdown in the base case configuration. When the front passes downwards, the peak E/N is about 400 Td in the channel. During the return strike, a front of E/N of 2000 Td passes through leaving a sheath-like region around the surface of the disk. Maximum values on 1-decade plots are indicated.

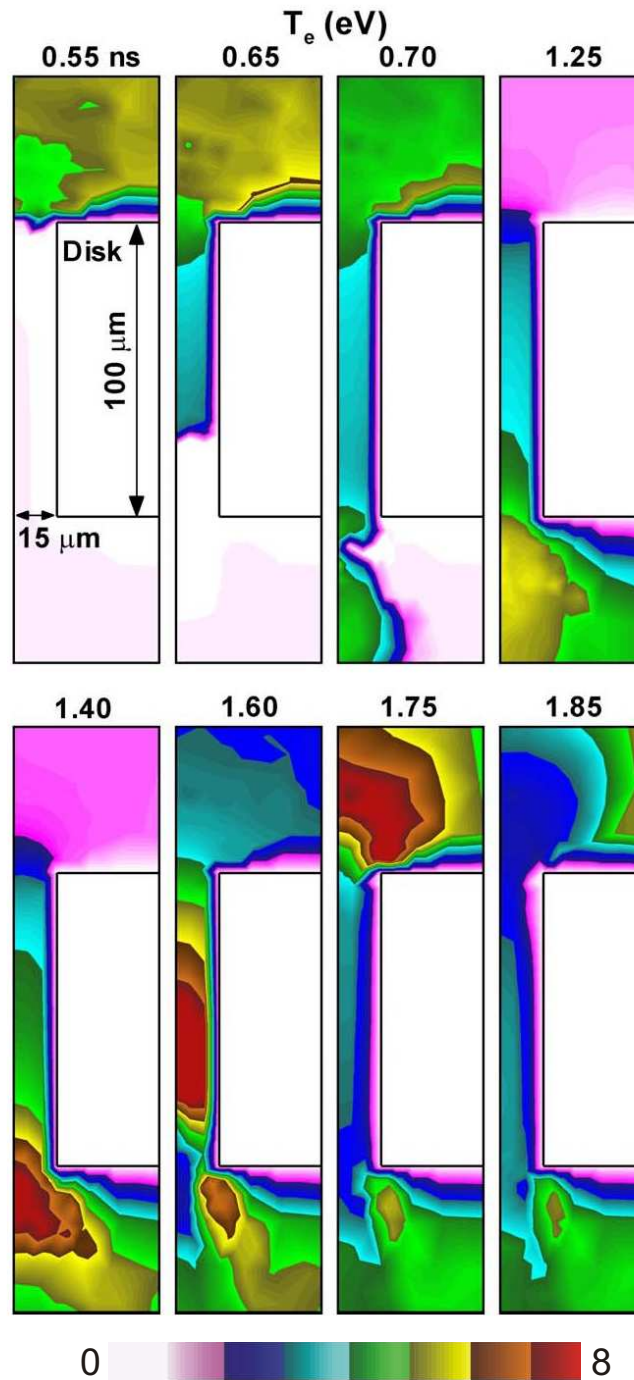


Fig. 9 Temporal dynamics of electron temperature near the disk during breakdown for the base case conditions. T_e is 2-3 eV in the channel as the avalanche propagates down at 0.7 ns. During the reverse strike, T_e in the channel momentarily increases to 6-7 eV as the avalanche passes.

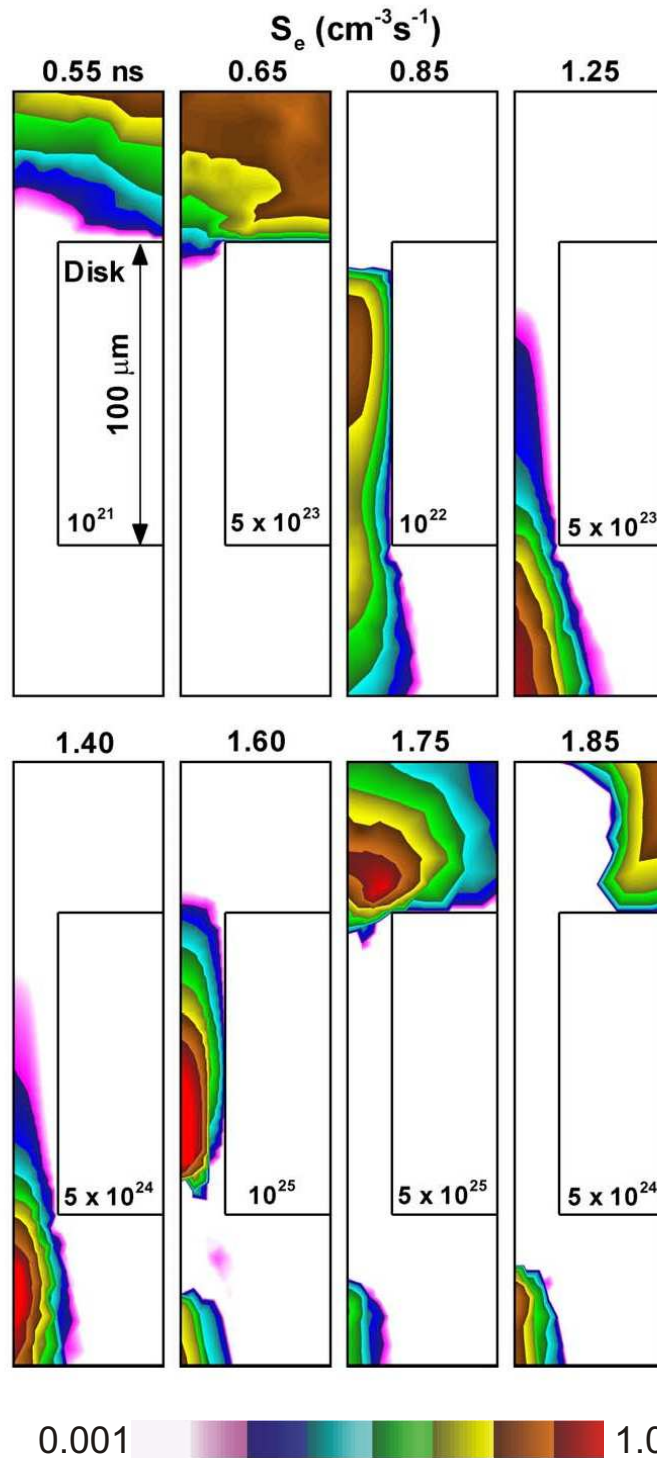


Fig. 10 Temporal dynamics of electron impact ionization sources (log scale) during breakdown in the base case. Ionization sources of $10^{22} \text{ cm}^{-3}\text{s}^{-1}$ in the channel aid the downward propagation of the avalanche. During the reverse strike, sources of $10^{25} \text{ cm}^{-3}\text{s}^{-1}$ are formed momentarily in the channel. Maximum values on the 3-decade plots are indicated.

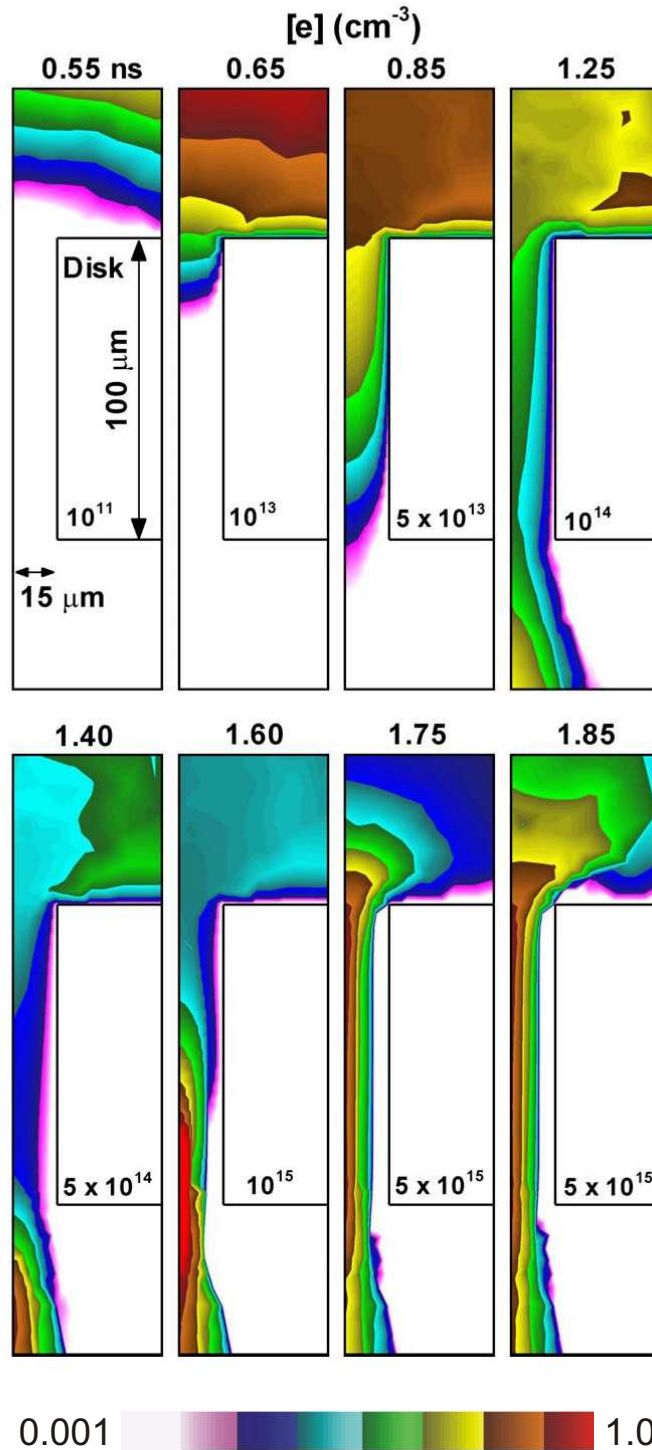


Fig. 11 Temporal dynamics of electron density (log scale) during breakdown for the base case. Electron density is 10^{13} cm^{-3} in the channel as the avalanche propagates downward. During the reverse strike, peak electron density rises to 10^{15} cm^{-3} in the channel. Maximum values on 3-decade plots are indicated.

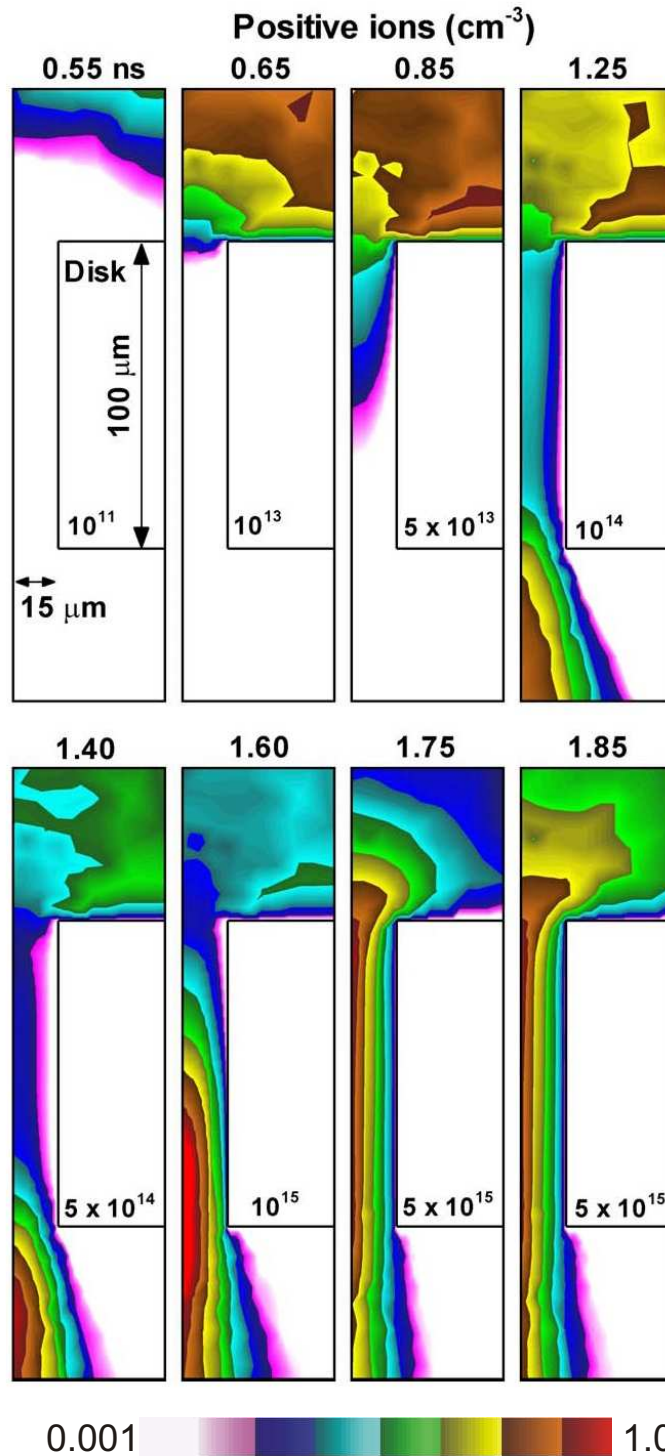


Fig. 12 Temporal dynamics of the total positive ion density (log scale) during breakdown in the base case. Ion density is 10^{13} cm⁻³ in the channel as the avalanche propagates downward. During the reverse strike, the peak density rises to 10^{15} cm⁻³ in the channel. Maximum values on 3-decade plots are indicated.

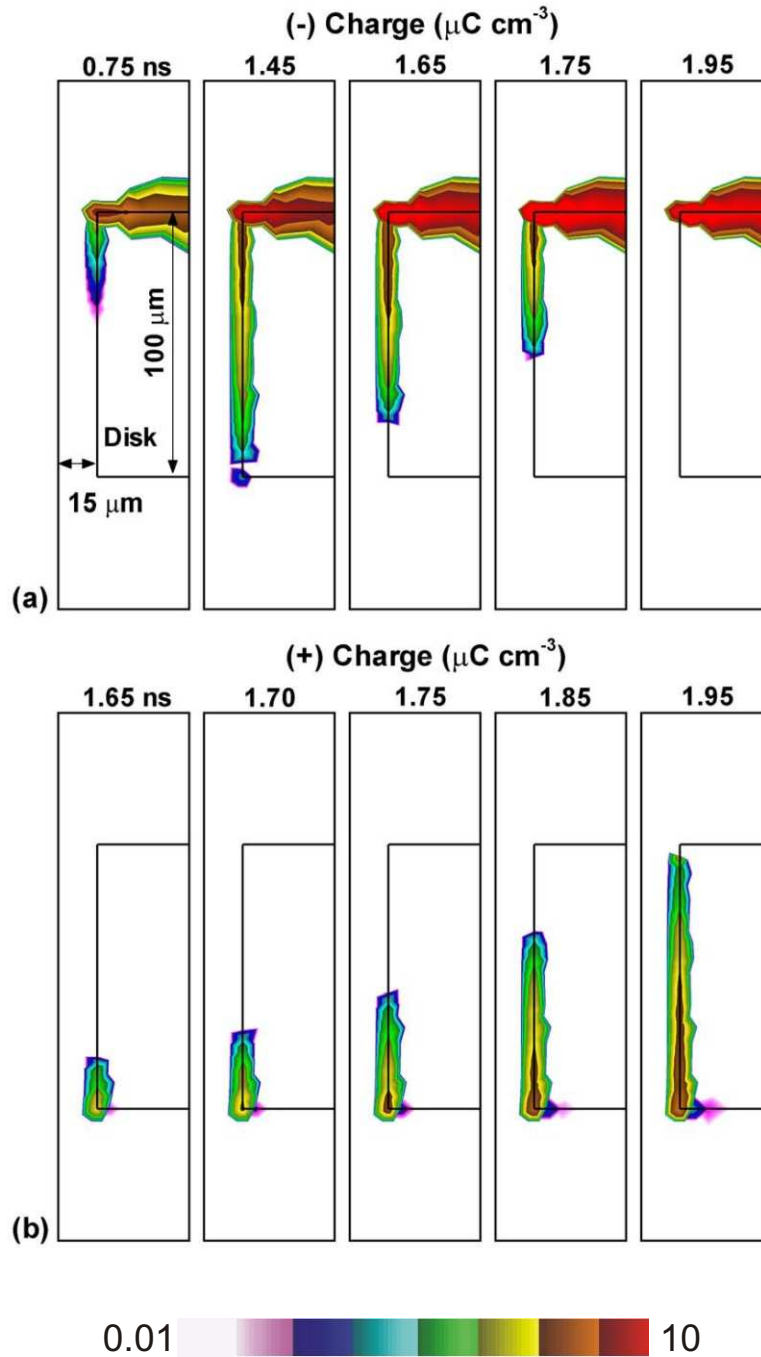


Fig. 13 Temporal dynamics of surface charge density (log scale) during breakdown in the base case configuration. (a) Negative surface charge density upto $10 \mu\text{C cm}^{-3}$ forms along the channel wall and upper surface of the disk as the avalanche propagates downward. During the reverse strike, increased ion flux through the sheath-region neutralizes the negative charge and (b) builds up positive surface charge on the channel wall.

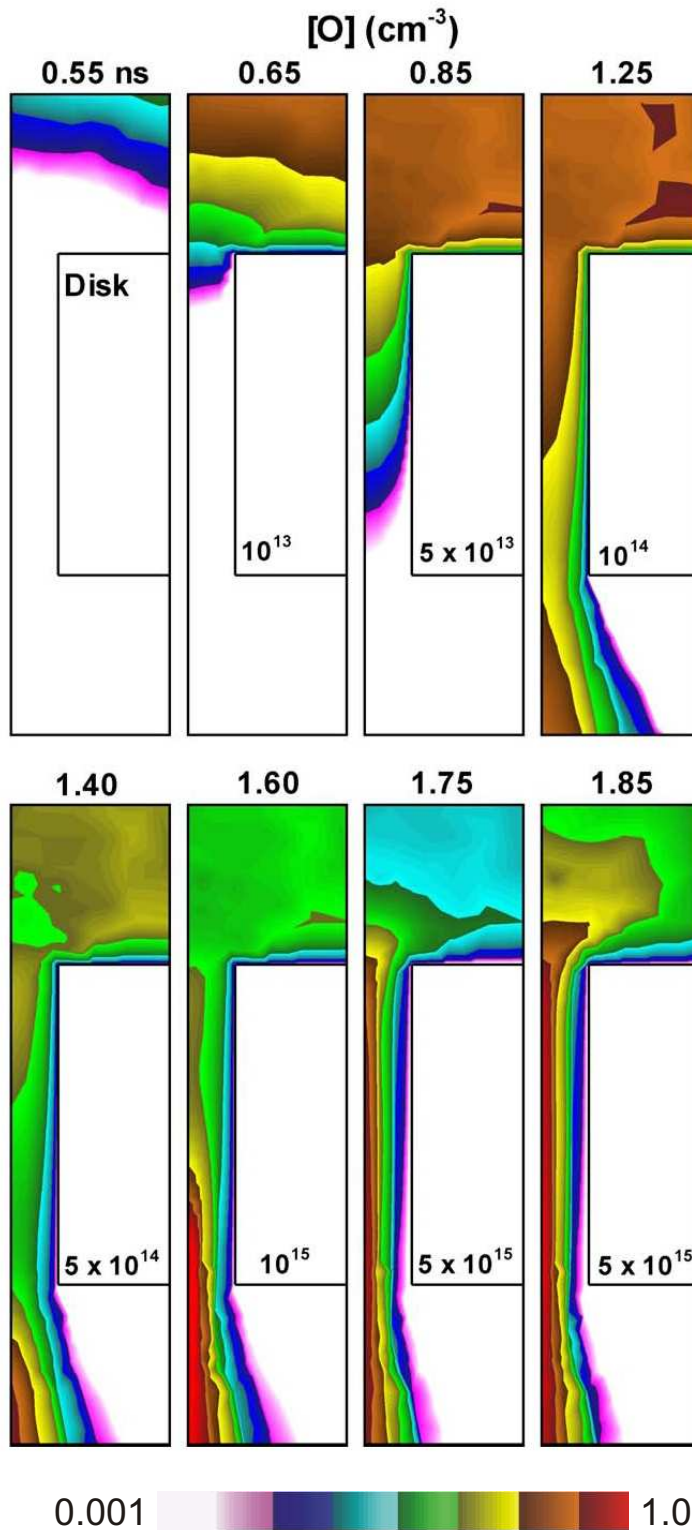


Fig. 14 Temporal dynamics of O atom density (log scale) during breakdown in the base case configuration. Density of O atoms is 10^{14} cm^{-3} in the channel as the avalanche propagates downward. During the reverse strike, peak [O] density rises to 10^{15} cm^{-3} in the channel. Maximum values on 3-decade plots are indicated.

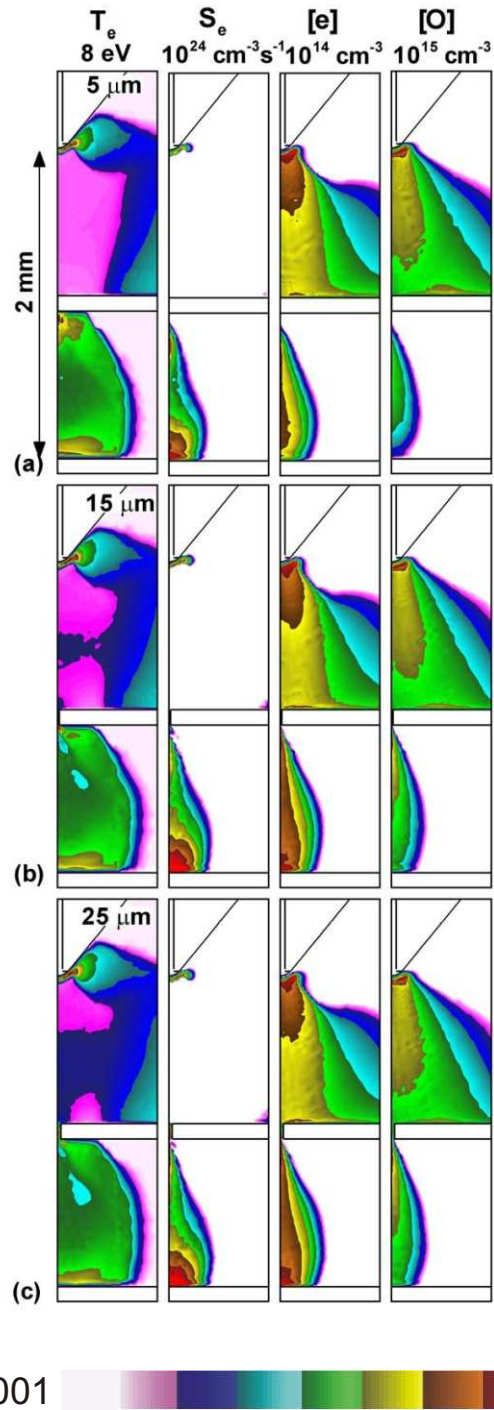


Fig. 15 Electron temperature, ionization sources (log scale) and electron density (log scale) after gap closure in a humid air corona with a dielectric plastic disk of thickness 100 μm placed midway in the 2 mm gas gap. The channel half-widths are (a) 5 μm , (b) 15 μm and (c) 25 μm . Breakdown in the 5 μm case is slower and though the discharge penetrates the channel, the plasma density below the disk is lower than with higher channel widths.

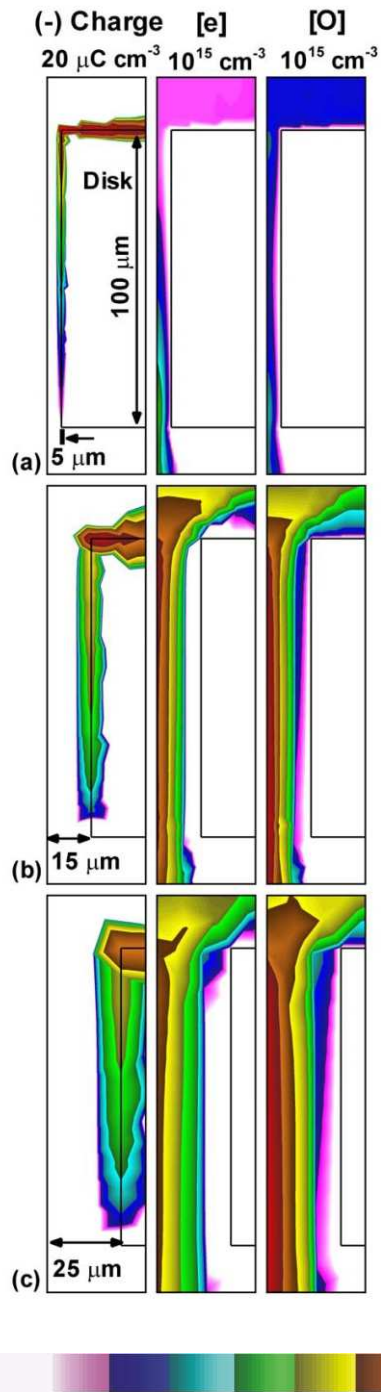


Fig. 16 Negative surface charge, electron density and O atom density (3-decade log scale), after gap closure in a humid air corona with a dielectric plastic disk of thickness 100 μm placed midway in the 2 mm gas gap. The channel half-widths are (a) 5 μm, (b) 15 μm and (c) 25 μm. The magnitude of surface charge is similar in all cases. Densities of electrons and O atoms in the channel increases with channel half-width due to lower wall losses.

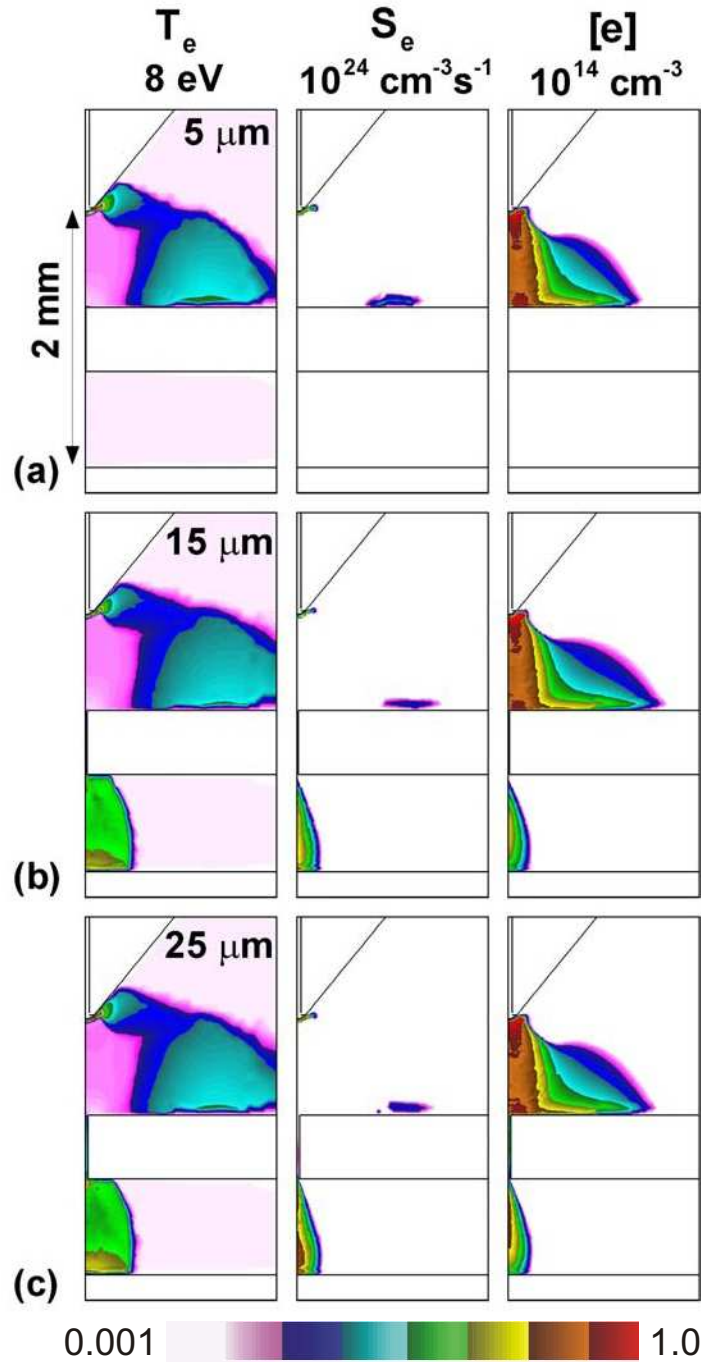


Fig. 17 Electron temperature, ionization sources (log scale) and electron density (log scale) after gap closure in a humid air corona with a dielectric plastic disk of thickness 500 μm placed midway in the 2 mm gas gap. The channel half-widths are (a) 5 μm , (b) 15 μm and (c) 25 μm . The avalanche is unable to penetrate the channel to attain gap closure in (a), but spreads along the upper surface of the disk. In (b) and (c), gap closure does occur but the plasma density is markedly lower below the disk.

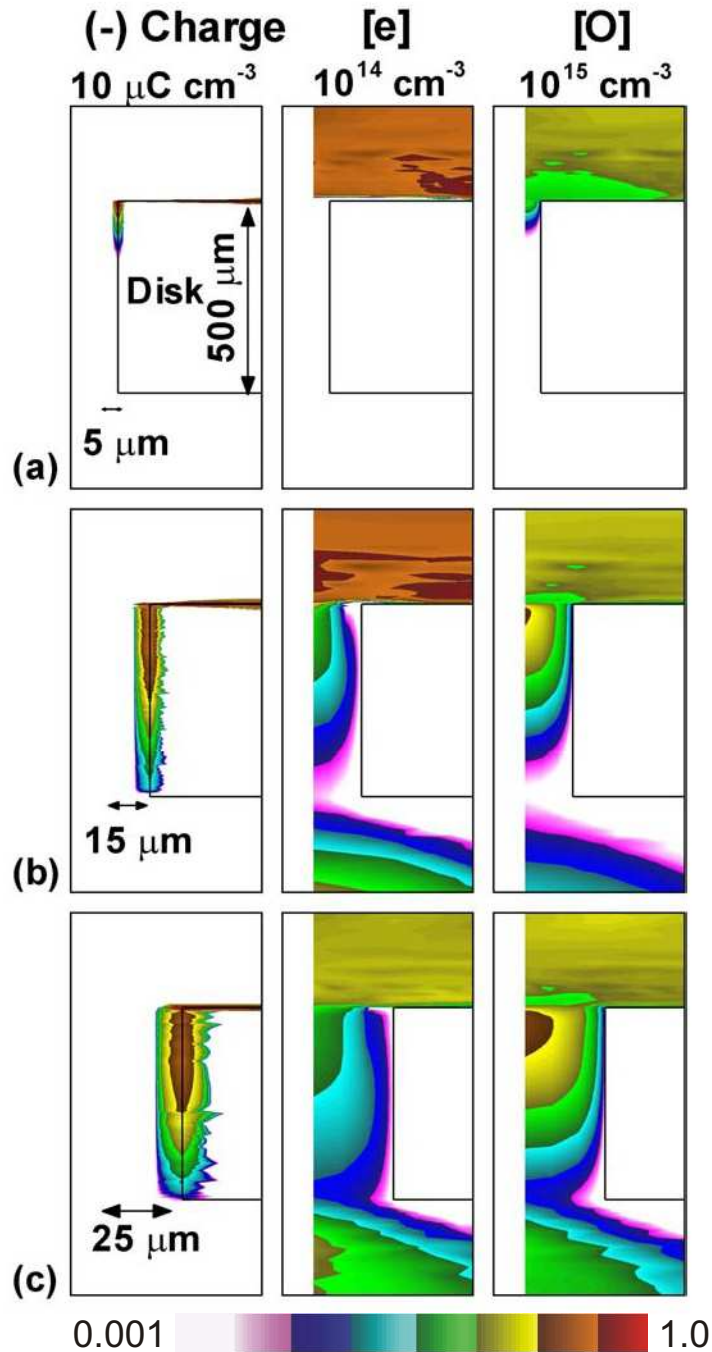


Fig. 18 Negative surface charge, electron density and O atom density (all on log scale), after gap closure in a humid air corona with a dielectric plastic disk of thickness $500 \mu\text{m}$ placed midway in the 2 mm gas gap. The channel half-widths are (a) $5 \mu\text{m}$, (b) $15 \mu\text{m}$ and (c) $25 \mu\text{m}$. There is no significant plasma penetration in (a), and surface charging is restricted to the upper regions of the channel. In (b) and (c), the magnitude of surface charging is similar with higher plasma density in the channel in (c).

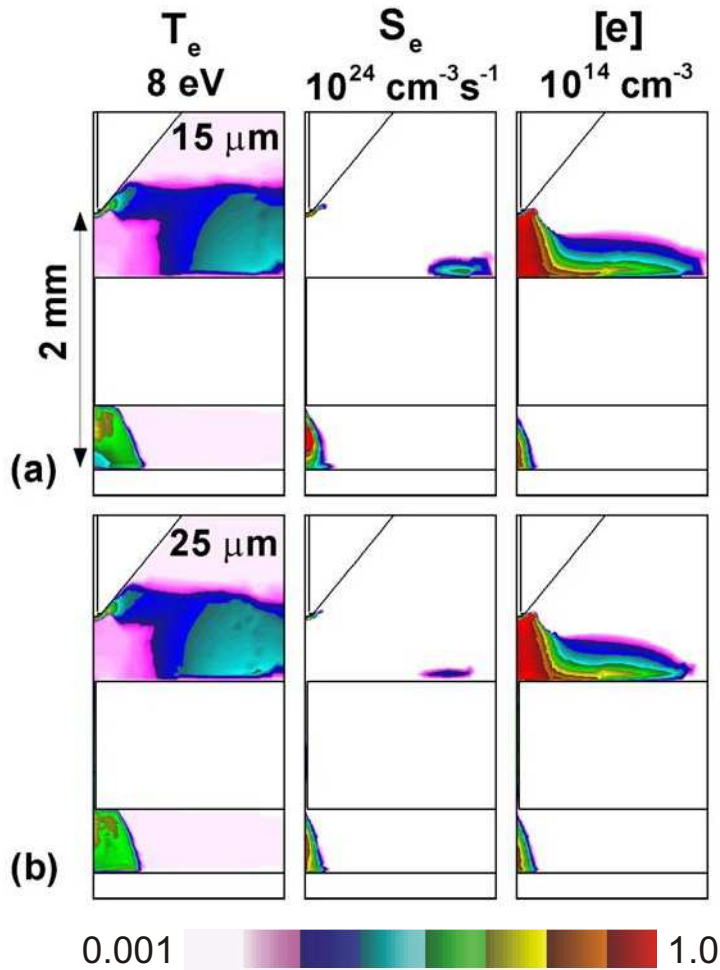


Fig. 19 Electron temperature, ionization sources (log scale) and electron density (log scale) after gap closure in a humid air corona with a dielectric plastic disk of thickness $1000\ \mu\text{m}$ placed midway in the $2\ \text{mm}$ gas gap. The channel half-widths are (a) $15\ \mu\text{m}$, and (b) $25\ \mu\text{m}$. The discharge spreads along the upper surface of the disk. The avalanche also penetrates the channel to attain gap closure in both cases, but the plasma density below the disk is 2 orders of magnitude lower.

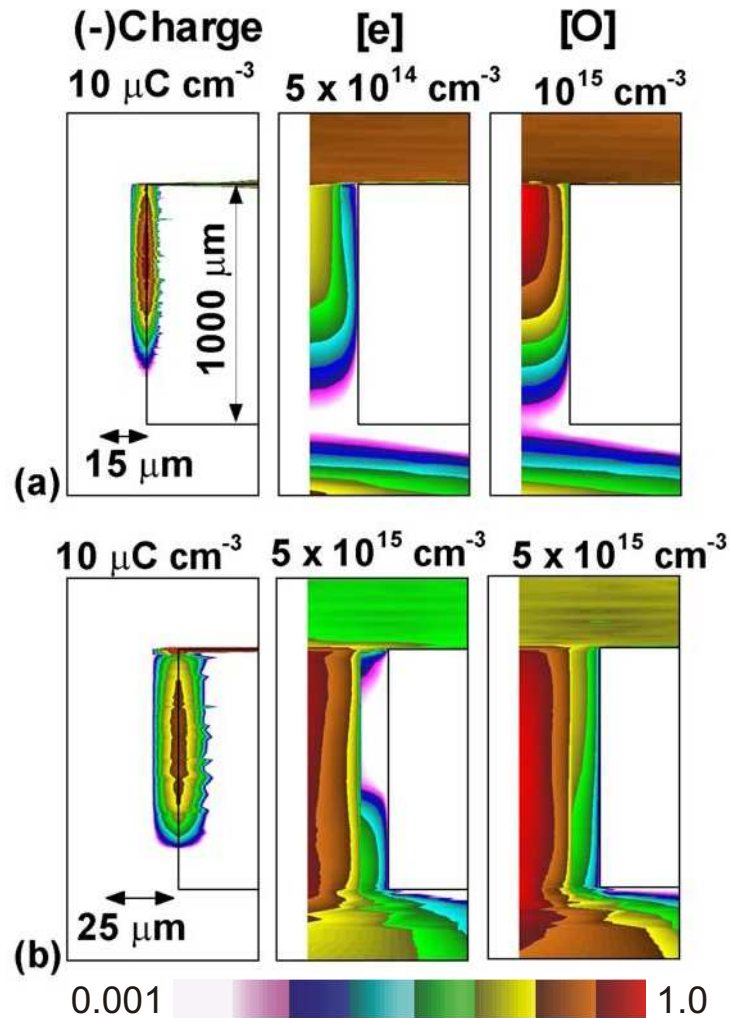


Fig. 20 Negative surface charge, electron density and O atom density (all on log scale), after gap closure in a humid air corona with a dielectric plastic disk of thickness 1000 μm placed midway in the 2 mm gas gap. The channel half-widths are (a) 5 μm and (b) 25 μm. Surface charge is lower and plasma density is higher in (b) due to lower wall losses.

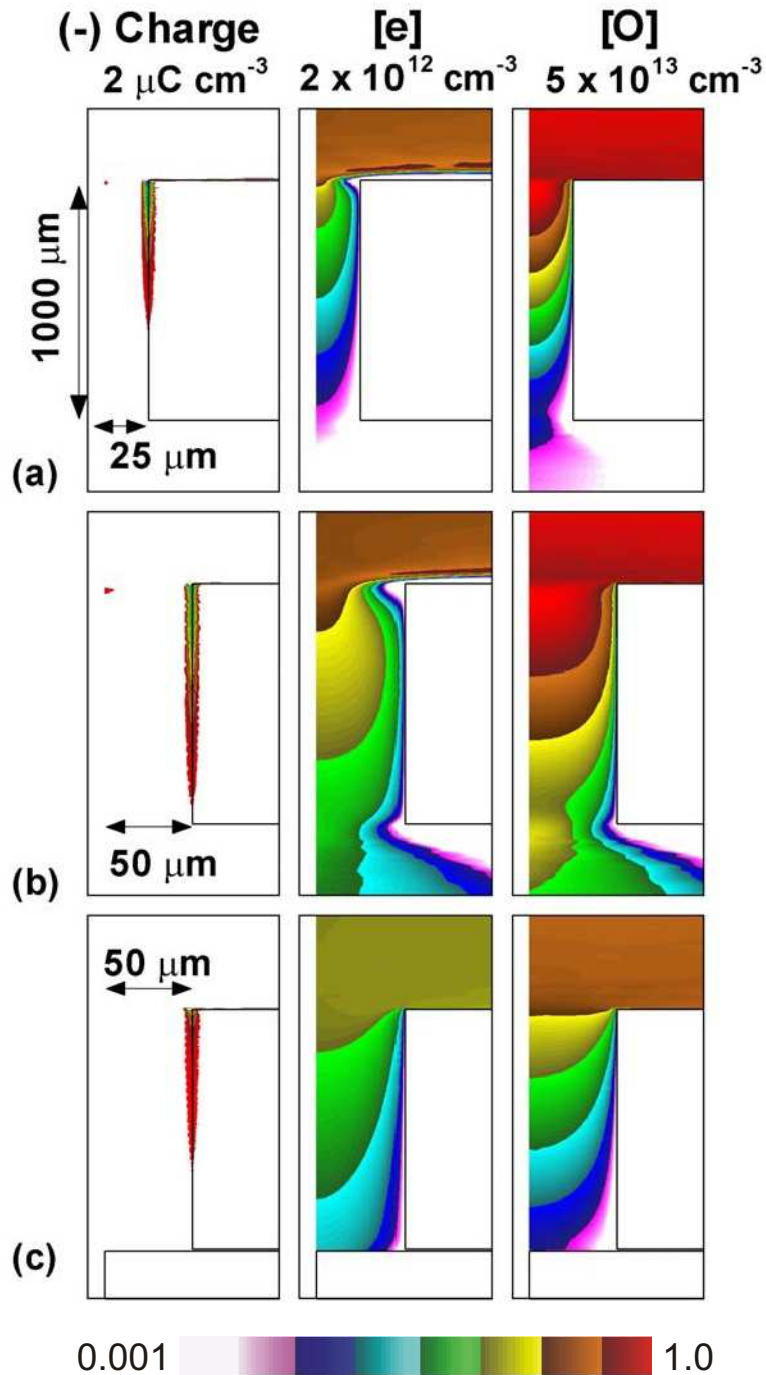


Fig. 22 Negative surface charge, electron density and O atom density (all on log scale), after gap closure in a humid air corona with a dielectric plastic disk of thickness 1000 μm placed in the 2 mm gas gap. The channel half-widths are (a) 25 μm , (b) 50 μm with the disk placed midway in the gap and (c) 50 μm with the disk placed on the lower grounded electrode. Surface charging occurs to all along the channel wall in (b) and to a lesser extent in (a) and (c). Plasma density in the channel is higher in (b).

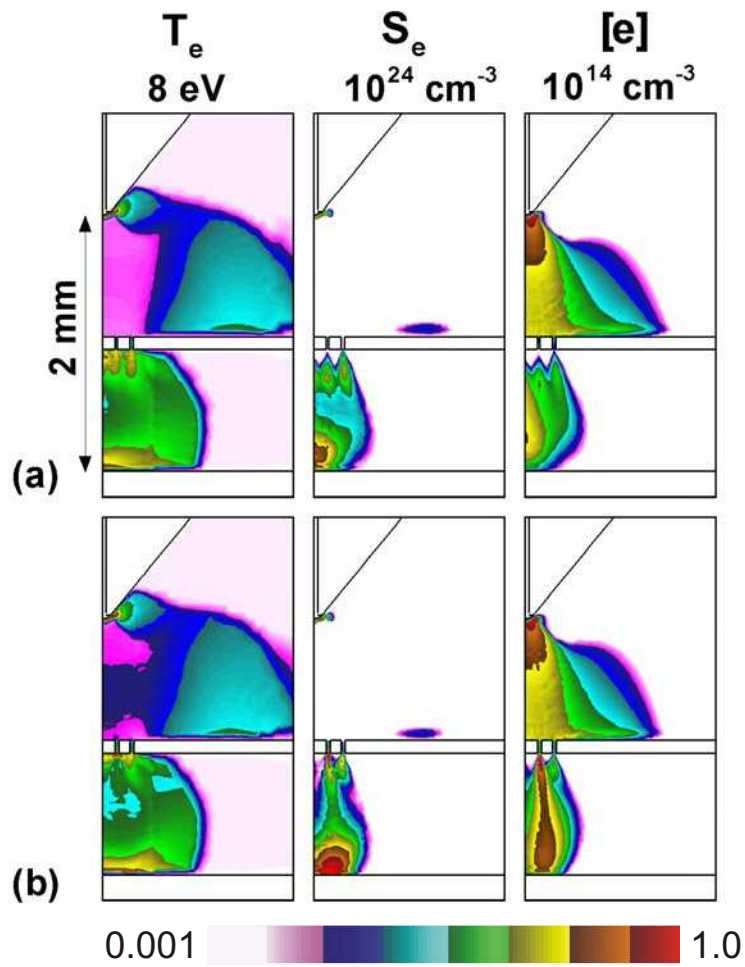


Fig. 23 Electron temperature, ionization sources (log scale) and electron density (log scale) after gap closure during breakdown in a humid air corona with a dielectric plastic disk 100 μm thick placed midway in the 2 mm gas gap. There are 3 channels in the disk, each consecutively of width (a) 10, 15 and 25 μm , and (b) 10, 30 and 30 μm . The discharge penetrates all the channels in both cases.

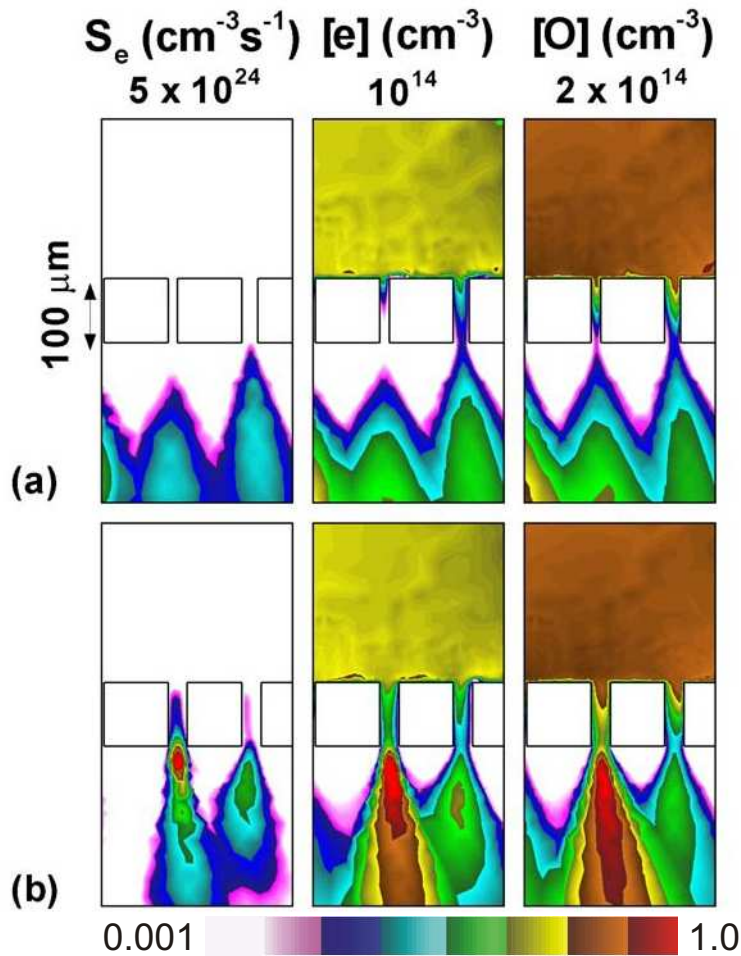


Fig. 24 Ionization sources, electron density and O atom density (all in log scale) during breakdown in a humid air corona with a dielectric plastic disk 100 μm thick placed midway in the 2 mm gas gap. There are 3 channels in the disk, each consecutively of width (a) 10, 15 and 25 μm , and (b) 10, 30 and 30 μm . The plasma density depends critically on the proximity of the channel to the discharge axis and its width, with higher plasma density in wider channels.

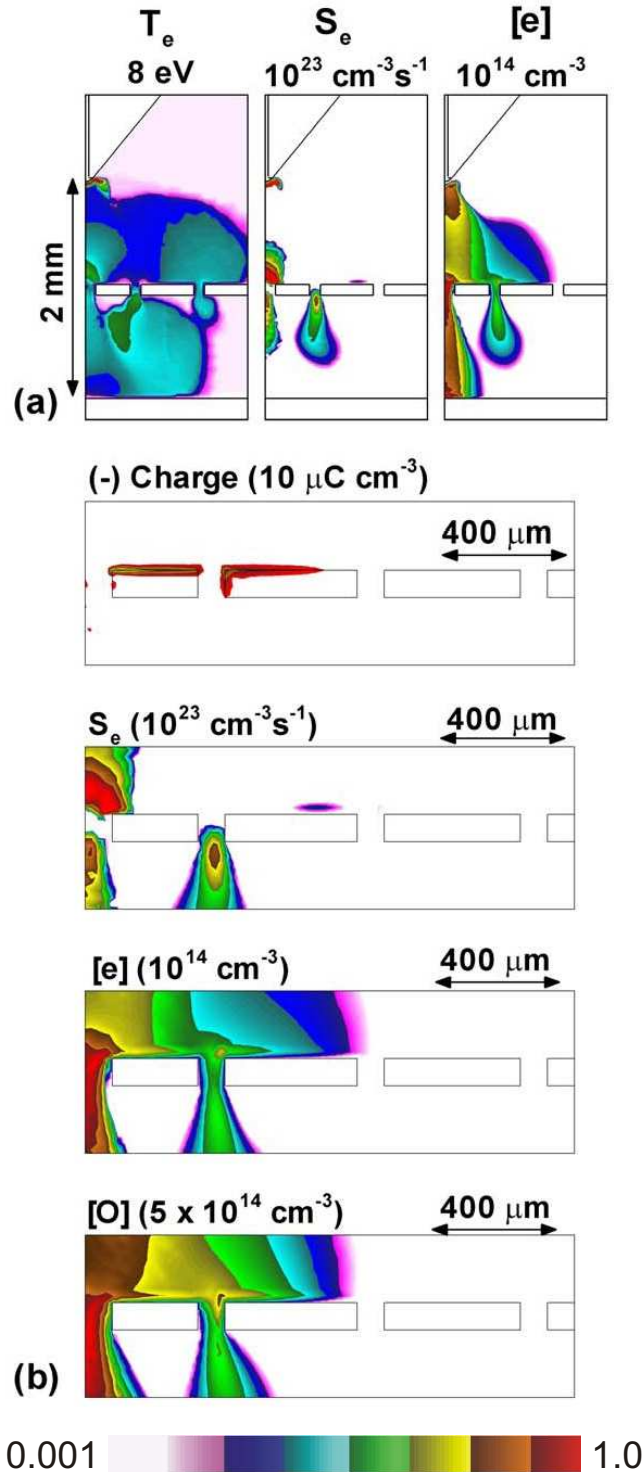


Fig. 25 Electron temperature, ionization sources (log scale), electron density (log scale) during breakdown in a humid air corona with a dielectric plastic disk 100 μm thick placed midway in the 2 mm gas gap. The channels in the disk are of varying widths and widely spaced. The impedance of the channel on the axis is much lower than its neighbors, so gap closure and the reverse strike occur through the channel on the axis before the streamer propagates through the second channel.

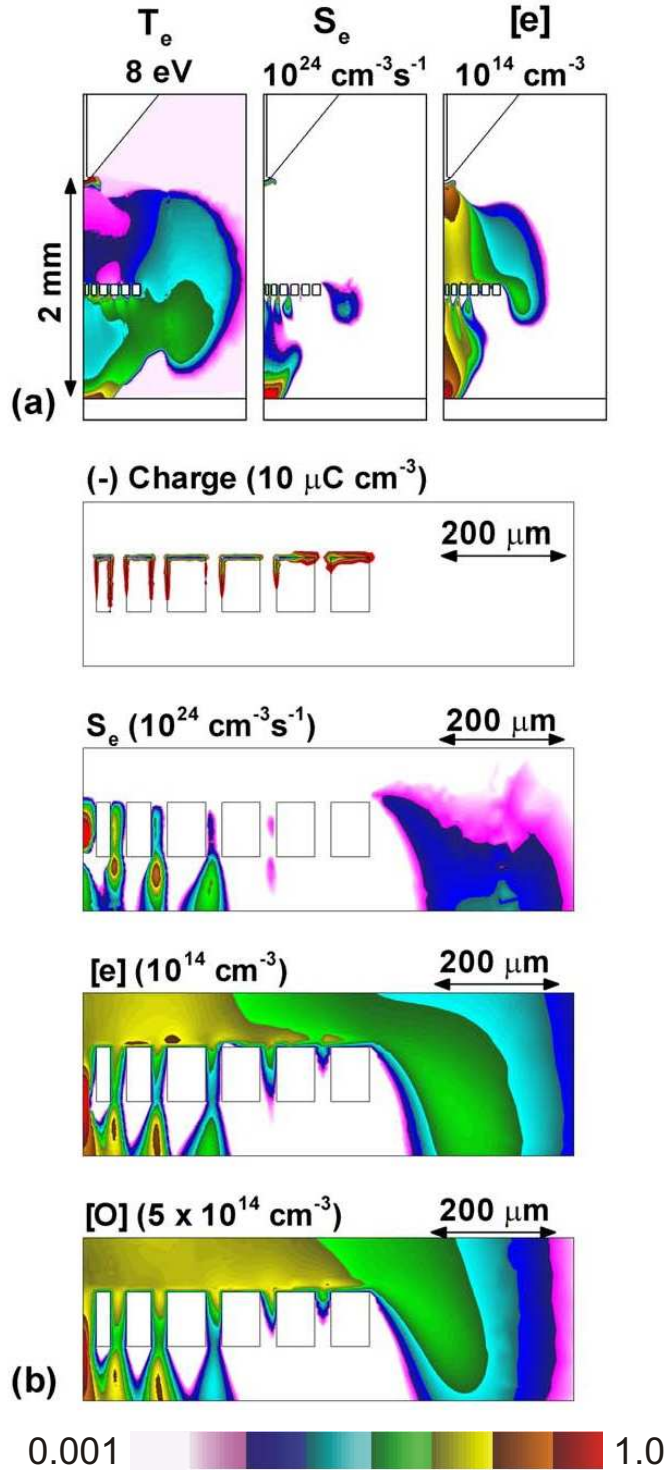


Fig. 26 Electron temperature, ionization sources (log scale), electron density (log scale) during breakdown in a humid air corona with a dielectric plastic disk 100 μm thick placed midway in the 2 mm gas gap. The channels in the disk are spaced 30-70 μm apart with widths varying from 20-30 μm . The plasma density in the channel depends on its impedance which is a function of its width, proximity to the axis and surface charging.

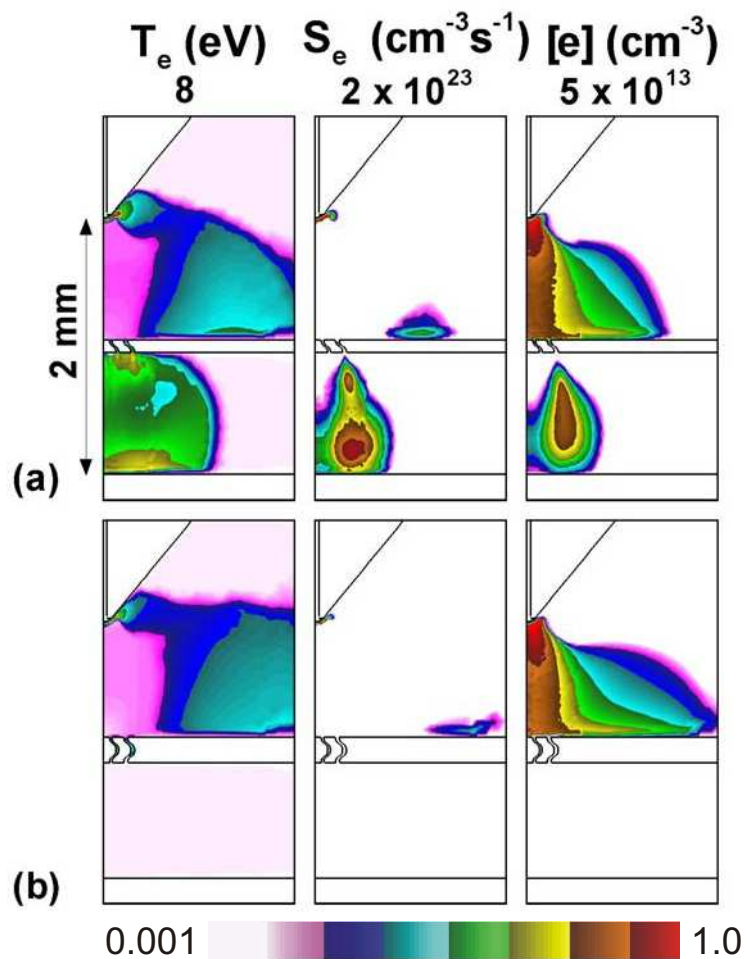


Fig. 27 Electron temperature, ionization sources (log scale) and electron density (log scale) during breakdown in a humid air corona with a dielectric plastic disk placed midway in the 2 mm gas gap. The disk thickness is (a) 100 μm and (b) 200 μm . The plasma penetrates through the disk in (a) but does not in (b) because of the greater path curvature.

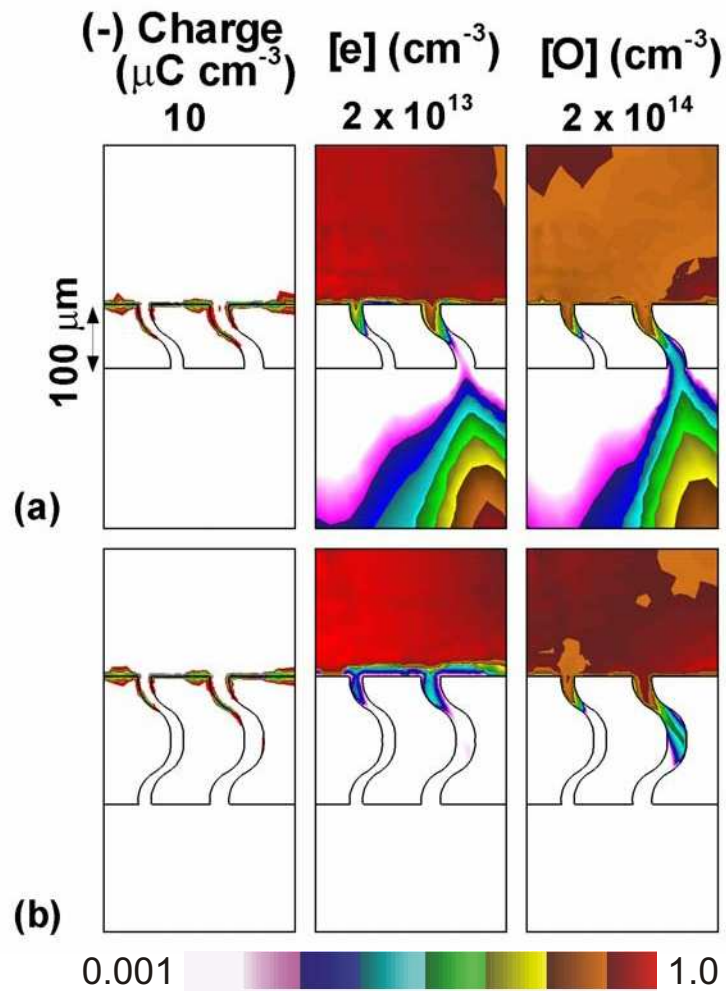


Fig. 28 Negative surface charge, electron density and O atom density (all in log scale) during breakdown in a humid air corona with a dielectric plastic disk placed midway in the 2 mm gas gap. The disk thickness is (a) 100 μm and (b) 200 μm . The degree of plasma penetration is controlled by surface charging and electric field directions within the curved channel paths.

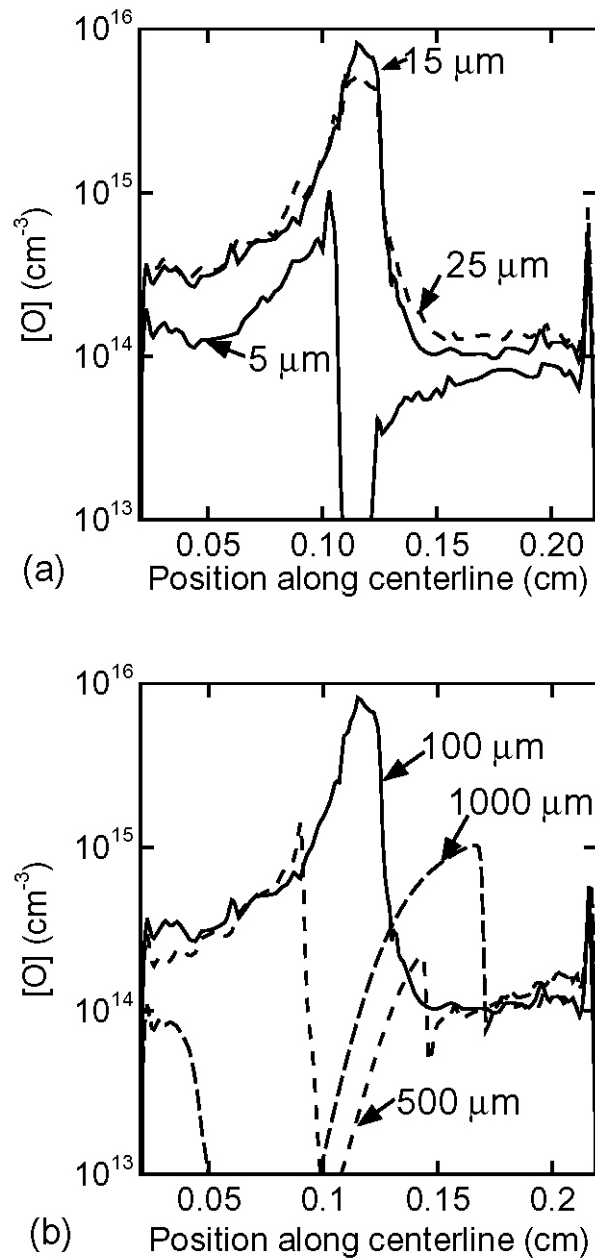


Fig. 29 Effect of varying (a) microchannel radius and (b) disk thickness on O atom densities along the discharge axis after breakdown. There is an optimum radius where the electric field is sufficiently enhanced in the channel without removing too much charge from the plasma. As thickness of disk increases, the discharge propagates with difficulty and O atom densities peak off-center below the disk. With further increase in disk thickness, the peak shifts above the disk.

5.6 References

1. T. Chandy, G. S. Das, R. F. Wilson and G.H.R. Rao, *Biomaterials*, **21**, 699 (2000).
2. S. Trigwell, N. Grable, C. U. Yurteri, R. Sharma, and M. K. Mazumder, *IEEE Transactions on Industry Applications*, **39**, 79 (2003).
3. E. F. C. Vidaurre, C. A. Achete, R. A. Simao and A. C. Habert, *Nuclear Instruments and Methods in Physics Research B*, **175-177**, 732 (2001).
4. M. Nitschke, G. Schmack, A. Janke, F. Simon, D. Pleul, C. Werner, *Journal of Biomedical Materials Research*, **59**, 632 (2002).
5. R. Latkany, A. Tsuk, M.-S. Sheu, I.-H. Loh and V. Trinkaus-Randall, *Journal of Biomedical Materials Research*, **36**, 29 (1997).
6. E. Piskin and A. G. Atac, *Journal of Biomedical Materials Research*, **30**, 493 (1996).
7. G. Borgia, C. A. Anderson and N. M. D. Brown, *Plasma Sources Science and Technology*, **12**, 335 (2003).
8. S. Kaplan, *Surface & Coatings Technology*, **186**, 214 (2004).
9. A. Hollander, J. Behnisch and H. Zimmermann, *Journal of Applied Polymer Science*, **49**, 1857 (1993).
10. F. Jones, Z. Lu and B. B. Elmore, *Applied Biochemistry and Biotechnology*, **98**, 627 (2002).
11. L. Ceriotti, K. Weible, N. F. deRoosj and E. Verpoorte, *Microelectronic Engineering*, **67-68**, 865 (2003).
12. A. Khademhosseini, K. Y. Suh, J. Sangyong, G. Eng, J. Yeh, G.-J. Chen and R.

- Langer, Analytical Chemistry, **76**, 3675 (2004).
13. H. Makamba, J. H. Kim, K. Lim, N. Park and J. H. Hahn, Electrophoresis, **24**, 3607 (2003).
14. Z. L. Zhang, C. Crozatier, M. LeBerre and Y. Chen, Microelectronic Engineering, **78-79**, 556 (2005).
15. J. K. Evju, P. B. Howell, L. E. Locascio, M. J. Tarlov and J. J. Hickman, Applied Physics Letters, **84**, 1668 (2004).
16. F. Gerdinand, M. Budde and M. Kurrat, Presentation at the 14th International Symposium on High Voltage Engineering, Tsinghua University, Beijing, China (2005). (<http://www.htee.tu-bs.de/forschung/veroeffentlichungen/veroff.htm>)

6. TREATMENT OF ROUGH POLYMER SURFACES IN REPETITIVELY PULSED O₂ DISCHARGES

6.1 Introduction

Plasma discharges generated at low or high pressures are often employed to functionalize polymer surfaces since they afford the advantages of short treatment times, the ability to treat temperature-sensitive and chemical-sensitive 'soft' materials at room temperatures and the absence of liquid handling. For instance, atmospheric pressure corona discharges are used to functionalize large areas of commodity polymer films (e.g. polypropylene) in industry offering the advantages of continuous processing and low processing costs of a few cents per m².

The objective of 'functionalization' or 'treatment' is to alter the chemical composition of the polymer surface by introducing O-containing groups such as alcohol (C-OH), peroxy (C-OO), carbonyl (R-C=O) or acid (O=C-OH) groups on the surface, [1] thereby increasing its surface energy and favorably modifying properties such as adhesion, wettability or reactivity. Using energy densities in the range of 1 - 10 J-cm⁻², the O/C ratio of polypropylene surface was increased from 0% to 10% after corona treatment.

In the textile industry, atmospheric pressure plasmas are replacing wet processing technologies to treat woven materials, since they are environmentally friendly and cost-effective. Surface functionalization of textiles helps improve properties such as color fastness and water repellency.[2] Textile fabrics usually consist of fibers in a warp and weave arrangement, creating surface features with characteristic length scales of few to tens of μm. Since the fabric surface is not completely exposed to the discharge, the ability of the

reactive species in the plasma to penetrate into these surface features is critical to the quality and uniformity of treatment.[3]

Biomaterial surfaces usually have rough microstructure such as scaffolds to enable cell adhesion.[4] The requirements for treating biocompatible materials are in general, quite stringent. The extent of functionalization across the surface topography must remain high as well as spatially uniform on the microscopic scale to ensure reliability. Such surfaces tend to be porous or have other non-planar features that are not always easily accessible to the plasma. Low pressure plasmas sustained in equipment similar to those used in the microelectronics industry are often used to functionalize the surfaces of high value-added polymers used for implants and as substrates for tissue engineering for biocompatibility. The issues encountered in biomaterials surface functionalization in low pressure plasmas often have to do with the low degree of functionalization or selectivity of treatment towards a particular functional group.[5]

Polymer surface treatment using plasmas, both at low and high pressures, result in a mixture of functional groups. Therefore, adapting industrial atmospheric pressure plasma sources used for commodity polymer treatment to treat high-value biocompatible materials may offer significant economic benefits. A better insight into the interaction between gas phase transport processes and surface reaction pathways leading to functionalization will help tailor the relative abundance of various functional groups on the surface using treatment process parameters, such as in the creation of functional group gradients.[6] In this chapter, we investigated the feasibility of employing repetitively pulsed atmospheric pressure discharges in O₂ containing gases such as humid air and He/O₂/H₂O mixtures to functionalize with high spatial uniformity rough polypropylene (PP) surfaces, representative of textiles or

scaffold-like surface cross-sections using the integrated plasma-surface kinetics model described in Chapter 2.

The model calculates the relative abundance of various functional groups as a function of position along the surface. The spatial extent and uniformity of surface treatment depend on the penetration of the plasma into the rough surface features. Various factors such as the discharge dynamics, reaction kinetics and transport processes affect the extent of penetration of the reactive gas phase species into surface features. Spatial uniformity is discussed over two length scales; the first in the range of a few tenths to a mm characterized by the spatial uniformity of the fluxes of reactive species to the surface and the second is on the scale of the surface features. In particular, the ability of the plasma to penetrate into the rough surface features and retain the ability to bring about the desired surface functionalization is important to the uniformity of treatment on the microscopic scale.

Discharges in air are efficient in functionalization of the surface with O-containing groups due to action of species such as O, OH and O₃. The polarity of the pulse has an effect on the extent of plasma penetration into rough features. During positive pulses, electron density near the features is low due to the formation of a sheath-like region. Radical densities close to these features increase only due to the diffusion and recombination of positive ions at the surface. We found that varying the relative humidity has a small impact on the degree of surface functionalization. In low humidity discharges, gas phase OH is generated by H-abstraction reactions of O atoms on the surface which in turn compensates for OH otherwise produced by electron impact of H₂O at higher humidity. Energy deposition has a significant effect with increase in the degree of incorporation of O-containing groups into the polymer surface at higher voltages due to increased production of radicals.

Microscopic uniformity of treatment is also improved due to higher penetration of reactive gas phase radicals.

The dependence of surface coverage of different functional groups on O₂ content was also investigated using He/O₂/H₂O mixtures at different O₂ fractions. The ratio of O/O₃ densities near the surface features depends on the O₂ content, which affects the transport and local reaction kinetic processes. As a result, different surface reaction pathways predominate changing the relative abundance of functional groups formed on the microscopic and macroscopic length scales.

6.2 Reactor Configuration and Reaction Mechanisms

The treatment of polypropylene (PP) with rough surface features having characteristic dimensions of a few μm was investigated in atmospheric pressure discharges in different gas mixtures using a corona-dielectric barrier configuration similar to industrial atmospheric pressure plasma treatment devices. The schematic of such a device is shown in Fig. 1(a). The geometry is symmetric across the centerline. The upper metal electrode is housed in dielectric material and exposed to the processing gas at its tip and is normally powered at a few kHz. The gap between the upper electrode and the lower grounded metal electrode is 2 mm. The rough polypropylene surface is placed on the lower grounded electrode, so it effectively operates as a dielectric-barrier discharge. Roughness on the polymer surface is resolved having strand-like features of few μm length scales to resemble textile or scaffolding-like surfaces for cell-adhesion as shown in Fig. 1(b).

An unstructured mesh with refinement zones is overlaid on the geometry. The mesh is refined locally in regions close to the powered electrode and near the surface features and is coarser further away from the main discharge zone, so it simultaneously resolves both the

reactor-scale and surface-scale processes. The total number of nodes is 21,296 with 9,643 of these being in the plasma. Refinements near the powered electrode result in node spacing of about 1 μm . There are similar refinements close to the surface to adequately resolve rough features. Regions away from the discharge zone have coarser resolution with nodes spaced 100 μm or more to manage the computational burden. Results for plasma dynamics and surface treatment obtained from computational comparisons with a smaller number of surface features and increased resolution over the entire mesh did not differ significantly.

A number of discharge pulses are simulated using the pulsing option mentioned in Chapter 2, to determine the number of pulses, n , it takes for the plasma to reach an approximate periodic steady state. The plasma dynamics and chemistry including charged species and neutrals as well as surface kinetics are resolved during every pulse. Only the neutral chemistry and surface kinetics are tracked in the interpulse period. After $n-1$ pulses, the fluxes of all plasma species at the polymer surface, including photons, are recorded during the course of the n^{th} pulse at various time instants, sufficient enough to resolve both the pulse and interpulse period. The pulse-to-pulse temporal variation in fluxes so obtained is used to integrate the surface kinetics model over subsequent pulses for longer timescales without following neutral gas-phase chemistry.

The discharge is initiated in each case with a voltage pulse of a few kV to the upper electrode. During the short pulse (usually < 10 ns), reactions involving electronic impact excitation, dissociation, attachment and ionization lead to the formation of a variety of radicals and ions. Charged species striking the polymer react with it and also build up surface charge that counteracts the voltage across the gas gap, and the plasma is extinguished. Photons emitted by the relaxation of excited species in the discharge are

energetic enough to break bonds on the polymer surface. Radicals have longer lifetimes than charged species and react with each other and with the polymer surface through the interpulse period. Surface functionalization occurs due to action of all these species from the plasma as well as surface-surface reactions on timescales spanning more than a few ms, over many such pulses. The gas phase and surface reaction mechanisms used in these investigations are described in Chapter 2.

6.3 Surface Treatment in Humid Air Discharges

The base case conditions correspond to atmospheric pressure gas composition of $N_2/O_2/H_2O=79/20/1$ reflecting a relative humidity of 30%. The discharge is operated at a repetition frequency of 10 kHz by biasing the powered electrode with unipolar 15 kV pulses of either negative or positive polarity. While the plasma dynamics are tracked during the pulse, neutral and surface chemistry are tracked in the interpulse period. In order to reduce computational burden, the fluxes of all plasma species on the surface during the pulse and interpulse duration can be recorded after a specified pulse. Thereafter, only the surface kinetics model is integrated using the recorded fluxes to simulate later pulses. The densities of surface functional groups typically reach steady state over 100s of ms.

The density of electrons, positive ions and O atoms after breakdown at 1.6 ns in the first pulse of the negative humid air discharge is shown in Fig. 2(a). The avalanche, terminated by charging of the PP dielectric produces a plasma density of 10^{13} cm^{-3} . The major radicals produced during the pulse include O atoms and OH with densities of 10^{14} cm^{-3} and 10^{13} cm^{-3} respectively. Conditions at the end of the pulse near the surface are shown in Fig. 2(b). The electrons and ions are able to penetrate into the surface features to a limited extent, though the ion density inside the features is low (10^{10} cm^{-3}). Surface features with a

large exposure to the avalanche are negatively charged due to the large electron flux, up to $1 \mu\text{C cm}^{-3}$. The penetration of plasma results in the generation of radicals such as O within the features as well.

The density of radicals including O, O₃ and OH at 50 μs is shown in Fig. 3(a). There is a dramatic reduction in the density of O atoms in the discharge by up to a factor of 10^2 . Most of the O atoms are converted to O₃ via three body reactions with O₂ on these timescales and consequently the density of O₃ increases to 10^{14} . Since the main pathway for the production of OH is the electron impact of H₂O, the density of OH decreases steadily in the interpulse period due to reaction kinetics and diffusion. The density of radicals near the surface features during the same time period is shown in Fig. 3(b). At this late time, diffusion has made radical densities essentially uniform over the roughness scale length. Neutral radicals are able to access interior surface features due to diffusion. The density of OH has reduced by a factor of 2 near the features at 100 μs compared to the pulse. On the other hand the density of O₃ has increased to about 10^{15} cm^{-3} .

The density of electrons, positive ions and O atoms after breakdown in the positive humid air discharge is shown in Fig. 4(a). The plasma density is higher at 10^{14} cm^{-3} while the density of O atoms is about the same as the negative discharge at 10^{15} cm^{-3} . The spatial extent of the positive discharge in the plasma is smaller than the negative discharge. As the avalanche reaches the surface, it spreads out moving along the surface. This is because a sheath-like region forms near the polymer surface and electrons do not enter this region. The inability of electrons to penetrate the surface features is evident in Fig. 4(b). Positive ions are able to penetrate well into the features with densities of 10^{11} - 10^{12} cm^{-3} due to favorable electric fields. The bulk of the ions are driven into the features by the electric field drift. In

this case, ion recombination at the polymer results in surface charge of up to a positive $1 \mu\text{C cm}^{-3}$. Since few electrons enter into the features, there is negligible O atom density inside the features during the pulse itself. The recombination of ions, such as O^+ that drift into these features creates more O atoms near the surface than is generated due to the electron impact.

The evolution of radical densities during the interpulse period of the positive discharge at $50 \mu\text{s}$ is shown in Fig. 5(a). Similar to the negative discharge, the density of O atoms decreases by at least a factor of 10^2 during the interpulse period. OH decreases due to gas phase reactions and diffusion to about 10^{12} cm^{-3} while the density of O_3 increases by a factor of 10^2 . The spatial profiles of the radicals strongly track the extent of the streamer that existed during the pulse. The density of radicals near the surface features is shown in Fig. 5(b) at $100 \mu\text{s}$ indicating the extent of radical penetration into surface features. The density of O_3 is about 10^{15} cm^{-3} near the surface while the density of O atoms decreases from 10^{15} cm^{-3} to 10^{12} cm^{-3} during the same period.

The time-averaged fluxes of O, OH, H and O_3 during the interpulse period as a function of position along the rough PP surface for the positive and negative discharges are compared in Fig. 6. For all species, the fluxes are higher in the positive discharge by a factor of 2 – 10 because the plasma density in the positive discharge pulse is higher. There are also interesting trends in the spatial variations of fluxes. The microscopic variation in fluxes results from the shadowing effect of surface features. The macroscopic variation in fluxes in both the positive and negative discharge arises from the spatial distribution of radicals in the discharge after the pulse and subsequent gas kinetic reactions and diffusion in the interpulse period. The macroscopic variations are significant in the negative discharge – for instance, the flux of H atoms is about $2 \times 10^{16} \text{ cm}^{-2}\text{s}^{-1}$ at position 0.1 cm from the centerline and $8 \times$

$10^{16} \text{ cm}^{-2}\text{s}^{-1}$ close to the centerline itself. In the positive discharge, the spreading of the plasma along the surface provides for more uniform fluxes. In both cases, the extent of the discharge and consequently the radical fluxes on the surface is limited to a region within about 1.5 mm from the centerline.

The temporal evolution of surface alkyl radical ($\text{R}\bullet$), alkoxy ($\text{R-O}\bullet$) and peroxy ($\text{R-OO}\bullet$) groups on the PP surface during the negative discharge are shown in Fig. 7. The density of alkyl radicals ($\text{R}\bullet$) are generated after a pulse is about 10^{11} cm^{-2} (10 μs). During the interpulse period, these radical sites are consumed by O, O_3 and O_2 from the gas phase resulting in the formation of alkoxy ($\text{R-O}\bullet$) and peroxy ($\text{R-OO}\bullet$) groups. The density of alkoxy ($\text{R-O}\bullet$) and peroxy ($\text{R-OO}\bullet$) groups increases with treatment time as shown in Fig. 11(b) and (c). The spatial uniformity of coverage of alkoxy ($\text{R-O}\bullet$) and peroxy ($\text{R-OO}\bullet$) groups depends on the spatial gradients in the O and O_3 fluxes. At 10 ms, the alkoxy coverage increases near the axis where the fluxes of O and O_3 are higher. By 100 ms, this gradient is exacerbated and results in a higher availability of alkyl ($\text{R}\bullet$) radicals away from the axis. O_2 saturates these available sites at a slower rate creating a gradient in the peroxy ($\text{R-OO}\bullet$) coverage from the axis at 100 ms.

Similarly, the evolution of alkyl ($\text{R}\bullet$), alkoxy ($\text{R-O}\bullet$) and peroxy ($\text{R-OO}\bullet$) coverages in the positive discharge are shown in Fig. 8. In this case as well, the alkyl ($\text{R}\bullet$) radicals are regenerated after the pulse to 10^{11} cm^{-2} and are consumed in the interpulse period. However, unlike the negative discharge, there is little macroscopic spatial gradient in the coverage of the alkoxy or the peroxy groups. This is explained by the lack of gradients in the fluxes of O and O_3 fluxes at the surface (Fig. 6). Diffusion of reactive radicals smoothens out the microscopic non-uniformities in alkoxy and peroxy coverages by 100 ms. The coverage of

carbonyl (R-C=O) and alcohol (R-OH) groups after 1 s of treatment is shown in Fig. 9 for the positive and negative discharge at 15 kV. In general, the surface coverage of both the carbonyl and alcohol groups is higher in the negative discharge as a result of better plasma penetration during the pulses that creates abundant radical density in close proximity to the surface features.

It was found that the most likely role of ions – abstracting H atoms from PP to create alkyl radical sites – was not significant in such discharges due to the short pulse durations. To confirm this, the reaction probability for an ion M^+ with a PP site to abstract an H atom, was varied between 10^{-5} and 1.0 in the surface reaction mechanism. The resulting change in the degree of surface functionalization of various groups over a treatment time of 1 s was negligible. Such a result was expected since the short pulse duration limits the ability of ions to contribute significantly when compared to the much longer lifetime of radicals such as O, OH or O_3 .

On the other hand, the contribution of photons to surface reactions is significantly higher. With photon transport, radiation from excited species in the discharge up to a length scale comparable to the mean free path of photon absorption can be significant enough to direct surface reaction pathways such as H abstraction, chain scission and crosslinking of radicals, provided they have sufficient energy. The photon flux along the surface after the pulse is shown in Fig. 10(a). The line of sight photon transport accounts for obstacles in the path and so shadowed surface features receive lower photon flux than sites that are exposed to the discharge. The density of crosslinked sites on the surface is shown in Fig. 10(b). Since crosslinking reactions compete with functionalization reactions of surface radicals with reactive gas phase radicals, the fraction of crosslinked sites is low, peaking at about 10^{10} - 10^{11}

cm⁻². The effect of photon-initiated reaction pathways on the coverage of alcohol (R-OH) and carbonyl (R-C=O) groups on the PP surface after 1 s of treatment in negative discharges and positive discharges at 15 kV is shown in Fig. 11. Photon fluxes increase microscopic non-uniformities by changing the relative abundance of reactive surface radicals formed at sites with larger and smaller view angles to the discharge.

The effect of applied voltage on surface functionalization is shown in Fig. 12. Alcohol (R-OH) groups are primarily formed by the abstraction of H atoms from surrounding PP (RH) sites by alkoxy (R-O•) groups. The density of PP sites is depleted with treatment time, more so on features with large view angles to the discharge. Inside the nooks and crannies, the rate of R-O• formation continues due to relatively higher availability of R• radicals and PP sites. As voltage increases to -15 kV, this causes significant microscopic spatial variations in the coverage of alcohol (R-OH) groups on the PP surface close to the discharge axis where radical fluxes peak. At even higher voltages of -17.5 kV, the fluxes of abstracting O and OH radicals are high enough to reduce inside the nooks and crannies that these microscopic non-uniformities are smoothed somewhat. Moving away from the axis, the R-OH formation is limited only by the formation of R• radicals since the density of PP sites available increases. On the other hand, R-C=O coverage tracks the variation in R-O• coverage, since it is formed primarily by chain scission around the R-O• site.

6.4 Surface Treatment in He/O₂/H₂O Discharges

The discharge is operated at a repetition frequency of 10 kHz by biasing the powered electrode with -5 kV, 10 ns pulses. Plasma dynamics, plasma chemistry, neutral gas phase chemistry and surface kinetics are fully resolved during the powered pulses. During the interpulse period (IP), only the neutral gas phase chemistry and surface kinetics are followed.

Typical conditions in the bulk plasma and near the surface at the end of the discharge pulse 3.5 ns after initiation in an atmospheric pressure mixture of He/O₂/H₂O = 98/1/1 are shown in Fig. 14. The avalanche, terminated by charging of the PP dielectric, produces electron densities and ion densities of 10¹³ cm⁻³, and densities of O atoms of 10¹³ cm⁻³. As the avalanche approaches the surface, electrons penetrate inside surface features to a limited extent, but withdraw due to surface charging. Surface features having large view angles to the plasma rapidly acquire a large negative charge, thereby preventing further penetration into the surface structure. Positive ions have similarly limited penetration due to the local ambipolar forces which constrain their transport. Neutral radicals such like O penetrate deeper inside the surface features by diffusion.

Surface treatment results from reactions with radicals such as O and O₃ during the IP for accumulated periods of tens to hundreds of ms following tens to hundreds of discharge pulses. In the results discussed here, the densities of surface functional groups reached a steady state over few hundreds of ms. The extent of functionalization was investigated as a function of O₂ fraction, f(O₂), which in large part determines the ratio of the flux of O and O₃ to the surface. O atoms are efficient at initiating surface reactions by H abstraction. O₃ initiates the rapid pathway leading to conversion of surface radicals to alcohol functional groups. The dependence of O fluxes to the surface is shown in Fig. 15(a) as a function of f(O₂). At the end of the discharge pulse (start of the IP period), the O atom flux monotonically increases with f(O₂) due to there being more electron impact dissociation of O₂. As f(O₂) increases, however, the rate of conversion of O to O₃ also increases. As a result, there is little O atom flux to the surface at the end of the IP period with large f(O₂). The O atoms have largely been converted to O₃.

Fluxes of O radicals and O₃ along the surface averaged over an IP period for f(O₂) of 10% and 75% are shown in Figs. 15(b) and 15(c). There is large scale and small scale structure. The large scale structure results from the spatial distribution of radicals incident onto the surface and the rate of conversion of O to O₃. At high f(O₂), O atoms are more rapidly converted to O₃ and so the transport of O atoms is reaction limited. The flux of O is larger near the axis where the O atom production by electron impact is largest. At low f(O₂), both the production of O atoms and the rate of conversion to O₃ are lower but the O-atoms are more mobile, thereby producing more uniform fluxes on a macro-scale. The small scale structure results from the ability of O, OH and O₃ to penetrate into the microstructure of the film. On a micro-scale, there is a ±30-40% variation in the fluxes to the surface. Protruding tips with larger view angles to the plasma receive larger fluxes of O and O₃ than the recesses of the surface structure.

Alcohol function groups, (R-OH) are formed under humid conditions where there is a reasonable flux of O atoms and a significant flux of OH radicals. The reaction sequence begins with abstraction of H from R-H by O or OH to form alkyls, R-•. In the absence of large O atom fluxes, the alkyl sites are passivated by O₂ to form peroxy sites, R-O-O•, which react with OH to yield R-OH on longer timescales. With moderate O-atom or O₃ fluxes, alkyl sites are passivated to form alkoxy sites, R-O•, which in turn abstracts H atoms on surrounding sites to form R-OH sites. With abundant formation of R-O•, the formation of R-OH by this surface-surface process is very rapid on timescales of tens of milliseconds. A secondary H abstraction reaction of R-OH by O atoms reforms alkoxy sites. One should therefore expect large alcohol functionalization for conditions that provide moderate fluxes of O and OH and low O₂ fluxes.

The surface coverages of alcohol [$s(\text{R-OH})$], peroxy [$s(\text{R-O-O}\bullet)$] and alkoxy [$s(\text{R-O}\bullet)$] functional groups for different $f(\text{O}_2)$ after a treatment time of 1 s are shown in Fig. 16(a). Due to the large fluxes of O_2 at any finite $f(\text{O}_2)$, $s(\text{R-O-O}\bullet)$ will exceed $s(\text{R-OH})$. The ratio between $s(\text{R-O-O}\bullet)$ and $s(\text{R-OH})$ can, however, be controlled by $f(\text{O}_2)$. At low $f(\text{O}_2)$, alkyl sites are passivated into predominantly peroxy rather than alkoxy, $\text{R-O}\bullet$, groups due to there being low fluxes of O_3 which would otherwise form alkoxy sites. As $f(\text{O}_2)$ decreases, more discharge energy is expended in the dissociation of H_2O rather than O_2 , thereby increasing OH fluxes. The larger rate of H abstraction by OH followed by passivation by O_2 results in $s(\text{R-O-O}\bullet)$ being maximum at approximately $f(\text{O}_2)=0.01$. Also, as $f(\text{O}_2)$ decreases, which increases the fluxes of OH, $s(\text{R-OH})$ increases reaching a maximum at $f(\text{O}_2) = 0.05$. $s(\text{R-OH})$ decreases at lower values of $f(\text{O}_2)$ primarily because the formation of alkoxy sites decreases due to the lower fluxes of O_3 . This reduces R-OH formation through the surface-surface reaction of $\text{R-O}\bullet$ abstracting H from an adjacent surface site.

As $f(\text{O}_2)$ increases beyond 5-10%, the fluxes of O and OH decrease while the flux of O_3 increases. The rate of formation of $\text{R-O-O}\bullet$ is lower, being replaced by formation of $\text{R-O}\bullet$ due to the larger flux of O_3 . Higher O_3 fluxes convert available alkyl sites into alkoxy groups which predominate over peroxy groups. In spite of the larger $s(\text{R-O}\bullet)$, the availability of alkyl sites is rate limiting and so formation of $s(\text{R-OH})$ by OH passivation decreases. As $f(\text{O}_2)$ increases beyond 30%, the creation of alkyl sites is the rate limiting step and $s(\text{R-O}\bullet)$ decreases.

$s(\text{R-OH})$ as a function of position for different $f(\text{O}_2)$ after a treatment time of 1 s are shown in Fig. 16(b). The macro-scale variations in $s(\text{R-OH})$ at large $f(\text{O}_2)$ are due to spatial gradients in radical fluxes, predominantly O, that make alkyl sites which are the precursor to

R-OH. Micro-scale variations in $s(\text{R-OH})$ are most significant at very low and higher $f(\text{O}_2)$. The uniformity of coverage is best at $f(\text{O}_2)$ of 10%. This variation is ultimately tied to the disposition of alkyl sites. At very low $f(\text{O}_2)$, alkyl sites are saturated into peroxy groups that contribute to alcohol formation and increase micro-scale non-uniformities. At higher $f(\text{O}_2)$ higher O_3 fluxes rapidly convert alkyl to alkoxy sites, thereby eliminating the R-OH precursor. The transport of O_3 is therefore important to the uniformity of functional groups on a micro-scale. For example, alkyl coverage along the surface after 0.05 s of treatment is shown in Fig. 16(c). The locations that have smaller alkyl coverage are at the tips of the surface structure. These are sites that have larger view angles and receive larger fluxes of O_3 which passivates alkyl sites.

6.5 Concluding Remarks

Using the 2-d integrated plasma dynamics – surface kinetics multi-scale model, the functionalization of rough PP surfaces, with characteristic features on length scales of a few μm , using repetitively pulsed atmospheric pressure discharges in various gas mixtures was investigated. In humid air discharges, charged species created in the discharge during the pulse penetrate into the rough surface features to a limited extent. The penetration of charged species depends on the discharge polarity. In positive discharges a sheath like region near the surface prevents electrons from getting into the surface features. Radicals are longer lived and able to penetrate into all surface features over timescales of a few 100s μs . Reactive radicals like OH are depleted near exposed surface features reducing fluxes inside the nooks and crannies. Together with the high density of O atoms, the abstraction of H atoms from the surface creates alkyl radicals during the pulse. Additionally, photons cause

cleavage of C-C and C-H bonds on the surface yielding surface radicals. Positive ions do contribute to surface reactions, but not very significantly because of short pulse duration.

Various functional groups such as R-OO•, R-O•, R-OH and R-COOH and R-C=O are created on the PP surface as a result of functionalization. The coverage of R-OO• predominates because of the large O₂ content in the gas. The coverage of R-O• is also significantly high as a result of large O₃ fluxes. The coverage of R-OH and R-COOH which are formed by reactions of groups already on the surface is lower because of their lower reaction rates. At lower voltages, lesser ionization results in lower O₃ content, so the R-O• pathway is slower compared to the R-OO•. At lower f(H₂O), the formation of OH is reduced and more electron energy is channeled into the formation of O atoms. As a result O₃ increases with f(H₂O) increasing the coverage of R-O•.

The R-OH functionalization of PP surfaces having microstructure by atmospheric corona discharges sustained in He/O₂/H₂O mixtures was investigated. Non-uniformity in functionalization on macro- and micro-scales is attributed to temporal and spatial variations in reactive fluxes, their ability to penetrate into the microstructure and the disposition of surface radical sites. In low f(O₂) mixtures, secondary reactions of peroxy groups with OH radicals increase micro-scale non-uniformities. The production of O₃ is low, which creates fewer alkoxy, alcohol and carbonyl groups on the surface. A large fraction of alkyl sites are therefore passivated with O₂ to form peroxy groups. With intermediate f(O₂) mixtures, about 10%, the flux of O atoms is more uniform and the formation of O₃ is low. As a result functionalization is more uniform on both macro- and micro-scales. With either lower or higher f(O₂), transport of O atoms and OH is limited by the rapid local reaction kinetics and

the formation of reactive O_3 , which result in larger variations in functionalization between surface sites that have large and small view angles to the plasma.

6.6 Figures

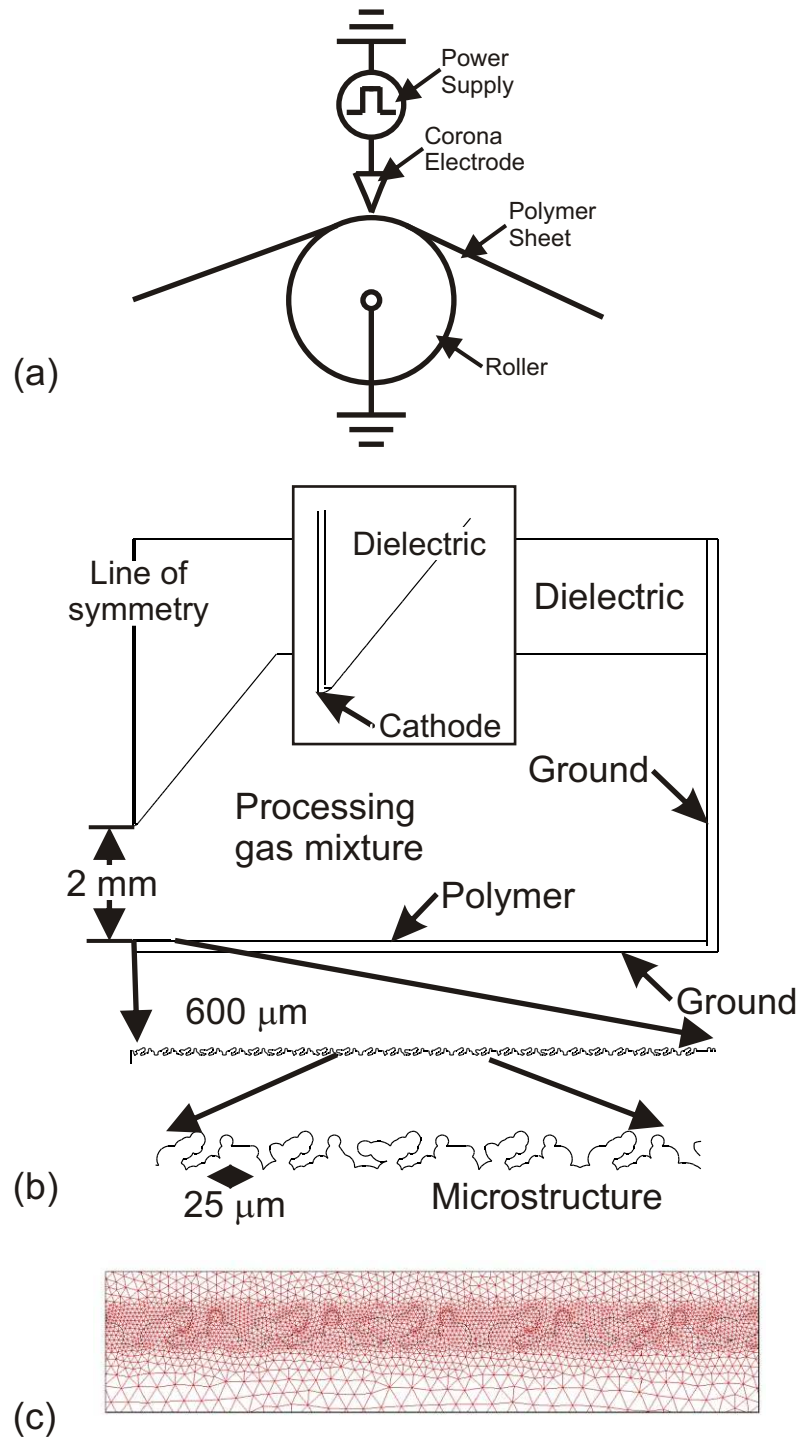


Fig. 1 Schematic of the corona treatment device. (a) The typical web-roller arrangement for polymer treatment and (b) Close-up magnification of the discharge region including the rough polymer surface having micron-sized strand-like features. (c) Refinement zones were used to resolve surface features with resolution of $< 1 \mu\text{m}$.

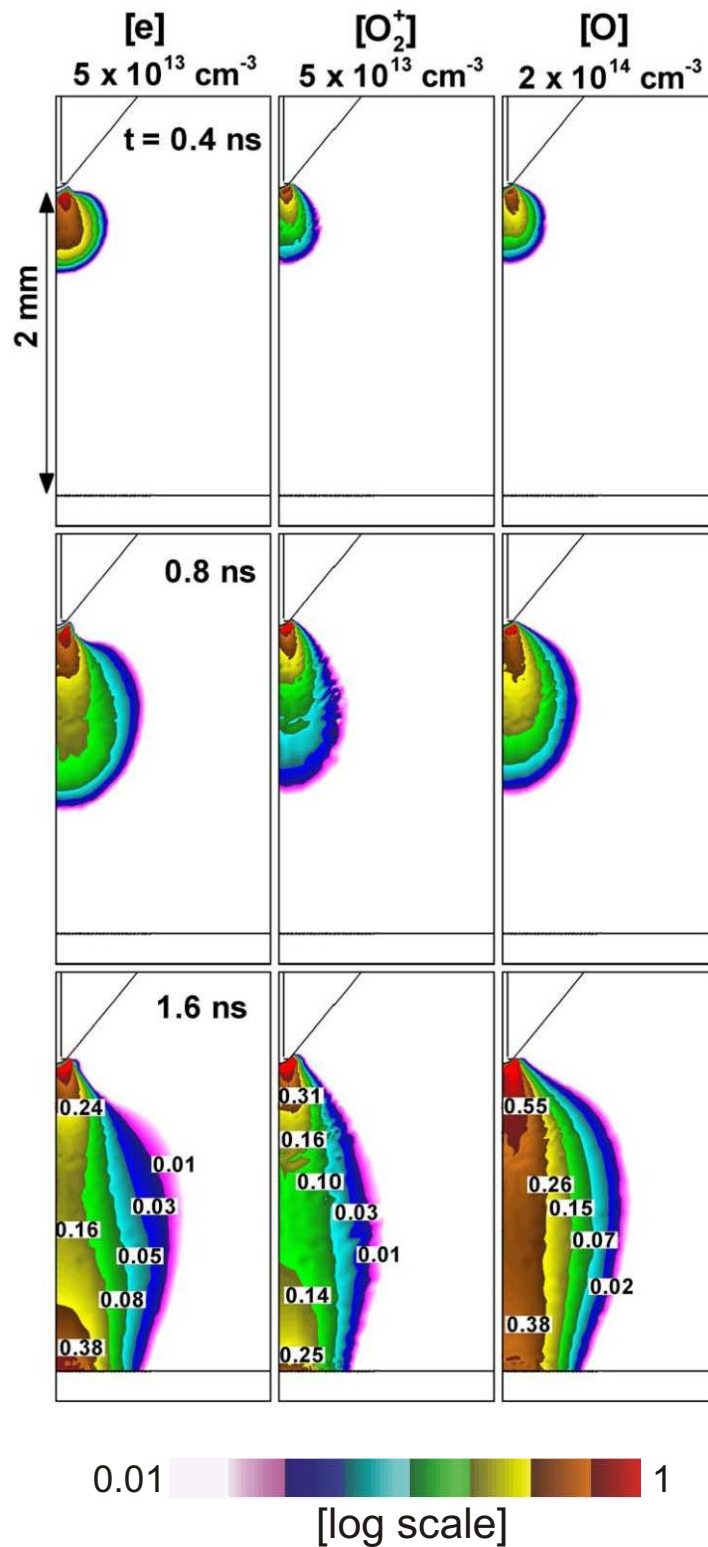


Fig. 2 Densities of [e], positive ions and [O] radicals during the first breakdown pulse in a negative humid air discharge.

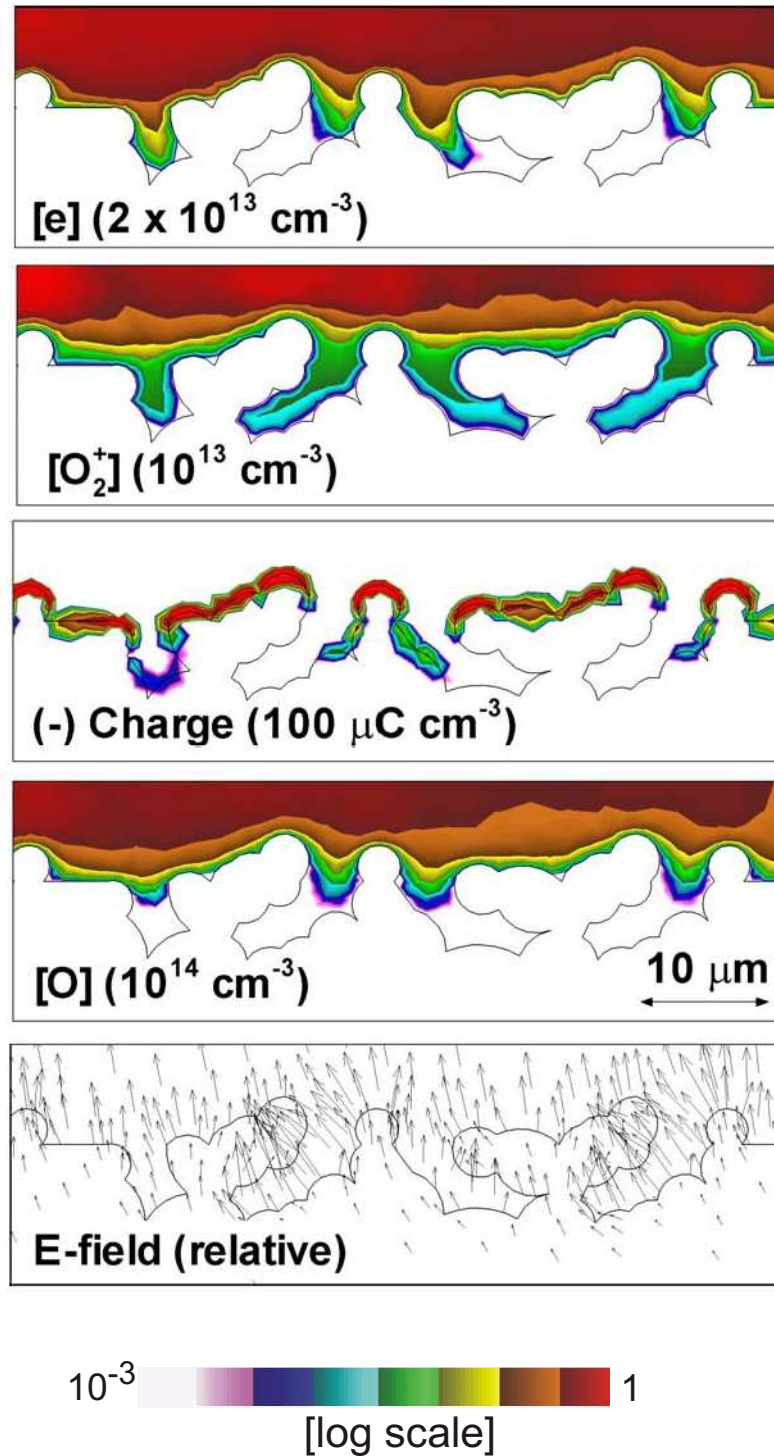


Fig. 3 Plasma penetration of rough polymer surface features during the pulse - (a) electrons, (b) positive ions, (c) negative surface charge and (d) O atoms in the negative humid air discharge..

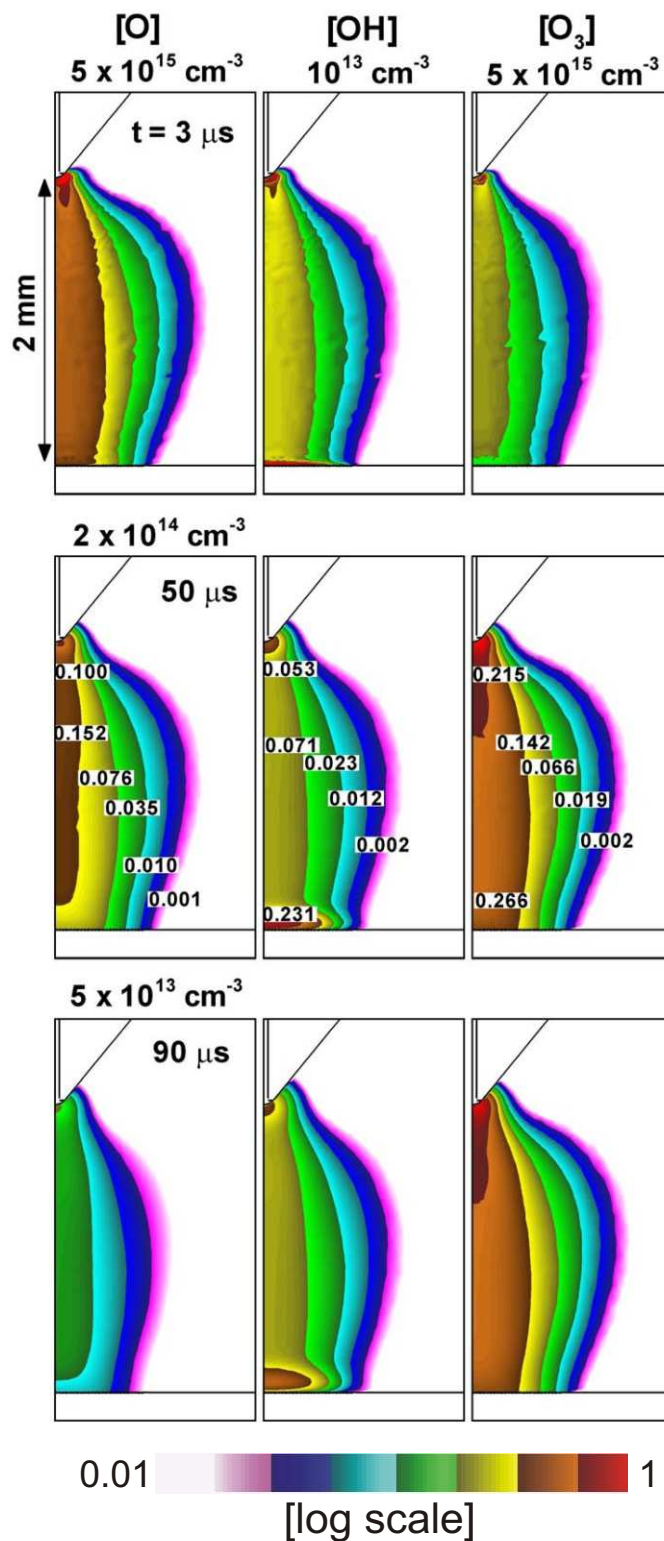


Fig. 4 Density of O atoms, OH and O₃ radicals at different times during the interpulse period (duration 100 μs) of the negative humid air discharge.

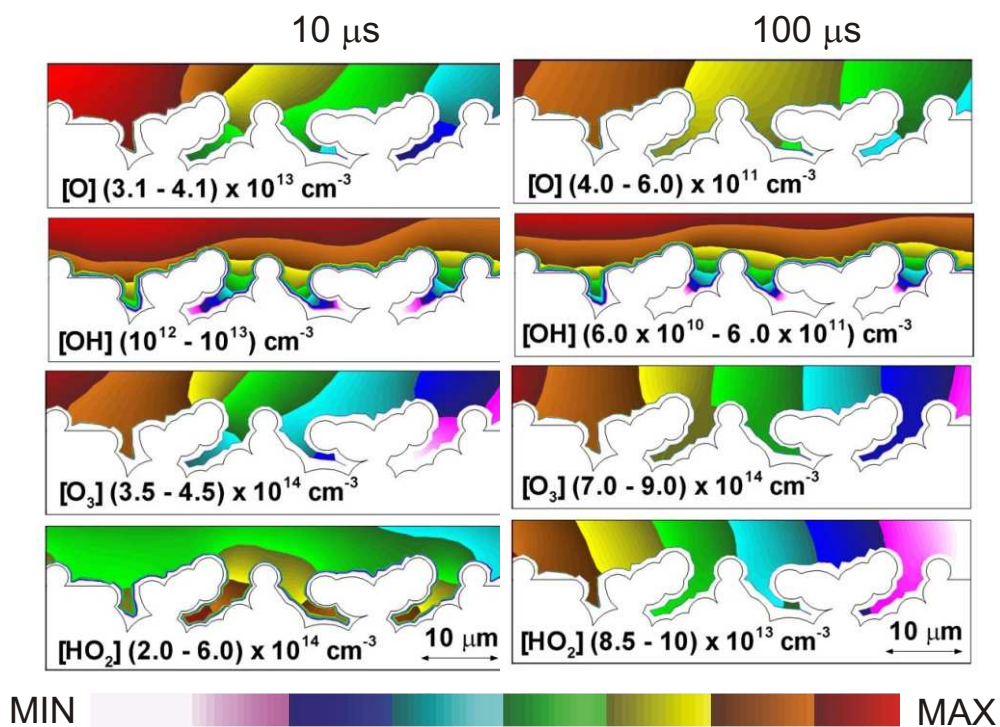


Fig. 5 Plasma penetration of rough polymer surface features during the interpulse period - (a) O atoms, (b) OH, (c) O_3 in the negative humid air discharge.

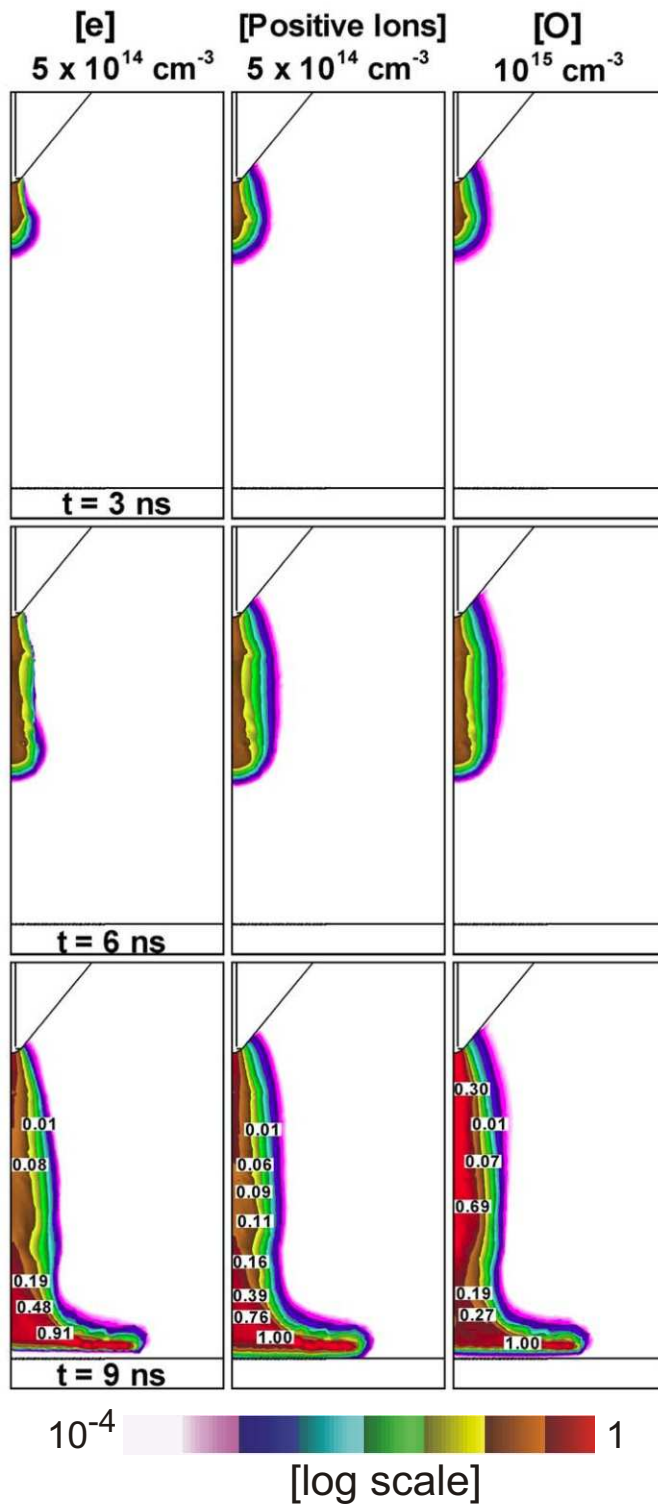


Fig. 6 Densities of [e], positive ions and [O] radicals during the first breakdown pulse in a positive humid air discharge.

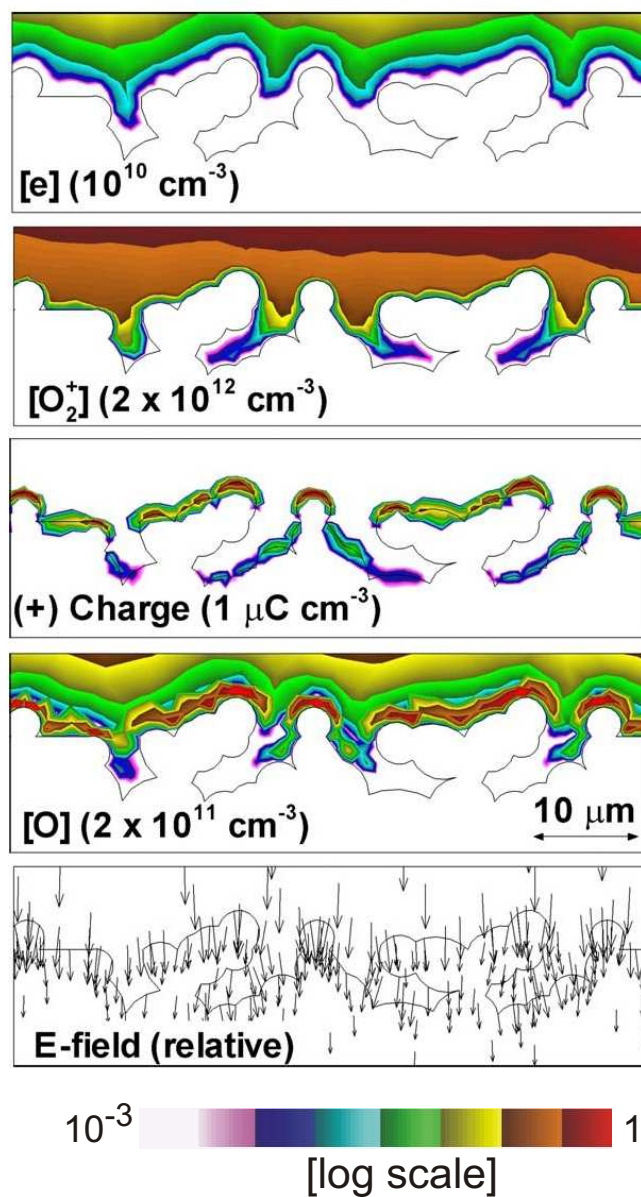


Fig. 7 Plasma penetration of rough polymer surface features during the pulse - (a) electrons, (b) positive ions, (c) positive surface charge and (d) O atoms in the positive discharge in humid air.

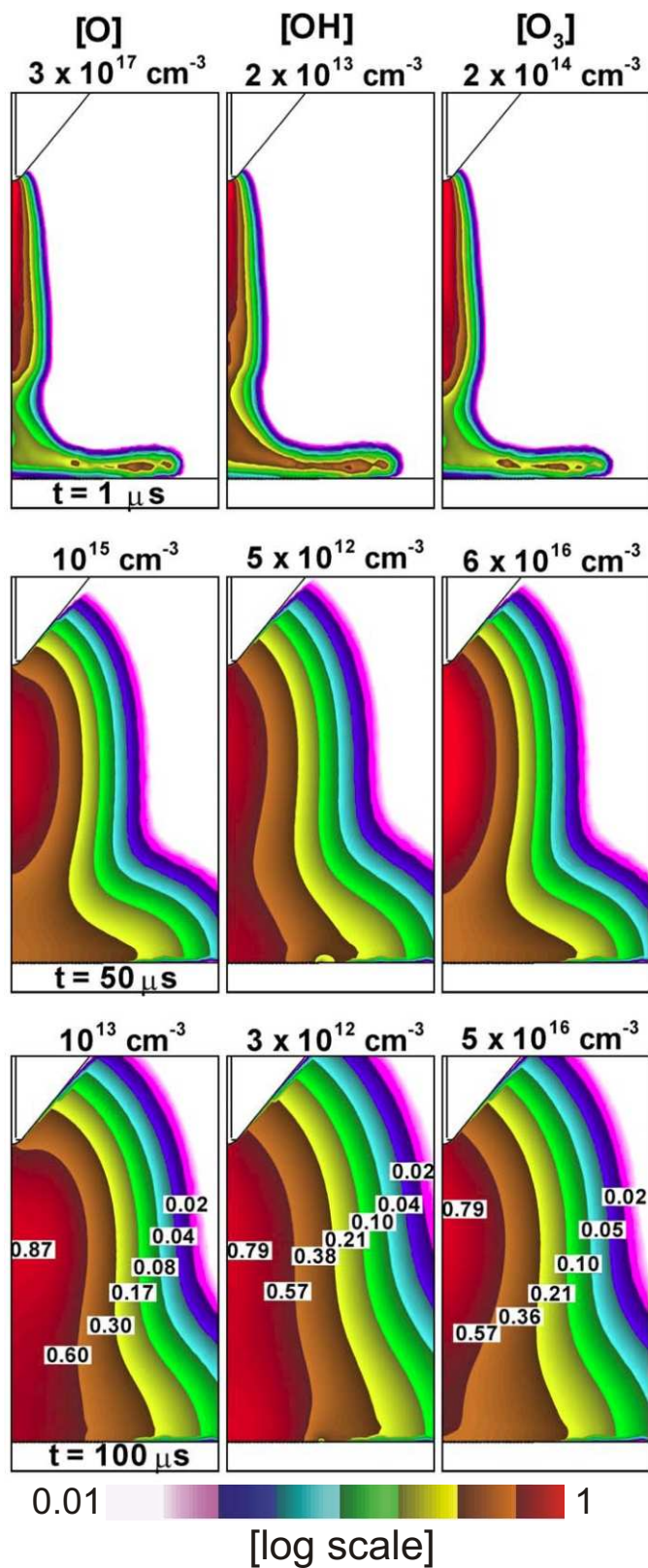


Fig. 8 Density of O atoms, OH and O₃ radicals at different times during the interpulse period (duration 100 μs) in the positive humid air discharge.

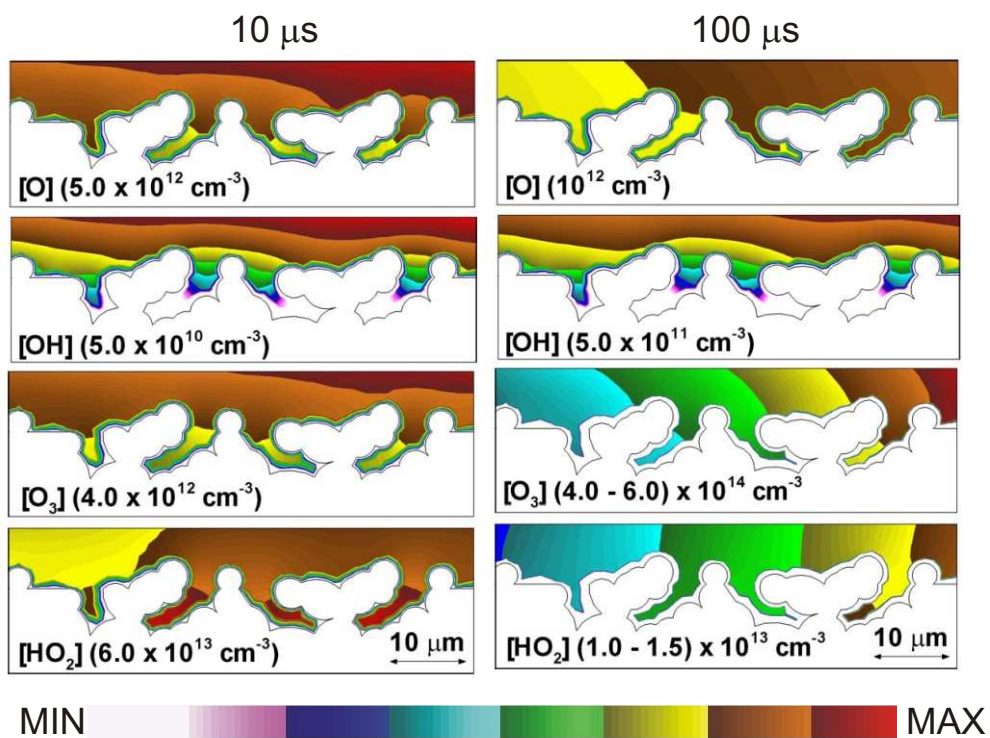
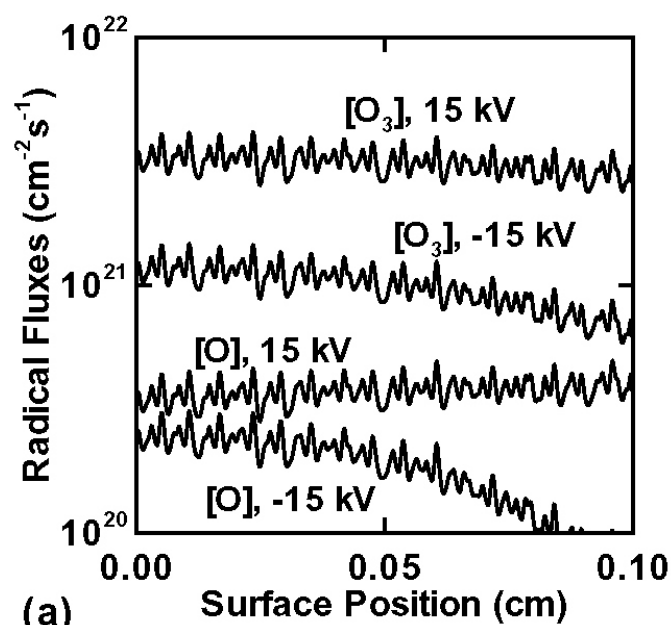
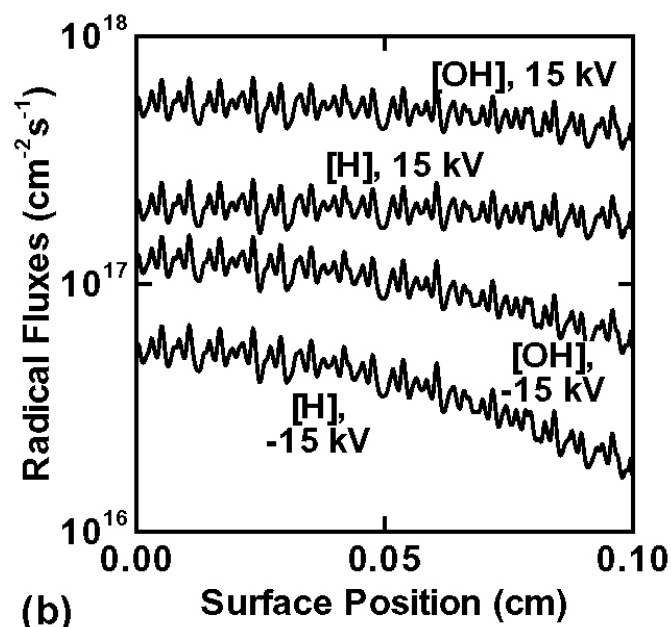


Fig. 9 Plasma penetration of rough polymer surface features during the interpulse period - (a) O atoms, (b) OH, (c) O₃ in the positive humid air discharge.



(a)



(b)

Fig. 10 Variation of averaged fluxes with position along the rough surface features, (a) O atoms and O₃ radicals and (b) OH and H atoms in the negative and positive humid air discharges.

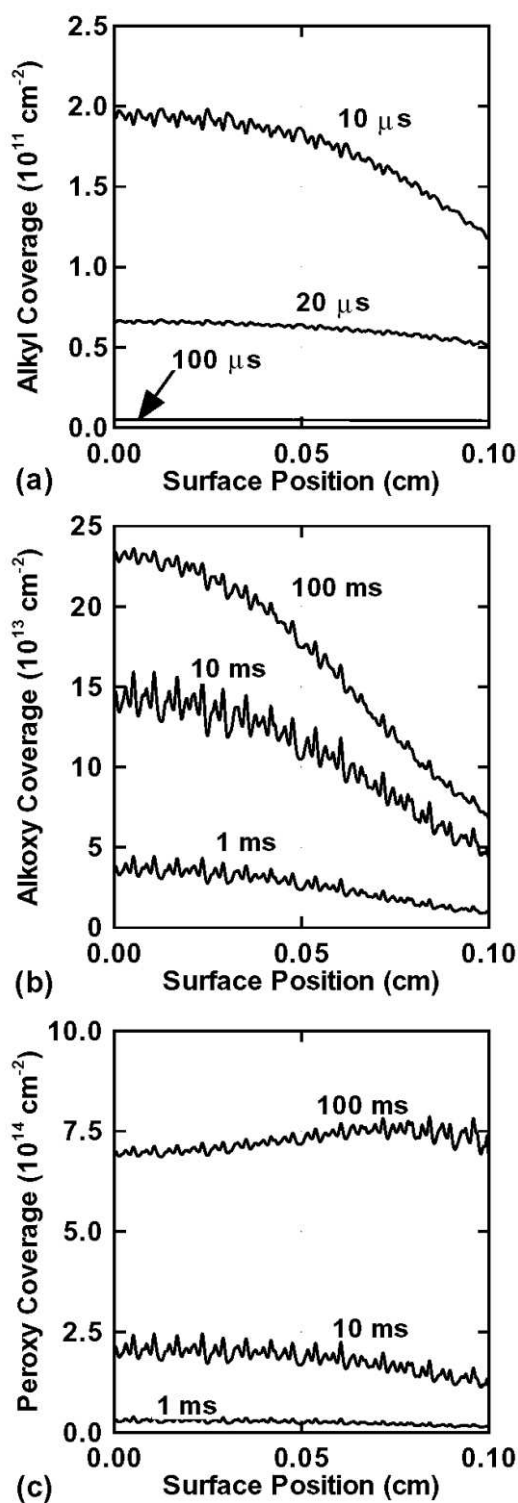


Fig. 11 Temporal variation of coverage of (a) alkyl radicals (R-), (b) alkoxy (R-O) and (c) peroxy (R-OO) groups with position along the rough surface features during treatment in the repetitively pulsed negative discharge in humid air.

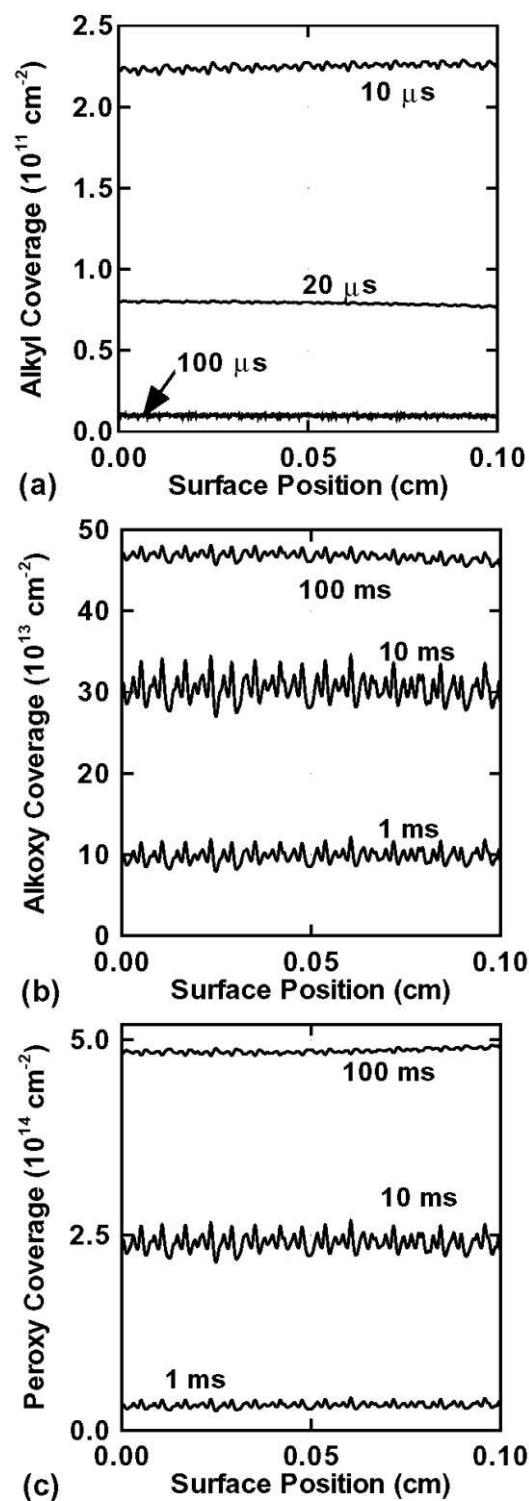


Fig. 12 Temporal variation of coverage of (a) alkyl radicals (R-), (b) alkoxy (R-O) and (c) peroxy (R-OO) groups with position along the rough surface features during treatment in the repetitively pulsed positive discharge in humid air.

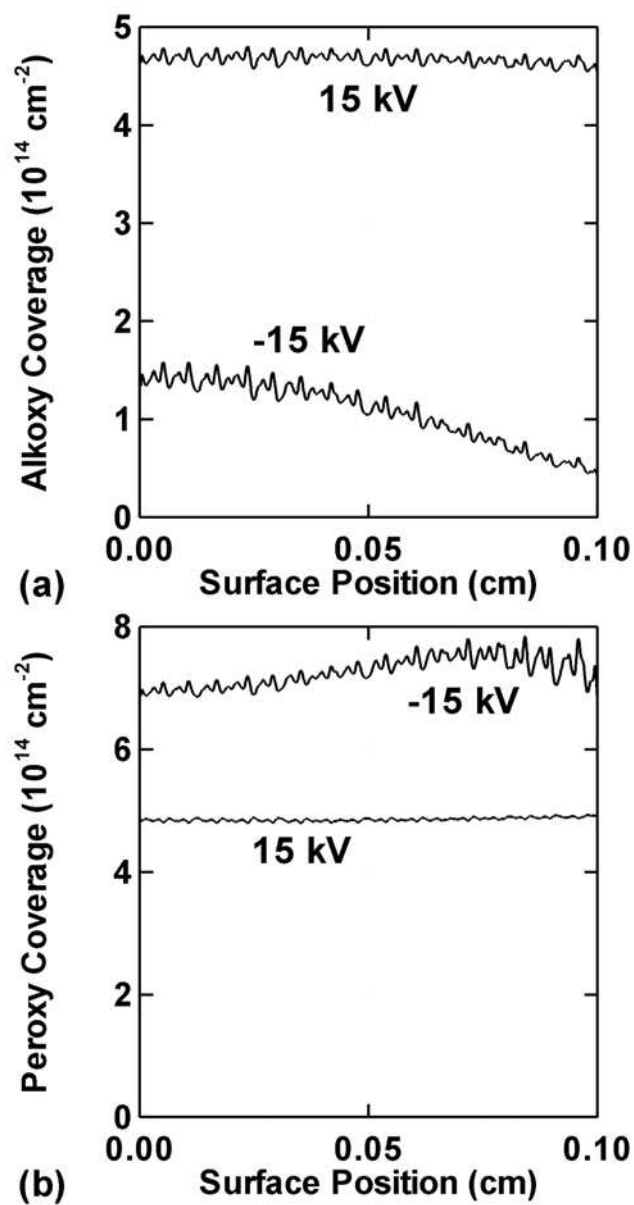


Fig. 13 Variation of coverage of (a) alkoxy (R-O) and (b) peroxy (R-OO) groups with position along the rough surface features in the repetitively pulsed negative and positive discharges.

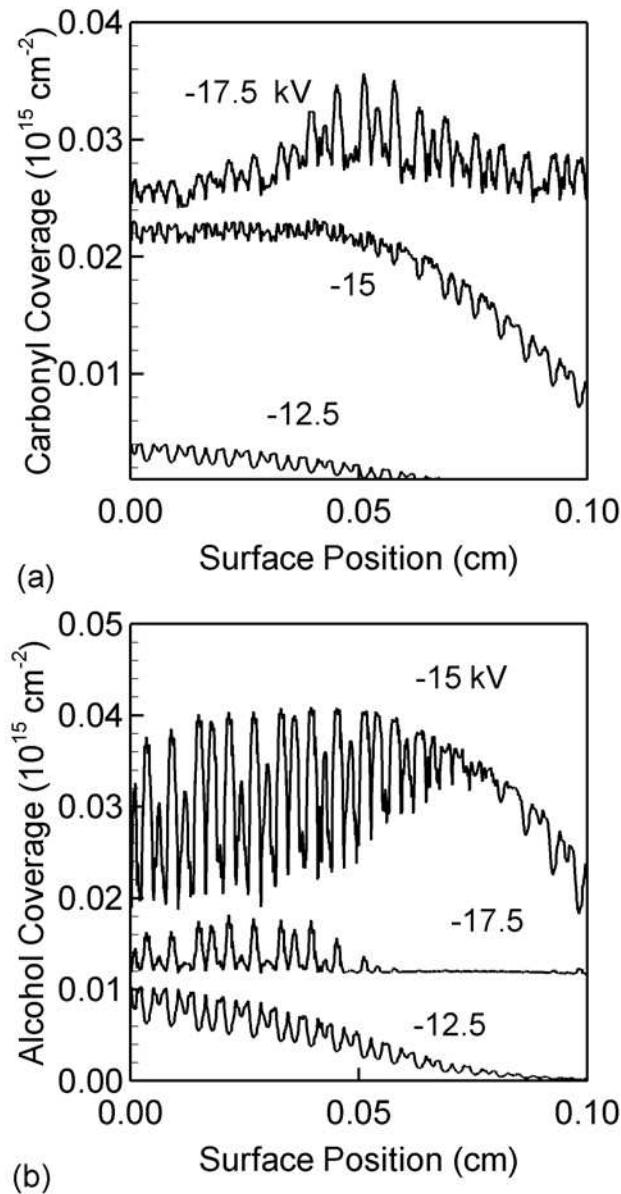


Fig. 14 Variation of coverage of (a) carbonyl (R-C=O) and (b) alcohol (R-OH) groups with position along the rough surface features in the repetitively pulsed negative discharges. Coverage increases with voltage, becoming more non-uniform closer to the discharge axis due to high fluxes of reactive species such as O atoms.

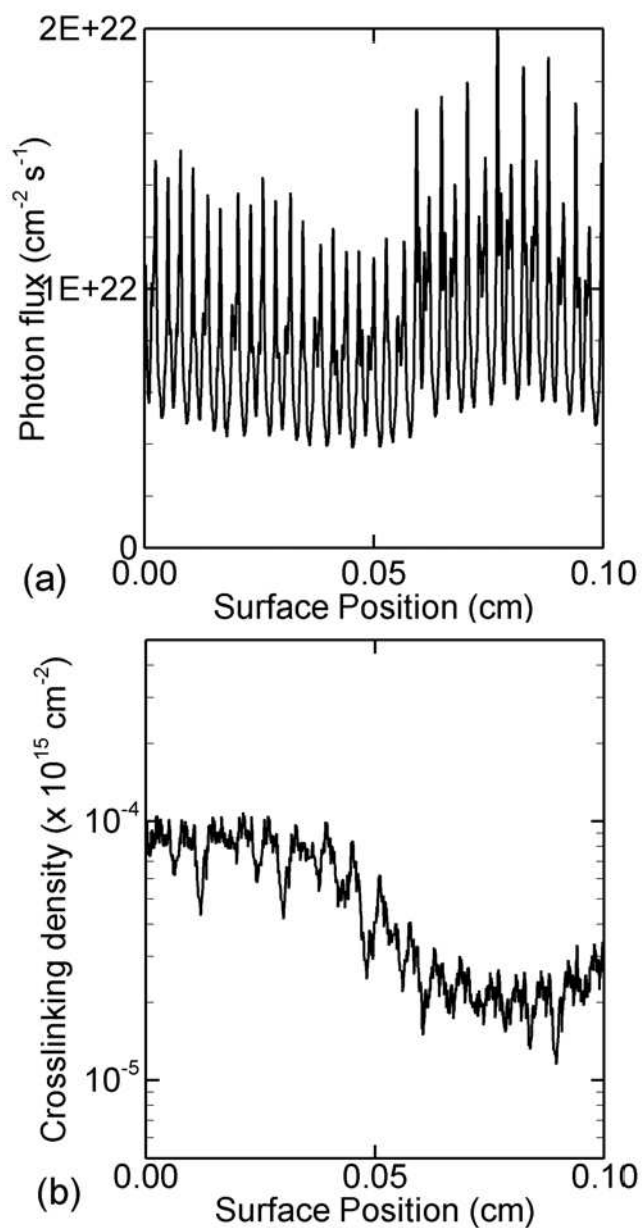


Fig. 15 (a) The flux of photons at the surface at the end of a -17.5 kV pulse. The sharp variations are caused by the line of sight photon transport which causes shadowed surface features to receive lesser flux. (b) The density of crosslinked sites on the surface after 1 s of treatment.

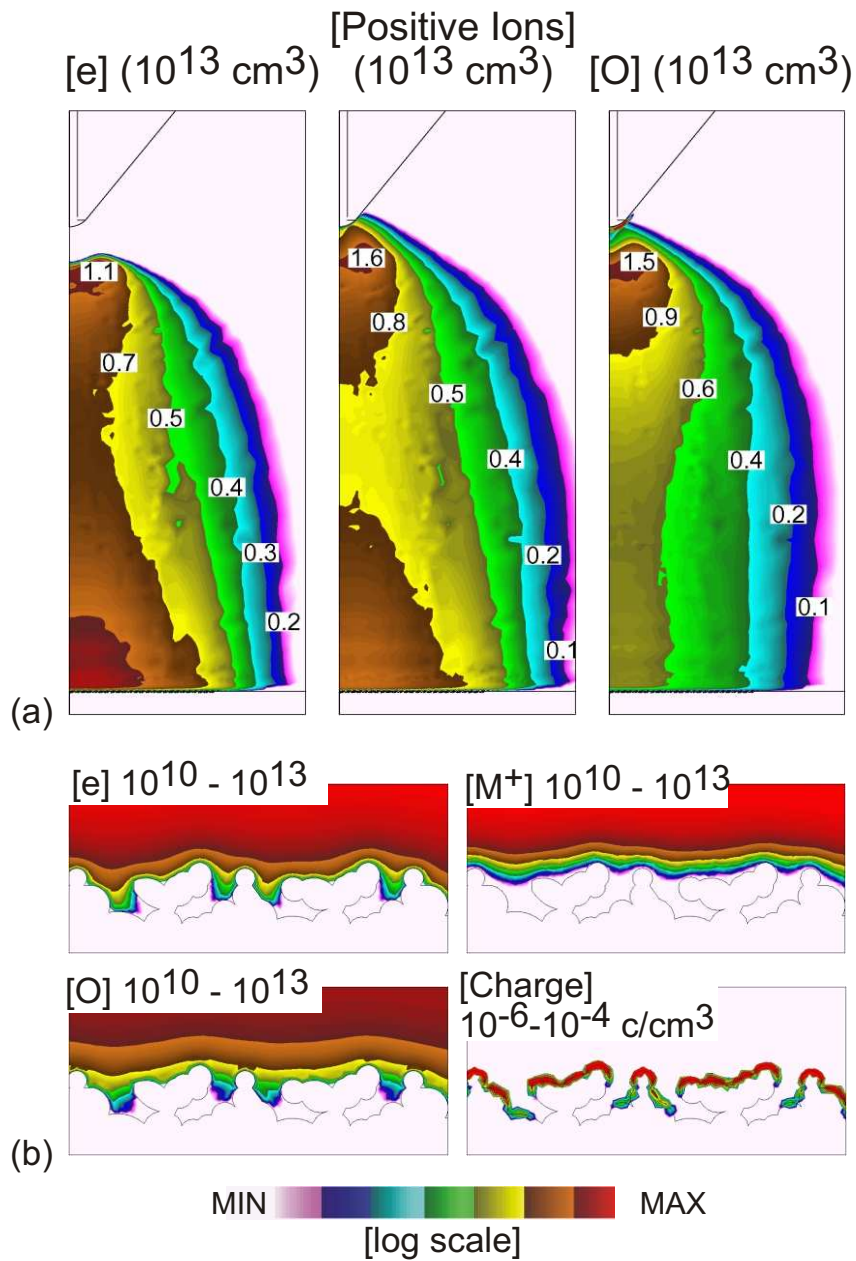


Fig. 16 Plasma and surface properties after the avalanche closes the gap for $\text{He}/\text{O}_2/\text{H}_2\text{O} = 98/1/1$. The densities of $[e]$, O atoms and positive ions are shown in the (a) bulk plasma and (b) near the surface (including surface charge). Charged species penetrate to a limited extent into surface features.

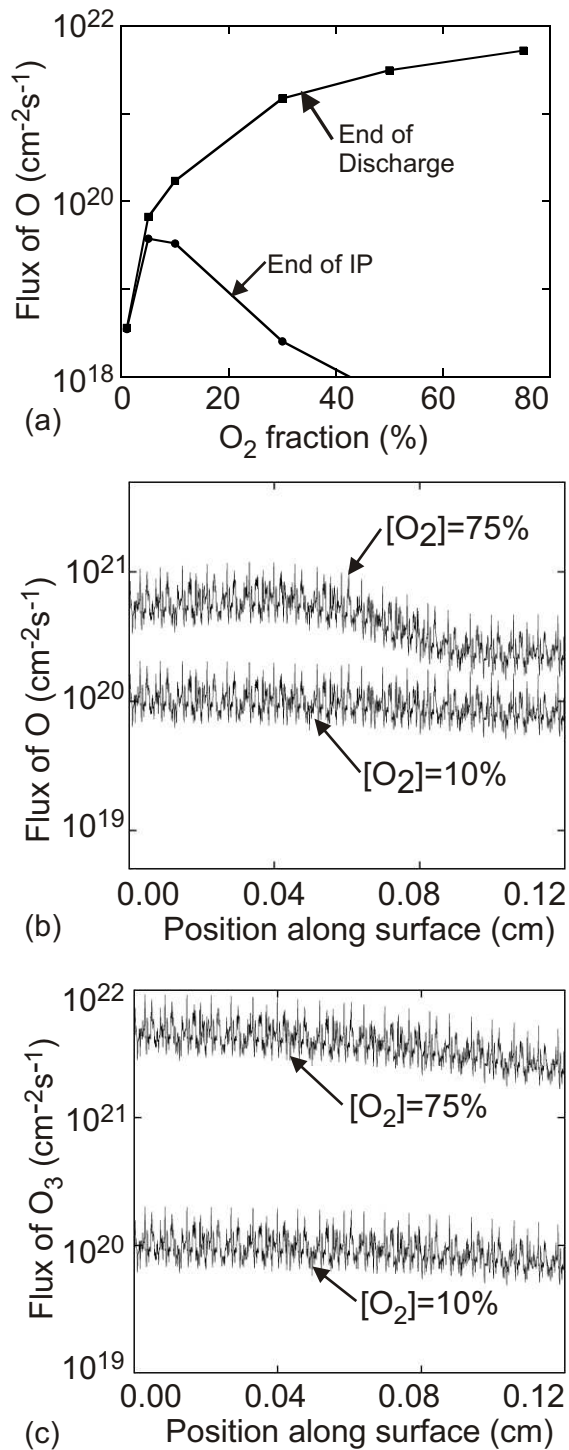


Fig. 17 Fluxes of O and O_3 to the surface. (a) O-atom fluxes at the end of the discharge pulse [start of interpulse period (IP)] and at the end of the IP at a position 0.05 cm along the surface from the axis. (b) O-atom fluxes along the surface averaged over an IP for $f(\text{O}_2)$ of 10% and 75%. (c) O_3 fluxes along the surface averaged over an IP for $f(\text{O}_2)$ fractions of 10% and 75%.

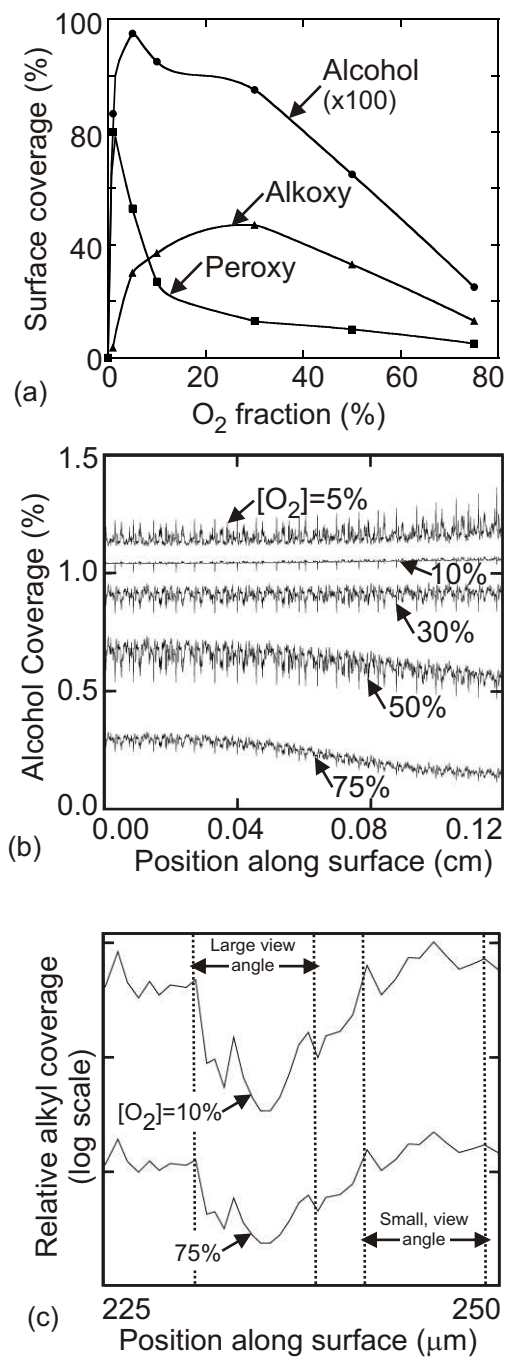


Fig. 18 Surface functionalization for different for $f(O_2)$ (a) Average surface coverage of alkoxy, peroxy and alcohol functional groups after 1 s treatment. (b) Coverage of alcohol groups with position along surface after 1 s treatment. (c) Surface coverage of alkyl radicals after 0.05 s treatment for $f(O_2)$ 10% and 75%.

6.7 References

1. L-A. O'Hare, S. Leadley and B. Parbhoo, *Surface and Interface Analysis*, **33**, 335 (2002).
2. N. De Geyter, R. Morent and C. Leys, *Plasma Sources Science and Technology*, **15**, 78, (2006).
3. U. Vohrer, M. Muller and C. Oehr, *Surface and Coatings Technology*, **98**, 1128 (1998).
4. M. Nitschke et al, *Journal of Biomedical Materials Research*, **59**, 632 (2002).
5. A. A. Meyer-Plath, K. Schroeder, B. Finke and A. Ohl, *Vacuum*, **71**, 391 (2003).
6. J. H. Lee, et al, *Journal of Polymer Science, Part A, Polymer Chemistry*, **32**, 1569 (1994).

7. TREATMENT OF ROUGH SURFACES AND POROUS POLYMER MICROSPHERES IN PULSED NH₃ AND O₂ DISCHARGES

7.1 Introduction

Polymer surfaces with functional groups are used in wide-ranging applications as biomaterials substrates for immobilization of biomolecules or enzymes [1], anti-coagulation surface, for cell patterning and tissue engineering [2]. In general, N-containing groups are favored in biomedical applications for their ability to interact with a wide variety of biomolecules. Often, the primary amino (-NH₂) groups serve as binding sites on the polymer surface for spacer molecules to interlock during immobilization. Traditionally, low pressure plasmas sustained in N₂ or N-containing gases such as NH₃ have been used for such treatments. Hayat *et al*, [3] used ammonia radiofrequency discharges at 75 mTorr and 10 W to modify polyethylene (PE) surfaces with -NH₂ groups to subsequently immobilize proteins. They found that the surface modification occurs rapidly within 1 min of treatment, increasing -NH₂ coverage from 0% up to 7%. For the same power input, higher treatment time was required to achieve a similar -NH₂ coverage at 300 mTorr.

Holmes and Schwartz [4] used NH₃-plasmas at 1 Torr to functionalize PE surfaces varying the power from 5-100 W and time of treatment from 1 to 10 minutes. They found that optimal -NH₂ coverages were obtained by using intermediate power input and treatment times. In the work of Liu *et al*, the surfaces of microporous polypropylene membranes were functionalized with -NH₂ groups using ammonia plasmas generated at higher pressures of 10s Torr to enable subsequent covalently bonding of polypeptides to the surface.[5] Such polymer surfaces can be rough to serve as scaffolds to promote cell growth in tissue engineering or to enhance the biocompatibility of implants.[6]

A state-of-the-art in plasma amino-functionalization of polymer surfaces is found in [7]. One of the issues encountered in the amine functionalization is the lack of detailed understanding of surface reaction mechanisms. Experiments are useful in determining possible reaction pathways, but rate coefficients are hard to obtain, unlike the case of discharges in O₂. Another is the lack of detailed description of the plasma dynamics that ultimately affects the polymer surface. Modeling the plasma dynamics involves the treatment of a large number of possible gas phase reactions, especially with polyatomic molecules, due to vibrational and dissociation losses and so on. Modeling may help determine the dominant species reacting with the surface how process conditions may be optimized for treatment.

The use of plasma-based techniques to functionalize surfaces of polymer microspheres and powders in order to improve properties such as surface reactivity and biocompatibility have been reported in literature.[8-10] For instance, Sipehia *et al*, used anhydrous ammonia plasma to generate amino (-NH₂) groups on the surfaces of polypropylene beads to bond with enzyme molecules.[11] The surface reactivity of the polymer can markedly change even when new chemical groups cover only a small fraction of the surface. The inert pore surfaces of macroporous polyethylene used in chromatographic columns were treated downstream of the ammonia discharge to make them reactive enough to bind colloidal particles.[12]

Accessibility of the surfaces of porous materials and powders that exhibit large surface-to-volume ratios is important in determining whether the surface treatment will be uniform. Innovative techniques may be needed to improve accessibility to the complex surface shapes that often require treatment. For instance, fluidized bed reactors have

improved uniformity in functionalization and deposition on the surfaces of powders and small particles by suspending particles effectively during the treatment.[13] Pharmaceutical powders have been treated in atmospheric pressure corona discharges using these methods to improve flow and surface charge properties and reduce agglomeration.[14] Low pressure O₂ plasma treatments of polymers produce O-groups on the surface. Similar groups are grafted during atmospheric pressure corona discharge treatment. In principle then, the type of surface functionalization achieved with plasmas at low pressures could be achieved with atmospheric pressure discharge treatments.

In this work, the possibility of using atmospheric pressure discharges in NH₃ containing gas mixtures to produce amine groups on polypropylene surfaces was investigated using the two-dimensional integrated plasma hydrodynamics-surface kinetics model described in Chapter 2. Features resembling rough and porous surfaces were modeled to investigate the plasma-surface interactions during treatment in NH₃ plasmas. NH₂ and NH fragments are efficiently generated in NH₃ containing plasmas by electron impact dissociation. The dependence of the spatial uniformity of surface –NH₂ groups with gas composition and applied voltage is discussed.

The treatment of porous microspheres 10s μm in size with pore diameters a few μm were simulated in He/NH₃/H₂O mixtures to determine the effect of surface shapes and sizes on the accessibility to the reactive species generated in the discharge. There was some effect on varying the size, with smaller microspheres being treated to a greater degree. There was little effect of varying pore diameters, in the range considered in these studies, on the degree of surface treatment. The outer surfaces of the microspheres were treated to a similar degree,

irrespective of their size, but significantly lower treatment ensued along the inner pore surfaces due to poor penetration of gas phase radicals.

The treatment of suspended microspheres was investigated by having three microspheres suspended within the discharge volume, randomly oriented. If such microspheres are treated by flowing them through the discharge, then treatment must be rapid (ms). Since discharges in O₂ are known to rapidly functionalize polymer surfaces, the oxidation of suspended polymer microspheres in He/O₂/H₂O discharges was investigated.

7.2 Treatment of Rough Polymer Surfaces

The corona configuration discussed in Chapter 5 was used in these investigations. The upper metal electrode is housed in dielectric material and exposed to the processing gas at its tip and is normally powered at a few kHz. The gap between the upper electrode and the lower grounded metal electrode is 2 mm. The rough polymer is placed on the grounded electrode. The base case conditions are atmospheric pressure, gas composition of He/NH₃/H₂O=98/1/1. The discharge is initiated in each case with short voltage pulses of a few kV lasting a few ns to the upper electrode.

During the pulse (usually < 10 ns), reactions involving electronic impact excitation and ionization lead to the formation of radicals and ions. Between pulses radical reactions dominate and three-body reactions lead to the formation of new species. The plasma dynamics and chemistry including charged species and neutral transport as well as surface kinetics are resolved during the pulse. The reaction kinetics, neutral transport and surface kinetics are tracked in the interpulse period. The reactive radicals generated in significant amounts in these discharges include OH, NH₂ and H atoms that react with the PP surface functionalizing it with N-containing groups such as R-NH₂ (amines) and R-NH (amino

radical) and R=NH (imines) groups. The reaction mechanisms used in these investigations are discussed in detail in Chapter 2.

Typical conditions at the end of the -5 kV pulse for the base case conditions are shown in Fig. 1. The avalanche creates an electron density of about 10^{13} cm^{-3} in the bulk plasma. NH_3 is efficiently dissociated by electron impact during the pulse forming significant amounts of NH_2 and H. The density of NH_2 radicals is about $5 \times 10^{13} \text{ cm}^{-3}$ after the pulse. The dissociation of H_2O leads to the formation of OH and additional H atoms. The density of plasma species near the surface is shown in Fig. 2. Electrons are present near the surface and penetrate into the surface features. Positive ions are kept out of the features due to the opposing direction of the electric field. The avalanche leads to the accumulation of surface charge of about $100 \mu\text{C cm}^{-3}$ at the surface. The density of H atoms is about 10^{12} - 10^{13} cm^{-3} , while the density of OH is about $5 \times 10^{11} \text{ cm}^{-3}$.

The density of radicals OH, H and NH_2 at the end of the interpulse period is shown in the bulk and near the surface features in Figs. 3(a) and (b) respectively. OH is depleted by gas kinetic reactions and diffusion with a peak density of $6 \times 10^{11} \text{ cm}^{-3}$ in the center of the discharge. Nearer to the surface, the density of OH is about 10^{10} cm^{-3} . The density of NH_2 decreases by a factor of 10 as they combine in three body reactions to form N_2H_4 , while the density of H atoms remains at 10^{13} cm^{-3} .

The fluxes of H, NH_2 and OH averaged over the interpulse period are shown in Fig. 4(a). There is significant microscopic structure in the OH flux with the exposed surfaces receiving about 10 times the flux at the shadowed nooks and crannies. Since OH is very reactive, the local surface kinetics dominates, depleting OH in the gas phase significantly as it diffuses into the features. The peak flux of OH is about $10^{16} \text{ cm}^{-2}\text{s}^{-1}$ at the exposed

surfaces. This is comparable to humid air discharges discussed in Chapter 5, where the high flux of O atoms ($10^{20} \text{ cm}^{-2}\text{s}^{-1}$) share in the abstraction reactions with OH but sharp microscopic variations do occur between shadowed and exposed regions. There is no significant microscopic structure in the fluxes of H and NH_2 radicals other than the shadowing effect of the surface features. The coverage of alkyl ($\text{R}\bullet$) radicals and amine (R-NH_2) groups after 100 ms are shown in Fig. 4(b). Since the OH is the primarily responsible for H abstraction, the microscopic variations in OH fluxes get mirrored into the coverages of alkyl ($\text{R}\bullet$) radicals and upon addition with NH_2 , the R-NH_2 coverage as well.

Parametric investigations were conducted varying the fraction of NH_3 , $f(\text{NH}_3)$, while keeping the fraction of H_2O constant at 1% and other conditions unchanged from the base case. The average fluxes of OH, H and NH_2 at the surface for $f(\text{NH}_3)$ at 1% , 10% and 30% are shown in Fig. 5. The microscopic structure in OH fluxes remains irrespective of $f(\text{NH}_3)$, though the magnitude of OH fluxes decreases by a factor of 10 as $f(\text{NH}_3)$ increases from 1% to 30%. This is because more electron energy is lost in inelastic modes such as vibration and excitation as $f(\text{NH}_3)$ increases and lesser energy is channeled into dissociation of H_2O creating OH. The average fluxes of H and NH_2 are about the same order of magnitude (10^{18} - $10^{19} \text{ cm}^{-2}\text{s}^{-1}$). No significant spatial gradients exist in the fluxes of any of these species at all $f(\text{NH}_3)$.

The coverage of amine groups (R-NH_2) for $f(\text{NH}_3)=1\%$ after 1 s of treatment is shown in Fig. 6(a). The peak coverage of R-NH_2 on the exposed surface features is about 3%, but less than 0.5% in the shadowed regions. This comes about due to the cumulative effect of multiple pulses having microscopic variations in OH fluxes at the surface. The variation of R-NH_2 coverage with $f(\text{NH}_3)$ is shown in Fig. 20(b) zooming into surface path of

100 mm. The peak coverage of R-NH₂ on the exposed surface features decreases from 3% to 1% as f(NH₃) increases from 1% to 30%. This results from the decrease in OH fluxes as f(NH₃) increases as discussed earlier, that translates into lower alkyl (R•) radical and R-NH₂ coverage. In the shadowed regions of the surface, the coverage of R-NH₂ is lower than 0.5% and independent of f(NH₃) as the creation of alkyl (R•) radical sites is the rate limiting step.

In He/NH₃/H₂O discharges, the uniformity of R-NH₂ coverage on rough PP surfaces is dependent on the alkyl radical density. This is partly controlled by f(H₂O) since OH radicals formed in the discharge actively participate in the abstraction reactions. The high reactivity of OH at the outer surface features results in lesser OH fluxes in the nooks and crannies. This creates non-uniformities along the surface with variations by a factor of 10 in alkyl radical and R-NH₂ surface coverages between exposed features and nooks and crannies. In high f(H₂O) mixtures, this non-uniformity decreases somewhat due to greater OH fluxes. But in low f(H₂O) mixtures, the flux of OH becomes negligible and the degree of abstraction and therefore functionalization of the PP surface itself is reduced by orders of magnitude. As f(NH₃) increases, more electron energy is spent in dissociating NH₃, leading to higher NH₂ but lower OH fluxes. As a result, the abstraction reactions become rate-limiting and the coverage of R-NH₂ decreases at higher f(NH₃).

7.3 Treatment of Porous Surfaces

Features resembling micron-sized porous beads or microspheres were used to investigate the treatment of porous surfaces. Features on few μm length scales were modeled inside the microspheres to represent some complex pore structure. A non-interconnected pore structure was developed to investigate the extent of plasma penetration and treatment as pore diameter and size of the microsphere were varied. The lower surface is grounded and

the microspheres are either placed on it or suspended in the discharge gap as shown in Fig. 7. The microspheres were located either near the grounded surface close to the discharge axis or by randomly orienting them at different locations suspended in the discharge gap.

The base case conditions consist of a gas mixture containing He/NH₃/H₂O=98/1/1 at 1 atm pressure powered by a -5 kV pulse of negligible rise time. Two identical porous microspheres of diameters 90 μm having pore opening diameter of 4.5 μm are located near the grounded metal surface with one located symmetrically on the centerline and the other a distance 270 μm off-axis. The plasma density after the first pulse is shown in Fig. 8. The electron and total positive ion density is about 10¹³-10¹⁴ cm⁻³ in the ionized channel with peak density near the cathode and the microspheres on the surface.

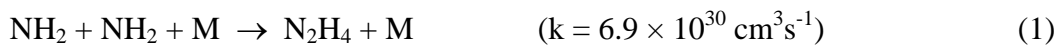
Since surface functionalization ultimately depends on the density of these radicals near the microsphere, the dynamics of plasma-surface interactions during the pulse was investigated. The temporal variation in the electron density as the avalanche closes in on the microsphere placed off-axis, during the pulse, is shown in Fig. 9. At about 1.6 ns, the leading edge of the avalanche begins to intersect the surface. By 1.7 ns, the electrons enter the vertical pore, increasing in density to 10¹⁰ - 10¹¹ cm⁻³, due to electric field drift. There is some penetration of electrons into the pores on either side of the vertical pore. By 1.8 ns, however, the electron density in pore P₁ decreases because they are lost in surface charging.

Surface charging rapidly builds up reversing local electric fields resulting in the expulsion of electrons from all pores. By 2 ns, there is no plasma present inside the pores. In the meanwhile, outside the pore the avalanche completely closes the gas gap increasing electron density to 10¹⁴ cm⁻³. The dynamics of the total positive ion density are different from those of electrons and are shown in Fig. 10. The total positive ion density inside the

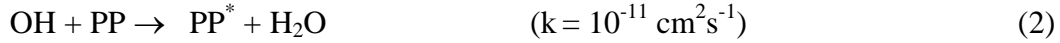
vertical pore increases to about 10^{10} - 10^{11} cm^{-3} at 1.7 ns, but there is little subsequent change in ion density. The differences in the behavior of electrons and positive ions inside the pores are explained by the effect of surface charge during the pulse as shown in Fig. 11.

As the avalanche arrives, the outer surfaces are the first to acquire surface charge. By 1.7 ns, as electron density increases around the microsphere, negative charging of a large fraction of the outer surface exposed to the avalanche is underway. The inside surfaces of the vertical pore are also charged to about 0.01 - 0.1 $\mu\text{C cm}^{-3}$ at this point. There is some surface charge near the openings of the pores on either side. Though the avalanche closes in by 3 ns, it does not penetrate further into the pores due to reversed electric fields brought about by negative charge on the surface. The ions created inside the pore by electron impact ionization remain as they are not as mobile as the electrons.

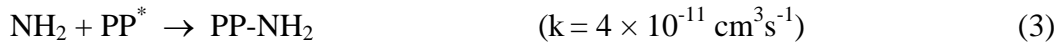
The temporal evolution of NH_2 density near the microsphere surface during the pulse is shown in Fig. 12. NH_2 density inside the pore increases to 10^{11} - 10^{12} cm^{-3} at 1.7 ns when electrons penetrate into that pore, but there is no increase in NH_2 inside other pores where plasma does not enter. By 3 ns, the NH_2 density in the bulk plasma around the microsphere has risen to 10^{14} cm^{-3} . Neutral chemistry dominates in the interpulse period as radicals are longer lived and continue to react with each other and diffuse into the pores. The bulk density of H, OH and NH_2 radicals at the end of the interpulse period are shown in Fig. 13(a). The peak density of H radicals in the bulk is 5×10^{14} cm^{-3} . The density of NH_2 peaks off-center, as much of the NH_2 near the center is consumed in the fast 3-body reaction pathway to form N_2H_4 .



The density of OH is 10^{12} cm^{-3} in the bulk and decreases closer to the microspheres. This is because of the consumption of the reactive OH radicals in surface reactions on the microspheres. The density of H, OH and NH_2 radicals near the microsphere surface is shown in Fig. 13(b). Much of the entering OH radicals are removed from the gas phase by surface reactions they undergo near the pore openings to abstract H atoms and form surface radicals.



Consequently, the OH density deeper within the pores is lower by upto 2 orders of magnitude. Unlike the OH radicals, H atoms have a higher density (10^{14} cm^{-3}) and they are comparatively less reactive. Though NH_2 radicals react fast in addition pathways with surface radicals,



the density of surface radicals limits the rate of consumption of NH_2 from the gas phase, so there is no appreciable gradient in NH_2 density within the pores.

The effect of varying the microsphere size on NH_2 radical density, keeping the pore opening diameters constant, is shown after the pulse and interpulse period in Fig. 14(a). When the microsphere size is reduced to $30 \mu\text{m}$, the density of NH_2 inside the pore is lower after the pulse than with the $90 \mu\text{m}$ size. This is because the $30 \mu\text{m}$ microsphere has a higher surface-to-volume area which results in quicker charging and expulsion of electrons that initially enter the pore. However, during the interpulse period, the density of NH_2 inside the pore is larger in the $30 \mu\text{m}$ microsphere, because of the shorter diffusion gradient for the radicals within the pores.

There is significant gradient in OH radical density inside the pores as the microsphere size increases from $30 \mu\text{m}$ to $90 \mu\text{m}$ because OH is consumed largely in surface reactions,

and the distance for OH radicals to reach deep into the pores is greater with the 90 μm microspheres. The coverage of amino (R-NH₂) groups on the microsphere surface after 1 s of treatment is shown in Fig. 14(b). The R-NH₂ coverage on the outer surfaces of the microsphere is similar in all cases. However, inside the pores there is significant variation, with higher R-NH₂ coverage in the smaller microspheres. The density of NH₂ inside the pores increases with microsphere size, whereas the density of OH decreases, so the decreased R-NH₂ inside the pores is rate-limited by the initiation step of H abstraction by OH to form surface radicals for larger microspheres.

The density of NH₂ radicals inside 90 μm beads of varying pore opening diameters is shown in Fig. 15(a). For smaller pore openings, there is a lower NH₂ density inside the pores during the pulse. During the interpulse period though, radical densities inside the pores are nearly the same for all cases. This is expected since the diffusion gradient inside the pores is independent of the pore size opening. The coverage of amine groups for these cases is shown in Fig. 15(b). Since the radical densities inside the pores are not very different, similar surface coverages of amine groups result.

The treatment of porous microspheres suspended in the discharge is briefly discussed. Since these particles are only a few 10s μm , they can be suspended in gas flow and passed through the discharge. The residence time of a bead in the discharge is then on the order of a few ms at best. The conditions after the pulse in He/O₂/H₂O=89/10/1 for three suspended microspheres is shown in Fig. 16. The plasma creates a wake around the three beads as shown in the inset in Fig. 16(b). There is virtually no plasma in the bead during the pulse.

The radical densities during the interpulse period are shown in Fig. 17. While the density of O and O₃ remain high, there is rapid consumption of OH due to reactions on the

microsphere surfaces. This creates local gradients in OH density both within the microsphere inside the pores and in the region surrounding the microspheres. Radical densities depend on the location of the microspheres but are little affected by the orientation of their pore openings in the discharge.

After 1 ms of treatment, the coverage of peroxy groups along each of the microspheres is shown in Fig. 18. The densities are shown along the surface of the bead and indicate a relatively high coverage for bead 2, which is placed on the axis of the discharge, because it sees higher radical fluxes on an average compared to the off-axis microspheres. It is noteworthy that there is no significant gradient in the coverage of peroxy groups with surface position. In this case, the generation of high O atom density results in the absence of any density gradients within the microspheres, whereby alkyl radicals are created throughout the microsphere, leading to high peroxy coverages.

7.4 Concluding Remarks

The treatment of rough polymers was examined in He/NH₃/H₂O discharges using scaffold like features. It was found that 1-2 % of R-NH₂ coverage can be obtained after long treatment times, but the uniformity of treatment was low. Gas composition could be used to adjust the coverage of R-NH₂ formed on the surface. The treatment of porous polymer surfaces was examined by modeling treatment of microspheres of varying size and porosity in He/NH₃/H₂O and He/O₂/H₂O discharges for beads placed on an electrode as well as those suspended in the discharge.

7.5 Figures

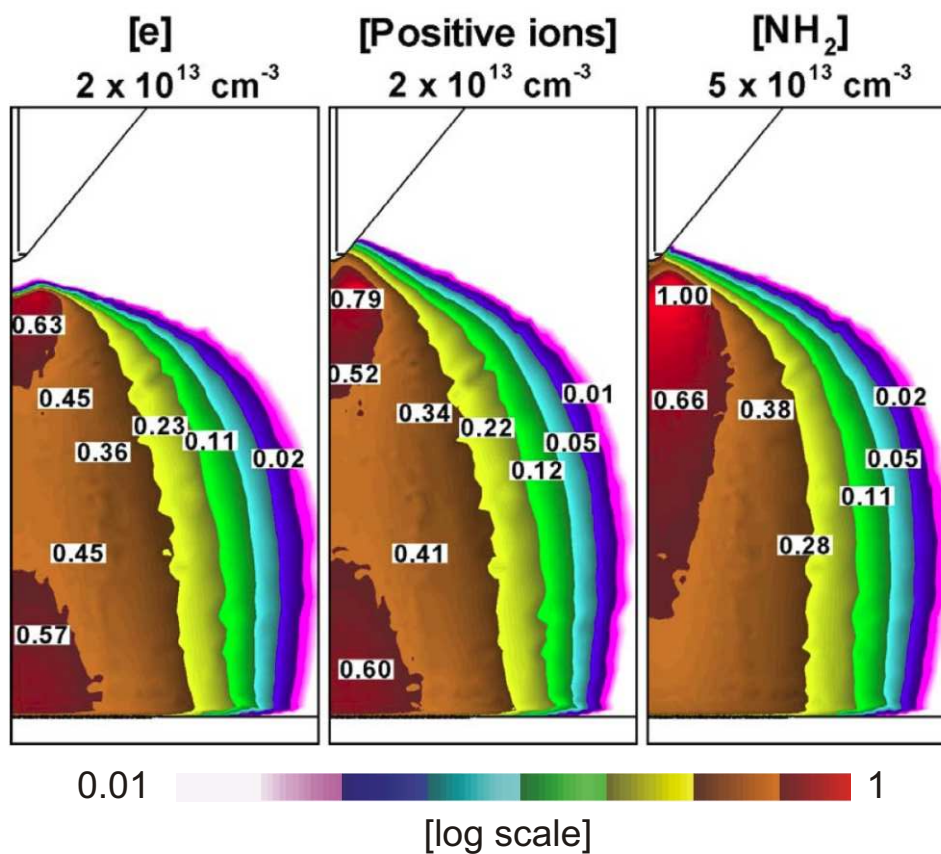


Fig. 1 Plasma density after the first pulse in the He/NH₃/H₂O=98/1/1 mixture - (a) electron density (b) total ion density and (c) NH₂ radicals. The configuration is the same as the one used in Chapter 5, Fig. 1. The upper electrode is powered to -5 kV and the pressure is 1 atm.

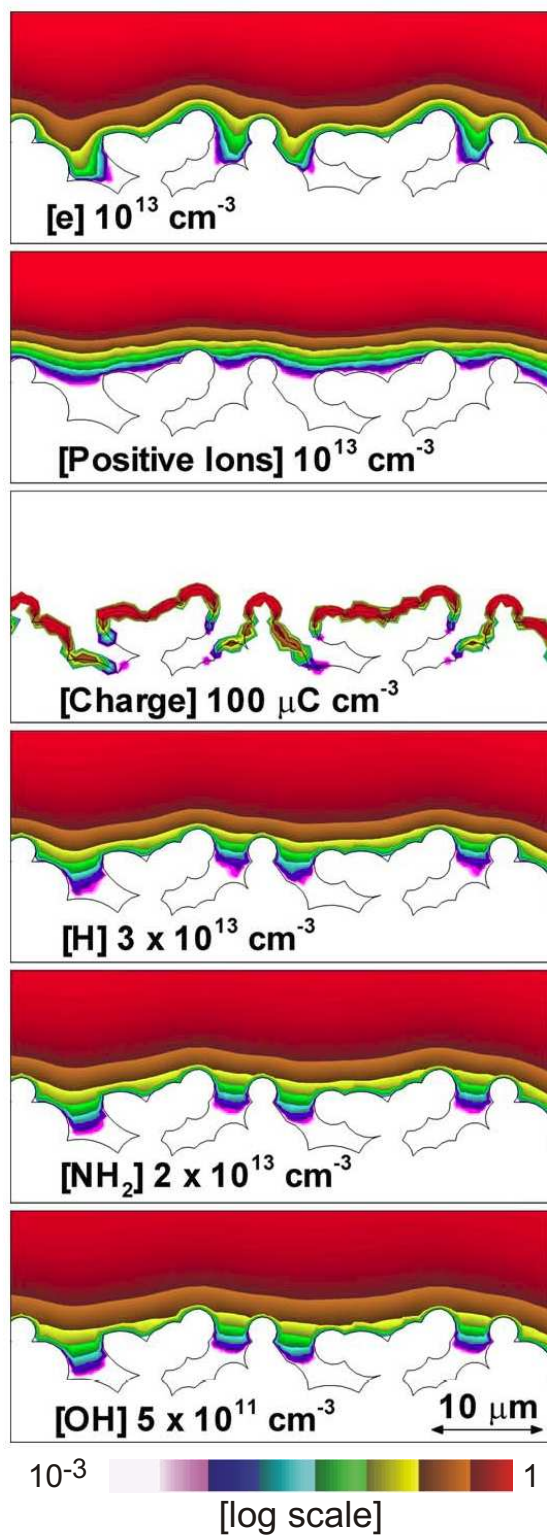
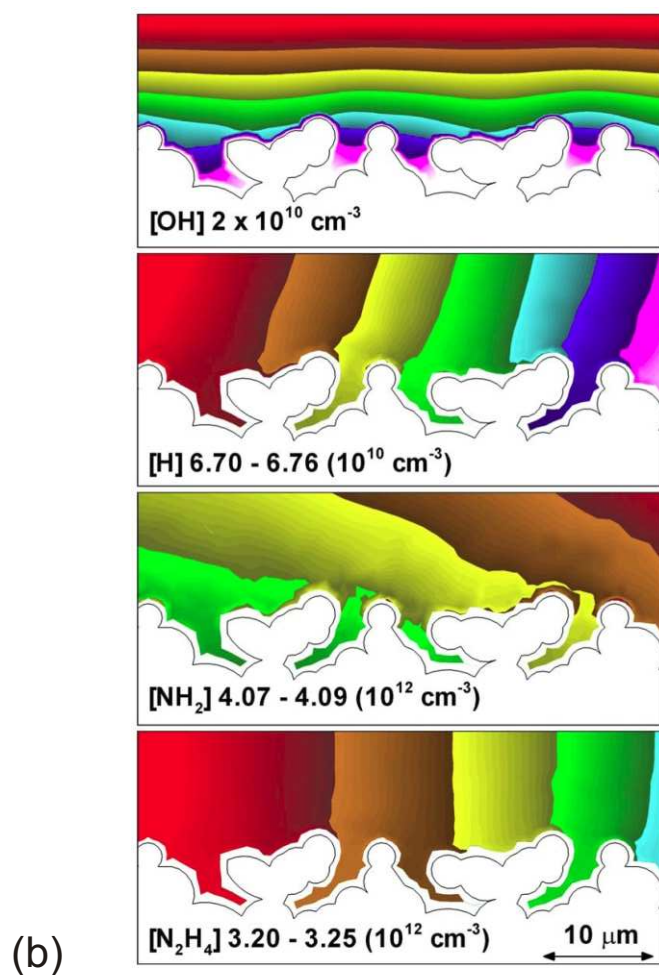
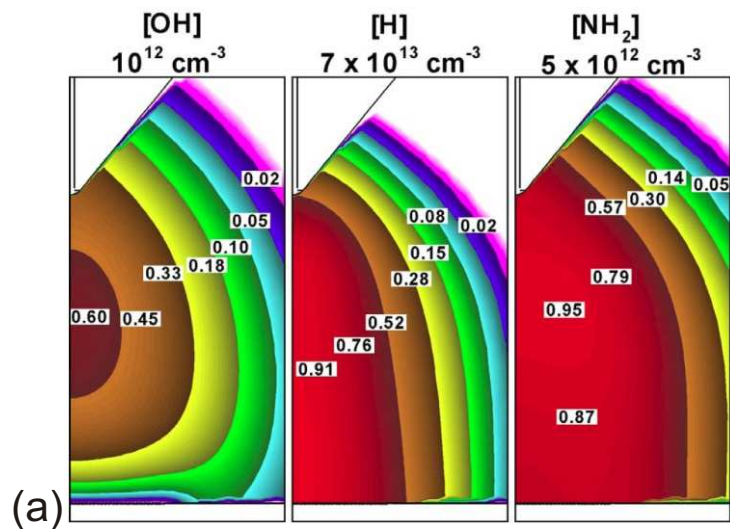


Fig. 2 Plasma density close to the rough surface after the first pulse in the He/NH₃/H₂O=98/1/1 mixture - (a) electron density, (b) total ion density, (c) surface charge, (d) H atoms, (e) NH₂ radicals, and (f) OH.



MIN  MAX

Fig. 3 Density of radicals during the first interpulse period in the He/NH₃/H₂O=98/1/1 mixture - (a) OH, H and NH₂ radicals in the discharge and (b) OH, NH₂, N₂H₄ and H near the surface.

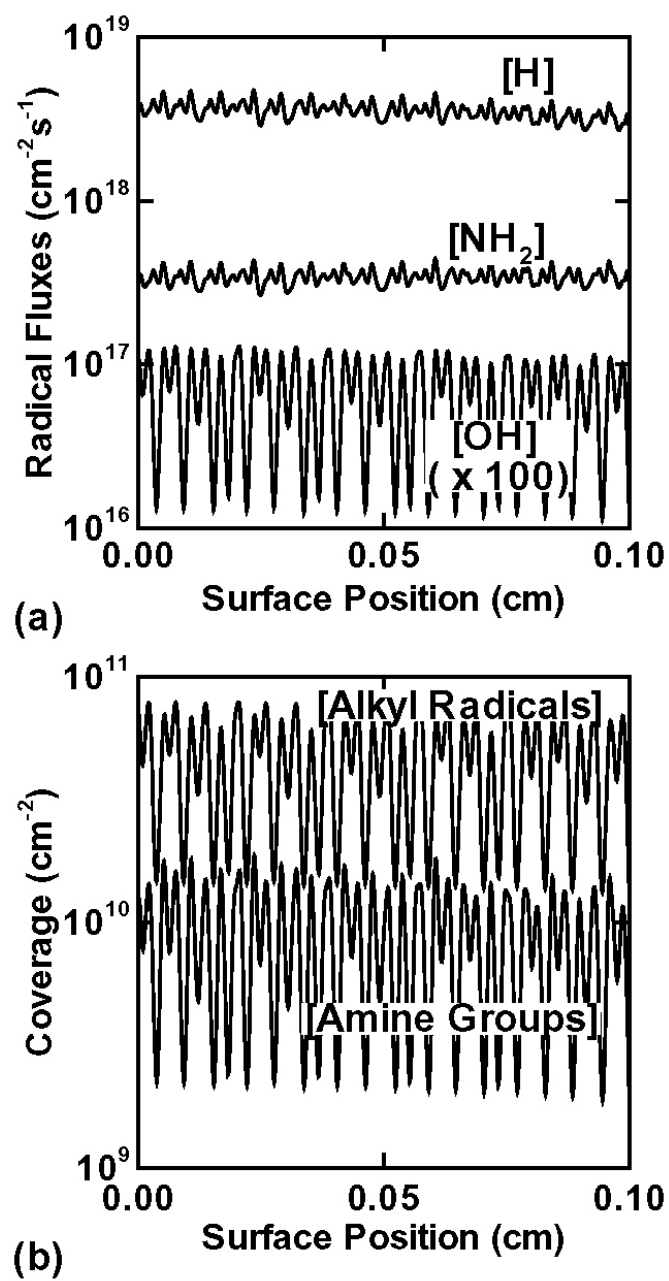


Fig. 4 (a) Radical fluxes averaged over the interpulse period and (b) The coverage of alkyl and amine groups after the interpulse period. Conditions are similar to Fig. 1.

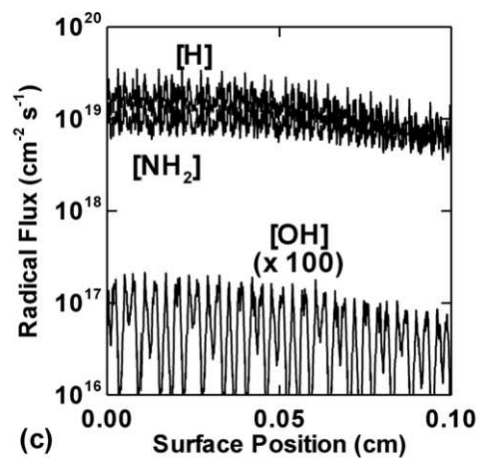
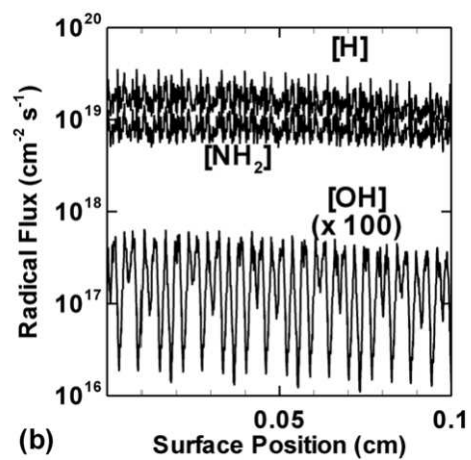
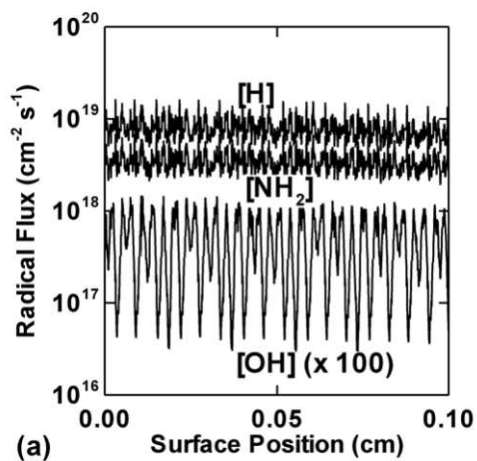


Fig. 5 Radical fluxes averaged over the interpulse period for different fractions, x , of NH_3 (a) 1%, (b) 10% and (c) 30% in negative $\text{He}/\text{NH}_3/\text{H}_2\text{O} = 99-x/x/1$ discharges. Conditions are otherwise similar to Fig. 1.

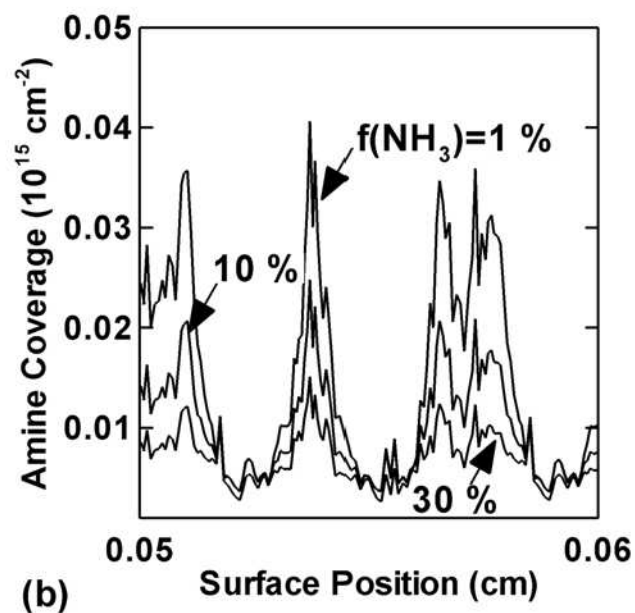
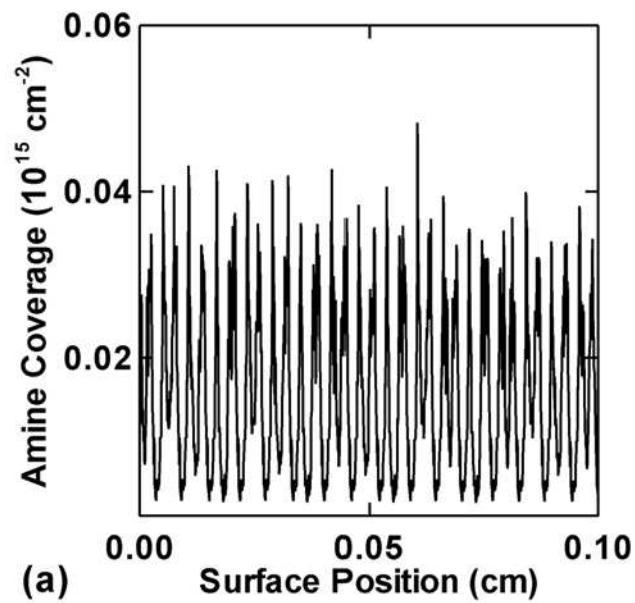


Fig. 6 Surface coverage of amine groups for (a) 1% NH_3 fraction and in (b) magnified view of amine coverage in the shadowed regions for different fractions, x , of NH_3 (a) 1%, (b) 10% and (c) 30% in negative $\text{He}/\text{NH}_3/\text{H}_2\text{O}=99-x/x/1$ discharges. Conditions are similar to Fig. 1.

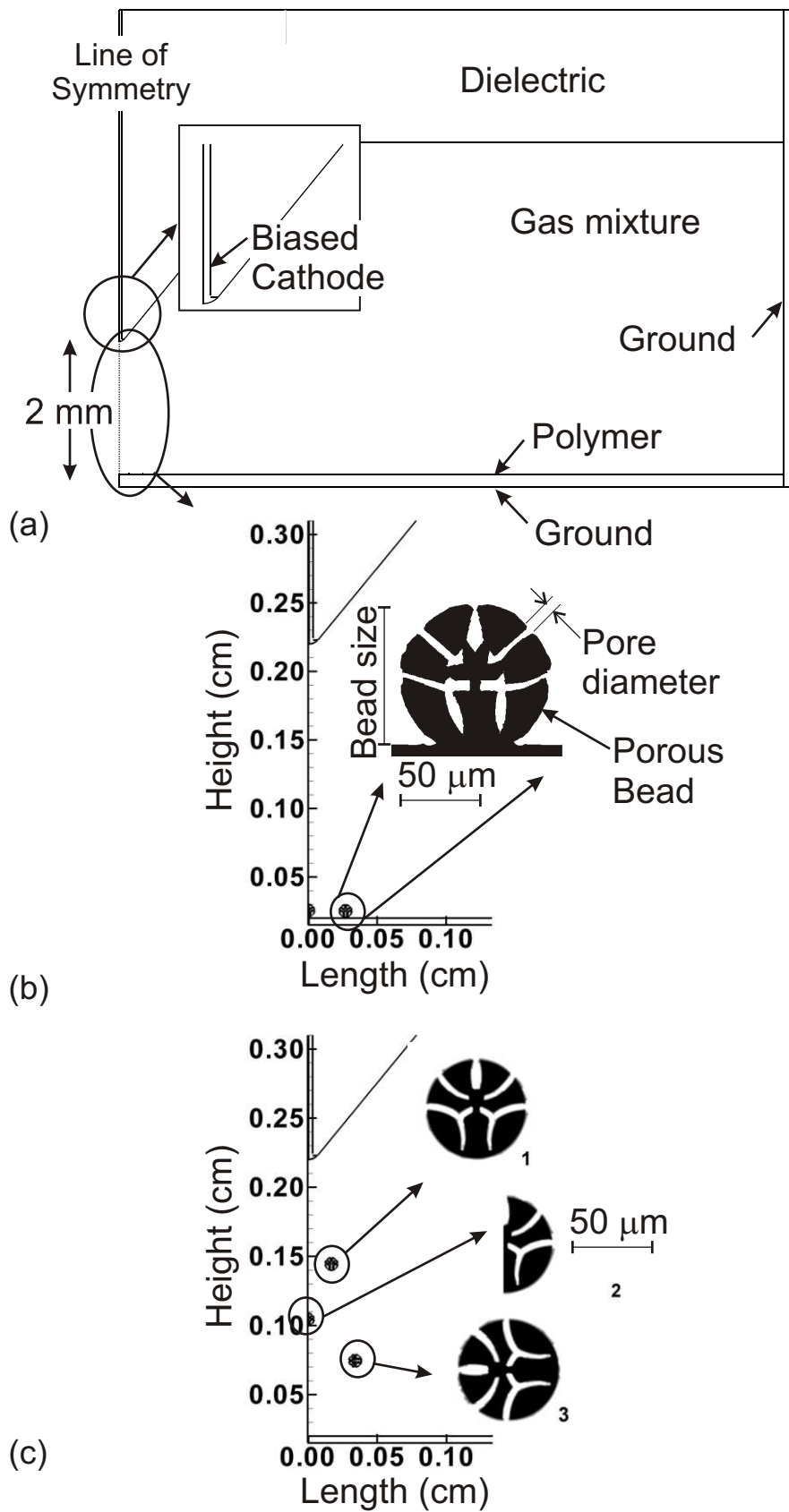


Fig. 7 (a) Schematic of the corona discharge configuration used to treat the microspheres placed either (b) near the grounded cathode or (c) suspended in the discharge gap.

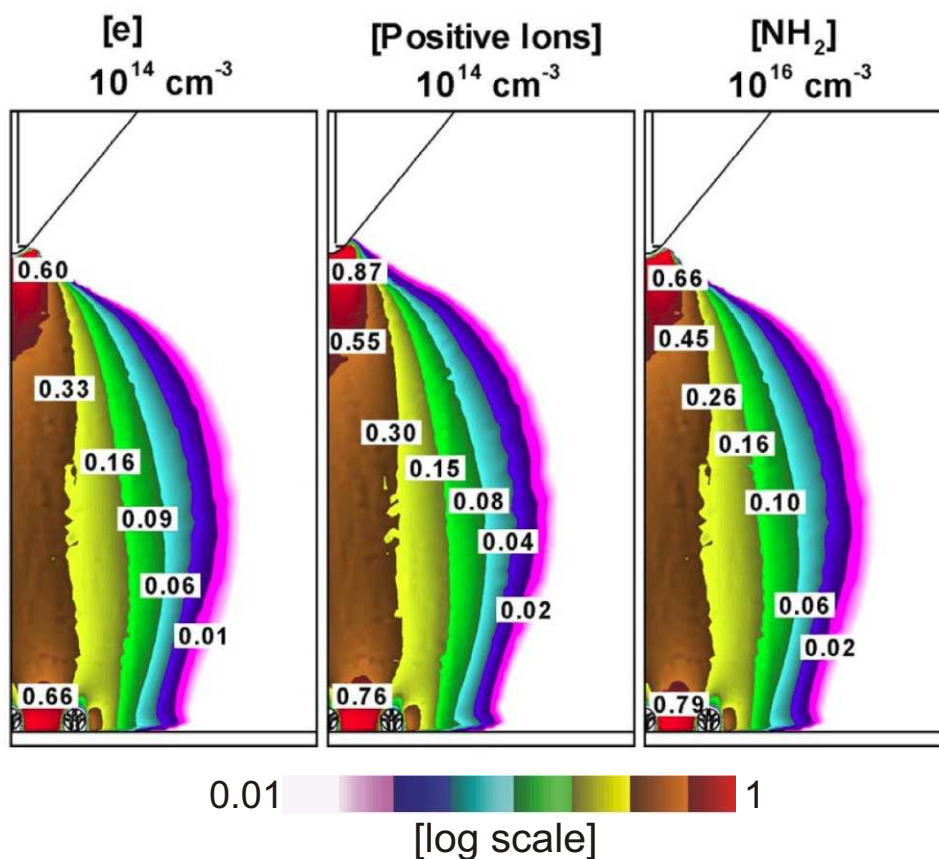


Fig. 8 Plasma density at the end of the avalanche is 10^{14} cm^{-3} while the density of NH_2 radicals peaks at 10^{16} cm^{-3} . Polymer beads of size $90 \mu\text{m}$ and pore diameter of $4.5 \mu\text{m}$ are placed on the grounded electrode with one symmetrically on the axis and the other placed a short distance off-axis. The discharge conditions are $\text{He}/\text{NH}_3/\text{H}_2\text{O}=98/1/1$ with an applied voltage of -5 kV to the upper electrode.

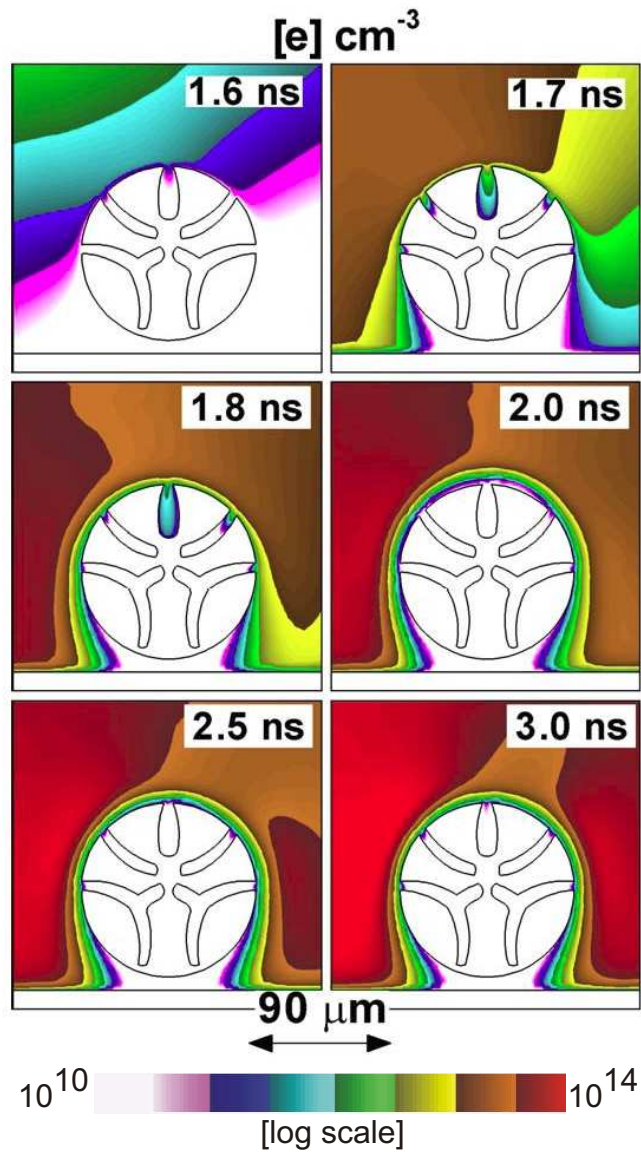


Fig. 9 Electron density near the microsphere increases to 10^{14} cm^{-3} outside the microsphere by the end of the avalanche. Electrons penetrate into the pore favorably oriented to the avalanche to 10^{11} cm^{-3} for 0.2 ns before withdrawing. The discharge conditions are the same as in Fig. 8.

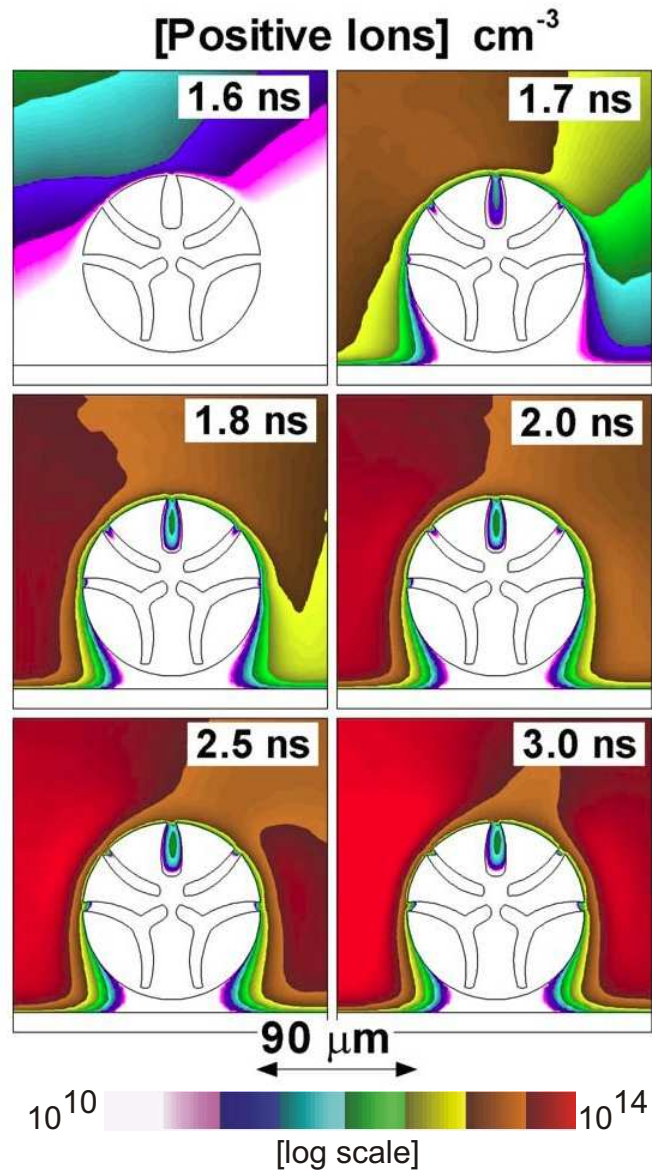


Fig. 10 Positive ion density near the microsphere increases to 10^{14} cm⁻³ during the avalanche. Ions density in the pore favorably oriented to the avalanche is 10^{12} cm⁻³. The conditions are the same as in Fig. 8.

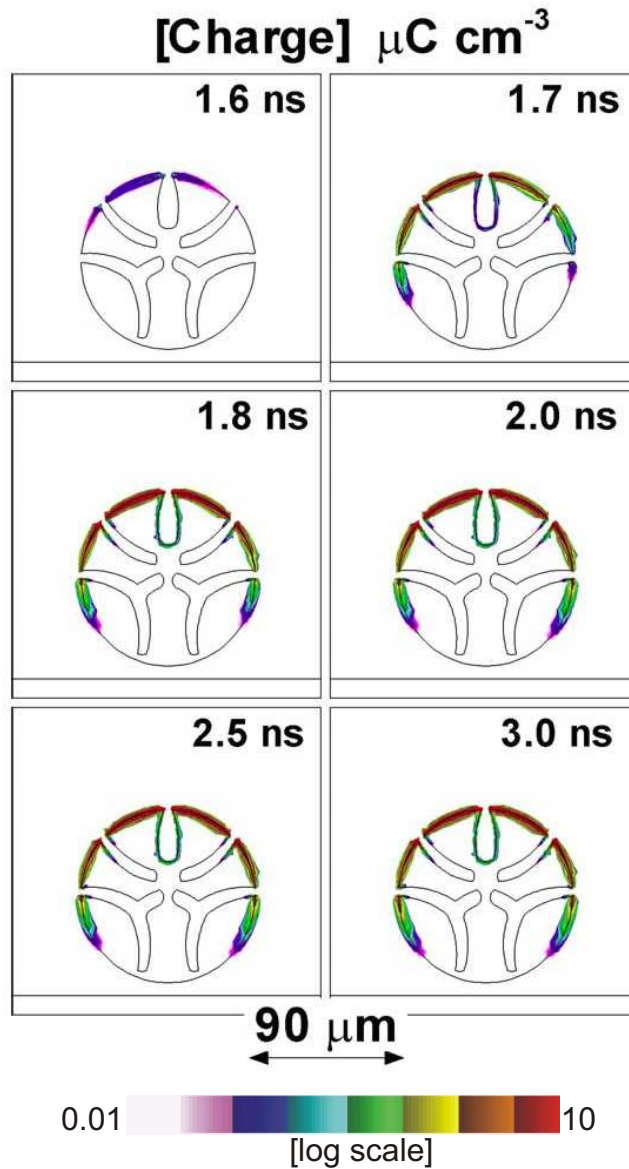


Fig. 11 The outer surfaces of the microsphere are charged up to $1 \mu\text{C cm}^{-3}$ during the avalanche. The internal surfaces of pores open to the avalanche are also charged. The conditions are the same as in Fig. 8.

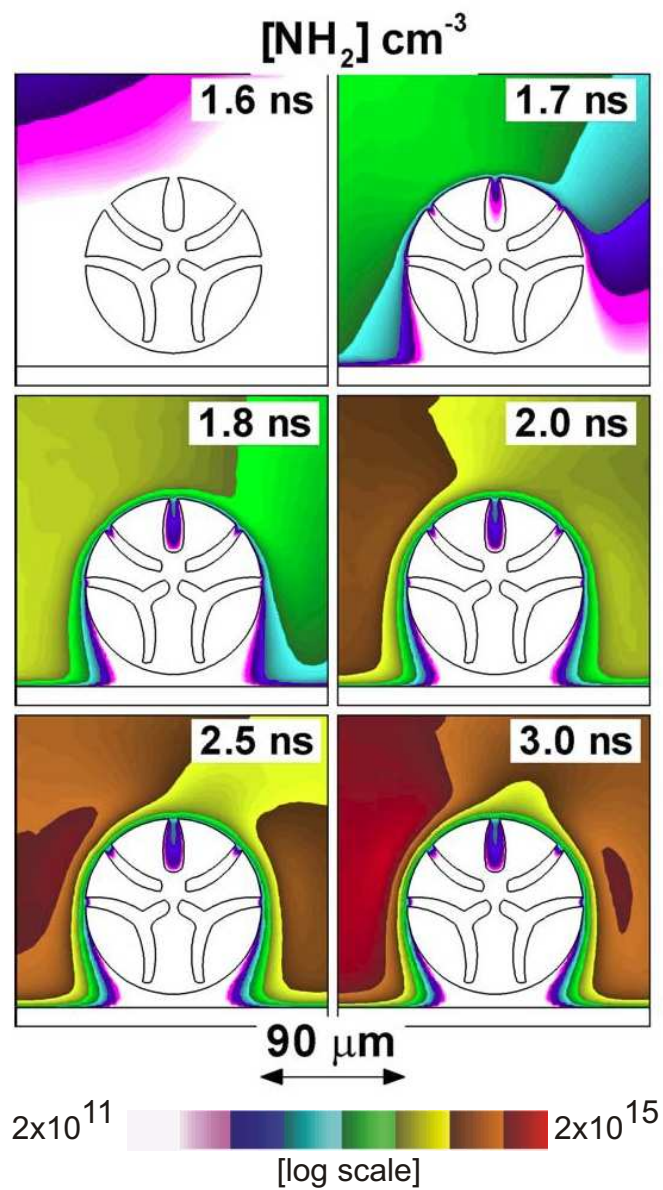


Fig. 12 Density of NH_2 near the microsphere at different times during the progress of the avalanche. The density of NH_2 inside the pore increases to 10^{12} cm^{-3} and about 10^{15} cm^{-3} outside the microsphere during the pulse. The conditions are the same as in Fig. 8.

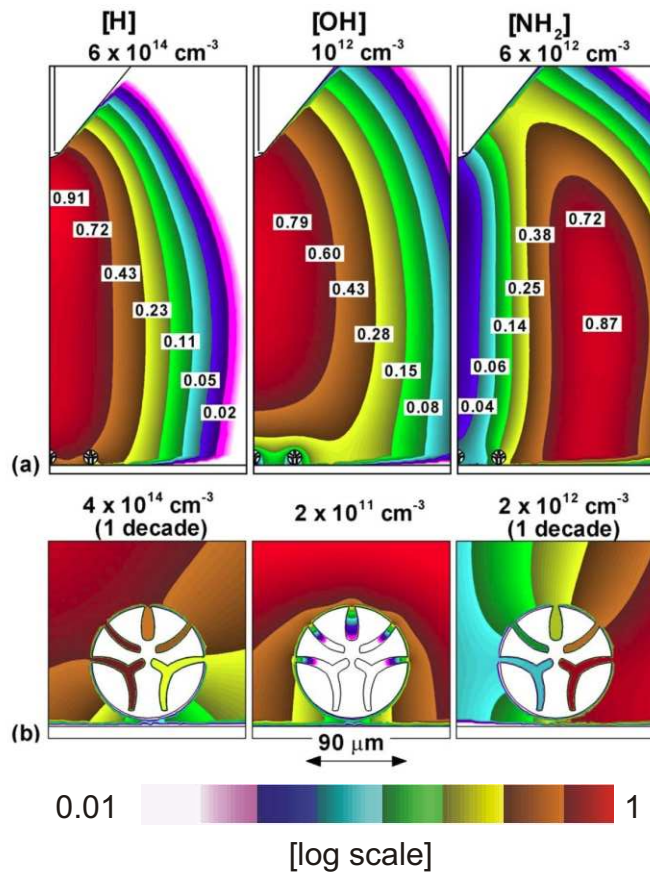


Fig. 13 The density of H, OH and NH₂ radicals after the interpulse period in (a) the discharge zone and (b) near the microsphere. The high reactivity and low density of OH results in its significant depletion before it fully penetrates into the pores. The conditions are the same as in Fig. 8.

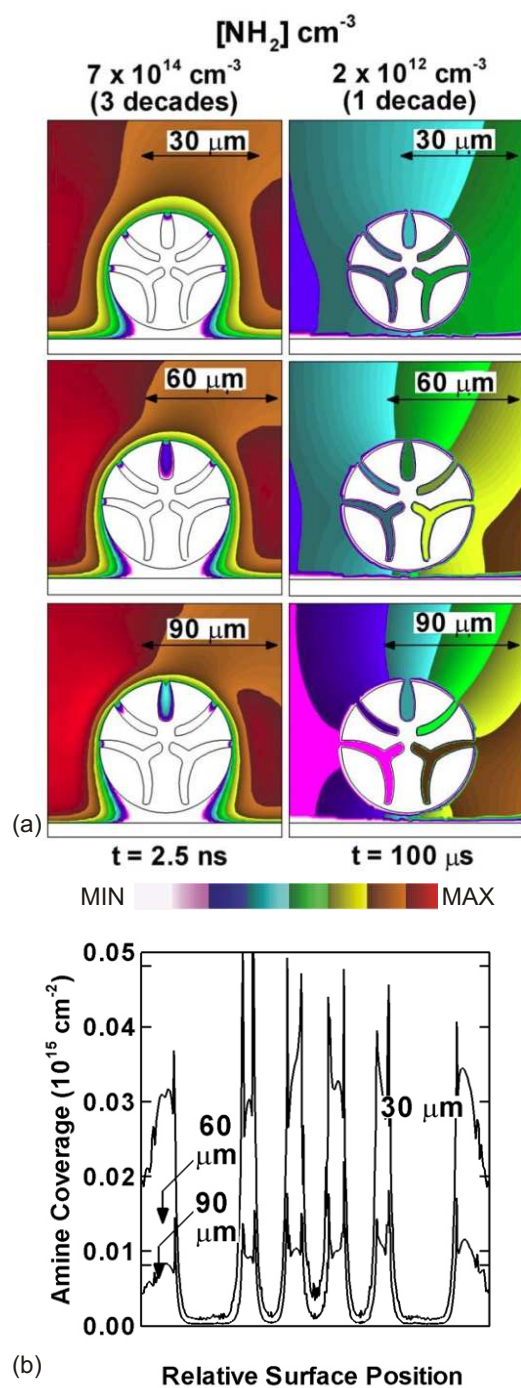


Fig. 14 The densities of NH_2 radicals during the pulse and interpulse period for microspheres of varying sizes. The coverage of NH_2 is higher on microspheres of smaller radii.

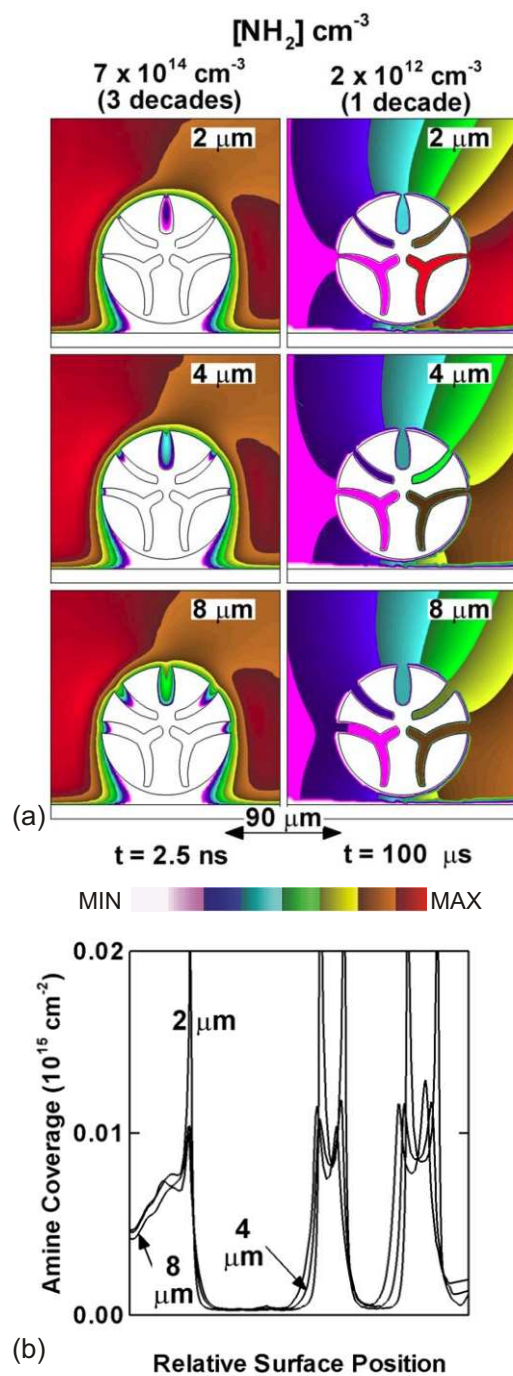


Fig. 15 The densities of NH_2 radicals during the pulse and interpulse period for microspheres of varying pore opening diameters. The coverage of amine groups is similar for all cases.

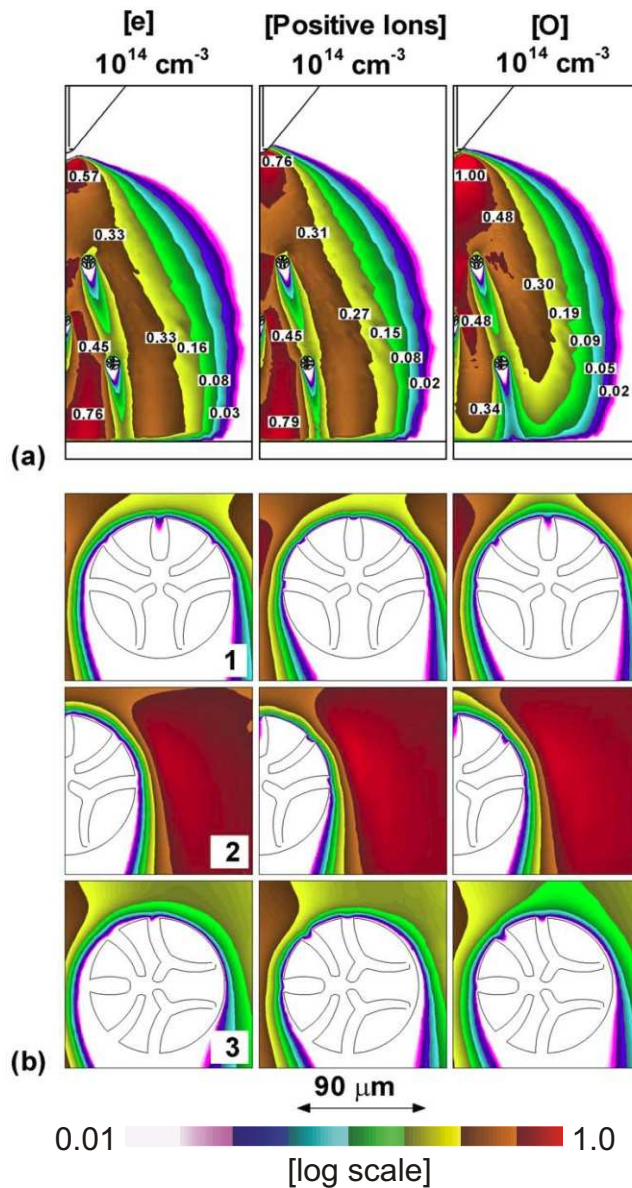


Fig. 16 The treatment of suspended polymer microspheres in He/O₂/H₂O=89/10/1 discharges at atmospheric pressure. The plasma forms a wake around the particles as the avalanche envelopes around the particles during breakdown.

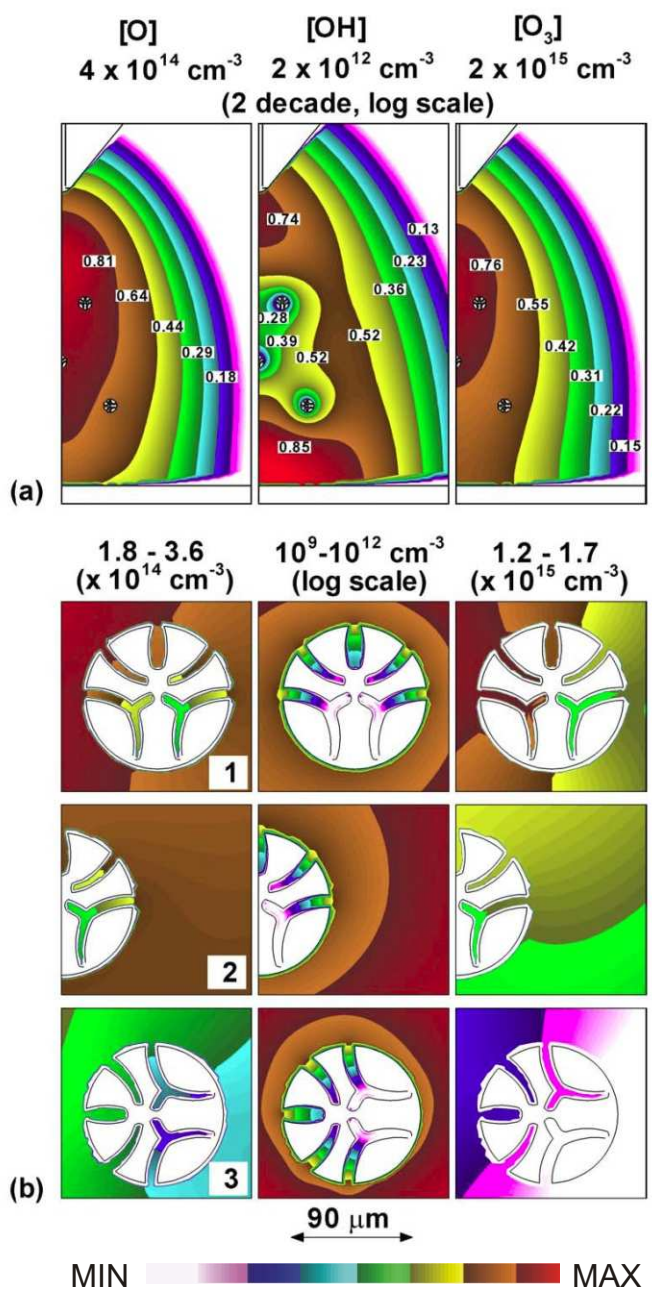
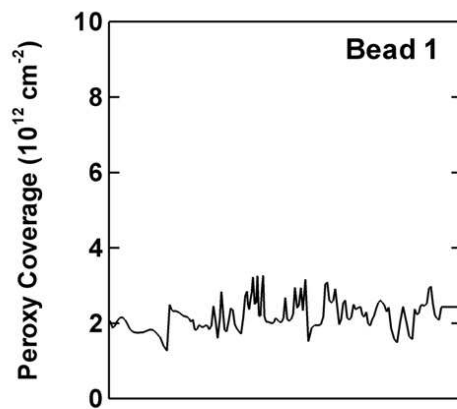
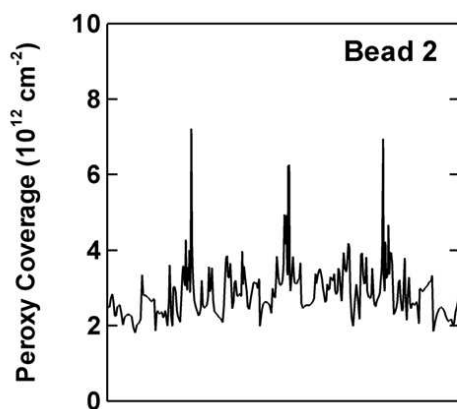


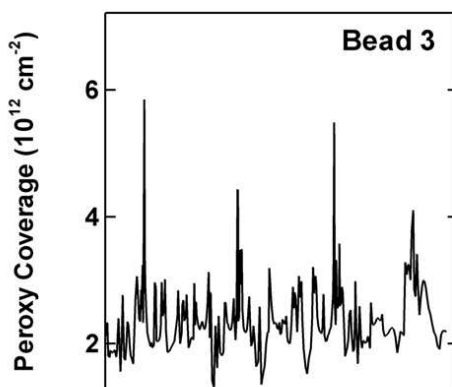
Fig. 17 The density of O, OH and O₃ during the interpulse period for the treatment of suspended microspheres. Conditions are the same as in Fig. 16. The radicals diffuse deep into the pores of the microsphere smoothing out gradients. OH radicals are consumed on the surfaces of the microspheres resulting in local gradients around these regions.



(a)



(b)



(c)

Fig. 18 Surface coverage of peroxy groups on the different microspheric beads after 1 ms of treatment. Conditions are the same as in Fig. 16. The coverage on bead 2 is higher since it is suspended on the axis and receives larger fluxes of reactive species.

7.6 References

1. M. V. Sefton et al, *Journal of Biomedical Materials Research*, **55**, 447 (2001).
2. U. Konig et al, *Surface and Coatings Technology*, **116-119**, 1011 (1999).
3. U. Hayat et al, *Biomaterials*, **13**, 801 (1992).
4. S. Holmes and P. Schwartz, *Composites Science and Technology*, **38**, 1 (1990).
5. Z. M. Liu et al, *European Polymer Journal*, **39**, 2291 (2003).
6. H. Chim. J. L. Ong, J-T. Schantz, D. W. Hutmacher and C. M. Agrawal, *Journal of Biomedical Materials Research*, **65A**, 327 (2002).
7. A. A. Meyer-Plath, K. Schroeder, B. Finke and A. Ohl, *Vacuum*, **71**, 391 (2003).
8. G. Oye et al, *Langmuir*, **18**, 8896 (2002).
9. G. Oye et al, *Journal of Physical Chemistry B*, **107**, 3496 (2003).
10. J. W. Kim and H. S. Choi, *Journal of Applied Polymer Science*, **83**, 2921 (2002).
11. R. Sipehia, A. S. Chawla and T. M. S. Chang, *Biomaterials*, **7**, 471, 1986.
12. S. L. Koontz et al, *Colloid and Polymer Science*, **277**, 557 (1999).
13. F. Bretagnol, M. Tatoulian, F. Arefi-Khonsari, G. Lorang and J. Amouroux, *Reactive and Functional Polymers*, **61**, 221 (2004).
14. R. Sharma, S. Trigwell, A. S. Biris, R. A. Sims and M. K. Mazumder, *IEEE Transactions on Industry Applications*, **39**, 87 (2003).

8. CONTINUOUS PROCESSING OF POLYMERS IN REPETITIVELY PULSED DISCHARGES WITH GAS FLOW

8.1 Introduction

Plasma discharges generated at high pressures are often employed to functionalize polymer surfaces to improve surface wettability [1] since they afford the advantages of short treatment times, room temperature operation and the absence of liquid handling and vacuum equipment. Typical plasma sources are atmospheric pressure coronas in a dielectric barrier configuration operating at a few kHz to tens of kHz having electrode separations of few mm.[2] For instance, atmospheric pressure corona discharges are used to functionalize large areas of commodity polymer films (e.g. polypropylene) in industry offering the advantages of continuous processing and low processing costs of a few cents per m². The polymer sheets or films to be treated are moved continuously through ‘webs’ with film speeds of 10s – 100s cm/s and residence times of 10s - 100s of ms in the discharge. In addition, gas flow is often employed to maintain constant pressure or to transport reactive species generated in the discharge over a larger surface area to reduce inhomogenities in surface treatment.[3,4]

The various physical processes occurring during such treatment include breakdown of the gas on application of the voltage pulse on timescales of ns, gas phase heavy particle reaction kinetics on timescales of μ s, convective and diffusive transport of heavy species and surface reaction kinetics on timescales of ms. Kogelschatz [5] and other early investigators [6] developed models mainly to understand the formation mechanisms and plasma chemistry processes in atmospheric pressure discharges.

Massines *et al*, investigated the correlation between polymer surface treatment and the physical processes in atmospheric pressure discharges.[7,8]

In this chapter, continuous treatment of polypropylene sheets in repetitively pulsed atmospheric pressure discharges with gas flow is investigated. Gas flow is employed to transport reactive species generated in the discharge over a larger surface area to reduce inhomogeneities in surface treatment. Processes occurring during such treatment include breakdown of the gas during the pulse on timescales of ns, gas phase kinetics on timescales of μ s, convective and diffusive transport and surface kinetics on timescales of ms.

The flow field of the background gas is calculated in the fluid dynamics model and is used in the transport equations of the plasma hydrodynamics model. Gas heating and momentum transport due to ion-neutral collisions are calculated in the plasma model and used as additional sources of energy and momentum in the fluid dynamics calculations of the background gas. Reactions on the polymer surface may emit or remove gaseous species, altering their densities and these are accounted in the gas phase. Tight coupling between the plasma hydrodynamics, fluid dynamics and surface kinetics modules of the plasma equipment model (described in detail in Chapter 2), was ensured to fully capture the interplay of the various processes.

In the presence of gas flow of a few liters per minute (lpm), radical transport to the surface is altered, affecting surface reaction pathways. This leads to a change in the relative proportions of surface functional groups on the polymer. Polymer sheets treated in corona discharges in the industry are continuously processed on ‘webs’ with film speeds of 10s – 100s cm/s. The residence time of the polymer in the apparatus is a few

10s of ms. Multiple passes of the polymer through the discharge zone may be required for effective surface functionalization.

The surface kinetics model described in Chapter 2 was improved to address web treatment by translating surface properties, including the coverage of surface resident species, on the unstructured mesh at specified film speeds. Locations on the surface with a finite residence time inside the discharge zone undergo reactions leading to the formation of active sites. These active sites continue to react downstream of the discharge zone as the polymer sheet is translated. In the presence of gas flow, active sites encounter a different distribution of fluxes downstream of the discharge depending on their residence time, leading to variations in the degree of surface treatment. With multiple discharges at different spatial locations, the moving surface receives renewed radical fluxes as it passes through each discharge even as active sites, created during passage through the last discharge, continue to react.

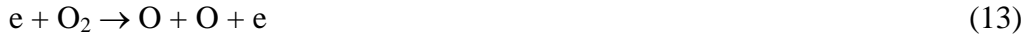
8.2 Repetitively Pulsed He/O₂/H₂O Discharges

A schematic of the corona discharge is shown in Fig. 1. The geometry extends up to 5 cm on either side of a powered metal electrode embedded in dielectric with its tip exposed to the processing gas. Gas enters through the nozzle on the left end and exits via the pump port on the right end. The discharge occurs between the powered electrode and the polypropylene (PP) sheet, which is placed on the lower grounded electrode, and located 2 mm away. The pulse duration is short (< 5 ns) and the pulse repetition frequency is 1 kHz. A few 10s of pulses are fully simulated.

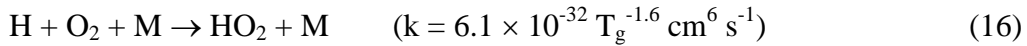
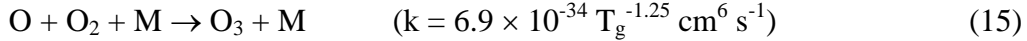
The base case conditions are He/O₂/H₂O=89/10/1 at atmospheric pressure with no gas flow and a continuously treated PP sheet with a film speed of 400 cm/s. The various

species and reactions included in the reaction chemistry are listed in Table 1. A few reactions relevant to the functionalization of PP are discussed below.

Electron impact reactions with O₂ and H₂O create O atoms and OH radicals,

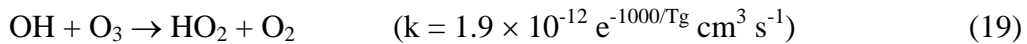
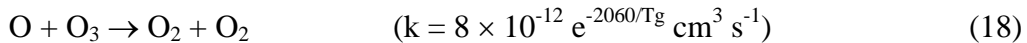
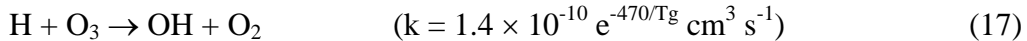


Three body reactions play an important role at atmospheric pressure. O atoms are very reactive and undergo three body reactions with O₂ to form O₃. H reacts at slower rates with O₂ in the presence of a third body (M) to form HO₂.

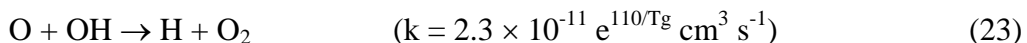
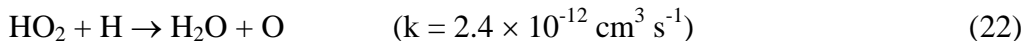
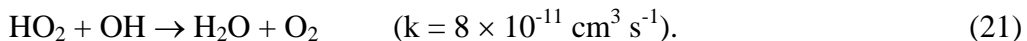
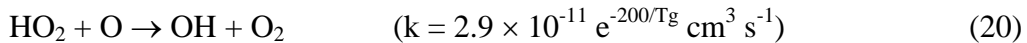


where k is the rate coefficient at room temperature unless noted otherwise.

There are no major consumption pathways for radicals such as O₃, which is relatively unreactive and tends to accumulate. O₃ does react at slow rates with H to form OH, with O to form O₂ and with OH to form HO₂.



HO₂ reacts slowly with radicals such as O, H and OH forming other radicals or stable products. OH and O react mutually at slow rates to form H.



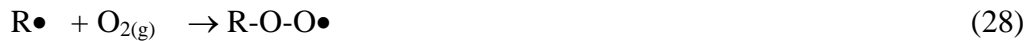
Surface treatment occurs over time due to the action of various plasma produced species such as O, OH and O₃ during multiple pulses. A reaction mechanism developed by Dorai and Kushner [13] is used in these investigations and a brief description of some of the salient features follow. Functionalization of PP comes about by initiation, propagation and termination reaction pathways, similar to free radical gas phase chemistry. The initiation reactions typically consist of reactions of a gas phase species with a virgin surface site (RH), which is similar to the Eley-Rideal mechanism for reaction of gaseous species on surfaces.



Alkyl (R•) radicals react with O and O₃ present in the discharge to form alkoxy (R-O•) groups, which is a rapid pathway with assigned probabilities of 0.1 and 1.0.



By contrast, a slower pathway is the reaction of R• radicals with O₂ to form peroxy (R-OO•) groups with probabilities of 10⁻⁴ – 10⁻³.



Reactions among surface sites can also occur (with the rate coefficients specified in units of cm²s⁻¹) which are subsequently scaled by the total density of surface sites in our model. These reactions can be thought to occur in a manner similar to Langmuir-Hinshelwood mechanisms, where a species from the gas phase first reacts and becomes a surface resident group and subsequently reacts with other surface resident groups. For

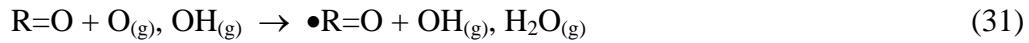
instance, rapid abstraction of H atoms from surrounding sites by R-O• groups results in alcohol (R-OH) groups with a rate of $10^{-16} - 10^{-15} \text{ cm}^2 \text{ s}^{-1}$.



Alternatively the C-C bond at the R-O• site cleaves, leading to chain scission and the formation of carbonyl (R=O) groups and the creation of a new R• radical site at rates of 10^3 s^{-1} .



Surface radicals created by the further abstraction of H atoms from carbonyl groups ($\bullet\text{R=O}$) followed by the addition of OH results in acid groups (HO-R=O).



Continued chain scission leads to CO_2 formation, a byproduct of surface treatment.



The termination steps for this mechanism include the recombination of alkyl radicals on the backbone by H and OH radicals with a probability of 0.2.



8.3 Effect of Gas Composition and Surface Residence Time

For the base case, we consider the treatment of a static (i.e., non-moving) polypropylene sheet placed on the grounded surface in repetitively pulsed He/O₂/H₂O=89/10/1 discharges with negligible gas flow. The applied voltage at the powered electrode is -5 kV. The plasma conditions after the first pulse are shown in Fig. 2. Electron and ion densities of up to 10^{14} cm^{-3} are created during the pulse. The peak

densities of radicals such as O and OH produced by electron impact of O₂ and H₂O are 10¹⁵ cm⁻³ and 10¹⁴ cm⁻³ respectively. Surface charging of the polypropylene ultimately causes the discharge to extinguish. The discharge zone is confined to the spatial region within approximately 0.5 mm of the vertical axis through the powered electrode, due to the transient nature of the discharge.

The density of radicals produced during the interpulse period is shown in Fig. 3 at 100 μs. O atoms are generated by electron impact of O₂ during every pulse. The peak density of O atoms is reduced by 2-3 orders of magnitude to 10¹² cm⁻³, while the density of O₃ increases to 10¹⁴ cm⁻³ at this time due to three-body association reactions of O with O₂.



OH is consumed in reactions with O and O₃, and the OH density after 100 μs reduces to 10¹² cm⁻³.



Diffusive transport outward from the discharge zone also leads to a smoothing of the sharp density gradients created during the pulse.

The discharge is repetitively pulsed to increase the density of reactive gas phase radicals and enable a higher degree of polymer surface treatment. The effect of repetitive pulsing on O atom densities after different number of pulses is shown in Fig. 4. The bulk of O atoms produced after 10 pulses is still confined to the narrow discharge zone, indicating that rapid local reaction kinetics dominates over diffusive transport. The maximum density of O atoms before the next pulse after 100 μs is about 10¹² cm⁻³ as

shown in Fig. 5(a). Similarly, much of the OH generated during a given pulse is consumed during the interpulse period in reactions with O, O₃ and HO₂. The density of O₃ generated due to repetitive pulsing is shown in Fig. 5(b). O₃ is relatively unreactive and accumulates from pulse-to-pulse with peak values of 10¹⁶ cm⁻³ near the discharge zone.

Surface alkyl radicals are created by H abstraction reactions of O and OH radicals from the polymer backbone (RH) within 20 μs mainly within the discharge zone. The density of alkyl (R•) radicals created along the surface immediately following the pulse is shown in Fig. 6(a). The production of surface radicals is confined to the region of surface lying within the discharge zone. The peak R• density locations on the surface are vertically below the powered electrode, where the avalanche front encounters the surface during breakdown, because the density of reactive radicals peaks here. Peroxy (R-OO•) groups are formed on the surface after 10s of μs, by reactions of alkyl sites with O₂ during the interpulse period. Since they are not as reactive, they tend to accumulate from over many pulses as shown in Fig. 6(b).

The continuous treatment of polypropylene sheets in repetitively pulsed He/O₂/H₂O=89/10/1 discharges with no gas flow is examined. Active R• sites formed on the polymer surface during its residence time inside the discharge zone can continue to undergo reactions as the polymer moves out of the discharge zone. The time variation of the coverage of R• and R-OO• groups is shown in Fig. 7 for a polypropylene sheet moving from the left end to the right at 400 cm/s. R• radicals are regenerated in every pulse on the surface at sites lying within the narrow discharge zone due to renewed fluxes of O and OH, leading to a spike in R• coverage following the pulse. But as the polymer

moves out of the discharge zone, these $R\bullet$ sites continue to react with O_2 to form $R-OO\bullet$, which increases downstream over many pulses as shown in Fig. 7(b). The coverage of peroxy groups approaches a steady state downstream of the discharge as the number of pulses increases.

The effect of surface residence time in the discharge zone on the coverage of $R-C=O$ and $R-OO\bullet$ groups is compared in Fig. 8 for constant energy deposition by varying the film speed and correspondingly the pulse repetition rate. At lower film speeds, the polymer surfaces receives on an average a higher average flux of radicals such as O and OH resulting in the creation of a larger fraction of active $R\bullet$ sites. The relative coverage of groups such as $R-O\bullet$, alcohol ($R-OH$) and carbonyl ($R-C=O$) to $R-OO\bullet$ groups is determined by the ratio of O_3/O_2 during the interpulse period, with higher ratios favoring greater $R-O\bullet$ coverage. With no gas flow, O_3 continues to accumulate in the discharge zone over multiple pulses (Fig. 5(b)). As the speed of the polypropylene sheet increases, the residence time in the discharge zone decreases. The degree of surface treatment is eventually determined by the time integrated flux of reactive O and OH radicals encountered by the surface. Therefore, the coverage of surface $R\bullet$ sites and subsequently other functional groups such as $R-OO\bullet$ and $R-C=O$ is higher at lower film speeds that provide for larger residence time in the discharge zone.

The effect of gas composition on surface treatment was examined by varying the O_2 fraction $f(O_2)$ in the discharge during the continuous treatment of polypropylene sheet at 400 cm/s. The coverage of $R-OO\bullet$ groups formed on the surface for $f(O_2)$ of 1, 5 and 10% is shown in Fig. 9(a). The total coverage of $R-OO\bullet$, which is formed by the passivation of $R\bullet$ sites by O_2 , is linked to the generation and consumption of $R\bullet$ sites on

the surface. As $f(\text{O}_2)$ increases, the O density during the pulse increases which results in higher H abstraction from the polymer and increased $\text{R}\bullet$ site coverage. The $\text{R}\bullet$ sites formed on the surface in the discharge zone continue to react downstream and are passivated with O_2 to form $\text{R-OO}\bullet$ sites. At constant film speed, the extent of passivation by O_2 , increases with $f(\text{O}_2)$. The variation in surface coverage of alkoxy groups is shown in Fig. 9(b). In the discharge zone, the ratio of O_3/O_2 is higher, leading to the formation of $\text{R-O}\bullet$ sites by the reactions of $\text{R}\bullet$ with O_3 . Since $\text{R-O}\bullet$ sites undergo scission reactions, they are consumed as the polypropylene sheet moves downstream.

8.4 Effect of Gas Flow Rate

To determine the influence of gas flow on polymer surface treatment, the flow rate of the $\text{He}/\text{O}_2/\text{H}_2\text{O}$ mixture entering the nozzle was varied from 1 to 30 liters per minute (lpm). In each case, the converged velocity field develops over time resulting in average gas speeds of 10s - 100s cm/s. For these runs, the fluid dynamics simulation was run long enough (a few ms) to ensure that the velocity field converged before starting the simulations of the repetitively pulsed discharge. The converged flow field obtained for a flow rate of 10 lpm is shown in Fig. 10. The axial velocity increases in the region near the powered electrode, where the cross-section for flow is least.

The effect of gas flow on O atom generation during repetitive pulsing is shown in Fig. 11 with a gas flow rate of 30 lpm. There is some variation in O atom densities especially near the polymer surface, after the same number of pulses compared to the case without gas flow (Fig. 4). With gas flow of 30 lpm, the density of O atoms generated in the avalanche during the pulse remains around 10^{14} cm^{-3} . Reaction kinetics

dominates, but the presence of gas flow allows for some convective flow of depleted O atoms downstream of the discharge zone as shown in Fig. 12(a).

The density of O₃ late in the interpulse period after a similar number of pulses is shown in Fig. 12(b). Convective transport dominates over diffusion and the little O₃ is found upstream of the discharge zone in the presence of gas flow. The peak density of O₃ of about $5 \times 10^{15} \text{ cm}^{-3}$ occurs close to the discharge zone where most of the O atoms are generated. However this is still an order of magnitude lower compared to the peak density with no gas flow (Fig. 5). Due to repetitive pulsing and gas flow, peak O₃ densities occur downstream of the discharge and reach steady-state values of about 10^{15} cm^{-3} .

The density of R•, R-OH, R-O• and R-OO• groups formed on the surface as a function of position is shown in Fig. 13 for three different cases. In Fig. 13(a), the coverage of various surface groups in the presence of gas flow at 30 lpm and static surface are shown. Most of the treatment is confined to a region close to the discharge zone. Gas flow creates some surface radicals downstream of the discharge. The density of R• is high since the polymer locations near the discharge zone constantly receive renewed fluxes of reactive species abstracting H from the polymer.

In Fig. 13(b), the surface speed of the polymer is set at 400 cm/s in addition to 30 lpm gas flow. In this case, there is a constant supply of R• sites near the discharge zone. Convective flow ensures the transport of O₃ downstream, so the relative fraction of R• sites is high. Downstream, the density of R• sites decreases by a factor of 6 due to polymer reacting with O₂ and other plasma species. Surface-surface reactions continue to occur as well. R-O• groups abstract H atoms from surrounding surface sites to form R-

OH groups, decreasing R-O• coverage, while the coverage of R-OH increases as the polymer moves out of the discharge zone. The density of R• sites decreases as they are saturated by O₂ to form R-OO• groups, which increases downstream. The pulse to pulse modulation in O and OH densities that initiate the surface reactions is reflected in the coverage of R-O• and R-OO• groups.

In Fig. 13(c), the continuous treatment of the polymer with a film speed of 400 cm/s but with no gas flow is considered. The surface coverage of various groups varies markedly from the case in Fig 13(b). In the absence of gas flow, the discharge zone has a high O₃/O₂ ratio due to accumulation of O₃ and most of R• sites in the discharge region are consumed in reactions with O₃ to form R-O• sites. However, newer R• sites are regenerated downstream, due to surface-surface reactions of R-O• sites, which also lead to a higher R-OH coverage compared to other conditions. Eventually, R• are saturated with O₂ downstream to form R-OO• groups.

To determine the effect of gas flow on continuous surface treatment, the density of R-C=O and R-OO• groups formed on a polypropylene sheet moving through the discharge at 400 cm/s with different gas flow rates are compared to treatment obtained at conditions in the absence of gas flow in Fig. 14. At higher flow rates, the coverage of R-O• drops because convective transport of O₃ significantly reduces the ratio of O₃/O₂ in the discharge zone. The lower O₃/O₂ ratio in the discharge zone at high gas flow rates causes a larger fraction of available R• sites to be saturated by O₂. Since R-C=O is formed via surface-surface reactions of R-O• sites, as the polymer moves downstream, the higher coverage of R-O• with no gas flow increases the R-C=O coverage as well.

8.5 Multiple Pulsed Discharges

The use of reactive gases (such as NH_3) in room air environments requires sophisticated gas injection and confinement systems.[14,15] A schematic of one such apparatus is shown in Fig. 15 and consists of a grounded drum electrode separated by a gas gap of 1 – 2 mm from powered shoe-shaped electrodes. The polymer to be treated is placed on the larger drum electrode and is moved into and out of the discharge zone as the drum rotates. The fixed shoe electrodes may be powered to voltages of 10s kV to breakdown the gas gap. Reactive gas mixtures are injected through the nozzle on the axis and the prospect of contamination of discharge zone by the room air environment is reduced by using high gas flow rates through the nozzle.

The continuous treatment of polypropylene sheets in such a configuration in $\text{He}/\text{O}_2=90/10$ mixtures was investigated. The gas mixture is injected through the nozzle at a flow rate of 100 slpm and upper electrode is powered at 15 kV with alternating polarities at a frequency of 1 kHz. Electrons are seeded at a finite number of fixed locations in the discharge zone with a Gaussian distribution during every pulse to help initiate the discharges. To simplify the problem and reduce computational time, the room air environment was also assumed to be He/O_2 .

The dynamics of electron density, O atom density and O_3 generated after one of the pulses is shown in Figs. 16. During any pulse, the peak electron density is about 10^{14} cm^{-3} and is generated adjacent to the momentary cathode in every discharge. Delta function sources of O atoms are produced in each discharge location during the pulse, with peak densities of 10^{15} cm^{-3} . Gas heating raises temperatures by only about 5 K. During the interpulse period, shown in Fig. 17, convective flow transport some of O atoms, but the bulk of O is consumed to form O_3 . O_3 accumulates around every

discharge location following a pulse. Convective transport helps smoothen out spatial gradients across the polymer sheet maintaining a relatively high O_3 density within the discharge zone.

The polymer sheet repeatedly encounters discharges at multiple spatial locations as it moves through the discharge zone. At those sites on the polymer surface that receive renewed fluxes of reactive species, such as O and OH, $R\bullet$ sites are regenerated by H abstraction reactions. These $R\bullet$ sites are quickly saturated during the interpulse period. It is possible that some locations on the polymer surface may receive higher radical fluxes than others, due to the dependence of film speed, spatial occurrence of the discharges and repetition frequency. Nevertheless, convective transport smoothen out spatial gradients to a large extent. The density of $R\bullet$ and $R-O\bullet$ groups formed during the continuous treatment of polypropylene sheets is shown in Fig 18. During successive pulses, the density of $R\bullet$ sites is renewed and consumed in reactions before the next pulse. The continuous renewal of $R\bullet$ sites and the high O_3 density increases the fraction $R-O\bullet$ coverage as the polymer exits.

8.6 Concluding Remarks

The control of process variables such as gas flow, composition and film speed during continuous treatment of polymer sheets may enable the tailoring of the composition of surface functional groups. During polypropylene treatment in repetitively pulsed He/ O_2 /H $_2$ O discharge, the relative fluxes of O_3/O_2 within the discharge zone are altered by the presence of gas flow. Reactive species such as O and OH are regenerated during every pulse, but are consumed during the interpulse period. Longer lived species such as O_3 accumulate over many pulses. Gas flow transports long lived radicals over a

larger surface area. During continuous treatment, both of these regimes play a role. In the presence of gas flow, active sites encounter a different distribution of fluxes downstream of the discharge depending on their residence time, leading to variations in the degree of surface treatment. With multiple discharges at different spatial locations, the moving surface receives renewed radical fluxes as it passes through each discharge even as active sites, created during passage through the last discharge, continue to react and high O_3/O_2 fluxes are maintained throughout the discharge region. The interplay between local rapid reactions and non-local, slower reactions may enable the customization of the relative abundance of various surface functional groups.

8.6 Figures

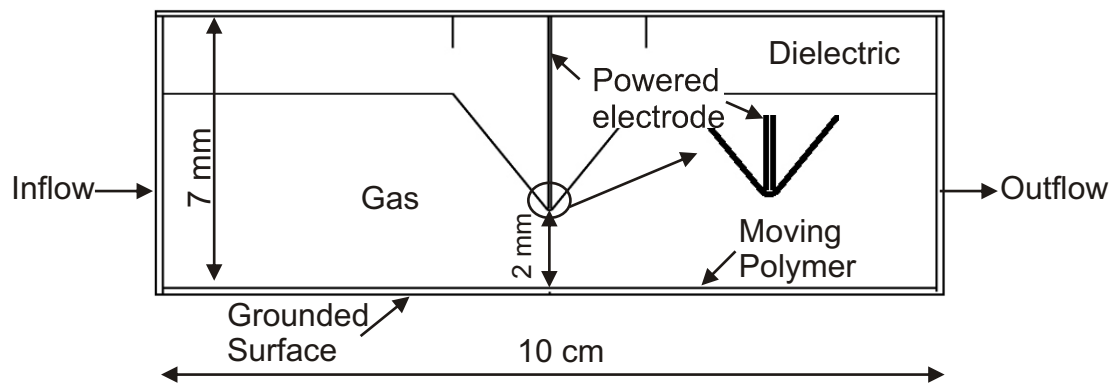


Fig. 1 Schematic representation of the corona configuration. The upper electrode is powered and the polymer is placed on the lower grounded electrode 2 mm away so the setup works like a dielectric-barrier discharge. During continuous processing, the polymer sheet moves at speeds of 100s cm/s. There may be gas flow through the discharge as well.

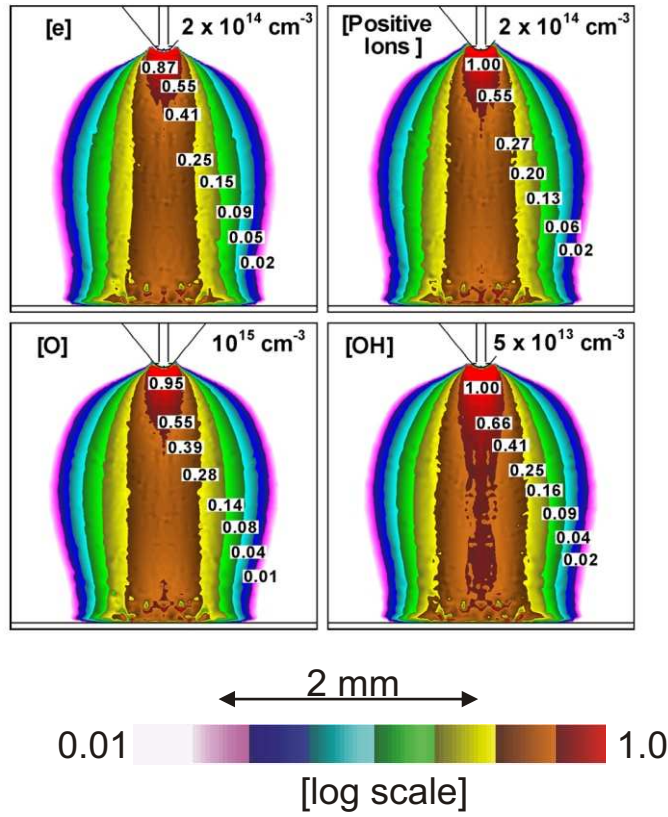


Fig. 2. Plasma density in the discharge zone resulting from breakdown in a -5 kV pulse in $\text{He}/\text{O}_2/\text{H}_2\text{O}=89/10/1$. Radical densities of 10^{13} - 10^{15} cm^{-3} are created during breakdown.

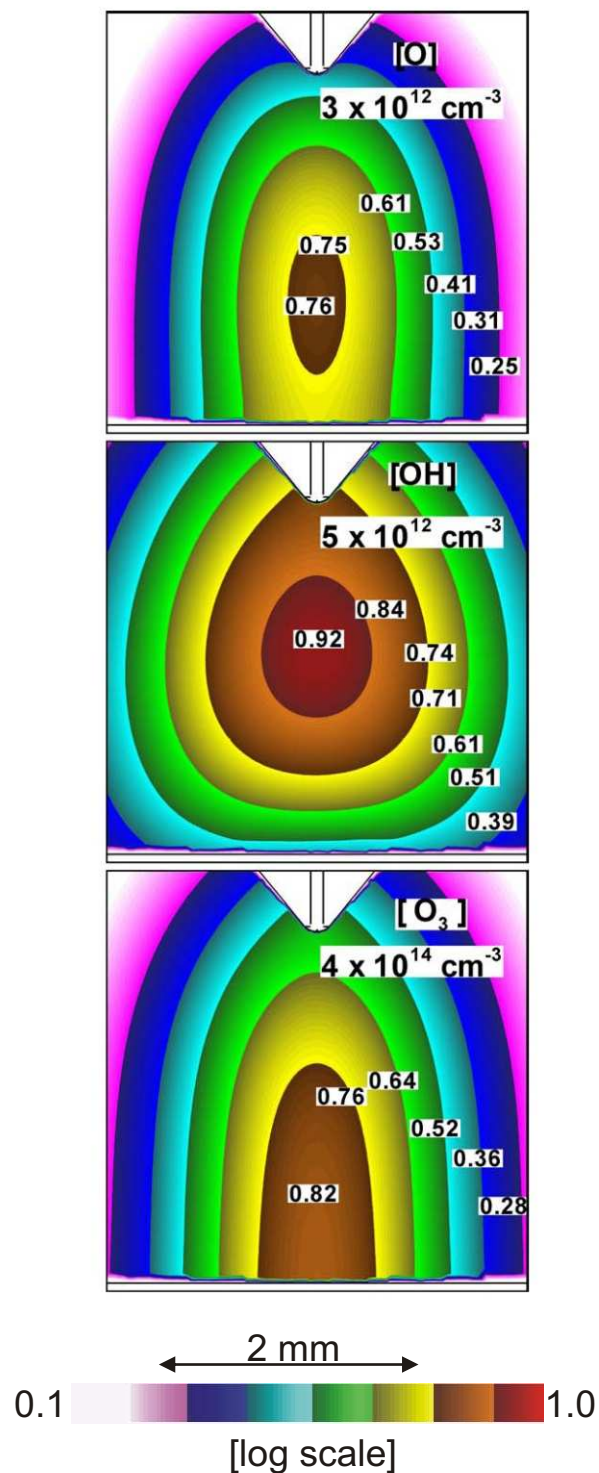


Fig. 3. Densities of reactive gas phase radicals: O, OH and O₃, during the interpulse period. The bulk of O atoms are converted to O₃ by three body association reactions with O₂.

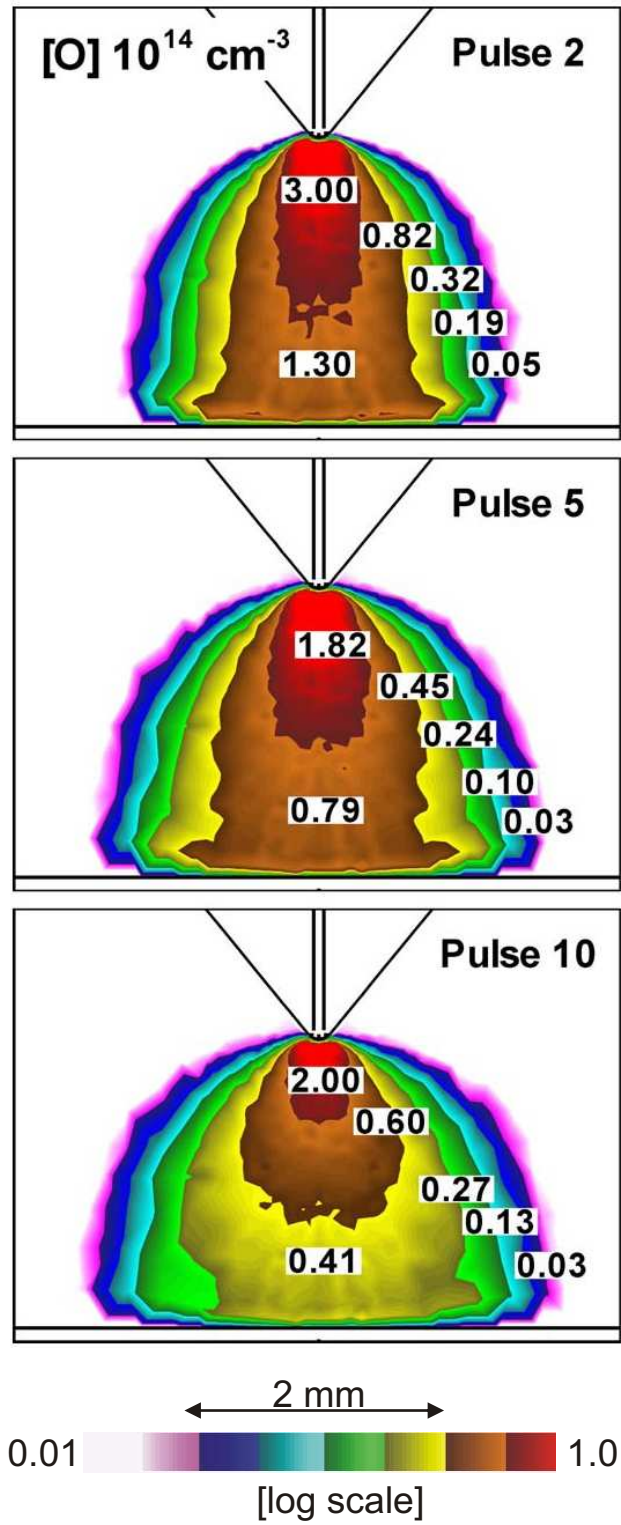


Fig. 4 The discharge is repetitively pulsed at a frequency of 1 kHz. The density of O atoms generated during different pulses decreases slightly with the increasing number of pulses as the composition of the background gas changes. Most O atoms generated during the previous pulse are consumed during the interpulse period. The gas composition is He/O₂/H₂O=89/10/1 at atmospheric pressure with negligible flow.

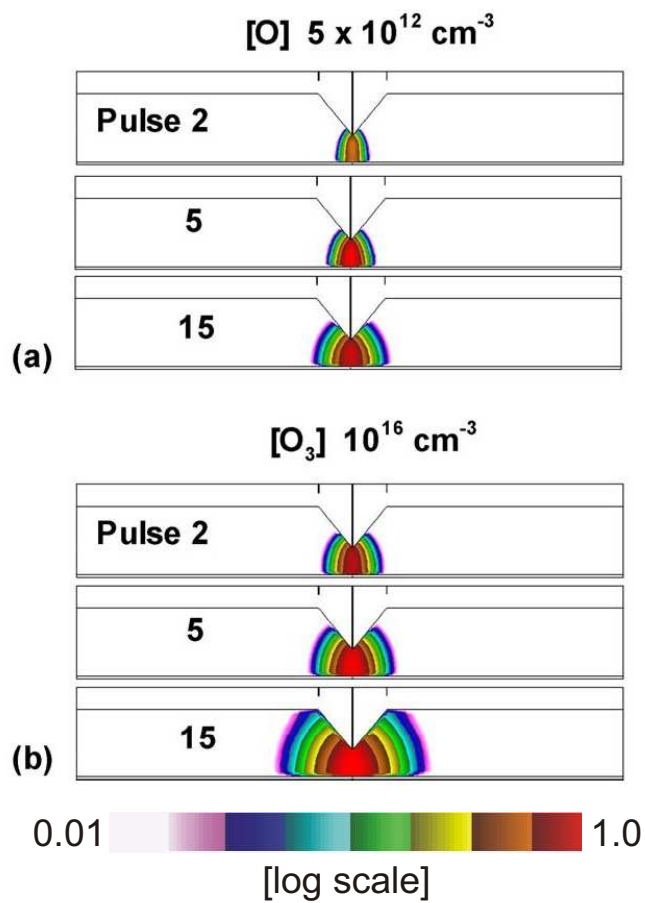


Fig. 5 (a) The density of O atoms and (b) O₃ after a number of pulses. Conditions are the same as in Fig. 5. In the absence of flow, O₃ merely diffuses in either direction away from the discharge zone.

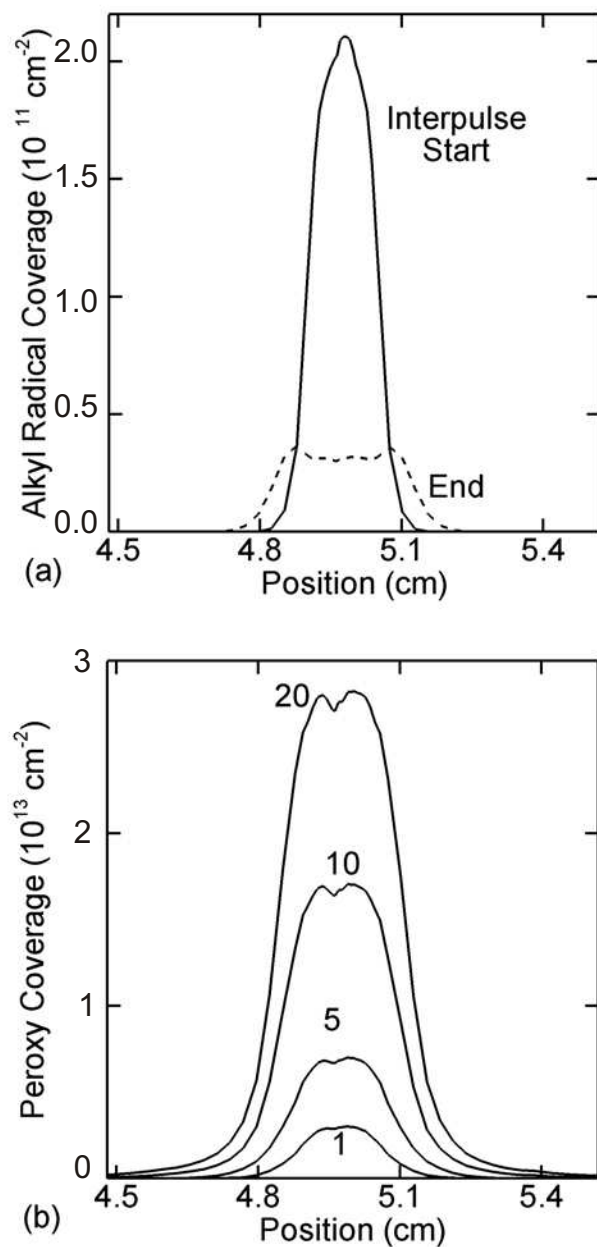


Fig. 6 The coverage of alkyl and peroxy groups with number of pulses with a static polypropylene surface (a) Alkyl groups are periodically regenerated and consumed in every pulse and (b) Peroxy groups accumulate from pulse to pulse.

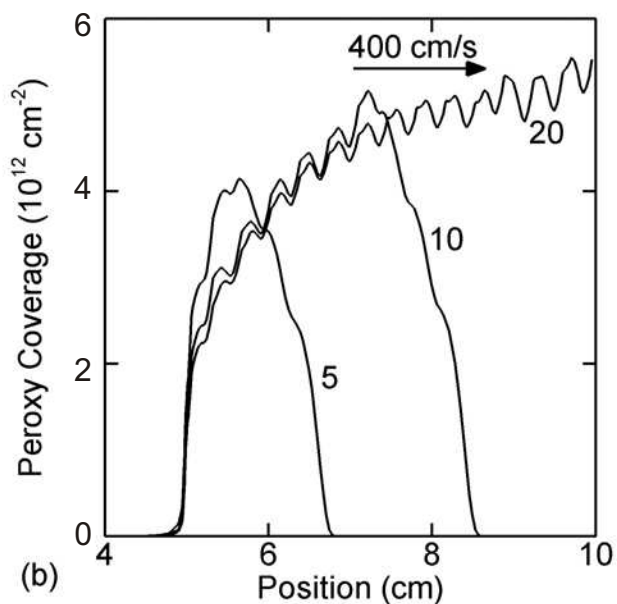
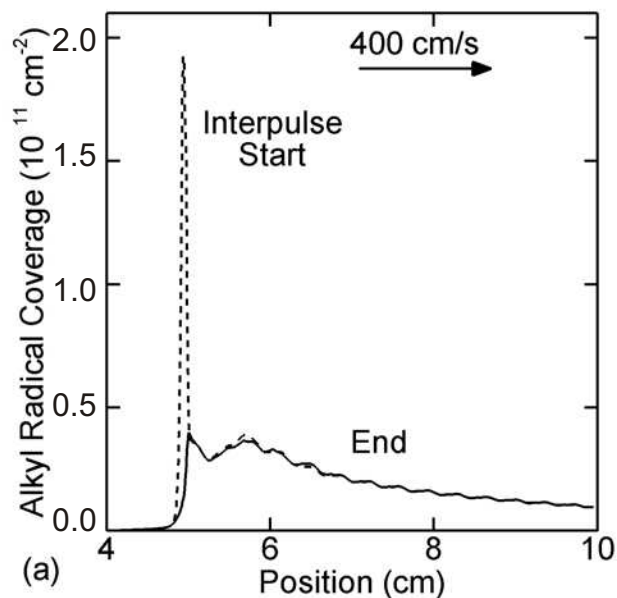


Fig. 7 The coverage of alkyl and peroxy groups with number of pulses with a moving polypropylene surface (a) Alkyl groups are periodically regenerated and consumed in every pulse and (b) Peroxy groups accumulate from pulse to pulse. The conditions are He/O₂/H₂O=89/10/1 at 1 atmosphere with a voltage of -5 kV applied with a pulsing frequency of 1 kHz. The polypropylene sheet moves at 400 cm/s.

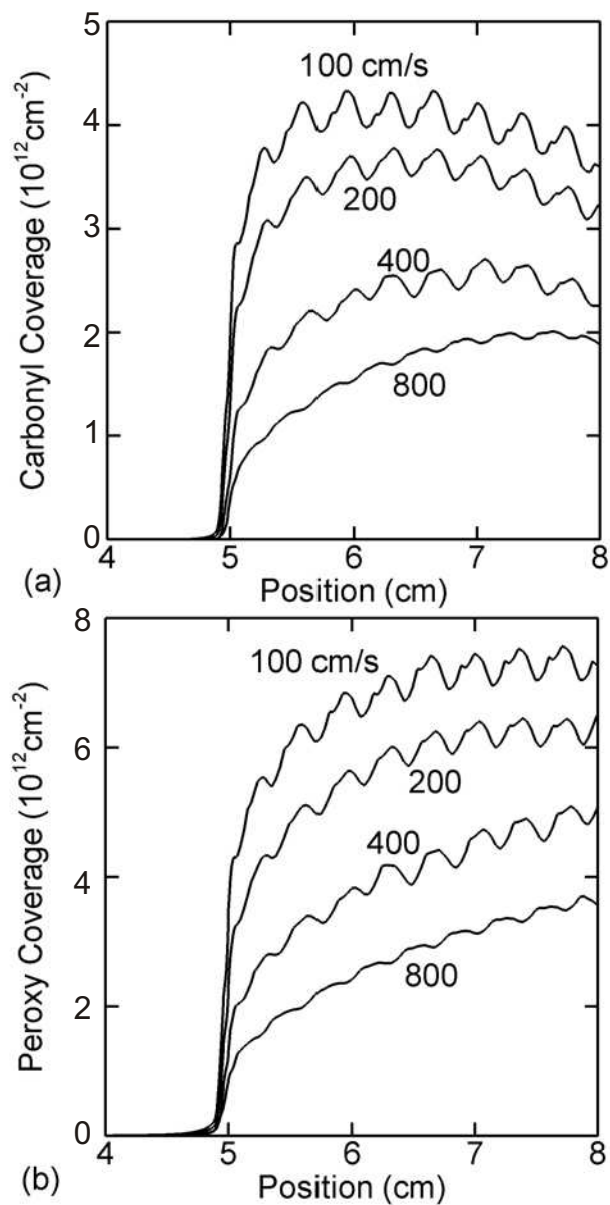


Fig. 8 Comparison the surface coverage of (a) carbonyl and (b) peroxy groups during the continuous treatment of polypropylene with no gas flow. Lower residence time increases the coverage of both carbonyl and peroxy groups. Conditions are otherwise the same as in Fig. 7.

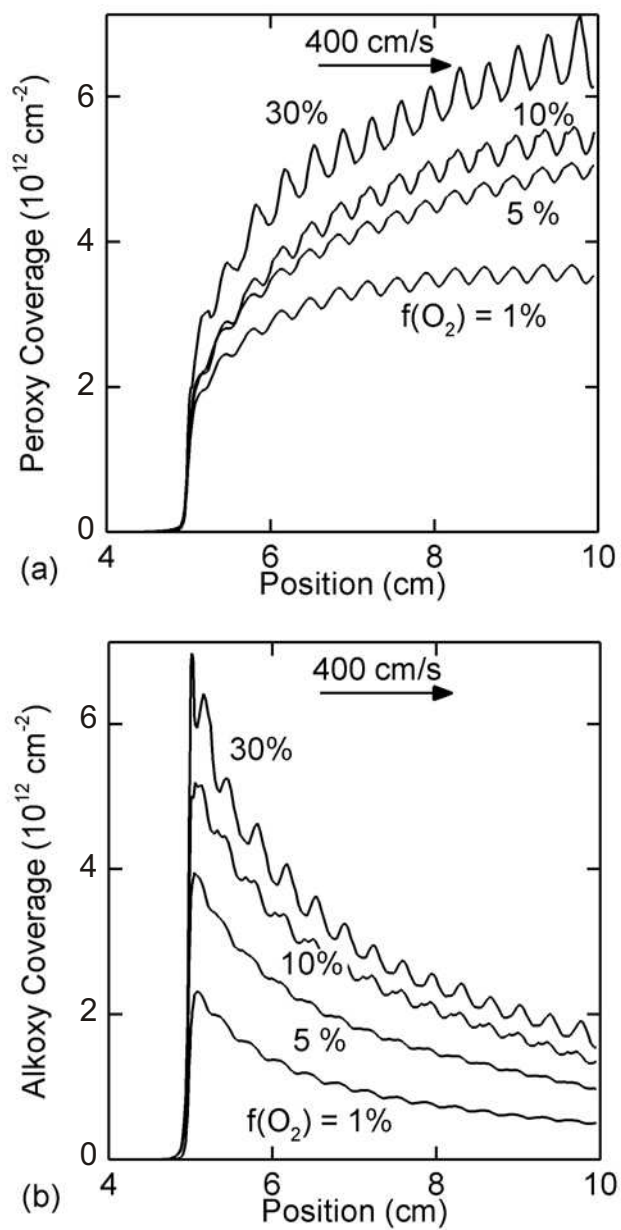


Fig. 9 The coverage of peroxy and alkoxy groups on a moving polypropylene sheet as a function of O_2 fraction. Conditions are otherwise the same as in Fig. 8.

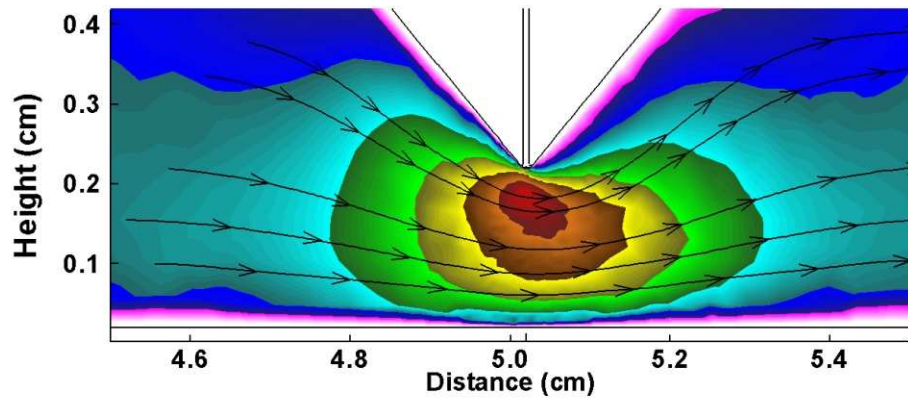


Fig. 10 Gas flow sets up a convective velocity field that transports plasma species downstream of the discharge. The velocity increases near the corona due to the smaller areal cross-section.

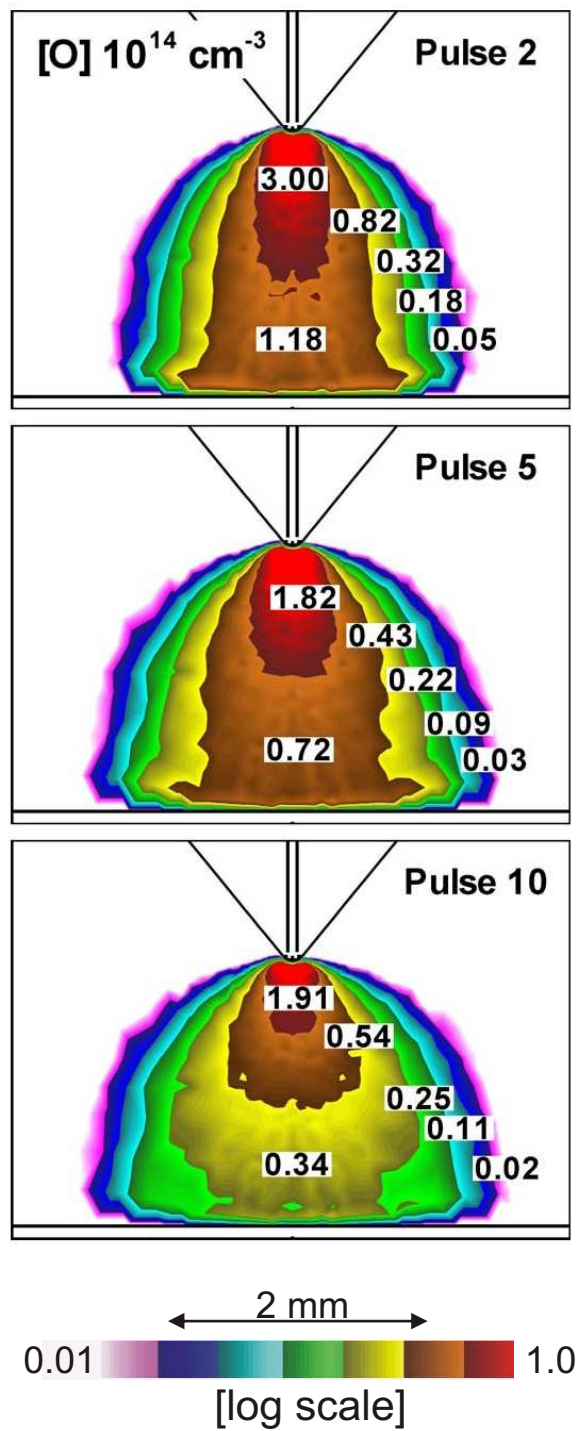


Fig. 11 Gas flow has little effect on the production of O atoms, with a density of 10^{14} - 10^{15} cm^{-3} in the discharge at 30 lpm. Conditions are otherwise similar to those in Fig. 8.

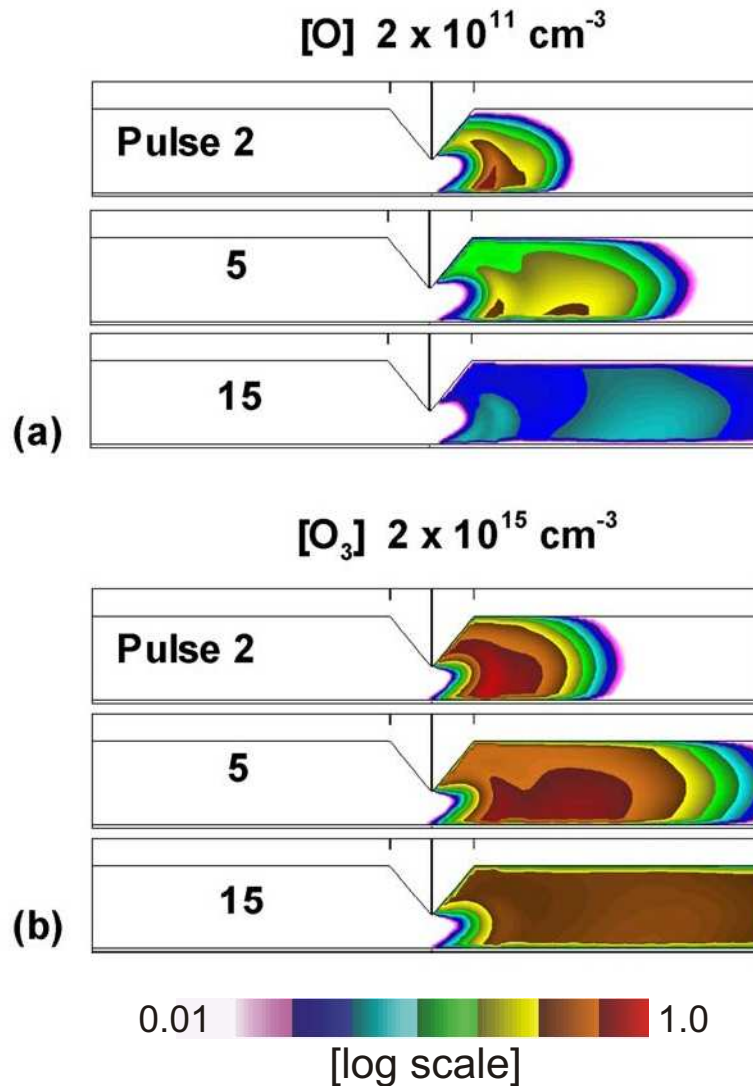


Fig. 12 The density of (a) O atoms and (b) O₃ after a number of different pulses with a gas flow rate of 30 lpm. The remaining conditions are the same as in Fig. 8. Though some O is convected downstream, its density is about 4 orders of magnitude lower than in the discharge zone after a pulse. Most O atoms are consumed in 3-body reactions with O₂ to form O₃. O₃ accumulates and is convected downstream, where its density is about 10¹⁵ cm⁻³.

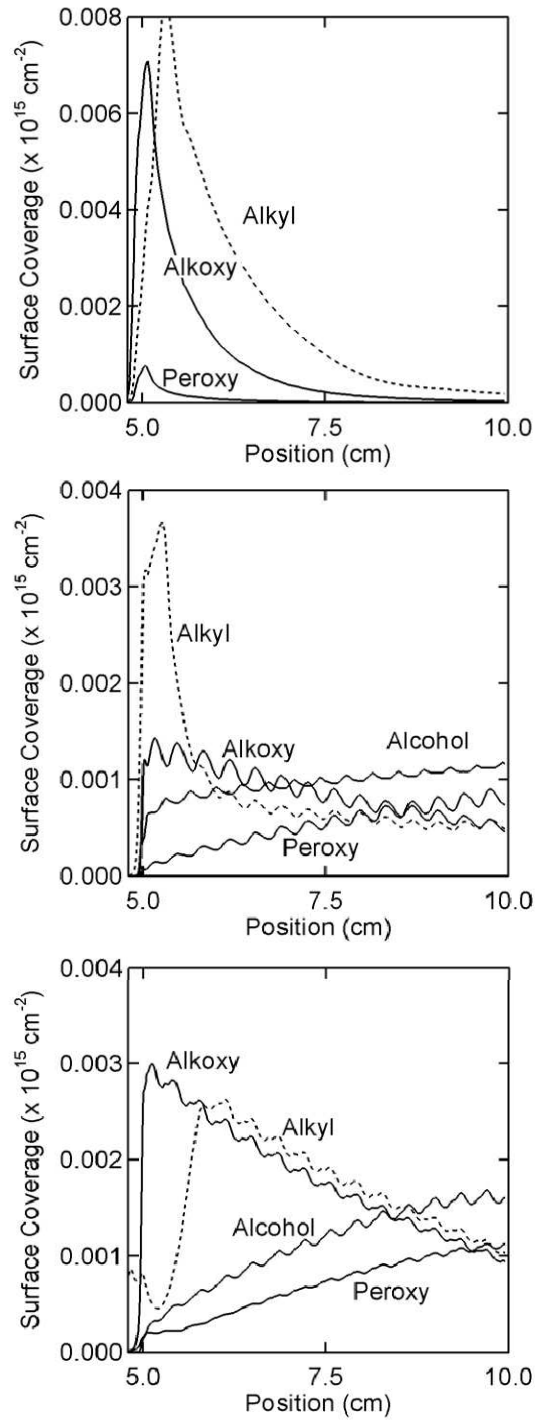


Fig. 13 Treatment for three cases are shown (a) gas flow of 20 lpm and no web speed (b) gas flow of 20 lpm with web speed of 400 cm/s and (c) No gas flow with web speed of 400 cm/s. Remaining conditions are the same as in Fig. 8.

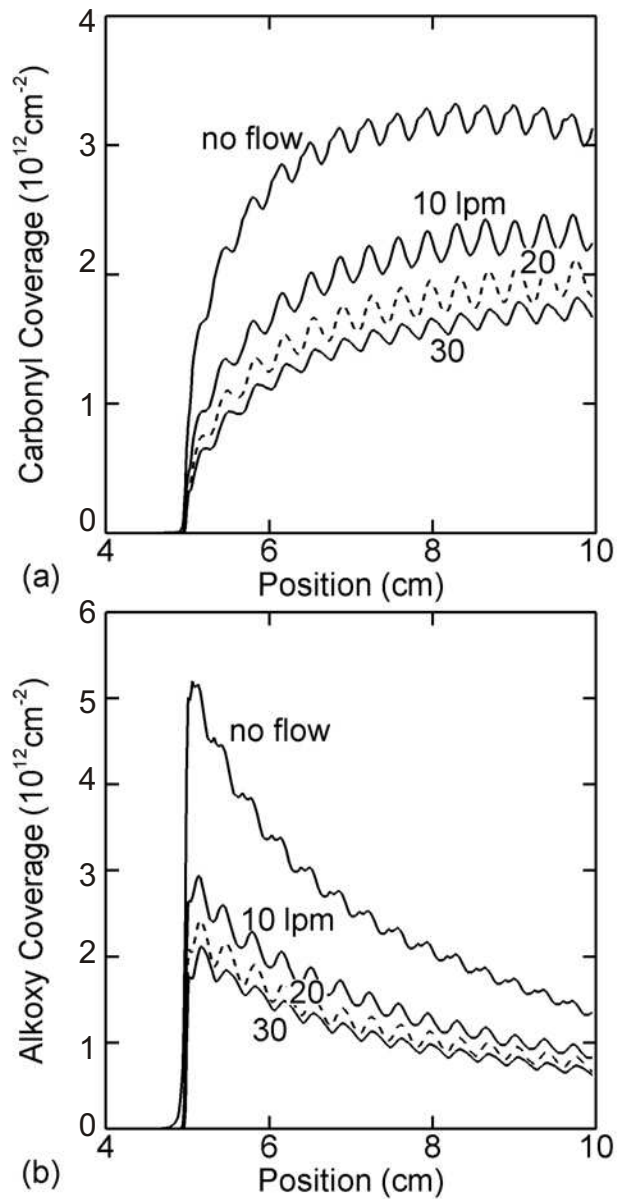


Fig. 14 Comparison the surface coverage of (a) carbonyl and (b) peroxy groups during the continuous treatment of polypropylene at 4 m/s with and without gas flow. Gas flow reduces alters the relative flux of O_3/O_2 across the surface resulting in changes in the carbonyl and peroxy groups. Remaining conditions are the same as in Fig. 8.

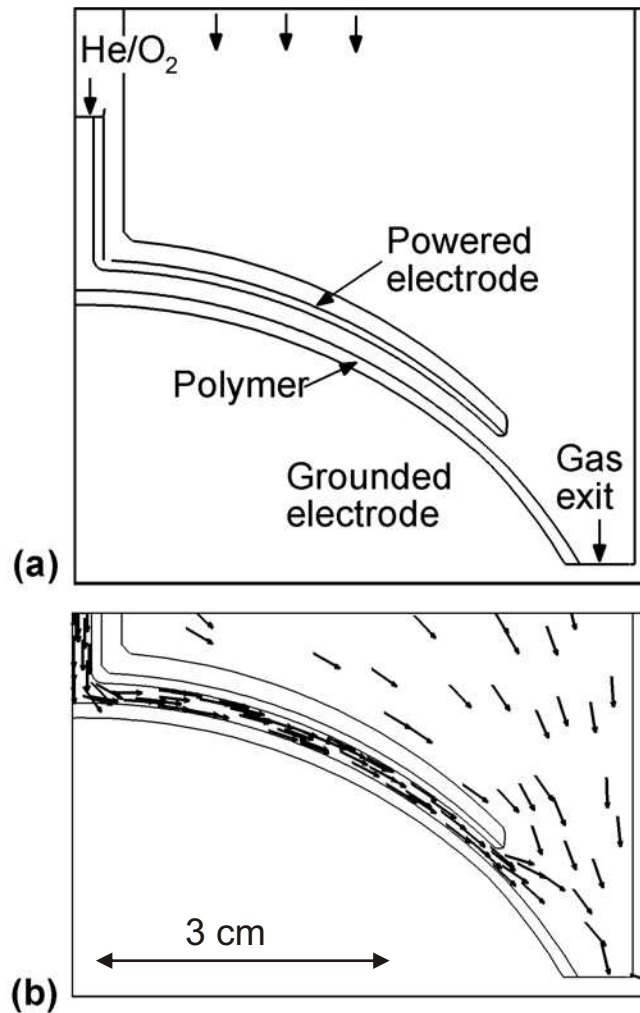


Fig. 15 (a) Schematic of the configuration typically used to treat polymer surfaces in reactive gas mixtures. The polymer is placed on the grounded drum electrode and moves as the drum rotates. The upper curved electrode is powered up to kV to breakdown the gas gap of 2 mm. Reactive gas mixtures such He/O₂ used here are introduced at few lpm through the nozzle on the axis. In this model, the surrounding environment is also assumed to be He/O₂. (b) The velocity flow field established for 100 lpm flow.

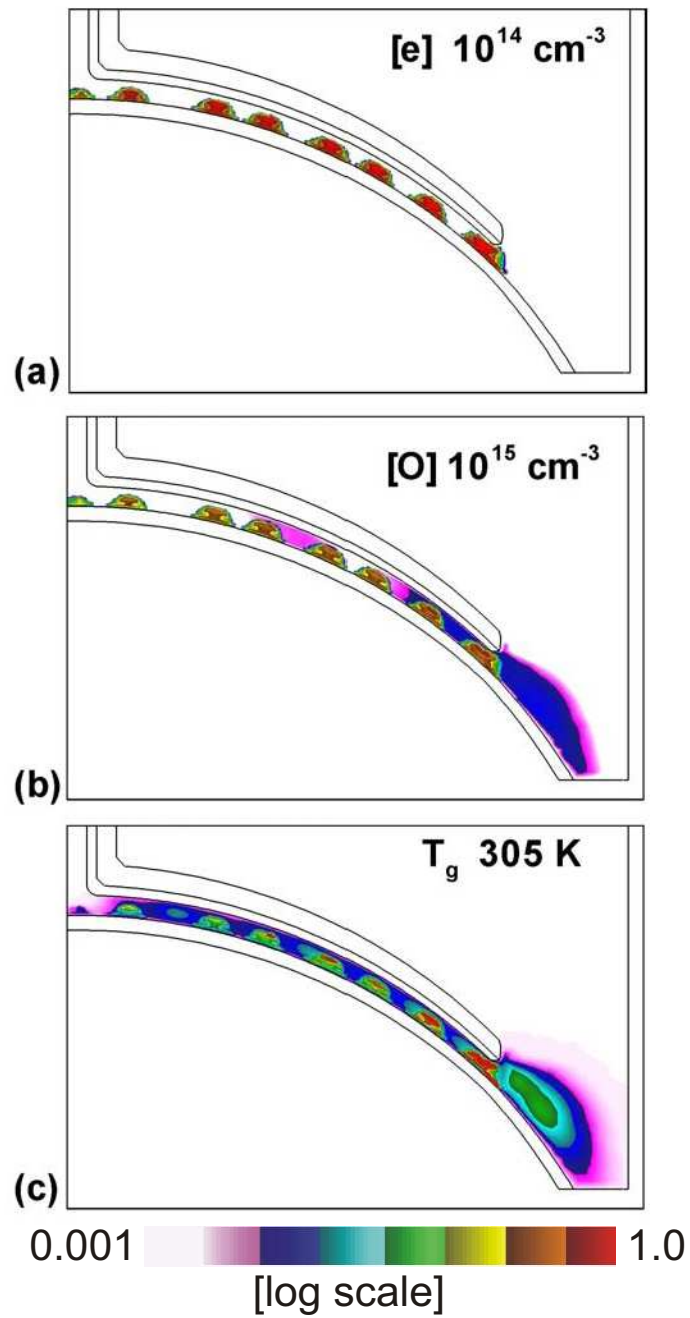


Fig. 16 Densities of (a) electrons and (b) O atoms generated in multiple discharges during a pulse. There is some background O density from the previous pulse. Gas temperature rises by 1 - 5 K in the discharges due to power deposition by ions.

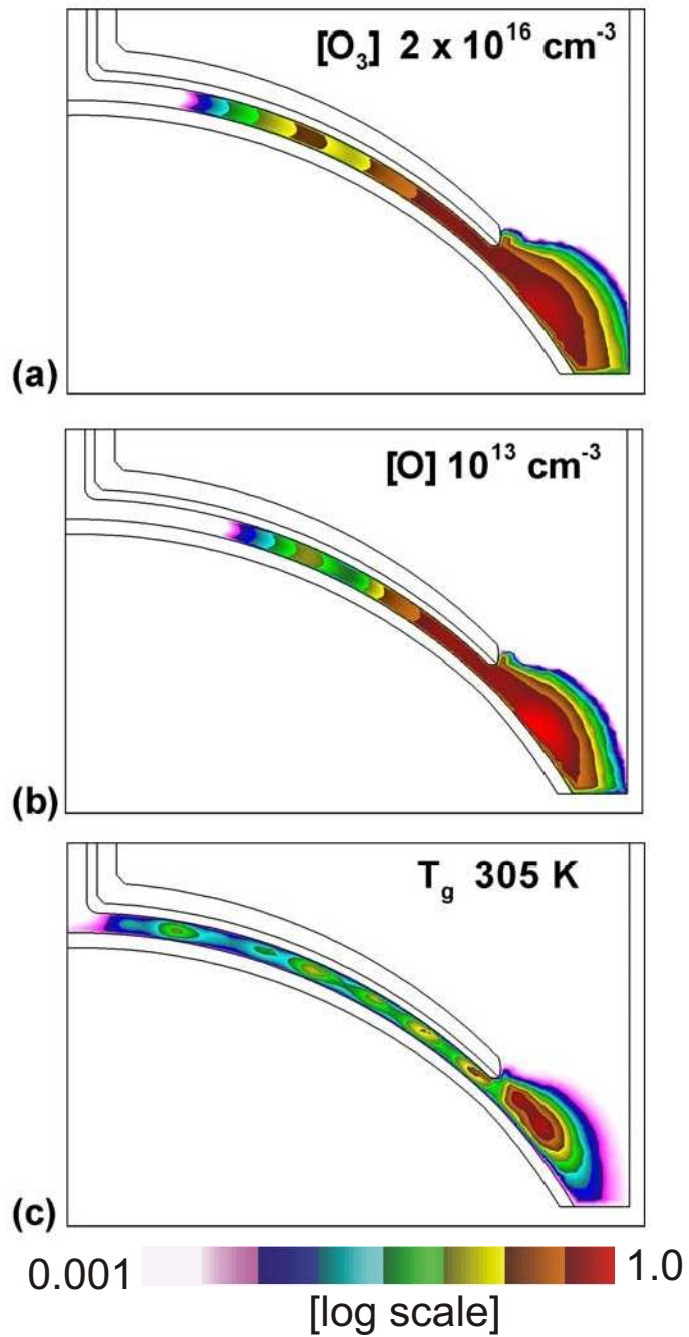


Fig. 17. Densities of (a) O_3 and (b) O atoms generated in multiple discharges during a pulse. There is some background O density from the previous pulse. (c) Convective transport increases gas temperature downstream by only 5 K.

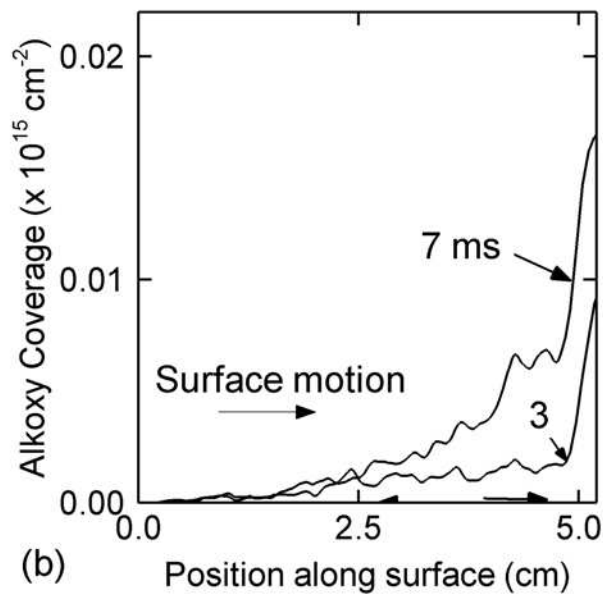
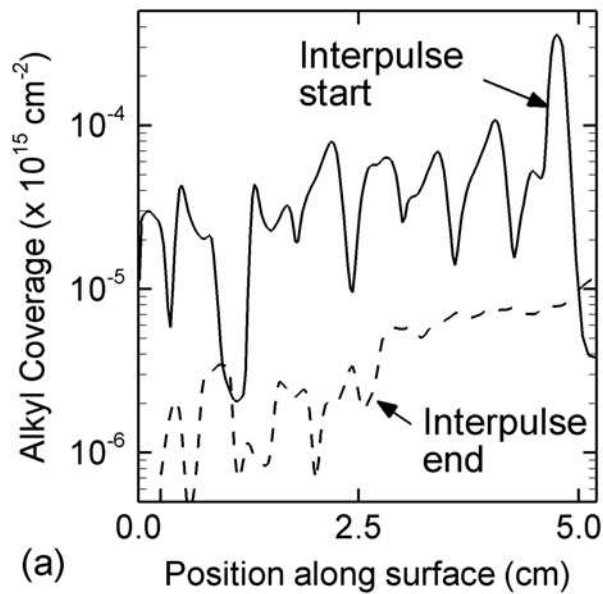


Fig. 18 (a) The densities of alkyl radicals increase across the polymer due to radical fluxes from multiple discharges during the pulse. In the interpulse period, alkyl radicals are consumed in further reactions. (b) The polymer is treated as it moves through multiple discharges increasing the alkoxy coverage to 1% near the exit.

8.8 References

1. C.-M. Chan, "Polymer Surface Modification and Characterization" (Hanser/Gardner, New York, 1994).
2. Viv Jones, M. Strobel and M. J. Prokosch, *Plasma Processes and Polymers*, **2**, 547 (2005).
3. M. Abdel-Salam, A. Mizuno, and K. Shimizu, *Journal of Physics D*, **30**, 864 (1997).
4. F. Massines, R. Messaoudi and C. Mayoux, *Plasmas and Polymers*, **3**, 43 (1998).
5. B. Eliasson and U. Kogelschatz, *IEEE Transactions on Plasma Science*, **19**, 309 (1991).
6. S. K. Dhali and P. F. Williams, *Journal of Applied Physics*, **62**, 4696 (1987).
7. N. Naude, J.-P. Cambronne, N. Gherardi and F. Massines, *Journal of Physics D*, **38**, 530 (2005).
8. F. Massines, G. Gouda, N. Gherardi, M. Duran and E. Croquesel, *Plasmas and Polymers*, **6**, 35 (2001).
9. F. Forster *et al*, *Surface Coatings and Technology*, **98**, 1121 (1998).
10. J. F. Behnke *et al*, *Vacuum*, **71**, 417 (2003).

APPENDIX A. LIST OF REACTIONS FOR HUMID AIR

List of Species

e		
N ₂	O ₂	H ₂ O
N ₂ (v)	O ₂ *	H ₂ O ⁺
N ₂ *	O ₂ ⁺	H ₂
N ₂ **	O ₂ ⁻	H
N ₂ ⁺	O	OH
N	O*	HO ₂
N ⁺	O ⁺	
N*	O ⁻	
N ₄ ⁺	O ₃	

<u>Reaction</u>	<u>Rate Coefficient^a</u>	<u>Reference</u>
$e + N_2 \rightarrow N_2(v) + e$	b	1
$e + N_2 \rightarrow N_2^* + e$	b	1
$e + N_2 \rightarrow N_2^* + e$	b	1
$e + N_2 \rightarrow N_2^* + e$	b	1
$e + N_2 \rightarrow N_2^* + e$	b	1
$e + N_2 \rightarrow N_2^{**} + e$	b	1
$e + N_2 \rightarrow N + N + e$	b	1

$e + N_2 \rightarrow N_2^+ + e + e$	b	1
$e + N_2(v) \rightarrow N_2(v) + e$	b	1
$e + N_2(v) \rightarrow N_2 + e$	b	1
$e + N_2(v) \rightarrow N_2^* + e$	b	1
$e + N_2(v) \rightarrow N_2^+ + e + e$	b	1
$e + N_2^* \rightarrow N_2^* + e$	b	1
$e + N_2^* \rightarrow N_2(v) + e$	b	1
$e + N_2^* \rightarrow N_2 + e$	b	1
$e + N_2^* \rightarrow N_2^+ + e + e$	b	2
$e + N_2^{**} \rightarrow N_2 + e$	b	1
$e + N \rightarrow N^* + e$	b	3
$e + N \rightarrow N^* + e$	b	3
$e + N \rightarrow N^+ + e + e$	b	4
$e + N^* \rightarrow N^* + e$	b	3
$e + N^* \rightarrow N + e$	b	3
$e + N^* \rightarrow N^+ + e + e$	b	3
$e + N_2^+ \rightarrow N^* + N$	$2 \times 10^{-7} T_e^{-0.5}$	5
$e + N_4^+ \rightarrow N_2 + N_2$	$2 \times 10^{-7} T_e^{-0.5}$	5
$e + O_2 \rightarrow O_2 + e$	b	6
$e + O_2 \rightarrow O^- + O$	b	6
$e + O_2 \rightarrow O_2^* + e$	b	6
$e + O_2 \rightarrow O + O + e$	b	6

$e + O_2 \rightarrow O_2^* + e$	b	6
$e + O_2 \rightarrow O_2^+ + e + e$	b	6
$e + O_2 \rightarrow O + O^+ + e + e$	b	6
$e + O_2 + O_2 \rightarrow O_2^- + O_2$	$2 \times 10^{-31} T_e^{-1.0}$	6
$e + O_2 + N_2 \rightarrow O_2^- + N_2$	$2 \times 10^{-31} T_e^{-1.0}$	6
$e + O_2^* \rightarrow O_2^* + e$	b	7,i
$e + O_2^* \rightarrow O^- + O$	b	8
$e + O_2^* \rightarrow O_2 + e$	b	6,h
$e + O_2^* \rightarrow O + O + e$	b	6
$e + O_2^* \rightarrow O + O + e$	b	6
$e + O_2^* \rightarrow O_2^+ + e + e$	b	9
$e + O_2^* \rightarrow O + O^+ + e + e$	b	6
$e + O_2^* + O_2 \rightarrow O_2^- + O_2$	$2 \times 10^{-31} T_e^{-1.0}$	6
$e + O_2^* + N_2 \rightarrow O_2^- + N_2$	$2 \times 10^{-31} T_e^{-1.0}$	6
$e + O \rightarrow O + e$	b	10
$e + O \rightarrow O^* + e$	b	11
$e + O \rightarrow O^+ + e + e$	b	11
$e + O^* \rightarrow O^* + e$	b	11
$e + O^* \rightarrow O + e$	b	11
$e + O^* \rightarrow O^+ + e + e$	b	11
$e + O_2^+ \rightarrow O + O$	$1.2 \times 10^{-8} T_e^{-0.7}$	11
$e + O_2^+ \rightarrow O^* + O$	$8.9 \times 10^{-9} T_e^{-0.7}$	11

$e + \text{H}_2\text{O} \rightarrow \text{O}^- + \text{H}_2$	b	12
$e + \text{H}_2\text{O} \rightarrow \text{H} + \text{OH} + e$	b	12
$e + \text{H}_2\text{O} \rightarrow \text{H} + \text{OH} + e$	b	12
$e + \text{H}_2\text{O} \rightarrow \text{H}_2\text{O}^+ + e + e$	b	12
$e + \text{H}_2\text{O}^+ \rightarrow \text{H} + \text{OH}$	$1.2 \times 10^{-8} T_e^{-0.7}$	11
$e + \text{H}_2 \rightarrow \text{H} + \text{H} + e$	b	13
$\text{O}_2^- + \text{O}_2^+ \rightarrow \text{O}_2 + \text{O}_2$	2×10^{-6}	14
$\text{O}_2^- + \text{O}^+ \rightarrow \text{O} + \text{O}_2$	2×10^{-6}	14
$\text{O}_2^- + \text{N}_2^+ \rightarrow \text{N}_2 + \text{O}_2$	2×10^{-6}	14
$\text{O}_2^- + \text{N}^+ \rightarrow \text{N} + \text{O}_2$	2×10^{-6}	14
$\text{O}_2^- + \text{N}_4^+ \rightarrow \text{N}_2 + \text{N}_2 + \text{O}_2$	2×10^{-6}	14
$\text{O}_2^- + \text{H}_2\text{O}^+ \rightarrow \text{H}_2\text{O} + \text{O}_2$	2×10^{-6}	14
$\text{O}^- + \text{O}_2^+ \rightarrow \text{O}_2 + \text{O}$	3×10^{-6}	14
$\text{O}^- + \text{O}^+ \rightarrow \text{O} + \text{O}$	3×10^{-6}	14
$\text{O}^- + \text{N}_2^+ \rightarrow \text{N}_2 + \text{O}$	3×10^{-6}	14
$\text{O}^- + \text{N}^+ \rightarrow \text{N} + \text{O}$	3×10^{-6}	14
$\text{O}^- + \text{N}_4^+ \rightarrow \text{N}_2 + \text{N}_2 + \text{O}$	3×10^{-6}	14
$\text{O}^- + \text{H}_2\text{O}^+ \rightarrow \text{H}_2\text{O} + \text{O}$	3×10^{-6}	14
$\text{O}^- + \text{O}^+ + \text{O}_2 \rightarrow \text{O}_2 + \text{O}_2$	1.2×10^{-25}	14
$\text{O}^- + \text{O}^+ + \text{N}_2 \rightarrow \text{O}_2 + \text{N}_2$	1.2×10^{-25}	14
$\text{O}^- + \text{O}^+ + \text{H}_2\text{O} \rightarrow \text{O}_2 + \text{H}_2\text{O}$	1.2×10^{-25}	14
$\text{O}^- + \text{O}_2 \rightarrow \text{O}_2^- + \text{O}$	1.5×10^{-20}	15

$O^- + O \rightarrow O_2 + e$	1.9×10^{-10}	15
$O^- + O_3 \rightarrow O_2 + O_2 + e$	$3 \times 10^{-10} T_g^{0.5}$	15
$O^- + O_3 \rightarrow O_2^- + O_2$	$1 \times 10^{-11} T_g^{0.5}$	15
$O_2^- + O \rightarrow e + O_3$	1.5×10^{-10}	15
$O_2^- + O \rightarrow O^- + O_2$	1.5×10^{-10}	15
$O_2^- + O_2^* \rightarrow e + O_2 + O_2$	2×10^{-10}	15
$N^+ + O_2 \rightarrow O_2^+ + N$	3×10^{-10}	15
$N_2^+ + N \rightarrow N^+ + N_2$	5×10^{-12}	15
$N_2^+ + N^* \rightarrow N^+ + N_2$	1×10^{-10}	f
$N_2^+ + O_2 \rightarrow O_2^+ + N_2$	5.1×10^{-11}	15
$N_4^+ + O_2 \rightarrow O_2^+ + N_2 + N_2$	2.5×10^{-10}	15
$N_2^+ + N_2 + O_2 \rightarrow N_4^+ + O_2$	$6.8 \times 10^{-29} T_g^{-1.64}$	15
$N_2^+ + N_2 + N_2 \rightarrow N_4^+ + N_2$	$6.8 \times 10^{-29} T_g^{-1.64}$	15
$N_4^+ + O_2 \rightarrow N_2^+ + N_2 + O_2$	$9.4 \times 10^{-13} T_g^{1.5} e^{-12638/T_g}$	15
$N_4^+ + N_2 \rightarrow N_2^+ + N_2 + N_2$	$9.4 \times 10^{-13} T_g^{1.5} e^{-12638/T_g}$	15
$O^+ + O_2 \rightarrow O_2^+ + O$	1.9×10^{-11}	15
$O^* + O_3 \rightarrow O_2 + O + O$	1.2×10^{-10}	16
$O^* + O_3 \rightarrow O_2 + O_2$	5×10^{-10}	16
$O^* + O \rightarrow O + O$	3×10^{-12}	14
$O^* + O_2^* \rightarrow O + O_2$	$1 \times 10^{-11} T_g^{0.5}$	17
$O^* + O \rightarrow O + O$	$1 \times 10^{-11} T_g^{0.5}$	14
$O^* + N_2 \rightarrow O + N_2$	$1.8 \times 10^{-11} e^{107/T_g}$	14

$O^* + O_2 \rightarrow O + O_2$	3.8×10^{-11}	17
$O_2^* + O_2 \rightarrow O_2 + O_2$	2.2×10^{-18}	17
$O_2^* + O_2 \rightarrow O + O_3$	3.0×10^{-21}	18
$O_2^* + O_3 \rightarrow O_2 + O_2 + O$	1×10^{-10}	14
$N^* + N_2 \rightarrow N + N_2$	2.4×10^{-14}	19
$N_2^* + N_2 \rightarrow N_2 + N_2$	1.9×10^{-13}	20
$N_2^* + O_2 \rightarrow O + O + N_2$	1.5×10^{-12}	20
$N_2^* + O_2 \rightarrow O_2 + N_2$	2.8×10^{-11}	20
$O + O_3 \rightarrow O_2 + O_2$	8×10^{-12}	21
$O + O_2 + O_2 \rightarrow O_3 + O_2$	$6.9 \times 10^{-34} T_g^{-1.25}$	21
$O + O_2 + N_2 \rightarrow O_3 + N_2$	$6.9 \times 10^{-34} T_g^{-1.25}$	21
$O + O + O_2 \rightarrow O_2 + O_2$	$5.2 \times 10^{-35} e^{900/T_g}$	21
$O + O + N_2 \rightarrow O_2 + N_2$	$5.2 \times 10^{-35} e^{900/T_g}$	21
$O + O + H_2O \rightarrow O_2 + H_2O$	$5.2 \times 10^{-35} e^{900/T_g}$	21
$N + N + O_2 \rightarrow N_2 + O_2$	3.9×10^{-33}	21
$N + N + N_2 \rightarrow N_2 + N_2$	3.9×10^{-33}	21
$N + N + H_2O \rightarrow N_2 + H_2O$	3.9×10^{-33}	21
$N_2 + O_2 \rightarrow N + N + O_2$	$4.3 \times 10^{-10} e^{-86460/T_g}$	21
$N_2 + N_2 \rightarrow N + N + N_2$	$4.3 \times 10^{-10} e^{-86460/T_g}$	21
$N_2 + H_2O \rightarrow N + N + H_2O$	$4.3 \times 10^{-10} e^{-86460/T_g}$	21
$O_2 + O_2 \rightarrow O + O + O_2$	$5.2 \times 10^{-10} e^{-58410/T_g}$	21
$O_2 + N_2 \rightarrow O + O + N_2$	$5.2 \times 10^{-10} e^{-58410/T_g}$	21

$O_2 + H_2O \rightarrow O + O + H_2O$	$5.2 \times 10^{-10} e^{-58410/Tg}$	21
$O_3 + O_2 \rightarrow O_2 + O + O_2$	$1.6 \times 10^{-9} e^{-11490/Tg}$	21
$O_3 + N_2 \rightarrow O_2 + O + N_2$	$1.6 \times 10^{-9} e^{-11490/Tg}$	21
$O_3 + H_2O \rightarrow O_2 + O + H_2O$	$1.6 \times 10^{-9} e^{-11490/Tg}$	21
$N_2^{**} \rightarrow N_2$	2×10^8	g
$N_2^{**} \rightarrow N_2^*$	2×10^8	g
$O_2 \rightarrow O_2^+ + e$	1×10^{-19}	g
$O + HO_2 \rightarrow OH + O_2$	2.90×10^{-11}	21
$O + OH \rightarrow H + O_2$	2.30×10^{-11}	21
$O + OH + O_2 \rightarrow HO_2 + O_2$	2.76×10^{-31}	21
$O + OH + N_2 \rightarrow HO_2 + N_2$	2.76×10^{-31}	21
$O + H_2O_2 \rightarrow OH + HO_2$	1.40×10^{-12}	21
$OH + HO_2 \rightarrow H_2O + O_2$	8.00×10^{-11}	21
$OH + O_3 \rightarrow HO_2 + O_2$	1.90×10^{-12}	21
$OH + H_2O_2 \rightarrow H_2O + HO_2$	2.90×10^{-12}	21
$OH + OH + O_2 \rightarrow H_2O_2 + O_2$	6.90×10^{-31}	21
$H + O_3 \rightarrow OH + O_2$	1.40×10^{-10}	21
$H + HO_2 \rightarrow H_2 + O_2$	1.1×10^{-10}	21
$H + HO_2 \rightarrow H_2O + O$	2.4×10^{-12}	21
$H + HO_2 \rightarrow OH + OH$	7.2×10^{-11}	21
$H + H_2O_2 \rightarrow H_2O + OH$	5×10^{-14}	21
$H + O_2 + O_2 \rightarrow HO_2 + O_2$	6.14×10^{-32}	21

$\text{H} + \text{O}_2 + \text{N}_2 \rightarrow \text{HO}_2 + \text{N}_2$	6.14×10^{-32}	21
$\text{HO}_2 + \text{O}_3 \rightarrow \text{OH} + \text{O}_2 + \text{O}_2$	1.40×10^{-14}	21
$\text{HO}_2 + \text{HO}_2 + \text{O}_2 \rightarrow \text{H}_2\text{O}_2 + \text{O}_2 + \text{O}_2$	1.90×10^{-33}	21
$\text{HO}_2 + \text{HO}_2 + \text{N}_2 \rightarrow \text{H}_2\text{O}_2 + \text{N}_2 + \text{O}_2$	1.90×10^{-33}	21

^aRate constant in $\text{cm}^3 \text{s}^{-1}$ for 2-body reactions, and $\text{cm}^6 \text{s}^{-1}$ for 3-body reactions.

^bRate constant calculated by using cross-section data from the indicated reference.

^cRate constant calculated using Gryzinski cross-sections,

$$2.36 \times 10^{-16} \left(\frac{E}{E_0} - 1 \right) \times a \log \left(1.25 \times \frac{E}{E_0} \right) \left(\frac{E}{E_0} \right)^{-2}.$$

^dRate constant for electron-ion recombination (without dissociation).

^eColoumb elastic cross-sections from Mitchner and Kruger.

^fRate constant estimated by analogy.

^gRate constant estimated.

^hCross section obtained by detailed balance.

ⁱDrawin-Born-Bethe fit to [7]

A. 1 References

1. Y. Itikawa, M. Hayashi, A. Ichimura, K. Onda, K. Sakimoto, K. Takayanagi, M. Nakamura, H. Nishimura, and T. Takayanagi, *Journal of Physical and Chemical Reference Data*, **15**, 985 (1986).
2. L. Vriens, *Physics Letters*, **8**, 260-261 (1964).
3. R.J.W. Henry, P. G. Burke and A.-L. Sinfailam, *Physical Review* **178**, 218, 1969.
4. A.C.H. Smith, *Physical Review* **127**, 1647 (1962).
5. J.B.A. Mitchell, *Physical Reports* **186**, 215-248 (1990).
6. A. V. Phelps, JILA Information Center Report Number 28, University of Colorado (1985).
7. Hall and Trajmar, *J. Phys. B*, **8**, L293, (1975).
8. P. D. Burrow, *Journal of Chemical Physics*, **59**, 4922 (1973).
9. E. Krishnakumar and S. K. Srivastava, *International Journal of Mass Spectrometry and Ion Processes* **113**, 1 (1992).
10. Y. Itikawa and A. Ichimura, *Journal of Physical and Chemical Reference Data*, **19**, 637 (1990).
11. R. R. Laher and F. R. Gilmore, *Journal of Physical and Chemical Reference Data*, **19**, 277 (1990).
12. M. Hayashi in "*Swarm studies and inelastic electron-molecular collisions*", edited by L.C. Pitchford, V. B. McKoy, A. Chutjian and S. Trajmar, Springer-Verlag, New York, (1987).
13. M. Hayashi, *Journal de Physique*, **40**, C7/45-46 (1979).
14. B. F. Gordiets *et al.*, *IEEE Transactions on Plasma Science* **23**, 750 (1995).

15. Y. Ikezoe, S. Matsuoka, M. Takebe, and A. Viggiano, *Gas Phase Ion-Molecule Reaction Rate Constants Through 1986* (Ion Reaction Research Group of the Mass Spectroscopy Society of Japan, Tokyo, Japan, 1987).
16. R. Atkinson *et al.*, *Journal of Physical and Chemical Reference Data* **26**, 1329 (1997).
17. R. Atkinson, *et al.*, *Journal of Physical and Chemical Reference Data* **26**, 521 (1997).
18. R. K. Datta and K. N. Rao, *Indian Journal of Chemistry A*. **18A**, 102 (1979).
19. J. C. Person and D. O. Ham, *Radiat. Phys. Chem.*, **31**, 1 (1988).
20. L. G. Piper, *J. Chem. Phys.* **87**, 1625 (1987).
21. *NIST Standard Reference Database 17-2Q98* (National Institute of Standards and Technology, Gaithersburg, MD, 1998).

APPENDIX B. LIST OF REACTIONS FOR He/O₂/H₂O MIXTURES

List of Species

e	O ₂ ⁺	OH
He	O ₂ ⁻	H
He*	He ^{**}	O
He ⁺	O*	H
O ₂	O ¹ S	H ₂ O ₂
O ₂ (v)	O ⁺	O ₃
O ₂ *	O ⁻	O ₃ ⁻
O ₂ * ¹ S	H ₂ O	HO ₂

<u>Reactions</u>	<u>Rate Coefficient^a</u>	<u>Reference</u>
e + He → He* + e	b	1
e + He → He ^{**} + e	b	1,n
e + He → He ⁺ + e + e	b	2
e + He* → He ⁺ + e + e	b	3
e + He* → He + e	b	c
e + He ⁺ → He*	$6.76 \times 10^{-13} T_e^{-0.5}$	4
e + e + He ⁺ → He* + e	$5.12 \times 10^{-27} T_e^{-4.5}$	4
e + O ₂ → O ⁻ + O	b	5

$e + O_2 \rightarrow O_2(v) + e$	b	5
$e + O_2 \rightarrow O_2(v) + e$	b	5
$e + O_2 \rightarrow O_2(v) + e$	b	5
$e + O_2 \rightarrow O_2(v) + e$	b	5
$e + O_2 \rightarrow O_2^* + e$	b	5
$e + O_2 \rightarrow O_2^*{}^1S + e$	b	5
$e + O_2 \rightarrow O + O + e$	b	5
$e + O_2 \rightarrow O^* + O + e$	b	5
$e + O_2 \rightarrow O_2^+ + e + e$	b	5
$e + O_2 \rightarrow O^+ + O + e + e$	b	5
$e + O_2(v) \rightarrow O^- + O$	b	d
$e + O_2(v) \rightarrow O_2 + e$	b	c
$e + O_2(v) \rightarrow O_2^* + e$	b	e
$e + O_2(v) \rightarrow O_2^*{}^1S + e$	b	e
$e + O_2(v) \rightarrow O + O + e$	b	e
$e + O_2(v) \rightarrow O^* + O + e$	b	e
$e + O_2(v) \rightarrow O_2^+ + e + e$	b	e
$e + O_2(v) \rightarrow O^+ + O + e + e$	b	e
$e + O_2^* \rightarrow O^- + O$	b	6
$e + O_2^* \rightarrow O_2(v) + e$	b	c
$e + O_2^* \rightarrow O_2^*{}^1S + e$	b	7
$e + O_2^* \rightarrow O_2 + e$	b	c

$e + O_2^* \rightarrow O + O + e$	b	e
$e + O_2^* \rightarrow O^* + O + e$	b	e
$e + O_2^* \rightarrow O_2^+ + e + e$	b	e
$e + O_2^* \rightarrow O^+ + O + e + e$	b	e
$e + O_2^*{}^1S \rightarrow O^- + O$	b	f
$e + O_2^*{}^1S \rightarrow O_2(v) + e$	b	g
$e + O_2^*{}^1S \rightarrow O_2^* + e$	b	g
$e + O_2^*{}^1S \rightarrow O_2 + e$	b	c
$e + O_2^*{}^1S \rightarrow O + O + e$	b	e
$e + O_2^*{}^1S \rightarrow O^* + O + e$	b	e
$e + O_2^*{}^1S \rightarrow O_2^+ + e + e$	b	e
$e + O_2^*{}^1S \rightarrow O^+ + O + e + e$	b	e
$e + O_2 + M \rightarrow O_2^- + M^h$	$3.6 \times 10^{-31} T_e^{-0.5}$	8
$e + O_2(v) + M \rightarrow O_2^- + M^h$	$3.6 \times 10^{-31} T_e^{-0.5}$	8, e
$e + O_2^+ \rightarrow O + O$	$1.2 \times 10^{-8} T_e^{-0.7}$	9
$e + O_2^+ \rightarrow O^* + O$	$8.88 \times 10^{-9} T_e^{-0.7}$	9
$e + O_3 \rightarrow O^- + O_2$	b	10
$e + O_3 \rightarrow O_2^- + O$	b	10
$e + O \rightarrow O^* + e$	b	11
$e + O \rightarrow O^1S + e$	b	11
$e + O \rightarrow O^+ + e + e$	b	11
$e + O^* \rightarrow O + e$	b	c

$e + O^* \rightarrow O^+ + e + e$	b	e
$e + O^1S \rightarrow O + e$	b	c
$e + O^1S \rightarrow O^+ + e + e$	$6.6 \times 10^{-9} T_e 0.6 e^{-9.43/T_e}$	e
$e + O^- \rightarrow O + e + e$	$1.95 \times 10^{-12} T_e^{0.5} e^{-3.4/T_e}$	12
$e + O^+ \rightarrow O^*$	$5.3 \times 10^{-13} T_e^{-0.5}$	4
$e + e + O^+ \rightarrow O^* + e$	$5.12 \times 10^{-27} T_e^{-4.5}$	4
$O^- + O_2^+ \rightarrow O + O_2$	$2 \times 10^{-7} T_g^{-1.0}$	9
$O^- + O_2^+ \rightarrow O + O + O$	1×10^{-7}	9
$O^- + O^+ \rightarrow O + O$	$2 \times 10^{-7} T_g^{-1.0}$	9
$O^- + He^+ \rightarrow O + He$	$2 \times 10^{-7} T_g^{-1.0}$	9
$O_2^- + O_2^+ \rightarrow O_2 + O_2$	$2 \times 10^{-7} T_g^{-1.0}$	9
$O_2^- + O_2^+ \rightarrow O_2 + O + O$	1×10^{-7}	9
$O_2^- + O^+ \rightarrow O_2 + O$	$2 \times 10^{-7} T_g^{-1.0}$	9
$O_2^- + He^+ \rightarrow O_2 + He$	$2 \times 10^{-7} T_g^{-1.0}$	9
$O_3^- + O_2^+ \rightarrow O_3 + O_2$	$2 \times 10^{-7} T_g^{-1.0}$	9
$O_3^- + O_2^+ \rightarrow O_3 + O + O$	1×10^{-7}	9
$O_3^- + O^+ \rightarrow O_3 + O$	$2 \times 10^{-7} T_g^{-1.0}$	9
$O_3^- + He^+ \rightarrow O_3 + He$	$2 \times 10^{-7} T_g^{-1.0}$	9
$O^- + O_2^+ + M \rightarrow O + O_2 + M^h$	$2 \times 10^{-25} T_g^{-2.5}$	9
$O^- + O^+ + M \rightarrow O + O + M^h$	$2 \times 10^{-25} T_g^{-2.5}$	9
$O^- + He^+ + M \rightarrow O + He + M^h$	$2 \times 10^{-25} T_g^{-2.5}$	9
$O^- + O \rightarrow O_2 + e$	$2 \times 10^{-10} T_g^{0.5}$	13

$O^- + O_2^* \rightarrow O_3 + e$	$3 \times 10^{-10} T_g^{0.5}$	13
$O^- + O_2^* {}^1S \rightarrow O + O_2 + e$	$6.9 \times 10^{-10} T_g^{0.5}$	9
$O^- + O_2 \rightarrow O_3 + e$	$5 \times 10^{-15} T_g^{0.5}$	9
$O^- + O_2(v) \rightarrow O_3 + e$	$5 \times 10^{-15} T_g^{0.5}$	9, i
$O^- + O_3 \rightarrow O_2 + O_2 + e$	$3 \times 10^{-10} T_g^{0.5}$	13
$O^- + O_3 \rightarrow O_3^- + O$	$2 \times 10^{-10} T_g^{0.5}$	13
$O^- + O_3 \rightarrow O_2^- + O_2$	$1 \times 10^{-10} T_g^{0.5}$	13
$O_2^- + O \rightarrow O^- + O_2$	$1.5 \times 10^{-10} T_g^{0.5}$	13
$O_2^- + O \rightarrow O_3 + e$	$1.5 \times 10^{-10} T_g^{0.5}$	13
$O_2^- + O_2^* \rightarrow e + O_2 + O_2$	$2 \times 10^{-10} T_g^{0.5}$	13
$O_2^- + O_3 \rightarrow O_3^- + O_2$	$6 \times 10^{-10} T_g^{0.5}$	13
$O_3^- + O \rightarrow O_2^- + O_2$	$2.5 \times 10^{-10} T_g^{0.5}$	13
$O + O^+ + M \rightarrow O_2^+ + M^h$	$1 \times 10^{-29} T_g^{0.5}$	9
$O^+ + O_2 \rightarrow O_2^+ + O$	$2 \times 10^{-11} T_g^{-0.4}$	13
$O^+ + O_3 \rightarrow O_2^+ + O_2$	1.00×10^{-10}	9
$O^* + O \rightarrow O + O$	8.00×10^{-12}	9
$O^* + O_2 \rightarrow O + O_2^* {}^1S$	$2.56 \times 10^{-11} e^{67/Tg}$	14
$O^* + O_2 \rightarrow O + O_2^*$	$1.6 \times 10^{-12} e^{67/Tg}$	14
$O^* + O_2 \rightarrow O + O_2$	$4.8 \times 10^{-12} e^{67/Tg}$	14
$O^* + O_3 \rightarrow O_2 + O + O$	1.20×10^{-10}	15
$O^* + O_3 \rightarrow O_2 + O_2$	1.20×10^{-10}	16
$O^* + He \rightarrow O + He$	1.00×10^{-13}	17

$O^1S + O_2 \rightarrow O^* + O_2$	$3.2 \times 10^{-12} e^{-850/T_g}$	16
$O^1S + O_2 \rightarrow O + O_2$	$1.6 \times 10^{-12} e^{-850/T_g}$	16
$O^1S + O_2(v) \rightarrow O^* + O_2(v)$	$3.2 \times 10^{-12} e^{-850/T_g}$	16, i
$O^1S + O_2(v) \rightarrow O + O_2(v)$	$1.6 \times 10^{-12} e^{-850/T_g}$	16, i
$O^1S + O_2^* \rightarrow O + O_2$	1.10×10^{-10}	9, j
$O^1S + O_2^* \rightarrow O^* + O_2^*1S$	2.90×10^{-11}	9
$O^1S + O_2^* \rightarrow O + O + O$	3.20×10^{-11}	9
$O^1S + O \rightarrow O^* + O$	$1.67 \times 10^{-11} e^{-300/T_g}$	16
$O^1S + O \rightarrow O + O$	$3.33 \times 10^{-11} e^{-300/T_g}$	16
$O^1S + O_3 \rightarrow O_2 + O_2$	5.80×10^{-10}	16, k
$O_2^* + O \rightarrow O_2 + O$	2.00×10^{-16}	16
$O_2^* + O_2 \rightarrow O_2 + O_2$	$3 \times 10^{-18} e^{-200/T_g}$	14
$O_2^* + O_2(v) \rightarrow O_2 + O_2(v)$	$3 \times 10^{-18} e^{-200/T_g}$	14, i
$O_2^* + O_2^* \rightarrow O_2 + O_2$	$9 \times 10^{-17} e^{-560/T_g}$	16, l
$O_2^* + O_2^* \rightarrow O_2^*1S + O_2$	$9 \times 10^{-17} e^{-560/T_g}$	1
$O_2^* + O_2^* + O_2 \rightarrow O_3 + O_3$	$9 \times 10^{-32} e^{-560/T_g}$	9
$O_2^* + O_2 \rightarrow O + O_3$	$2.95 \times 10^{-21} T_g^{0.5}$	18
$O_2^* + O_2(v) \rightarrow O + O_3$	$2.95 \times 10^{-21} T_g^{0.5}$	18, i
$O_2^* + O_3 \rightarrow O_2 + O_2 + O$	$5.2 \times 10^{-11} e^{-2840/T_g}$	15
$O_2^* + He \rightarrow O_2 + He$	$8 \times 10^{-21} T_g^{0.5}$	19
$O_2^*1S + O_2^*1S \rightarrow O_2^* + O_2$	$3.6 \times 10^{-17} T_g^{0.5}$	14, i
$O_2^*1S + O_2 \rightarrow O_2^* + O_2$	$3.6 \times 10^{-17} T_g^{0.5}$	14

$O_2^*{}^1S + O_2 \rightarrow O_2 + O_2$	$4 \times 10^{-18} T_g^{0.5}$	14
$O_2^*{}^1S + O_2(v) \rightarrow O_2^* + O_2(v)$	$3.6 \times 10^{-17} T_g^{0.5}$	14, i
$O_2^*{}^1S + O_2(v) \rightarrow O_2 + O_2(v)$	$4 \times 10^{-18} T_g^{0.5}$	14, i
$O_2^*{}^1S + O \rightarrow O_2^* + O$	$7.2 \times 10^{-14} T_g^{0.5}$	14
$O_2^*{}^1S + O \rightarrow O_2 + O$	$8 \times 10^{-15} T_g^{0.5}$	14
$O_2^*{}^1S + O_3 \rightarrow O + O_2 + O_2$	$7.3 \times 10^{-12} T_g^{0.5}$	20
$O_2^*{}^1S + O_3 \rightarrow O_2^* + O_3$	$7.3 \times 10^{-12} T_g^{0.5}$	20
$O_2^*{}^1S + O_3 \rightarrow O_2 + O_3$	$7.3 \times 10^{-12} T_g^{0.5}$	20
$O_2^*{}^1S + He \rightarrow O_2^* + He$	$1 \times 10^{-17} T_g^{0.5}$	m
$O_2(v) + M \rightarrow O_2 + M^h$	$1 \times 10^{-14} T_g^{0.5}$	14, m
$O + O + O_2 \rightarrow O_2 + O_2$	$2.6 \times 10^{-34} T_g^{-0.63}$	9
$O + O + O_2(v) \rightarrow O_2 + O_2(v)$	$2.6 \times 10^{-34} T_g^{-0.63}$	9
$O + O + O \rightarrow O_2 + O$	$9.2 \times 10^{-34} T_g^{-0.63}$	9
$O + O + He \rightarrow O_2 + He$	1.20×10^{-33}	9, 19
$O + O + O_2 \rightarrow O_2^* + O_2$	$1.9 \times 10^{-35} T_g^{-0.63}$	9
$O + O + O_2(v) \rightarrow O_2^* + O_2(v)$	$1.9 \times 10^{-35} T_g^{-0.63}$	9, i
$O + O + O \rightarrow O_2^* + O$	$6.9 \times 10^{-35} T_g^{-0.63}$	9
$O + O + He \rightarrow O_2^* + He$	9.90×10^{-35}	9, 19
$O + O_2 + O_2 \rightarrow O_3 + O_2$	$6 \times 10^{-34} T_g^{-2.8}$	14
$O + O_2 + O_2(v) \rightarrow O_3 + O_2(v)$	$6 \times 10^{-34} T_g^{-2.8}$	14, i
$O + O_2 + He \rightarrow O_3 + He$	$3.4 \times 10^{-24} T_g^{-1.2}$	19
$O + O_2 + O \rightarrow O_3 + O$	$3.4 \times 10^{-24} T_g^{-1.2}$	m

$O + O_3 \rightarrow O_2 + O_2$	$8 \times 10^{-12} e^{-2060/T_g}$	14
$O_3 + M \rightarrow O_2 + O + M^h$	$1.6 \times 10^{-9} e^{-11490/T_g}$	21, m
$He^* + He^* \rightarrow He + He^+ + e$	$1.6 \times 10^{-9} T_g^{0.5}$	22
$He^* + O_2 \rightarrow O_2^+ + He + e$	$2.54 \times 10^{-10} T_g^{0.5}$	23
$He^* + O_2(v) \rightarrow O_2^+ + He + e$	$2.54 \times 10^{-10} T_g^{0.5}$	23, i
$He^* + O_3 \rightarrow O_2^+ + O + He + e$	$2.54 \times 10^{-10} T_g^{0.5}$	23, i
$He^* + O_2^*1S \rightarrow O_2^+ + He + e$	$2.54 \times 10^{-10} T_g^{0.5}$	23, i
$He^* + O \rightarrow O^+ + He + e$	$2.54 \times 10^{-10} T_g^{0.5}$	23, i
$He^* + O^* \rightarrow O^+ + He + e$	$2.54 \times 10^{-10} T_g^{0.5}$	23, i
$He^* + O^1S \rightarrow O^+ + He + e$	$2.54 \times 10^{-10} T_g^{0.5}$	23, i
$He^+ + O_2 \rightarrow O^+ + O + He$	$1.07 \times 10^{-9} T_g^{0.5}$	13
$He^+ + O_2(v) \rightarrow O^+ + O + He$	$1.07 \times 10^{-9} T_g^{0.5}$	13, i
$He^+ + O_3 \rightarrow O^+ + O_2 + He$	$1.07 \times 10^{-9} T_g^{0.5}$	13, m
$He^+ + O_2 \rightarrow O_2^+ + He$	$3.3 \times 10^{-11} T_g^{-0.5}$	13
$He^+ + O_2^* \rightarrow O^+ + O + He$	$1.07 \times 10^{-9} T_g^{0.5}$	13, i
$He^+ + O_2^* \rightarrow O_2^+ + He$	$3.3 \times 10^{-11} T_g^{-0.5}$	13, i
$He^+ + O \rightarrow O^+ + He$	$5 \times 10^{-11} T_g^{0.5}$	m
$He^+ + O^* \rightarrow O^+ + He$	$5 \times 10^{-11} T_g^{0.5}$	m
$He^+ + O^1S \rightarrow O^+ + He$	$5 \times 10^{-11} T_g^{0.5}$	m
$He + He^+ \rightarrow He + He^+$	$5 \times 10^{-11} T_g^{0.5}$	m
$e + H_2O \rightarrow O^- + H_2$	b	24
$e + H_2O \rightarrow H + OH + e$	b	24

$e + \text{H}_2\text{O} \rightarrow \text{H} + \text{OH} + e$	b	24
$e + \text{H}_2\text{O} \rightarrow \text{H}_2\text{O}^+ + e + e$	b	24
$e + \text{H}_2\text{O}^+ \rightarrow \text{H} + \text{OH}$	$1.2 \times 10^{-8} T_e^{-0.7}$	9
$e + \text{H}_2 \rightarrow \text{H} + \text{H} + e$	b	25
$\text{O}^- + \text{H}_2\text{O}^+ \rightarrow \text{O} + \text{H} + \text{OH}$	1×10^{-7}	9
$\text{O}_2^- + \text{H}_2\text{O}^+ \rightarrow \text{O}_2 + \text{H} + \text{OH}$	1×10^{-7}	9
$\text{O}_2^- + \text{H}_2\text{O}^+ \rightarrow \text{O}_3 + \text{H} + \text{OH}$	1×10^{-7}	9
$\text{O} + \text{O} + \text{H}_2\text{O} \rightarrow \text{O}_2 + \text{H}_2\text{O}$	$5.2 \times 10^{-35} e^{900/T_g}$	19
$\text{O} + \text{HO}_2 \rightarrow \text{OH} + \text{O}_2$	$2.9 \times 10^{-11} e^{-200/T_g}$	19
$\text{O} + \text{OH} \rightarrow \text{H} + \text{O}_2$	$2.3 \times 10^{-11} e^{110/T_g}$	19
$\text{O} + \text{OH} + \text{O}_2 \rightarrow \text{HO}_2 + \text{O}_2$	2.76×10^{-31}	19
$\text{O} + \text{OH} + \text{O}_2(\text{v}) \rightarrow \text{HO}_2 + \text{O}_2(\text{v})$	2.76×10^{-31}	19
$\text{O} + \text{OH} + \text{He} \rightarrow \text{HO}_2 + \text{He}$	2.76×10^{-31}	19
$\text{O} + \text{H}_2\text{O}_2 \rightarrow \text{OH} + \text{HO}_2$	$1.4 \times 10^{-12} e^{-2000/T_g}$	19
$\text{OH} + \text{HO}_2 \rightarrow \text{H}_2\text{O} + \text{O}_2$	8.00×10^{-11}	19
$\text{OH} + \text{O}_3 \rightarrow \text{HO}_2 + \text{O}_2$	$1.9 \times 10^{-12} e^{-1000/T_g}$	19
$\text{OH} + \text{H}_2\text{O}_2 \rightarrow \text{H}_2\text{O} + \text{HO}_2$	$2.9 \times 10^{-12} e^{-160/T_g}$	19
$\text{OH} + \text{OH} + \text{O}_2 \rightarrow \text{H}_2\text{O}_2 + \text{O}_2$	$6.9 \times 10^{-31} T_g^{-0.8}$	19
$\text{H} + \text{O}_3 \rightarrow \text{OH} + \text{O}_2$	$1.4 \times 10^{-10} e^{-470/T_g}$	19
$\text{H} + \text{O}_2 + \text{O}_2 \rightarrow \text{HO}_2 + \text{O}_2$	$6.14 \times 10^{-32} T_g^{-1.6}$	19
$\text{H} + \text{O}_2 + \text{O}_2(\text{v}) \rightarrow \text{HO}_2 + \text{O}_2(\text{v})$	$6.14 \times 10^{-32} T_g^{-1.6}$	19
$\text{H} + \text{O}_2 + \text{He} \rightarrow \text{HO}_2 + \text{He}$	$6.14 \times 10^{-32} T_g^{-1.6}$	19

$\text{HO}_2 + \text{O}_3 \rightarrow \text{OH} + \text{O}_2 + \text{O}_2$	$1.4 \times 10^{-14} e^{-600/T_g}$	19
$\text{HO}_2 + \text{HO}_2 + \text{O}_2 \rightarrow \text{H}_2\text{O}_2 + \text{O}_2$	$1.9 \times 10^{-33} e^{980/T_g}$	19
$\text{HO}_2 + \text{HO}_2 + \text{O}_2(\text{v}) \rightarrow \text{H}_2\text{O}_2 + \text{O}_2(\text{v})$	$1.9 \times 10^{-33} e^{980/T_g}$	19
$\text{HO}_2 + \text{HO}_2 + \text{He} \rightarrow \text{H}_2\text{O}_2 + \text{He}$	$1.9 \times 10^{-33} e^{980/T_g}$	19

- a. Rate coefficient in $\text{cm}^3 \text{s}^{-1}$ for 2-body reactions, and $\text{cm}^6 \text{s}^{-1}$ for 3-body reactions.
- b. Rate coefficients calculated using cross-section data from the indicated reference.
- c. Super elastic collision rates calculated by detailed balance.
- d. Estimated to have the same cross section as the ground state.
- e. Cross section estimated by shifting and scaling the ground state cross section by the excitation threshold.
- f. Cross section estimated by shifting and scaling the $\text{O}_2(^1\Delta)$ cross section by the excitation threshold.
- g. Superelastic collision rates calculated by detailed balance for excitation from $\text{O}_2(^1\Delta)$.
- h. for all neutral species.
- i. Analogous to reaction with the ground state O_2 .
- j. Assuming branching to ground state.
- k. Rate given by Ref. 16 with branching given by Ref. 9.
- l. Rate given by Ref. 16; assumed 50% branching to O_2 , and 50% to $\text{O}_2(^1\Delta)$.
- m. Estimated.
- n. He^{**} is tracked as He^*

B.1 References

1. J. P. Boeuf and E. Marode, *Journal of Physics D* **15**, 2169 (1982).
2. D. Rapp and P. Englander-Golden, *Journal of Chemical Physics* **43**, 1464 (1965).
3. L. Vriens, *Physical Letters* **8**, 260 (1964).
4. G. Bekefi, *Radiation Processes in Plasmas* (Wiley, New York, 1966).
5. A. V. Phelps, JILA Information Center Report No. 28 (1985).
6. P. D. Burrow, *Journal of Chemical Physics* **59**, 4922 (1973).
7. R. I. Hall and S. Trajmar, *Journal of Physics B* **8**, L293 (1975).
8. Y. Itikawa *et al.*, *Journal of Physical and Chemical Reference Data* **18**, 23 (1989).
9. B. F. Gordiets *et al.*, *IEEE Transactions on Plasma Science* **23**, 750 (1995).
10. S. Matejcek *et al.*, *Plasma Sources Science and Technology* **6**, 140 (1997).
11. R. R. Laher and F. R. Gilmore, *Journal of Physical and Chemical Reference Data* **19**, 277 (1990).
12. E. Meeks *et al.*, *Journal of Vacuum Science and Technology A* **16**, 544 (1998).
13. Y. Ikezoe, S. Matsuoka, M. Takebe, and A. Viggiano, *Gas Phase Ion-Molecule Reaction Rate Constants Through 1986* (Ion Reaction Research Group of the Mass Spectroscopy Society of Japan, Tokyo, Japan, 1987).
14. R. Atkinson, *et al.*, *Journal of Physical and Chemical Reference Data* **26**, 521 (1997).
15. R. Atkinson *et al.*, *Journal of Physical and Chemical Reference Data* **26**, 1329 (1997).
16. J. T. Herron and D. S. Green, *Plasma Chemistry and Plasma Processing* **21**, 459 (2001).

17. J. Shi and J. R. Barker, *International Journal of Chemical Kinetics* **22**, 1283 (1990).
18. R. K. Datta and K. N. Rao, *Indian Journal of Chemistry A*. **18A**, 102 (1979).
19. *NIST Standard Reference Database 17-2Q98* (National Institute of Standards and Technology, Gaithersburg, MD, 1998).
20. K. W. Choo and M. T. Leu, *International Journal of Chemical Kinetics* **17**, 1155 (1985).
21. B. Eliasson and U. Kogelschatz, Brown Boveri Technical Report LKR 86-11 C, (1986).
22. R. Deloche, P. Monchicourt, M. Cheret, and F. Lambert, *Physical Review A* **13**, 1140 (1976).
23. J. M. Pouvesle *et al.*, *Journal of Chemical Physics* **88**, 3061 (1988).
24. M. Hayashi in "*Swarm studies and inelastic electron-molecular collisions*", edited by L.C. Pitchford, V. B. McKoy, A. Chutjian and S. Trajmar, Springer-Verlag, New York, (1987).
25. S.J.B. Corrigan, *Journal of Chemical Physics*, **43**, 4381-4386 (1965)

APPENDIX C. LIST OF REACTIONS FOR He/NH₃ MIXTURES

List of Species

e	NH ₂	N ₂
He	NH ₂ ⁻	N ₂ H ₂
He [*] (4s)	NH ⁺	N ₂ H ₃
He ⁺	N ⁺	N ₂ H ₄
NH ₃	H ₂ ⁺	H
NH ₃ (v)	H ⁻	H ₂
NH ₄ ⁺	H ⁺	NH
NH ₃ ⁺	H ₃ ⁺	OH
NH ₂ ⁺	N	HNO
		H ₂ O

<u>Reaction</u>	<u>Rate coefficient^a</u>	<u>Reference</u>
e + He → He + e	b	1
e + He → He [*] + e	b	1
e + He → He ⁺ + e + e	b	2
e + He [*] → He ⁺ + e + e	b	2
e + He [*] → He + e	b	1
e + NH ₃ → NH ₃ + e	b	3
e + NH ₃ → NH ₃ (v) + e	b	3
e + NH ₃ → NH ₂ + H ⁻	b	3
e + NH ₃ → NH ₂ + H + e	b	3

$e + \text{NH}_3 \rightarrow \text{NH} + \text{H} + \text{H} + e$	b	3
$e + \text{NH}_3 \rightarrow \text{NH}_3^+ + e + e$	b	3
$e + \text{NH}_3 \rightarrow \text{NH}_2^+ + \text{H} + e + e$	b	4
$e + \text{H}_2\text{O} \rightarrow \text{O}^- + \text{H}_2$	b	3
$e + \text{H}_2\text{O} \rightarrow \text{H} + \text{OH} + e$	b	3
$e + \text{H}_2\text{O} \rightarrow \text{H} + \text{OH} + e$	b	3
$e + \text{H}_2\text{O} \rightarrow \text{H}_2\text{O}^+ + e + e$	b	3
$e + \text{H}_2\text{O}^+ \rightarrow \text{H} + \text{OH}$	$1.2 \times 10^{-8} T_e^{-0.7}$	3
$e + \text{NH}_3(\text{v}) \rightarrow \text{NH}_3(\text{v}) + e$	b	3
$e + \text{NH}_3(\text{v}) \rightarrow \text{NH}_3 + e$	b	3
$e + \text{NH}_3(\text{v}) \rightarrow \text{NH}_2 + \text{H}^-$	b	3
$e + \text{NH}_3(\text{v}) \rightarrow \text{NH}_2 + \text{H} + e$	b	3
$e + \text{NH}_3(\text{v}) \rightarrow \text{NH} + \text{H} + \text{H} + e$	b	3
$e + \text{NH}_3(\text{v}) \rightarrow \text{NH}_3^+ + e + e$	b	4
$e + \text{NH}_3(\text{v}) \rightarrow \text{NH}_2^+ + \text{H} + e + e$	b	4
$e + \text{NH}_2 \rightarrow \text{NH} + \text{H}^-$	b	5
$e + \text{NH}_2 \rightarrow \text{NH} + \text{H} + e$	b	5
$e + \text{NH}_2 \rightarrow \text{N} + \text{H} + \text{H} + e$	b	5
$e + \text{NH}_2 \rightarrow \text{NH}_2^+ + e + e$	b	5
$e + \text{NH}_2 \rightarrow \text{NH}^+ + \text{H} + e + e$	b	5
$e + \text{NH} \rightarrow \text{N} + \text{H} + e$	b	5
$e + \text{NH} \rightarrow \text{N}^+ + \text{H} + e + e$	b	5

$e + \text{NH} \rightarrow \text{NH}^+ + e + e$	b	5
$e + \text{N} \rightarrow \text{N}^+ + e + e$	b	6
$e + \text{N}_2 \rightarrow \text{N} + \text{N} + e$	b	7
$e + \text{H} \rightarrow \text{H}^+ + e + e$	b	c
$e + \text{H}_2 \rightarrow \text{H}_2^+ + e + e$	b	8
$e + \text{H}_2 \rightarrow \text{H} + \text{H} + e$	b	8
$e + \text{H}_2 \rightarrow \text{H} + \text{H} + e$	b	9
$e + \text{H}^+ \rightarrow \text{H}$	$4 \times 10^{-13} T_e^{-0.5}$	d
$e + \text{H}_2^+ \rightarrow \text{H}^+ + \text{H} + e$	b	10
$e + \text{H}_2^+ \rightarrow \text{H} + \text{H}$	$1 \times 10^{-7} T_e^{-0.4}$	11
$e + \text{H}_3^+ \rightarrow \text{H}_3^+ + e$	b	e
$e + \text{H}_3^+ \rightarrow \text{H}^+ + \text{H}_2$	b	10
$e + \text{H}_3^+ \rightarrow \text{H} + \text{H}_2$	b	10
$e + \text{N}^+ \rightarrow \text{N}$	$4 \times 10^{-13} T_e^{-0.5}$	d
$e + \text{NH}^+ \rightarrow \text{N} + \text{H}$	$1 \times 10^{-7} T_e^{-0.5}$	12
$e + \text{NH}_2^+ \rightarrow \text{NH} + \text{H}$	$1 \times 10^{-7} T_e^{-0.5}$	12
$e + \text{NH}_3^+ \rightarrow \text{NH}_2 + \text{H}$	$1 \times 10^{-7} T_e^{-0.5}$	12
$e + \text{NH}_4^+ \rightarrow \text{NH}_3 + \text{H}$	$9 \times 10^{-7} T_e^{-0.6}$	13
$\text{He}^+ + \text{He} \rightarrow \text{He} + \text{He}^+$	4.6×10^{-10}	14
$\text{He}^+ + \text{NH}_3 \rightarrow \text{NH}_2^+ + \text{H} + \text{He}$	5.52×10^{-11}	15
$\text{He}^+ + \text{NH}_3 \rightarrow \text{NH}_3^+ + \text{He}$	1.3×10^{-9}	15
$\text{He}^+ + \text{NH}_3(\text{v}) \rightarrow \text{NH}_2^+ + \text{H} + \text{He}$	5.52×10^{-11}	f

$\text{He}^+ + \text{NH}_3(\text{v}) \rightarrow \text{NH}_3^+ + \text{He}$	1.3×10^{-9}	f
$\text{He}^+ + \text{NH}_2 \rightarrow \text{NH}^+ + \text{H} + \text{He}$	5.52×10^{-11}	15
$\text{He}^+ + \text{NH}_2 \rightarrow \text{NH}_2^+ + \text{He}$	5.0×10^{-10}	15
$\text{He}^+ + \text{NH} \rightarrow \text{NH}^+ + \text{He}$	5.0×10^{-10}	15
$\text{He}^+ + \text{H}_2 \rightarrow \text{H}_2^+ + \text{He}$	1.0×10^{-9}	15
$\text{He}^+ + \text{H}_2 \rightarrow \text{H}^+ + \text{H} + \text{He}$	1.0×10^{-9}	15
$\text{He}^+ + \text{N} \rightarrow \text{N}^+ + \text{He}$	1.0×10^{-11}	15
$\text{He}^+ + \text{N}_2 \rightarrow \text{N}^+ + \text{N} + \text{He}$	5.0×10^{-12}	15
$\text{He}^+ + \text{H} \rightarrow \text{H}^+ + \text{He}$	1.0×10^{-10}	15
$\text{H}_2^+ + \text{N} \rightarrow \text{N}^+ + \text{H}_2$	5×10^{-10}	16, f
$\text{H}_2^+ + \text{H} \rightarrow \text{H}^+ + \text{H}_2$	6.4×10^{-10}	16
$\text{H}_2^+ + \text{H}_2 \rightarrow \text{H}_3^+ + \text{H}$	2.1×10^{-9}	16
$\text{H}_2^+ + \text{NH} \rightarrow \text{NH}^+ + \text{H}_2$	5×10^{-10}	16, f
$\text{H}_2^+ + \text{NH} \rightarrow \text{NH}_2^+ + \text{H}$	5×10^{-11}	16, f
$\text{H}_2^+ + \text{NH}_2 \rightarrow \text{NH}_2^+ + \text{H}_2$	5×10^{-10}	16, f
$\text{H}_2^+ + \text{NH}_2 \rightarrow \text{NH}_3^+ + \text{H}$	5×10^{-11}	16, f
$\text{H}_2^+ + \text{NH}_3 \rightarrow \text{NH}_3^+ + \text{H}_2$	5×10^{-10}	16, f
$\text{H}_2^+ + \text{NH}_3(\text{v}) \rightarrow \text{NH}_3^+ + \text{H}_2$	5×10^{-10}	16, f
$\text{H}_2^+ + \text{NH}_3 \rightarrow \text{NH}_4^+ + \text{H}$	5×10^{-11}	16, f
$\text{H}_2^+ + \text{NH}_3(\text{v}) \rightarrow \text{NH}_4^+ + \text{H}$	5×10^{-11}	16, f
$\text{N}^+ + \text{H} \rightarrow \text{N} + \text{H}^+$	2×10^{-9}	16, f
$\text{N}^+ + \text{H}_2 \rightarrow \text{NH}^+ + \text{H}$	5.6×10^{-10}	16

$\text{N}^+ + \text{NH} \rightarrow \text{NH}^+ + \text{N}$	2.4×10^{-9}	16, f
$\text{N}^+ + \text{NH}_2 \rightarrow \text{NH}_2^+ + \text{N}$	2.4×10^{-9}	16, f
$\text{N}^+ + \text{NH}_3 \rightarrow \text{NH}_3^+ + \text{N}$	2.4×10^{-9}	16
$\text{N}^+ + \text{NH}_3(\text{v}) \rightarrow \text{NH}_3^+ + \text{N}$	2.4×10^{-9}	16, f
$\text{H}^+ + \text{NH}_3 \rightarrow \text{NH}_3^+ + \text{H}$	5×10^{-11}	g
$\text{H}^+ + \text{NH}_3(\text{v}) \rightarrow \text{NH}_3^+ + \text{H}$	5×10^{-11}	g
$\text{H}^+ + \text{NH}_2 \rightarrow \text{NH}_2^+ + \text{H}$	5×10^{-11}	g
$\text{H}^+ + \text{NH} \rightarrow \text{NH}^+ + \text{H}$	5×10^{-11}	g
$\text{NH}^+ + \text{NH}_3 \rightarrow \text{NH}_3^+ + \text{NH}$	2.4×10^{-9}	16
$\text{NH}^+ + \text{NH}_3 \rightarrow \text{NH}_4^+ + \text{N}$	1.8×10^{-9}	16, f
$\text{NH}^+ + \text{NH}_3(\text{v}) \rightarrow \text{NH}_3^+ + \text{NH}$	2.4×10^{-9}	16, f
$\text{NH}^+ + \text{NH}_3(\text{v}) \rightarrow \text{NH}_4^+ + \text{N}$	1.8×10^{-9}	16, f
$\text{NH}^+ + \text{H}_2 \rightarrow \text{NH}_2^+ + \text{H}$	1×10^{-9}	16
$\text{NH}_2^+ + \text{NH}_3 \rightarrow \text{NH}_3^+ + \text{NH}_2$	2.2×10^{-9}	16
$\text{NH}_2^+ + \text{NH}_3 \rightarrow \text{NH}_4^+ + \text{NH}$	2.2×10^{-9}	16
$\text{NH}_2^+ + \text{NH}_3(\text{v}) \rightarrow \text{NH}_3^+ + \text{NH}_2$	2.2×10^{-9}	16, f
$\text{NH}_2^+ + \text{NH}_3(\text{v}) \rightarrow \text{NH}_4^+ + \text{NH}$	2.2×10^{-9}	16, f
$\text{NH}_2^+ + \text{H}_2 \rightarrow \text{NH}_3^+ + \text{H}$	1×10^{-9}	16
$\text{H}_3^+ + \text{NH}_3 \rightarrow \text{NH}_4^+ + \text{H}_2$	4.4×10^{-9}	16
$\text{NH}_3^+ + \text{NH}_3 \rightarrow \text{NH}_4^+ + \text{NH}_2$	2.2×10^{-9}	16
$\text{NH}_3^+ + \text{NH}_3(\text{v}) \rightarrow \text{NH}_4^+ + \text{NH}_2$	2.2×10^{-9}	16, f
$\text{NH}_3^+ + \text{H}_2 \rightarrow \text{NH}_4^+ + \text{H}$	4×10^{-13}	16

$\text{NH}_2^- + \text{H}_2 \rightarrow \text{H}^- + \text{NH}_3$	2.3×10^{-11}	16
$\text{H}^- + \text{H} \rightarrow \text{H}_2 + \text{e}$	1.8×10^{-9}	16
$\text{H}^- + \text{NH}_3 \rightarrow \text{NH}_2^- + \text{H}_2$	8.8×10^{-13}	16
$\text{H}^- + \text{NH}_3(\text{v}) \rightarrow \text{NH}_2^- + \text{H}_2$	8.8×10^{-13}	16, f
$\text{H}^- + \text{N}^+ \rightarrow \text{N} + \text{H}$	3×10^{-6}	g
$\text{H}^- + \text{NH}^+ \rightarrow \text{NH} + \text{H}$	3×10^{-6}	g
$\text{H}^- + \text{NH}_2^+ \rightarrow \text{NH}_2 + \text{H}$	3×10^{-6}	g
$\text{H}^- + \text{NH}_3^+ \rightarrow \text{NH}_3 + \text{H}$	3×10^{-6}	g
$\text{H}^- + \text{NH}_4^+ \rightarrow \text{NH}_3 + \text{H}_2$	3×10^{-6}	g
$\text{H}^- + \text{He}^+ \rightarrow \text{H} + \text{He}$	2×10^{-7}	g
$\text{H}^- + \text{H}^+ \rightarrow \text{H} + \text{H}$	2×10^{-7}	g
$\text{H}^- + \text{H}_2^+ \rightarrow \text{H}_2 + \text{H}$	2×10^{-7}	g
$\text{H}^- + \text{H}_3^+ \rightarrow \text{H}_2 + \text{H}_2$	1×10^{-7}	g
$\text{H}^- + \text{H}_3^+ \rightarrow \text{H}_2 + \text{H} + \text{H}$	1×10^{-7}	g
$\text{NH}_2^- + \text{N}^+ \rightarrow \text{N} + \text{NH}_2$	2×10^{-7}	g
$\text{NH}_2^- + \text{NH}^+ \rightarrow \text{NH}_2 + \text{NH}$	2×10^{-7}	g
$\text{NH}_2^- + \text{NH}_2^+ \rightarrow \text{NH}_2 + \text{NH}_2$	2×10^{-7}	g
$\text{NH}_2^- + \text{NH}_3^+ \rightarrow \text{NH}_3 + \text{NH}_2$	2×10^{-7}	g
$\text{NH}_2^- + \text{NH}_4^+ \rightarrow \text{NH}_3 + \text{NH}_2 + \text{H}$	2×10^{-7}	g
$\text{NH}_2^- + \text{He}^+ \rightarrow \text{NH}_2 + \text{He}$	2×10^{-7}	g
$\text{NH}_2^- + \text{H}^+ \rightarrow \text{NH}_2 + \text{H}$	2×10^{-7}	g
$\text{NH}_2^- + \text{H}_2^+ \rightarrow \text{H}_2 + \text{NH}_2$	2×10^{-7}	g

$\text{NH}_2^- + \text{H}_3^+ \rightarrow \text{NH}_3 + \text{H}_2$	1×10^{-7}	g
$\text{NH}_2^- + \text{H}_3^+ \rightarrow \text{NH}_2 + \text{H}_2 + \text{H}$	1×10^{-7}	g
$\text{He}^* + \text{He}^* \rightarrow \text{He}^+ + \text{He} + \text{e}$	1×10^{-9}	17
$\text{He}^* \rightarrow \text{He}$	1×10^1	18
$\text{He}^* + \text{NH}_3 \rightarrow \text{NH}_3^+ + \text{He} + \text{e}$	4.2×10^{-11}	19
$\text{He}^* + \text{NH}_3(\text{v}) \rightarrow \text{NH}_3^+ + \text{He} + \text{e}$	4.2×10^{-11}	19, f
$\text{He}^* + \text{NH}_3 \rightarrow \text{NH}_2^+ + \text{H} + \text{He} + \text{e}$	1.8×10^{-10}	19
$\text{He}^* + \text{NH}_3(\text{v}) \rightarrow \text{NH}_2^+ + \text{H} + \text{He} + \text{e}$	1.8×10^{-10}	19
$\text{He}^* + \text{NH}_3 \rightarrow \text{NH}_2 + \text{H} + \text{He}$	5.8×10^{-11}	20
$\text{He}^* + \text{NH}_3 \rightarrow \text{NH} + \text{H} + \text{H} + \text{He}$	5.2×10^{-11}	20
$\text{He}^* + \text{NH}_3 \rightarrow \text{NH} + \text{H}_2 + \text{He}$	5.8×10^{-12}	20
$\text{He}^* + \text{NH}_3(\text{v}) \rightarrow \text{NH}_2 + \text{H} + \text{He}$	5.8×10^{-11}	20, f
$\text{He}^* + \text{NH}_3(\text{v}) \rightarrow \text{NH} + \text{H} + \text{H} + \text{He}$	5.2×10^{-11}	20, f
$\text{He}^* + \text{NH}_3(\text{v}) \rightarrow \text{NH} + \text{H}_2 + \text{He}$	5.8×10^{-12}	20, f
$\text{N}_2 + \text{N}_2 \rightarrow \text{N} + \text{N} + \text{N}_2$	$4.3 \times 10^{-10} e^{-86.460/T_g}$	21
	6.5×10^{-13}	22
$\text{NH}_3 + \text{H} \rightarrow \text{H}_2 + \text{NH}_2$	$(T_g/300)^{2.76} e^{-5.135/T_g}$	
	6.5×10^{-13}	22
$\text{NH}_3(\text{v}) + \text{H} \rightarrow \text{H}_2 + \text{NH}_2$	$(T_g/300)^{2.76} e^{-5.135/T_g}$	
$\text{NH}_2 + \text{H} \rightarrow \text{NH} + \text{H}_2$	$1.1 \times 10^{-10} e^{-4.451/T_g}$	23
$\text{NH}_2 + \text{H}_2 \rightarrow \text{H} + \text{NH}_3$	$2.1 \times 10^{-12} e^{-4.277/T_g}$	20

$\text{NH}_2 + \text{NH}_2 \rightarrow \text{N}_2\text{H}_2 + \text{H}_2$	1.3×10^{-12}	24
	1.8×10^{-14}	25
$\text{NH}_2 + \text{NH}_2 \rightarrow \text{NH}_3 + \text{NH}$	$(T_g/300)^{2.79} e^{-660/T_g}$	
$\text{NH}_2 + \text{N} \rightarrow \text{N}_2 + \text{H} + \text{H}$	1.2×10^{-10}	20
$\text{NH}_2 + \text{NH} \rightarrow \text{N}_2\text{H}_2 + \text{H}$	$2.5 \times 10^{-9} (T_g/300)^{-0.5}$	20
$\text{NH}_2 + \text{NH} \rightarrow \text{N}_2\text{H}_3$	1.2×10^{-10}	26
$\text{NH} + \text{N} \rightarrow \text{N}_2 + \text{H}$	2.5×10^{-11}	27
$\text{NH} + \text{H} \rightarrow \text{H}_2 + \text{N}$	$6 \times 10^{-11} e^{-166/T_g}$	20
$\text{NH} + \text{NH} \rightarrow \text{N}_2 + \text{H} + \text{H}$	1.2×10^{-9}	28
$\text{NH} + \text{NH} \rightarrow \text{N}_2\text{H}_2$	3.5×10^{-12}	29
	1.4×10^{-14}	30
$\text{NH} + \text{NH} \rightarrow \text{NH}_2 + \text{N}$	$(T_g/300)^{2.89} e^{1.015/T_g}$	
$\text{N} + \text{H}_2 \rightarrow \text{H} + \text{NH}$	$2.7 \times 10^{-10} e^{-12,609/T_g}$	31
	4.5×10^{-13}	32
$\text{N}_2\text{H}_2 + \text{H} \rightarrow \text{N}_2 + \text{H}_2 + \text{H}$	$(T_g/300)^{2.63} e^{115/T_g}$	
$\text{H} + \text{H} + \text{NH}_3 \rightarrow \text{H}_2 + \text{NH}_3$	1.4×10^{-31}	33
$\text{H} + \text{H} + \text{NH}_3(\text{v}) \rightarrow \text{H}_2 + \text{NH}_3(\text{v})$	1.4×10^{-31}	33, f
$\text{H} + \text{H} + \text{NH}_2 \rightarrow \text{H}_2 + \text{NH}_2$	1.4×10^{-31}	33, f
$\text{H} + \text{H} + \text{He} \rightarrow \text{H}_2 + \text{He}$	5.79×10^{-33}	34
$\text{H} + \text{H} + \text{H}_2 \rightarrow \text{H}_2 + \text{H}_2$	$8.9 \times 10^{-33} (T_g/300)^{-6}$	35
$\text{H} + \text{H} + \text{H} \rightarrow \text{H}_2 + \text{H}$	8.9×10^{-33}	36
$\text{H} + \text{N} + \text{NH}_3 \rightarrow \text{NH} + \text{NH}_3$	5×10^{-32}	20

$\text{H} + \text{N} + \text{NH}_3(\text{v}) \rightarrow \text{NH} + \text{NH}_3(\text{v})$	5×10^{-32}	20
$\text{H} + \text{N} + \text{H} \rightarrow \text{NH} + \text{H}$	5×10^{-32}	20, f
$\text{H} + \text{NH}_2 + \text{NH}_3 \rightarrow \text{NH}_3 + \text{NH}_3$	6×10^{-30}	20
$\text{H} + \text{NH}_2 + \text{NH}_3(\text{v}) \rightarrow \text{NH}_3(\text{v}) + \text{NH}_3$	6×10^{-30}	20
$\text{H} + \text{NH}_2 + \text{He} \rightarrow \text{He} + \text{NH}_3$	6×10^{-30}	20
$\text{H} + \text{NH}_2 + \text{H} \rightarrow \text{NH}_3 + \text{H}$	6×10^{-30}	20, f
$\text{H} + \text{NH}_2 + \text{NH}_2 \rightarrow \text{NH}_3 + \text{NH}_2$	6×10^{-30}	20, f
$\text{H}_2 + \text{N} + \text{NH}_3 \rightarrow \text{NH}_2 + \text{NH}_3$	1×10^{-36}	37
$\text{H}_2 + \text{N} + \text{NH}_3(\text{v}) \rightarrow \text{NH}_2 + \text{NH}_3(\text{v})$	1×10^{-36}	37
$\text{N} + \text{N} + \text{N}_2 \rightarrow \text{N}_2 + \text{N}_2$	7.2×10^{-33}	38
$\text{N} + \text{N} + \text{NH}_3 \rightarrow \text{N}_2 + \text{NH}_3$	7.2×10^{-33}	38
$\text{N} + \text{N} + \text{H} \rightarrow \text{N}_2 + \text{H}$	7.2×10^{-33}	38
$\text{N} + \text{N} + \text{NH}_3(\text{v}) \rightarrow \text{N}_2 + \text{NH}_3(\text{v})$	7.2×10^{-33}	38
$\text{NH} + \text{NH}_3 + \text{NH}_3 \rightarrow \text{N}_2\text{H}_4 + \text{NH}_3$	1×10^{-33}	39
$\text{NH} + \text{NH}_3(\text{v}) + \text{NH}_3 \rightarrow \text{N}_2\text{H}_4 + \text{NH}_3$	1×10^{-33}	39, f
$\text{NH} + \text{NH}_3(\text{v}) + \text{He} \rightarrow \text{N}_2\text{H}_4 + \text{He}$	4×10^{-35}	39, f
$\text{NH} + \text{NH}_3 + \text{He} \rightarrow \text{N}_2\text{H}_4 + \text{He}$	4×10^{-35}	39, f
$\text{NH}_2 + \text{NH}_2 + \text{NH}_3 \rightarrow \text{N}_2\text{H}_4 + \text{NH}_3$	6.9×10^{-30}	20
$\text{NH}_2 + \text{NH}_2 + \text{He} \rightarrow \text{N}_2\text{H}_4 + \text{He}$	6.9×10^{-30}	20
$\text{N}_2\text{H}_2 + \text{NH}_2 \rightarrow \text{N}_2 + \text{H} + \text{NH}_3$	1.5×10^{-13}	32
	$(T_g/300)^{4.05} e^{810/T_g}$	
$\text{N}_2\text{H}_3 + \text{H} \rightarrow \text{NH}_2 + \text{NH}_2$	2.7×10^{-12}	40

$\text{N}_2\text{H}_3 + \text{N}_2\text{H}_3 \rightarrow \text{NH}_3 + \text{NH}_3 + \text{N}_2$	5×10^{-12}	41
$\text{N}_2\text{H}_3 + \text{N}_2\text{H}_3 \rightarrow \text{N}_2\text{H}_4 + \text{N}_2\text{H}_2$	2×10^{-11}	42
$\text{N}_2\text{H}_4 + \text{N} \rightarrow \text{N}_2\text{H}_2 + \text{NH}_2$	1.3×10^{-13}	40
$\text{N}_2\text{H}_4 + \text{H} \rightarrow \text{N}_2\text{H}_3 + \text{H}_2$	$1.2 \times 10^{-11} e^{-1260/T_g}$	43
$\text{N}_2\text{H}_4 + \text{NH}_2 \rightarrow \text{NH}_3 + \text{N}_2\text{H}_3$	5.2×10^{-13}	40
$\text{H} + \text{N} + \text{He} \rightarrow \text{NH} + \text{He}$	5.0×10^{-32}	45
$\text{H}_2 + \text{N} + \text{He} \rightarrow \text{NH}_2 + \text{He}$	1×10^{-36}	37
$\text{N} + \text{N} + \text{He} \rightarrow \text{N}_2 + \text{He}$	2.22×10^{-32}	46
$\text{OH} + \text{N} \rightarrow \text{NO} + \text{H}$	4.2×10^{-11}	47
$\text{OH} + \text{NH} \rightarrow \text{H} + \text{HNO}$	3×10^{-12}	47
$\text{OH} + \text{NH}_x \rightarrow \text{H}_2\text{O} + \text{NH}_{x-1}$	3.32×10^{-11}	47
$\text{HNO} + \text{OH} \rightarrow \text{H}_2\text{O} + \text{NO}$	2.4×10^{-12}	47
$\text{HNO} + \text{NH}_2 \rightarrow \text{NH}_3 + \text{NO}$	5.36×10^{-12}	47
$\text{HNO} + \text{H} \rightarrow \text{H}_2 + \text{NO}$	3×10^{-11}	47
$\text{NO} + \text{N} \rightarrow \text{O} + \text{N}_2$	3×10^{-11}	47
$\text{NO} + \text{NH}_2 \rightarrow \text{N}_2 + \text{H} + \text{OH}$	1.7×10^{-11}	47

^aRate constant in $\text{cm}^3 \text{s}^{-1}$ for 2-body reactions, and $\text{cm}^6 \text{s}^{-1}$ for 3-body reactions.

^bRate constant calculated by using cross-section data from the indicated reference.

^cRate constant calculated by the Gryzinski crosssection

$$2.36 \times 10^{-16} \left(\frac{E}{E_0} - 1 \right) \times a \log \left(1.25 \times \frac{E}{E_0} \right) \left(\frac{E}{E_0} \right)^{-2}.$$

^dRate constant for electron-ion recombination (without dissociation).

^cColoumb elastic cross-section from [44].

^fRate constant estimated by analogy.

^gRate constant estimated.

C.1 References

1. J. P. Boeuf and E. Marode, *Journal of Physics D* **15**, 2169 (1982).
2. L. Vriens, *Physics Letters*, **8**, 260 (1964).
3. M. Hayashi, *Non-equilibrium Processes in Partially Ionized Gases*, Plenum, NY (1990).
4. T. D. Mark, *Electron impact ionization*, Springer-Verlag, Wien, Austria (1985).
5. V. Tarnovsky, H. Deutsch and K. Becker, *International Journal of Mass Spectrometry and Ion Processes* **167/168**, 69 (1997).
6. A. C. H. Smith, *Physical Review* **127**, 1647 (1962).
7. A.V. Phelps and L.C. Pitchford, *Physical Review* **31**, 2932 (1985).
8. M. Hayashi, *Journal de Physique*, **40**, C7/45-46 (1979).
9. S. J. B. Corrigan, *Journal of Chemical Physics* **43**, 4381 (1965).
10. C. F. Chan, *Reaction cross sections and rate coefficients related to production of positive ions*, LBNL LBID-632, (1983).
11. W. L. Morgan, *Advanced Atomic Molecular and Optical Physics* **43**, 79 (2000).
12. A. I. Florescu and J. B. A. Mitchell, *Physical Reports*. **430**, 277 (2006).
13. J.Öjekull *et al*, *Journal of Chemical Physics* **120**, 7391 (2004).
14. H. W. Ellis *et al*, *Transport Properties of gaseous ions over a wide energy range. Part III. Atomic Data and Nuclear Data Tables*, **31**, 113-151 (1984).

15. M. Hayashi, Nagoya Inst. Tech. Report No: IPPJ-AM-19 (1991).
16. Y. Ikezoe, S. Matsuoka, M. Takebe and A. Viggiano, *Gas Phase Ion-Molecule Reaction Rate Constants*, Mass Spectroscopy Society of Japan, Japan (1987).
17. R. Deloche, *et al*, Physical Review A, **13**, 1140 (1976).
18. R. S. Van Dyck Jr., C. E. Johnson and H. A. Shugart, Physical Review A, **4**, 1327 (1971).
19. R. A. Arakoni, D. S. Stafford, N. Y. Babaeva and M. J. Kushner, Journal of Applied Physics, **98**, 073304 (2005).
20. M. J. Kushner, Journal of Applied Physics **71**, 4173 (1992).
21. K. Thielen and P. Roth, American Institute of Aeronautics and Astronautics Journal **24**, 1102 (1986).
22. J. C. Corchado and J. Espiona-Garcia, Journal of Chemical Physics **106**, 4013 (1997).
23. M. Rohrig and H. G. Wagner, Symp. Int. Combust. Proc. **25**, 975 (1994).
24. N. Stothard, R. Humpfer and H-H. Grotheer, Chemical Physics Letters **240**, 474 (1995).
25. Z-F. Xu, D-C. Fang and X-Y Fu, International Journal of Quantum Chemistry **70**, 321 (1998).
26. P. B. Pagsberg J. Eriksen and H. C. Christensen, Journal of Physical Chemistry **83**, 582 (1979).
27. W. Hack, H. Gg. Wagner and A. Zaspypkin, Berichte der Bunsen-Gesellschaft - Physical Chemistry **98**, 156 (1994).
28. G. M. Meaburn and S. Gordon, Journal of Physical Chemistry **72**, 1592 (1968).

29. J. E. Nicholas, A. I. Spiers and N. A. Matin, *Plasma Chemistry and Plasma Processing* **6**, 39, (1986).
30. Z-F Xu, D-C Fang, X-Y Fu, *Chemical Physics Letters* **275**, 386 (1997).
31. M. Koshi, M. Yoshimura, K. Fukuda and H. Matsui, *Journal of Chemical Physics* **93**, 8703 (1990).
32. D. P. Linder, X. Duan and M. Page, *Journal of Chemical Physics* **104**, 6298 (1996).
33. L. Teng, C. A. Winkler, *Canadian Journal of Chemistry* **51**, 3771 (1973).
34. D. N. Mitchell and D. J. LeRoy, *Journal of Chemical Physics*, **67**, 1042 (1977).
35. D. L. Baulch *et al*, *Journal of Physical and Chemical Reference Data* **21**, 411 (1992).
36. N. Cohen and K. R. Westberg, *Journal of Physical and Chemical Reference Data* **12**, 531 (1983).
37. V. A. Petrishchev and A. Yu. Sapozhkov, *Kinetics and Catalysis* **22**, (1981).
38. T. Yamashita, *Journal of Chemical Physics* **70**, (1979).
39. C. Zetsch and F. Stuhl, *Berichte der Bunsen-Gesellschaft - Physical Chemistry*, **85**, (1981).
40. M. Gehring, K. Hoyer mann, H. Gg. Wagner and J. Wolfrum, *Berichte der Bunsen-Gesellschaft - Physical Chemistry* **75**, (1971).
41. M. Schiavello and G. G. Volpi, *Journal of Chemical Physics*, **37**, 1510 (1962).
42. L. J. Stief, *Journal of Chemical Physics* **52**, 4841 (1970).
43. G. L. Vaghjiani, *Internation Journal of Chemical Kinetics* **27**, 777 (1995).
44. M. Mitchner and C. H. Kruger, *Partially Ionized Gases*, Wiley, New York (1973).

45. R. L. Brown, *International Journal of Chemical Kinetics*, **5**, 663 (1973).
46. W. Brennen and E. C. Shane, *Journal of Physical Chemistry*, **75**, 1552 (1971).
47. *NIST Standard Reference Database 17-2Q98* (National Institute of Standards and Technology, Gaithersburg, MD, 1998).

APPENDIX D. POLYPROPYLENE SURFACE REACTION CHEMISTRY

<u>Reaction^a</u>	<u>Rate Coefficient^b</u>	<u>Reference</u>
$O_g + PP-H \rightarrow PP\cdot + OH_g$	$10^{-3}, 10^{-4}, 10^{-5}$	1, c
$OH_g + PP-H \rightarrow PP\cdot + H_2O_g$	0.25, 0.05, 0.0025	1, c
$H_g + PP-H \rightarrow PP\cdot + H_{2g}$	$10^{-5}, 10^{-6}, 10^{-7}$	2, c
$O^+ + PP-H \rightarrow PP\cdot + OH$	0.01	3
$O_2^+ + PP-H \rightarrow PP\cdot + H + O_2$	0.01	3
$He^+ + PP-H \rightarrow PP\cdot + H + He$	0.01	3
$NH_2^+ + PP-H \rightarrow PP\cdot + H + NH_2$	0.01	3
$NH^+ + PP-H \rightarrow PP\cdot + H + NH$	0.01	3
$h\nu + PP-H \rightarrow PP\cdot + H$	0.2	4, 5, d
$h\nu + PP-H \rightarrow \cdot PP + H_2$	0.2	4, 5, d
$h\nu + PP-H \rightarrow PP\cdot + CH_3$	0.2	4, 5, d
$PP\cdot + O_g \rightarrow PP-O\cdot$	$10^{-1}, 10^{-2}, 10^{-3}$	1, c
$PP\cdot + O_{2,g} \rightarrow PP-O_2\cdot$	$10^{-3}, 2.3 \times 10^{-4}, 5.0 \times 10^{-4}$	1, c
$PP\cdot + O_{3,g} \rightarrow PP-O\cdot + O_{2,g}$	1.0, 0.5, 0.5	1, c
$PP-O_2\cdot + PP-H \rightarrow PP-OOH + PP\cdot$	$5.5 \times 10^{-16} \text{ cm}^2 \text{ s}^{-1}$	1
$PP-O\cdot \rightarrow \text{aldehydes} + PP\cdot$	10 s^{-1}	1
$PP-O\cdot \rightarrow \text{ketones} + PP\cdot$	500 s^{-1}	1
$O_g + PP=O \rightarrow OH_g + \cdot PP=O$	0.04	1
$OH_g + PP=O \rightarrow H_2O_g + \cdot PP=O$	0.4	1

$O_g + \cdot PP=O \rightarrow CO_{2,g} + PP-H$	0.4	1
$OH_g + \cdot PP=O \rightarrow (OH)PP=O$	0.12	1
$PP-O\cdot + PP-H \rightarrow PP-OH + PP\cdot$	$8.0 \times 10^{-14} \text{ cm}^2 \text{ s}^{-1}$	1
$O_g + PP-OH \rightarrow PP-O + OH_g$	7.5×10^{-4}	1
$OH_g + PP-OH \rightarrow PP-O + H_2O_g$	8.2×10^{-3}	1
$PP-H + N_g \rightarrow PP-NH$	10^{-2}	e
$PP-H + NH_g \rightarrow PP-NH_2$	10^{-5}	f
$PP\cdot + N_g \rightarrow PP=NH$	0.4	e
$PP\cdot + NH_g \rightarrow PP-NH$	0.4	g
$PP\cdot + NH_{2,g} \rightarrow PP-NH_2$	0.4	6, k
$PP-NH + H_g \rightarrow PP-NH_2$	0.2	h
$PP-NH + H_g \rightarrow PP=NH + H_{2,g}$	10^{-6}	i
$PP-NH_2 + H_g \rightarrow PP-NH + H_{2,g}$	10^{-6}	j
$PP-NH_2 + OH_g \rightarrow PP-NH + H_2O_g$	0.0025	j
$PP=NH + H_{2(g)} \rightarrow PP-NH_2$	10^{-5}	k
$H_g + PP\cdot \rightarrow PP-H$	0.2	1
$OH_g + PP\cdot \rightarrow PP-OH$	0.2	1

^a Subscript g denotes gas phase species. PP-H denotes polypropylene.

^b Coefficients without units are reaction probabilities.

^c For tertiary, secondary, and primary carbon centers respectively.

^d Pathways described in [5] for energetic photons; quantum yield estimate from [4].

^e Insertion analogous to gas phase reaction in [8] followed by double bond formation.

^f Insertion analogous to gas phase reaction in [7]

^g By analogy to NH₂.

^h By analogy to reactions with alkyl radicals in [1].

ⁱ Proposed abstraction of H followed by double bond formation.

^j By analogy to reactions with alkanes in [9].

^k By analogy to gas phase reactions in [9].

D. 1 References

1. R. Dorai and M. J. Kushner, *Journal of Physics D*, **36**, 666 (2003).
2. By analogy with gas phase abstraction reactions of H with alkanes.
3. F. Tochikubo, T. Chiba and T. Watanabe, *Japanese Journal of Applied Physics*, **38**, 5244 (1999).
4. E. V. Kuvaldina, V. V. Rybkin, V. A. Titov, T. G. Shikova and D. A. Shutov, *High Energy Chemistry*, **38**, 411 (2004).
5. V. E. Skurat and Y. I. Dorofeev, *Die Angewandte Makromolekulare Chemie*, **216**, 205 (1994).
6. R. Lesclaux and M. Desmissy, *International Journal of Chemical Kinetics*, **14**, 1 (1982).
7. Z. B. Alfassi, ed., *N-centered Radicals*, John Wiley and Sons, West Sussex, England (1998).
8. J. T. Herron, *Journal of Physical and Chemical Reference Data*, **28**, 1453 (1999).
9. *NIST Standard Reference Database 17-2Q98* (National Institute of Standards and Technology, Gaithersburg, MD, 1998).